AD NUMBER

AD869823

LIMITATION CHANGES

TO:

Approved for public release; distribution is unlimited.

FROM:

Distribution authorized to U.S. Gov't. agencies and their contractors; Critical Technology; MAR 1970. Other requests shall be referred to U.S. Army Aviation Materiel Laboratories, Fort Eustis, VA 23604. This document contains export-controlled technical data.

AUTHORITY

USAAMRDL ltr, 18 Jun 1971

USAAVLABS TECHNICAL REPORT 70-2

INVESTIGATION OF HELICOPTER CONTROL LOADS INDUCED BY STALL FLUTTER

By

P. J. Arcidiacono
F. O. Carta
L. M. Casellini
H. L. Elman

March 1970

U. S. ARMY AVIATION MATERIEL LABORATORIES
FORT EUSTIS, VIRGINIA

CONTRACT DAAJ02-68-C-0048
SIKORSKY AIRCRAFT
DIVISION OF UNITED AIRCRAFT CORPORATION
STRATFORD, CONNECTICUT

DISCLAIMER NOTICE

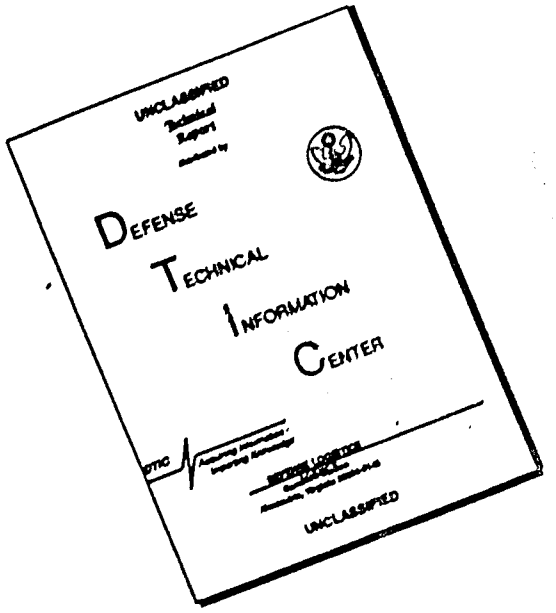

THIS DOCUMENT IS BEST QUALITY AVAILABLE. THE COPY FURNISHED TO DTIC CONTAINED A SIGNIFICANT NUMBER OF PAGES WHICH DO NOT REPRODUCE LEGIBLY.

Disclaimers

The findings in this report are not to be construed as an official Department of the Army position unless so designated by other authorized documents.

When Government drawings, specifications, or other data are used for any purpose other than in connection with a definitely related Government procurement operation, the United States Government thereby incurs no responsibility nor any obligation whatsoever; and the fact that the Government may have formulated, furnished, or in any way supplied the said drawings, specifications, or other data is not to be regarded by implication or otherwise as in any manner licensing the holder or any other person or corporation, or conveying any rights or permission, to manufacture, use, or sell any patented invention that may in any way be related thereto.

Disposition Instructions

Destroy this report when no longer needed. Do not return it to the originator.

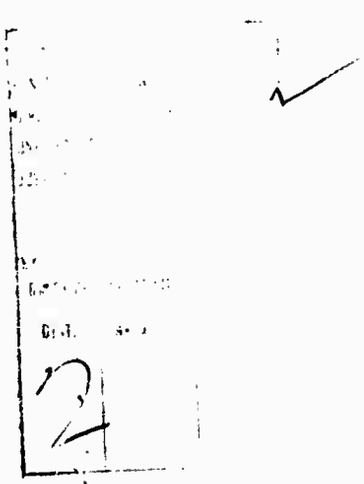

DEPARTMENT OF THE ARMY
US ARMY AVIATION MATERIEL LABORATORIES
FORT EUSTIS, VIRGINIA 23604

This report has been reviewed by the U. S. Army Aviation Materiel Laboratories. It is considered that limitations in availability of oscillating airfoil properties and certain linearizations limit the immediate application of this analysis. Nonetheless, it is believed that this work offers a significant contribution toward the development of a more comprehensive analysis as pertinent factors become available.

The report is published for the dissemination of information and the stimulation of thought.

Task 1F162204A14604
Contract DAAJ02-68-C-0048
USAAVLABS Technical Report 70-2
March 1970

INVESTIGATION OF HELICOPTER CONTROL LOADS INDUCED BY STALL FLUTTER

Final Report

By

P. J. Arcidiacono
F. O. Carta
L. M. Casellini
H. L. Elman

Prepared By

Sikorsky Aircraft
Division of United Aircraft Corporation
Stratford, Connecticut

for

U. S. ARMY AVIATION MATERIEL LABORATORIES
FORT EUSTIS, VIRGINIA

ABSTRACT

An analytical study was conducted to determine if available unsteady normal force and moment aerodynamic test data could be used in conjunction with existing helicopter rotor aeroelastic and variable inflow analyses to provide a method for predicting the stall flutter response of a helicopter rotor blade. For this purpose, incompressible unsteady aerodynamic data for an NACA 0012 airfoil executing pure sinusoidal pitching motions were employed. To apply such data under rotor blade operating conditions where multiharmonic motions and velocity variations exist, the data were expressed as functions of instantaneous section angle of attack, angular velocity, and angular acceleration. In addition, scaling procedures were developed in an attempt to account for the effects of compressibility.

Limited application of the resulting analysis to define the aeroelastic characteristics of several blade designs showed that significant self-excited torsional oscillations of the stall flutter type could, in fact, be predicted for certain combinations of flight conditions and blade designs. Correlation studies, to evaluate the ability of the analysis to predict control loads, were performed with CH-53A maneuvering flight test data and with level flight test data from the NH-3A (S-61F). Although the analyses produced self-excited stall flutter oscillations, the degree of correlation indicates the need for further development. In level flight, the oscillations occurred only at rotor thrusts in excess of those observed in flight tests. Oscillations were predicted during certain maneuvers with good agreement with the persistence of stall flutter and the azimuthal onset of the oscillation. Although essential to the prediction of stall flutter, unsteady aerodynamics are shown to result in a degradation of blade bending stress prediction, which appears to be a significant factor affecting control load correlation.

It is recommended that studies be undertaken to investigate the validity of a basic assumption of this analysis; namely, that unsteady aerodynamic characteristics of an airfoil subjected to a nonsinusoidal angle of attack variation into stall can be synthesized from unsteady data obtained for sinusoidal motions. In addition, attempts should be made to improve the accuracy of the analytical method described in this report through possible semiempirical modifications to the unsteady data and scaling techniques as well as possible refinements to rotor trimming and inflow modeling procedures.

TABLE OF CONTENTS

LIST OF ILLUSTRATIONS

LIST OF TABLES

LIST OF SYMBOLS

a	lift curve slope, Eq. (2)
a_0	dimensionless distance of pitch axis downstream of the mid-chord, in semichords, Eq. (4)
A	angular velocity parameter $\frac{c\dot{\alpha}}{2U}$, Eq. (12)
A_1, B_1	arbitrary values of A and B
A_{1_S}	lateral cyclic pitch, coefficient of $-\cos\psi$ term in Fourier expansion of θ_0, deg or rad
b	number of rotor blades
B	angular acceleration parameter $\left(\frac{c}{2U}\right)^2\ddot{\alpha}$, Eq. (13)
B_{1_S}	longitudinal cyclic pitch, coefficient of $-\sin\psi$ term in Fourier expansion of θ_0, deg or rad
c	blade chord, ft
c_d	section drag coefficient: section drag force per unit span divided by $\frac{1}{2}\rho U^2 c$
c_l	section lift coefficient: section lift force per unit span divided by $\frac{1}{2}\rho U^2 c$
cg	abbreviation indicating section center of gravity
C_{BPM}	blade pitching moment about the blade elastic axis, evaluated at the root of the blade and divided by $\rho\pi R^3(\Omega R)^2$, positive nose up
C_L	rotor lift coefficient: rotor lift divided by $\rho\pi R^2(\Omega R)^2$
c_m	section pitching moment coefficient (a_0 axis): section aerodynamic pitching moment about the axis at a_0 divided by $\frac{1}{2}\rho U^2 c^2$, positive nose up
$c_{m_{c/4}}$	section aerodynamic pitching moment coefficient (quarter-chord): section aerodynamic pitching moment about the quarter-chord divided by $\frac{1}{2}\rho U^2 c^2$, positive nose up

c_n	section normal force coefficient: section aerodynamic force normal to chord divided by $\frac{1}{2}\rho U^2 c$
$c_{n_{max,u}}$	maximum unsteady normal force coefficient, Eq. (3) and Figure 3
$c_{n_{STALL,SS}}$	steady-state normal force coefficient at the stall angle, Eq. (3)
C_{PF}	rotor propulsive force coefficient: rotor propulsive force divided by $\rho\pi R^2(\Omega R)^2$
C(k)	Theodorsen circulation function, Eq. (6)
C_T	rotor thrust coefficient: rotor thrust divided by $\rho\pi R^2(\Omega R)^2$
f	oscillatory frequency in pitch, cps
F(k)	real part of Theodorsen function, Eq. (6)
g	acceleration of gravity, ft/sec^2
G(k)	imaginary part of Theodorsen function, Eq. (6)
i	$\sqrt{-1}$
k	reduced frequency parameter, Eq. (14)
M	Mach number
M_1, M_2	limit Mach numbers to which scaled unsteady aerodynamic data are used for α's above and below steady-state stall (see Fig. 31)
q_{θ_j}	amplitude of j^{th} elastic torsional mode
$\bar{r}$	nondimensional radial coordinate, local radius/R
R	rotor radius, ft
t	time, sec
U_p	component of U nominally in plane of blade span and rotor shaft axis and normal to local span axis, ft/sec

U_T	component of U parallel to plane of rotation and normal to local span axis of blade, ft/sec
U	velocity relative to airfoil, ft/sec, Eq. (4)
V	flight velocity, ft/sec
$y_{IO_{cg}}$	local distance between elastic and center-of-gravity axes of blade, positive when cg axis is between the elastic axis and the leading edge, ft
α	section angle of attack, deg or rad
α^*	complex section angle of attack, deg or rad, Eq. (4)
$\bar{\alpha}$	amplitude of oscillatory component of α, deg or rad, Eq. (7)
α_M	mean value of α, deg or rad, Eq. (7)
$\alpha_{max,\mu}$	maximum unsteady angle of attack, deg or rad, Eq. (3) and Figure 3
α_{OL}	section angle of attack for zero lift, deg or rad, Eq. (1) and Figure 3
α_s	rotor shaft angle of attack, positive when tilted downstream, deg or rad
α_{sm}	steady-state stall angle for pitching moment coefficient, deg or rad, Tables III, IV
α_{sn}	steady-state stall angle for normal force coefficient, deg or rad, Eq. (17), Tables III, IV
α_{75}	section angle of attack at 75 percent blade span
β	blade flap angle, deg or rad
γ_{θ_j}	j^{th} torsional uncoupled mode shape
$\Delta\psi$	increment of azimuth angle, deg or rad
θ_e	local elastic twist angle, $\sum_{j=1}^{2} \gamma_{\theta_j} q_{\theta_j}$

θ_0	blade pitch angle due to control system input, deg or rad
θ_1	rate of change of local blade pitch angle due to built-in linear twist with respect to blade spanwise direction, positive when tip is twisted nose up relative to root, deg or rad
θ_{75}	blade collective pitch as measured at three-quarter span station, deg or rad
μ	rotor advance ratio, $V \cos \alpha_S / \Omega R$
$\Xi_{\alpha 2}$	two-dimensional aerodynamic damping parameter in pitch, Figure 14
ρ	air density, lb-sec^2/ft^4
σ	rotor solidity, $(bc/\pi R)$
σ_m	pitching moment stall angle parameter
σ_n	normal force stall angle parameter, Eq. (17)
ϕ	local inflow angle, $\tan^{-1} \frac{U_P}{U_T}$, deg or rad
ψ	blade azimuth angle measured from downstream blade position, $\psi = \Omega t$, deg or rad
ω	frequency, rad/sec
ω_{θ_j}	frequency of j^{th} torsional mode, rad/sec
$\bar{\omega}_{\theta_1}$	ratio of ω_{θ_1} to Ω
Ω	rotor angular velocity, rad/sec

SUBSCRIPTS

A	denotes quantity evaluated at specific value of A
B	denotes quantity evaluated at specific value of B
M	denotes quantity evaluated at specific value of M

SUPERSCRIPT

$(\ )^*$	denotes complex quantity

MISCELLANEOUS

$(\overset{x}{\ })$	derivative of ( ) with respect to ψ
$(\dot{\ })$	derivative of ( ) with respect to t
$\frac{1}{2}$PTP	abbreviation of $\frac{1}{2}$ peak-to-peak
P	abbreviation denoting cycles per rotor revolution; e.g., 8P indicates a frequency of 8 cycles per rotor revolution

INTRODUCTION

The subject investigation was conducted jointly by Sikorsky Aircraft and United Aircraft Research Laboratories under U. S. Army Aviation Materiel Laboratories Contract DAAJ02-68-C-0048. The objective was to determine whether existing unsteady aerodynamic test data and rotor aeroelastic analyses can accurately predict stall-flutter-induced control loads.

The maximum speed of helicopters is currently limited by the occurrence of stall on the retreating blades of the rotor. Such stall manifests itself in a performance degradation and, more importantly, in an increase in the vibratory loads generated by the rotor. In particular, the buildup in control system loads as steady-state stall angles are exceeded on the rotor appears to be critical and is believed to be directly associated with the occurrence of stall flutter of the blades (see, for example, References 1 through 4). Stall flutter is defined as a self-excited, single-degree-of-freedom torsional oscillation of an elastic blade which can occur when the blade is operated at angles above stall. Such oscillations impose large moments on the rotor control system and are often the determining factor in limiting the maximum speed of a helicopter.

It is now well established that classical rotor theories are incapable of predicting overall rotor performance characteristics in stall (References 5 through 9), let alone the details of rotor loading required for the accurate definition of critical vibratory loads. Such theories generally assume that two-dimensional, steady-state airfoil data are applicable and, further, that the inflow velocities induced at the rotor blades by the vortex system (or wake) of the rotor are constant with respect to both time and space. In an attempt to provide a more suitable analysis for predicting self-excited control system loads, available two-dimensional unsteady airfoil data have been integrated into an existing aeroelastic variable inflow analysis for rotors. This modified analysis will hereafter be referred to as the Modified UAC Rotor Analysis. The unsteady data originally considered for this purpose were those presented in References 10 and 11 for airfoils executing pure sinusoidal pitching motion (i.e., motion having but one harmonic or frequency component). However, as discussed in this report, only the data for Reference 10 were ultimately used to obtain the results presented. Since rotor blades do not execute pure sinusoidal motion as they penetrate the stall regime, a unique feature of this investigation was the conversion of the available sinusoidal results to a more general form in which the local section normal force and moment are expressed in terms of instantaneous section angle of attack, angular velocity, angular acceleration, and Mach number. A conversion of this type, or its equivalent, is required before section forces and moments associated with typical rotor blade angle of attack variations can be computed in a rational manner.

The portion of the study conducted by the Research Laboratories had as its principal objectives: (1) the generalization of the available sinusoidal unsteady data to the form described above, (2) the integration of the generalized data into the existing rotor analysis, and (3) the

application of the resulting analysis to investigate the effect of certain blade design and operating conditions on blade stall flutter characteristics. In addition, since there was some evidence that sustained stall flutter could be encountered in certain aircraft maneuvers, a final objective of the Research Laboratories efforts involved the modification of the existing rotor analysis to include the effect of prescribed fuselage motions on blade aerodynamic and dynamic forces.

Sikorsky Aircraft conducted a correlation study which had as its objective the determination of the accuracy of the analyses developed. The correlation study included comparison of analysis with NH-3A (S-61F) level flight and CH-53A maneuvering flight test data. CH-53A correlation used a constant inflow model, while both constant and variable inflow are used in the NH-3A analysis. In an attempt to account for rotor-wing interference, a semiempirical modification to the NH-3A inflow model was included. Further studies of the mechanism of stall flutter were initiated because of instability in regions of the rotor disc where the blades appear to be free from stall.

METHOD OF ANALYSIS

The results presented in this report were obtained using the Modified UAC Rotor Analysis. This section of the report describes the technical features of the analysis, indicates the nature of the modifications made as part of the present investigation, and summarizes the assumptions made.

MODIFIED UAC ROTOR ANALYSIS

A simplified block diagram of the Modified UAC Rotor Analysis is shown in Figure 1. As indicated, there are two principal parts to the overall analysis. The first is the Blade Response Program, where the motions of the rotor blade are computed for a given combination of blade control angles, fuselage motions, and distribution of induced velocity over the rotor disc. The second part, namely, the Circulation Program, is used to compute the velocities (rotor inflow) induced at the rotor by its vortex system (rotor wake). Because of the complexity of the rotor aeroelastic problem, it is necessary to perform an iteration, using the programs as shown, to insure that the input and output quantities of each are reasonably self-consistent. The principal modifications to the basic analysis incorporated as part of this study (indicated in Figure 1 by the dashed arrows) include (1) use of unsteady, two-dimensional normal force and pitching moment aerodynamic coefficients in certain blade section operating regimes and (2) modification of the blade equations of motion to include aerodynamic and dynamic forces associated with prescribed time histories of fuselage motion and blade control angles. A more detailed description of the two individual programs is presented below.

Blade Response Program

This program determines the fully coupled response of a flexible rotating blade, given the distribution of induced velocities over the disc, the blade control angles, and the fuselage motions. The blade deflection is expanded in terms of its uncoupled natural vibratory modes (normal modes). The normal mode technique is widely used to solve aeroelastic problems (see, for example, Reference 12, p. 125) and facilitates the numerical integration of the blade equations of motion through elimination of dynamic coupling terms. In this investigation, the blade response is assumed to be composed of a rigid-body flapping mode, three elastic flatwise modes, a rigid-body lagging mode, two elastic edgewise modes, and two elastic torsional modes. The basic differential equations of motion governing the response of each of the blade modes are given in Reference 13

for rotor blades having chordwise mass unbalance and operating in steady, level flight. The dynamic and aerodynamic terms associated with accelerated flight of the aircraft are given in Reference 14 for mass balanced blades. For this investigation, these terms were added directly to the equations of motion of Reference 13. (This, in effect, assumes that terms involving cross products of the nondimensional fuselage accelerations and the chordwise distance between the center of gravity and elastic axes are of second order and can be neglected.) For convenience, the specific modifications to the important equations of Reference 13 are given in Appendix I.

The aerodynamic model used in the analyses of References 13 and 14 was based on the use of steady-state, two-dimensional airfoil data. In accordance with quasi-steady theory (Reference 12, p. 279), (1) the local section angle of attack was defined by the velocity components at its three-quarter chord point and (2) the theoretical damping moment in pitch was included. In defining the local angle of attack, the inflow at the rotor induced by the vortex system representing the rotor wake was included using an analysis similar to that of Reference 15. Before this basic type of analysis could be applied to the stall flutter problem, it was necessary to incorporate a better representation of the effects of the shed wake vorticity (wake vorticity arising from timewise variation of blade bound vorticity) at all angles of attack, particularly those above steady-state stall. To accomplish this, an attempt was made to replace, where possible, steady-state airfoil data by unsteady data. The latter were derived from available data for a two-dimensional airfoil executing forced, pure sinusoidal pitching motion and operating at a constant air velocity (hereafter referred to as sinusoidal data). Under such conditions, the reduced frequency parameter $k = c\omega/2U$ is constant with time. Conversely, typical rotor blade section operating conditions involve variations in k due to changes in both the velocity of the section U and the effective frequency of the motion ω that occur as the blade rotates. A rigorous method for applying sinusoidal data, particularly above stall, has not been established. In this investigation, it has been hypothesized that the sinusoidal data could be generalized, through cross plots, to functions of section instantaneous angle of attack, angular velocity, angular acceleration, and Mach number. Given the local values of these parameters for each section, the unsteady lift and moment of each section can be computed.

As originally envisioned, unsteady normal force and moment data from References 10 and 11 for the NACA 0012 airfoil were to be generalized to functions of the parameters noted above, with the Mach number range covered extending up to 0.6. However, it was found that the test matrix employed in Reference 11 was not sufficiently complete to permit conversion of the data by the process described in Appendix II. Therefore, an attempt was

made to scale the incompressible data of Reference 10 to approximate compressibility effects. The scaling relations that were employed basically assume that the ratio of actual angle of attack to steady-state stall angle is the critical parameter that must be duplicated. This is discussed in more detail in a later section. Provision was made in the program for investigating the sensitivity of the results to certain of the parameters introduced by the scaling procedures, in particular the Mach number range over which the incompressible unsteady data are scaled. The results of the sensitivity studies are also discussed in a later section. Conventional, steady-state lift and moment data for the NACA 0012 airfoil section were used for those combinations of angle of attack and Mach number for which either unsteady data were not available or the scaling procedures were suspect. Thus, for example, steady-state data were used for reverse flow operating conditions because applicable unsteady data were not available. Also, because of the effect of Mach number on airfoil stall characteristics, use of scaled, incompressible unsteady data at conditions involving Mach numbers above 0.5 and angles of attack above steady-state stall was not considered valid. Finally, steady-state drag data were used throughout the program. Further discussion of the treatment of the unsteady data is given in the section of the report entitled UNSTEADY AIRFOIL DATA.

The modified modal equations are nonlinear and are solved using a numerical integration technique to permit realistic coupling between the airloads and the blade response. The procedure thus has the capability of analyzing transient as well as forced-response motions. The calculation generally proceeds by alternately computing the modal accelerations (from the generalized forces exciting each mode) at a given blade azimuth angle ψ and numerically integrating these accelerations over a small azimuth increment $\Delta\psi$ to determine the modal displacements and velocities at the next blade azimuth ($\psi + \Delta\psi$). To avoid possible mathematical convergence problems with such a procedure, it is necessary that (1) $\Delta\psi$ be small and (2) the accelerations of a given mode not be expressed in terms of the acceleration of any other mode. These requirements present no difficulty with a normal mode type of analysis when the rotor is in steady flight and when conventional, steady aerodynamic characteristics are used to define blade airloads. When accelerated flight is considered in conjunction with the particular unsteady aerodynamic formulation of section normal force and moment discussed previously, the generalized force exciting each mode becomes a function of the various modal accelerations as well as a function of the fuselage accelerations. In determining the results presented, it was assumed that (1) the fuselage accelerations were prescribed in advance (e.g., from flight test results) and, initially, (2) the blade section angular acceleration parameter β used in part to define the unsteady aerodynamic coefficients could be determined from numerical differentiation of

the previously generated local angle of attack time history. The former assumption is believed to be justified because of the relatively low frequency of the fuselage compared to that of the blades. The latter assumption implies that the calculated value of B will lag the true value. The results of initial calculations indicated that significant values of B were generated only when a high-frequency, stall flutter type of torsional oscillation occurred. This suggested the possibility of approximating B by the expression

$$B = \left(\frac{c}{2U}\right)^2 \ddot{\alpha} = \left(\frac{c}{2U}\right)^2 \left(\ddot{\theta}_0 + \ddot{\phi} + \sum_{j=1}^{2} \gamma_{\theta_j} \ddot{q}_{\theta_j}\right) \cong \left(\frac{c}{2U}\right)^2 \gamma_{\theta_1} \ddot{q}_{\theta_1}$$

where the second portion of this expression is the component representation of total section angular acceleration. This approach, which permitted the azimuthal lag in B to be reduced to the order $\Delta\psi$ (approximately 3 deg), was used in obtaining the results presented herein. (Further details on the concept of the angular acceleration parameter will be presented in the next section of this report.)

Pertinent output from the Blade Response Program for this study consisted primarily of integrated rotor loads (thrust, propulsive force, etc.), time histories of section operating conditions (α, A, B), section aerodynamic coefficients (c_l, $c_{m_{c/4}}$, c_d), blade elastic response, and pitching moment at the blade root (i.e., pitching moment imposed on the control system).

Circulation Program

The function of this program is to compute the circulation distribution over the rotor, given the distributions of section angle of attack α, angular velocity parameter A, and angular acceleration parameter B over the blade, as well as a specified geometry of the rotor wake. For this study, the wake was approximated by the classical skewed helicoid defined when the vortex elements generated by the blade are convected downstream relative to the blade at a resultant velocity equal to the vector sum of the blade rotational velocity, rotor forward velocity, and average momentum velocity through the disc. Once the circulation distribution is known, the inflow velocities induced at the blade by the bound and wake vorticity of the rotor can be computed. An iteration between the Circulation and Blade Response Programs is then used to assure compatibility of the inflow velocities and the blade aerodynamic and dynamic boundary conditions (see, for example, Figure 1).

The technical approach used in the Circulation Program is basically similar to that described in Reference 15 and generally represents a rotary-wing equivalent of the classical lifting-line approach used successfully for fixed wings. There are, however, some differences between the UAC Circulation Program and that described in Reference 15. These are discussed below.

The first of these differences is the elimination of all shed vorticity elements (elements arising from variations of blade bound vorticity with time) in the wake model, a modification that contributed substantially to reducing computing time without significantly altering computed circulations and associated inflow velocities. Thus, the only vortex elements retained in the wake are trailing elements; i.e., those arising from spanwise variations in bound circulation. As in Reference 15, the strength of the trailing elements is permitted to vary from point to point in the wake to reflect the variation in bound circulation that occurs as the blade rotates. It is believed that a more accurate representation of shed vorticity effects is obtained by the previously mentioned use of unsteady airfoil data in the Blade Response Program. The use of two-dimensional, unsteady data basically implies that the primary effects of the shed vorticity in a helical rotor wake are due to the wake region near the blade and thus can be approximated by those in a fixed-wing type of wake, as indicated in Figure 2. Miller, in Reference 16, shows that this approximation is reasonable at rotor advance ratios μ of interest to this study. This type of approach greatly facilitates the inclusion of nonlinear, unsteady aerodynamic effects due to stall.

Another significant difference between the UAC Circulation Program and that of Reference 15 lies in the treatment of unsteady effects on lift curve slope a, angle for zero lift α_{OL}, and stall angle $\alpha_{max,u}$. In Reference 15, steady-state values were used for these quantities. In the present study, a, α_{OL}, and $\alpha_{max,u}$ were considered to be functions of the section angular velocity and angular acceleration parameters as well as Mach number. As in Reference 15, the local bound circulation is assumed to be proportional to section angle of attack (measured from the zero lift angle) until $\alpha_{max,u}$ is reached, following which no further increase in circulation is permitted. To determine the functional relationships involved, the normal force data of Reference 10 (also presented in Table I) were plotted and approximated as in Figure 3. The results are shown in Figure 4 for incompressible flow, and the effect of Mach number on these results was approximated by using the following equations:

$$(\alpha_{OL})_{M,A,B} = (\alpha_{OL})_{M=0,A,B} \tag{1}$$

$$(a)_{M,A,B} = \frac{(a)_{M=0,A,B}}{\sqrt{1-M^2}} \tag{2}$$

$$(\alpha_{max,u})_{M,A,B} = (\alpha_{OL})_{M,A,B} + \frac{1}{(a)_{M,A,B}} \frac{(c_{n_{STALL,SS}})_M}{(c_{n_{STALL,SS}})_{M=0}} (c_{n_{max,u}})_{M=0,A,B} \tag{3}$$

These equations state that (1) the angle for zero lift is independent of Mach number, (2) the variation of unsteady lift curve slope in potential flow with Mach number follows the Prandtl-Glauert relation, and (3) the unsteady stall angle of attack at any Mach number can be determined from the assumption that the variation in maximum unsteady lift coefficient with Mach number follows the same variation as the maximum steady-state lift coefficient.

Finally, provision has been made in the UAC Circulation Program to eliminate unrealistically large induced velocities which would otherwise be computed if the lifting line representing the blade section was very near a vortex element. This was formally accomplished by setting such velocities to zero whenever the distance between any blade section and vortex element was less than a prescribed distance assumed to be equal to the vortex core radius. This distance was selected as 0.02R, a value believed to be representative.

It is recognized that factors such as self-induced rotor wake distortions (Reference 17) and finite blade chord effects have been neglected. Their inclusion, however, was beyond the scope of this investigation.

SUMMARY OF ASSUMPTIONS

Since major portions of the Modified UAC Rotor Analysis used in the performance of this study are documented elsewhere in the literature (References 13 through 15), the principal assumptions discussed herein and in those references are summarized below for the convenience of the reader.

1. The aircraft is in steady, level flight or in accelerated flight where the fuselage velocities and accelerations are prescribed. The rotor rotational velocity is constant.

2. Two-dimensional unsteady normal force and moment data obtained for an airfoil executing forced sinusoidal pitch oscillations under constant velocity conditions can be applied under rotor blade operating conditions involving velocity variations and multiharmonic angle of attack variations. It is assumed that this application can be accomplished by generalizing the basic data to functions of section angle of attack, angular velocity, and angular acceleration.

3. The effects of compressibility on unsteady airfoil characteristics can be approximated by scaling the generalized incompressible unsteady data using scaling procedures that generally predict the effect of compressibility on steady-state airfoil characteristics.

4. Quasi-steady, two-dimensional aerodynamic theory is applicable for those blade sections operating at conditions of high Mach number and high angle of attack or in reversed flow.

5. Section drag coefficients are given by steady-state values.

6. The velocities induced at the rotor by the vortex system representing the rotor wake can be computed using a lifting-line type of analysis in which wake distortions are neglected.

7. The blade has an elastic axis so that blade deflections can be considered as the superposition of two orthogonal translations of this axis and a rotation about it.

8. Principal blade flexibility effects can be accounted for by considering only three flatwise, two edgewise, and two torsional vibratory modes.

9. Blade flap and lag hinges are coincident for articulated rotors.

10. The local center of gravity is assumed to lie on the major principal axis of the section.

11. The blade is linearly twisted along its span.

12. The following quantities can be assumed to be small in comparison to unity:

    a. Flap and lead angles (in radians) and their derivatives

    b. Ratios of elastic deflections to rotor radius and their derivatives

    c. Ratios of chordwise distances (i.e., chord, center-of-gravity offset, etc.) to rotor radius

    d. Built-in twist (in radians)

    e. Ratio of flap-lag hinge radial distance from center of rotation to rotor radius

    f. Froude number $(g/\Omega^2 R)$

    g. Ratios of blade thickness dimensions to chord

    h. Ratios of fuselage angular velocities to rotor angular velocity; ratios of fuselage angular accelerations to square of rotor angular velocity.

13. On the basis of Assumptions 11 and 12, the following types of terms in the equations noted can be neglected as higher order:

    a. Flatwise and edgewise bending equations:

        (1) Second-order products involving elastic coordinates, fuselage angular velocities, fuselage accelerations, and distance between blade elastic axis and center-of-gravity axis.

        (2) Third-order products involving elastic coordinates, chordwise distances, flap angle, lead angle, built-in twist, and flap-lag hinge offset.

    b. Torsional equation:

        (1) Third-order products involving elastic coordinates, fuselage angular velocities, fuselage accelerations, and distance between blade elastic axis and center-of-gravity axis.

(2) Fourth-order products involving elastic coordinates, chordwise distances, flap angle, lead angle, built-in twist, and flap-lag hinge offset.

c. Flap angle and lead angle equations - second-order terms involving products of elastic coordinates, fuselage angular velocities, fuselage accelerations, chordwise distances, and built-in twist.

d. Section velocity equations:

(1) Second-order products of elastic coordinates

(2) Third-order products involving the elastic coordinates, chordwise distances, flap angle, lead angle, built-in twist, and flap-lag hinge offset as factors.

e. All equations - the spanwise component of acceleration due to gravity.

UNSTEADY AIRFOIL DATA

DESCRIPTION OF ORIGINAL UAC DATA

The oscillating airfoil data used in the present analysis were obtained in an experiment previously conducted at the United Aircraft Research Laboratories (UARL) for the Sikorsky Aircraft Division (Reference 10). Portions of these data were used in a previous analysis of incipient stall flutter sponsored by USAAVLABS, and a complete description of the test program will be found in Reference 2. A brief summary of the test program is included herein to provide necessary background for subsequent sections of this report.

The test data were obtained from differential pressure transducers mounted on a 2-ft-chord NACA 0012 model. The tests were conducted in the two-dimensional channel of the UARL 8-ft main wind tunnel. Data were obtained for most, but not all, combinations of the following parameter values:

Amplitude of motion, $\bar{\alpha} = \pm 4, 6, 8$ deg
Mach number, $M = 0.2, 0.3, 0.4$
Mean angle of attack, $\alpha_M = 0$ to 33 deg in 3-deg increments
Frequency, $f = 0.0, 0.5, 1, 2, 4, 8, 12, 16$ cps

The actual points for which data were taken can be found in Tables I, II, and III of Reference 2, for $M = 0.2$, 0.3, and 0.4, respectively. It can be seen from these tables that most of the test points were taken at the lower Mach numbers and at the higher amplitudes. This fact influenced certain choices that were made in the course of the data analysis and which will be described in subsequent sections.

GENERALIZATION OF UAC UNSTEADY SINUSOIDAL DATA

Conversion of Data to α, A, B Dependency

Earlier in this report, it was pointed out that it was necessary to operate on data obtained from sinusoidal tests to provide a set of coefficients applicable to operating conditions for a helicopter rotor blade, where several harmonics of motion are present. No definitive analytical or experimental study has been conducted regarding the best procedures for applying sinusoidal data under such conditions. In this investigation, it has been hypothesized that the sinusoidal data can be

generalized by converting them to functions of the instantaneous angle of attack α, angular velocity parameter A, and angular acceleration parameter B for a given Mach number. A necessary (but not a sufficient) condition for the validity of this approach lies in the ability to characterize the essential features of the sinusoidal data in terms of only these three parameters. While such is the case in potential flow, as shown below, the ability to do so in nonpotential flow had not been completely proven. Even assuming that the essential features of the sinusoidal data can, in fact, be adequately expressed in terms of α, A, and B, it remains to be shown that such a characterization will predict unsteady aerodynamic characteristics in nonpotential flow for multi-harmonic motions. This can be demonstrated only by correlation with experimental results. The theoretical background and the broad concepts of the data conversion technique used in the present study are described below. A detailed discussion of the process used is given in Appendix II.

Consider first the case of a linearized, potential, incompressible flow past an airfoil oscillating sinusoidally in pitch. The normal force coefficient c_n and the pitching moment coefficient c_m can be expressed in terms of three constant coefficients which multiply the angular displacement α, the angular velocity $\dot{\alpha}$, and the angular acceleration $\ddot{\alpha}$ (see p. 272 of Reference 12). (The theoretical moment coefficient given below is resolved about an axis at a_0, measured in semichords aft of the midchord of the blade in accordance with accepted practice. The experimentally determined moment coefficient, from Reference 10, is referred to later in the text as $c_{m_{c/4}}$.)

$$c_n^* = 2\pi C(k)\alpha^* + \frac{\pi c}{2U}\left[1 + 2C(k)\left(\frac{1}{2} - a_0\right)\right]\dot{\alpha}^* - \pi a_0\left(\frac{c}{2U}\right)^2\ddot{\alpha}^* \qquad (4)$$

$$c_m^* = \pi\left(a_0 + \frac{1}{2}\right)C(k)\,\alpha^* + \frac{\pi c}{2U}\left(\frac{1}{2} - a_0\right)\left[\left(a_0 + \frac{1}{2}\right)C(k) - \frac{1}{2}\right]\dot{\alpha}^* - \frac{\pi}{2}\left(\frac{c}{2U}\right)^2\left(\frac{1}{8} + a_0^2\right)\ddot{\alpha}^* \qquad (5)$$

In these equations the starred quantities are complex. However, following tradition, the Theodorsen circulation function

$$C(k) = F(k) + iG(k) \qquad (6)$$

will remain unstarred.

The complex angle of attack α^* may be expressed as the sum of the mean angle of attack α_M and the instantaneous displacement from the mean $\bar{\alpha} e^{i\omega t}$ or

$$\alpha^* = \alpha_M + \bar{\alpha} e^{i\omega t} \tag{7}$$

This expression implies that the C_n and C_m responses each consist of a steady part dependent on the mean angular position, and an unsteady, time-dependent part associated with the instantaneous displacement from the mean. These steady-state force and moment expressions are not included in Eqs. (4) and (5) because the original expressions in Reference 12 were written for displacements relative to the mean position. Hence, in making use of these equations, one must be careful to include an additional term in each of them to account for the steady-state response. This is done later in Appendix III.

Equation (7) has a real part given by

$$\alpha = \alpha_M + \bar{\alpha} \cos\omega t \tag{8}$$

and the first two time derivatives of the real part can be written as

$$\dot{\alpha} = -\omega\bar{\alpha}\sin\omega t = \pm\omega\sqrt{\bar{\alpha}^2 - (\alpha - \alpha_M)^2} \tag{9}$$

$$\ddot{\alpha} = -\omega^2\bar{\alpha}\cos\omega t = -\omega^2(\alpha - \alpha_M) \tag{10}$$

The second form of each equation is obtained by eliminating the time parameter through the use of elementary trigonometric identities. At this point, it is convenient to define the dimensionless angular velocity parameter A and the dimensionless angular acceleration parameter B, which together with Eq. (8) make up the fundamental three-parameter set of the present study,

$$\alpha = \alpha_M + \bar{\alpha}\cos\omega t \tag{11}$$

$$A \equiv \frac{c\dot{\alpha}}{2U} = \pm k\sqrt{\bar{\alpha}^2 - (\alpha - \alpha_M)^2} \tag{12}$$

$$B \equiv \left(\frac{c}{2U}\right)^2 \ddot{\alpha} = -k^2(\alpha - \alpha_M) \tag{13}$$

where k is the reduced frequency for sinusoidal motion, defined by the expression

$$k = \frac{c\omega}{2U} \tag{14}$$

Conceptually, Eqs. (4) and (5) can be expressed in real form as functions of the angular displacement, angular velocity, and angular acceleration; hence, both c_n and c_m can be functionally written in terms of the fundamental three-parameter set, α, A, B, as

$$c_n = c_n(\alpha, A, B) \tag{15}$$

$$c_m = c_m(\alpha, A, B) \tag{16}$$

The conversion of Eqs. (4) and (5) to this functional form for potential flow is a relatively straightforward task and is done in Appendix III. In the case of nonpotential flow (i.e., for incidence angles greater than the stalling angle), the relationships are no longer linear, and the simple

expressions of Appendix III are no longer valid. However, it is possible to use the results of the experiment described in Reference 10 to tabulate both C_n and $C_{m_{c/4}}$ as functions of these three parameters. It is the purpose of this section and of Appendix II to show how such a tabulation can be constructed, and it is a further purpose of this report to show how such a tabulation can be used to predict stall flutter instabilities of helicopter rotor blades.

As described in Appendix II, the first task in converting the sinusoidal data to a generalized form was to select an interpolation parameter. The frequency f was found to be the most convenient parameter for this purpose, and a series of cross plots was then prepared for $C_{m_{c/4}}$ versus f for constant values of the remaining parameters. Specific values of the fundamental three-parameter set, α, A, B, were then chosen for the coordinate points of the final tabulation. The values chosen were:

$$\alpha = 0, 1, 2, 3, \ldots, 26, 27 \text{ deg}$$
$$A = 0, \pm 0.01, \pm 0.025, \pm 0.04$$
$$B = 0, \pm 0.001, \pm 0.004, \pm 0.007, \pm 0.01$$

Once these values had been selected, the procedure described in Appendix II was followed, in which data points were interpolated versus f, plotted versus A, faired, cross-plotted versus B, faired again, cross-plotted versus α, and faired once again. Selected points from these smoothed curves were then checked against comparable points from the original sinusoidal loops, and adjustments were made in the faired curves to reduce the error between the original loops and the final faired data. The agreement between the two is discussed in the following section.

Finally, these unsteady moment coefficient data were tabulated and are presented in Table II. Further details of the tabulation will be found in Appendix II. The original table of unsteady normal force coefficient, first presented in Reference 10, has also been included in the present report as Table I.

A few selected plots of $C_{m_{c/4}}$ versus α are shown in Figures 5, 6, and 7 for B = -0.01, 0, and 0.01, respectively, and the three curves in each figure are for A = -0.025, 0, and 0.025. Values of $C_{m_{c/4}}$ for zero angle of attack were obtained from the theoretical formula discussed in Appendix III. In each of the figures presented here, a basic behavior or trend of the curves can be seen (which is exhibited by the entire set of $C_{m_{c/4}}$, α cross plots), but this trend is most clearly observed in Figure 5 for B = -0.01. The most striking thing about the dynamic moment response is the delay in the occurrence of stall when the angular velocity is positive and

the reversion to a stalled condition when the angular velocity is negative. This is clearly seen in Figure 5 in the curve for $A = 0.025$, which remains level (and hence unstalled) beyond $\alpha = 20$ deg and does not exhibit any sharp decreases until $\alpha = 25$ deg. These values of α are considerably greater than the steady-state stalling angle of $\alpha = 13$ deg (see the curve for $A = B = 0$ in Figure 6). The curve for $A = 0$ lies above the curve for $A = 0.025$ when α is small and crosses below it when α is large. Similarly, the curve for $A = -0.025$ lies above both the other curves for small α and crosses below both curves for large α. A similar behavior is observed in Figure 6 for $B = 0$, although the maximum angle attained before the curve departs from the horizontal (which may be regarded as the dynamic stall angle) is smaller for each value of A than the comparable value attained in Figure 5 for negative B. Finally, Figure 7, for positive B, shows the same typical behavior, although the curves beyond dynamic stall are more irregular than those shown in the previous two figures. Furthermore, the dynamic stall angle is again smaller for positive B than it was for either zero B or negative B.

This graphical inversion of the order of the curves is responsible for the loop crossovers (discussed in Reference 2 and in more detail in the following section of this report), which contribute to the negative aerodynamic damping in stall flutter. To illustrate this behavior, refer to Figure 8, which is identical to Figure 7 except that the right halves of two hypothetical moment loops have been superimposed on the curves, one for the potential flow regime at small α and one for the stalled flow regime at large α. The right half of each loop has been chosen because this is the portion for which the angular acceleration is negative. Actually, a true loop would have variations in B, ranging from zero at the mean angle of attack to maximum negative B at the maximum angle of attack. However, the use of hypothetical loops in a constant B plot will be permissible for illustrative purposes.

First consider the loop in the potential flow regime, limited in this case to $\alpha \leq 8$ deg, with numbered points 1, 2, and 3. At point 1, the acceleration has just become negative during the positive A portion of the motion. At point 2, the B parameter has reached its negative maximum value and A is zero. At point 3, B is again approaching zero and A is negative. Note that the portion of the loop shown here is elliptical and traverses the $C_{m_{c/4}}$, α plane in the counterclockwise direction. As shown in Reference 2, this is a stable loop which produces positive aerodynamic damping.

Now consider the loop in the stalled flow regime with numbered points 4, 5, and 6. The description from the previous paragraph concerning the relative values of A and B can be applied here with points 1, 2, and 3 replaced by points 4, 5, and 6, respectively. However, this time the portion of the loop shown here crosses itself, and a portion of the loop is traversed in the clockwise direction. As shown in Reference 2, this is a destabilizing portion of the loop. Under some circumstances, this portion can grow at the expense of the stabilizing portion, and the result is a self-excited, single-degree-of-freedom stall flutter in the pitching mode. However, this phenomenon is usually self-limiting because enough positive damping can be produced by a stable left half of the loop to balance the negative damping of the right half of the loop.

Verification of Conversion Process

The usefulness of the $C_{m_{c/4}}$ tabulation hinges on its ability to produce the correct value of the unsteady moment coefficient for a variety of motions typical of helicopter rotor blade displacements. A necessary (but not sufficient) condition, then, is that the tabulated values must produce reasonable facsimiles of the original sinusoidal loops. As part of the cross-plotting and smoothing procedures described in the previous section, a number of loops were reproduced from the tabulated data and were compared with the appropriate original loops. Satisfactory agreement between the original and reconstructed loops was achieved, and the results are shown in Figures 9 through 13 for a variety of conditions.

In most cases the agreement is moderately good; in a few cases it is excellent, and in a few cases it is poor. However, it must be remembered that each original loop represents only a single cycle of an oscillation that exhibits a random, stall-induced characteristic superimposed on the basic wave form. Since any individual reconstructed loop was produced by an averaging process, it is not surprising that there are individual departures from the original data. Indeed, it is encouraging to note that there is an overall agreement in the trends exhibited by these figures.

This overall agreement is further amplified in the discussion of integrated effects which follows below. First, however, it is instructive to consider the individual comparisons. Figures 9 and 10 contain loops for constant reduced frequencies of $k = 0.112$ and 0.225 ($f = 4$ and 8 cps), respectively, which are frequencies representative of the middle of the original test range and are probably most representative of the helicopter operating range. As stated above, the agreement is generally good, particularly at the lowest mean angles of attack, but even when the curve

values do not match, the locations of the curve crossovers are in reasonably good agreement. These crossover points are of vital importance to the stall flutter prediction because, as described in Reference 10, the transition from a counterclockwise enclosure of the loop to a clockwise enclosure represents the transition from positive aerodynamic pitch damping to negative aerodynamic pitch damping.

Figures 11, 12, and 13 contain loops for mean angles of attack of 15, 18, and 21 deg, respectively, and indicate the ability of the tabulation to predict the effect of reduced frequencies. This is the angle of attack region which is most susceptible to stall flutter, as discussed in Reference 2. In these figures, the agreement between the reconstructed loops and the original loops is generally good for reduced frequencies of 0.112, 0.225, and 0.338. The agreement is only fair at the lowest and highest reduced frequencies, $k = 0.056$ and 0.450, but the directions and/or crossovers of the loops are correct. It should be noted that in Figure 13, for $\alpha_M = 21$ deg, the reconstructed loops for the highest frequencies exhibit flat regions in the vicinity of $\alpha = 27$ deg. These flat spots occur because one or more of the parameters α, A, or B have exceeded the tabular values given in Table II, and the computer program has selected "corner values" in these regions. The parameter values at which these corner values are selected are generally outside the range of interest in helicopter applications, and these discrepancies are not believed to be important in their effect on the stall flutter prediction.

As a final check on the overall agreement between the reconstructed loops and the original data, the aerodynamic damping parameter $\Xi_{\alpha 2}$ was calculated for the reconstructed loops. Use was made of Eq. (40) of Reference 2, and the integrated damping for the reconstructed loops was compared with the results published in Figures 14 and 15 of Reference 2 for $\bar{\alpha} = 8$ deg. This comparison is presented in Figure 14. The results shown here corroborate the statement made earlier that the overall behavior of the reconstructed loops is in good agreement with that of the original data. In every panel of Figure 14, except the panel for the highest mean angle ($\alpha_M = 27$ deg), the agreement between the two sets of results is good. In fact, a comparison of Figure 14 with Figures 14 and 15 of Reference 2 shows that the disagreement between the damping for the original and the reconstructed loops for the selected amplitude is generally less than the experimental scatter of the data for all amplitudes shown in Reference 2. (The faired curves of Reference 2, representing all amplitudes, are included in Figure 14 for the convenience of the reader.) Furthermore, in the last panel of Figure 14, for $\alpha_M = 27$ deg, where a substantial disagreement is observed, the damping for the reconstructed loops is in agreement for low values of reduced frequency and is conservatively destabilizing for large values of reduced frequency.

Additionally, some comparisons of reconstructed normal force loops and the original loops from Reference 10 are shown in Figures 15 and 16. These figures show, respectively, the effect of varying mean angle of attack at a typical value of reduced frequency and the effect of varying reduced frequency at a typical mean angle of attack. As with the comparison of the moment loops, the agreement is generally good, although individual loops have local discrepancies. One significant aspect of the unsteady normal force at angles above the steady-state stall angle is the tendency to overshoot the steady-state maximum normal force by a considerable margin. These figures show that the maximum value of the unsteady normal force can be as large as 2.2, whereas the maximum steady-state value at low Mach numbers is approximately 1.2 to 1.3. This phenomenon is noted later in the text in connection with observed delays in rotor lift stall.

SCALING OF UNSTEADY DATA

The unsteady aerodynamic characteristics of an NACA 0012 airfoil executing forced, pure sinusoidal pitching motion form the basis of this stall flutter study. As originally planned, experimental data describing the two-dimensional normal force and pitching moment characteristics over a wide subsonic Mach number range were to be employed to provide an improved analytical method capable of predicting stall flutter. The unsteady airfoil data were available from two sources. One series of tests, conducted at UARL a number of years ago, is described in Reference 2. In these tests, most of the data were obtained at Mach numbers less than 0.4 and at reduced frequencies less than 0.45. More recent tests, conducted by Boeing under USAAVLABS sponsorship, are documented in Reference 11. In the Boeing tests, the Mach number range was extended to 0.6 and the reduced frequency range was extended to 0.72.

As described earlier, the application of unsteady data to rotor blade operating conditions required that airfoil characteristics be expressed as functions of four variables: Mach number M, instantaneous angle of attack α, angular velocity parameter A, and angular acceleration parameter B. In processing the Boeing data, it was found that the test matrix employed by Boeing was not sufficiently complete to permit conversion of the data (through cross plots) to the required M, α, A, B form needed for this study. (It should be stressed that the Boeing tests and the present study were not designed to be compatible, although agreement between comparable UAC and Boeing data points was generally found to be reasonable, especially when differences in steady-state stall angles were considered.)

To satisfy the need for higher Mach number data in the form required by the present method, a Mach number scaling procedure based on the steady-state stall angle was developed. In the absence of unsteady data at higher Mach numbers, the steady-state normal force and pitching moment characteristics of the NACA 0012 airfoil, normalized in terms of stall angle, were used to evolve separate scaling laws for normal force and moment. These steady-state scaling laws were then assumed to apply to the unsteady blade characteristics as well. A discussion of this application and examples of scaled loops are contained in the following sections.

Normal Force

First consider the steady-state normal force characteristics, as shown in Figure 17 for $0.2 \leq M \leq 0.7$. These data were obtained from lift and drag data presented in Reference 18. For the purpose of this discussion, a normal force "stall" angle α_{sn} is defined as that angle at which the normal force characteristic at any M initially departs from linearity. Also, a dimensionless normal force stall angle parameter σ_n is defined as the ratio of the angle of attack α to the normal force stall angle α_{sn},

$$\sigma_n = \alpha / \alpha_{sn} \tag{17}$$

When Figure 17 is examined, three significant variations with increasing Mach number are clearly evident in the potential flow regime (i.e., $\alpha < \alpha_{sn}$ where, as noted above, α_{sn} is the angle at which the normal force curve initially departs from linearity). These variations are an increase in normal force curve slope in the potential flow regime ($\alpha < \alpha_{sn}$), a reduction in the value of c_n at the stall angle α_{sn}, and a reduction in the normal force stall angle itself. By properly manipulating these three factors, the higher Mach number curves can be derived, in the potential flow regions, from a single incompressible normal force characteristics curve. In particular, it can readily be shown that in the potential flow region the steady-state normal force at any Mach number can be related to the incompressible normal force by the expression

$$(c_n)_{\sigma_n, M} = \frac{(c_n)_{\sigma_n, M=0}}{\sqrt{1 - M^2}} \; \frac{(c_{n_{STALL,SS}})_M}{(c_{n_{STALL,SS}})_{M=0}} \tag{18}$$

This same expression was then assumed to apply in the unsteady situation. Note that Eq. (18) can also be written in the following alternate form:

$$\sqrt{1-M^2}\,\frac{(c_n)_{\sigma_n,\,M}}{(c_{n_{STALL,SS}})_M} = \frac{(c_n)_{\sigma_n,\,M=0}}{(c_{n_{STALL,SS}})_{M=0}} \tag{19}$$

This expression effectively states that at any Mach number, the ratio of the normal force coefficient (steady or unsteady) to the steady-state normal force coefficient at the stall angle α_{sn} is equal to the ratio at M = 0, provided both ratios are evaluated at the same value of σ_n.

As a first limited test of the applicability of this scaling technique, Eq. (18) was used in conjunction with the incompressible c_n data of Table I (A = B = 0) to compute steady-state lift characteristics at several Mach numbers. These were then compared with actual data given in Figure 17. The comparisons are shown in Figure 18, where the values of α_{sn} and ($c_{n_{STALL,SS}}$) used in scaling are also noted. Below α_{sn}, agreement between measured and scaled results is excellent, as might be expected. The agreement above α_{sn} is less faithful, but acceptable.

As a further check on the general accuracy of the scaling techniques, several normal force hysteresis loops were generated for M = 0.4 and 0.6. These were compared with experimental results from Reference 11. In obtaining the scaled results, the data of Table I were used in conjunction with Eq. (18) and values of α_{sn} and ($c_{n_{STALL,SS}}$) for the Boeing airfoil (see Table III). Figure 19 compares loops for M = 0.4, $\alpha_M \sim 9.8$ deg, and $\bar{\alpha} \sim 4.8$ deg. Experimental loops are shown as solid curves, while the dashed curves represent loops constructed and scaled from the UAC incompressible unsteady normal force data of Table I. Figure 20 gives similar results for M = 0.6. Agreement between experimental and scaled loops is seen to be reasonable for M = 0.4. However, at M = 0.6, the comparisons are less favorable.

In applying the scaling techniques for the investigation reported herein, the following computation procedure was required to make the transition from the real blade conditions to the data tabulation and then to scale the data back to the blade conditions.

1. Compute the following two-dimensional conditions at a rotor blade section: α, M, A, B

2. Compute the dimensionless stall angle parameter $\sigma_n = \alpha/\alpha_{sn}$ where α_{sn} corresponds to the blade section Mach number M

3. Compute the equivalent incompressible angle of attack
$\alpha_{M=0} = \sigma_n (\alpha_{sn})_{M=0}$

4. Enter the unsteady normal force tabulation with $\alpha_{M=0}$, A, B, and extract the normal force coefficient $(c_n)_{\sigma_n, M=0}$ for use in Eq. (18)

5. Compute a maximum normal force coefficient at stall $(c_{n_{STALL,SS}})_M$ that corresponds to the blade section Mach number M

6. Apply Eq. (18) to scale $(c_n)_{\sigma_n, M=0}$ to the blade section Mach number M

7. Result: $(c_n)_{\sigma_n, M}$

The normal force coefficient is then trigonometrically converted to the lift coefficient at each spanwise station. An integration over the blade span is performed to determine rotor blade loading, and the sequence is repeated at each blade azimuth angle.

The scaling parameters used in applying this scaling technique to the unsteady data in the blade response calculations presented herein are given in Table IV. Note that for M = 0.2, the values of α_{sn} and $(c_{n_{STALL,SS}})$ are different from those used in the calculation of the M = 0.2 curve of Figure 18. This results from the differences in steady-state normal force response indicated between the M = 0.2 data from Reference 18 and the steady-state results extracted from Table I for A = B = 0.

Pitching Moment

As in the case of the normal force, the scaling procedure used for the pitching moment is based on the steady-state stall angle. Consider the unpublished steady-state pitching moment characteristics, Figure 21, corresponding to the lift and drag data of Reference 18. A pitching moment "stall" angle α_{sm} is defined to be an angle near the point where the steady-state moment at any M departs from zero. Also, a dimensionless pitching moment stall angle parameter σ_m is defined as the ratio of the angle of attack α to the pitching moment stall angle α_{sm}. Unlike the normal force, the pitching moment stall angle α_{sm} is not necessarily related to the departure of the pitching moment from linearity. Rather, it was initially defined as that angle which, when used, permitted the steady-state pitching moments for the higher Mach numbers (Figure 21) to be predicted with reasonable accuracy from the incompressible pitching moment data (assumed to be

the M = 0.2 data in Figure 21). Table IV lists the values of α_{sm} found to be acceptable on the basis of this criterion (see original α_{sm} column in Table IV). The actual scaling procedure is one of operating on the incompressible data with the following simple expression, which primarily manipulates the location of the pitching moment breakpoint:

$$\left(c_{m_{\frac{c}{4}}}\right)_{\sigma_m, M} = \frac{\left(c_{m_{\frac{c}{4}}}\right)_{\sigma_m, M=0}}{\sqrt{1-M^2}} \tag{20}$$

Figure 22 compares the values of steady-state moment coefficients calculated using results from Table IV and Eq. (20). No comparison is shown for M = 0.2, as the agreement is exact for this Mach number. Up to M = 0.4, the agreement between experimental and scaled curves is seen to be very good. As might be expected from previously presented lift results, the agreement is less favorable at M = 0.5 and 0.6.

The scaling procedures were also applied to generate several unsteady pitching moment hysteresis loops from the unsteady data of Table II for comparison with experimental loops from Reference 11 for M = 0.4 and 0.6. Results are shown in Figures 23 and 24. In obtaining these results, the values of α_{sm} were determined from the Boeing steady-state moment data (Reference 11) and are given in Table III. The comparisons shown in Figures 23 and 24 are generally not favorable, although in some instances reasonable agreement in loop shape and crossover points can be noted.

As with normal force, in applying the steady moment data of Table II in the Blade Response Program, the computation procedure must first transform from the real blade conditions to the M = 0 data tabulation and then scale back to real blade conditions. A description of this sequence follows:

1. Compute the following two-dimensional conditions at a rotor blade section: α, M, A, B

2. Compute the dimensionless stall angle parameter $\sigma_m = \alpha / \alpha_{sm}$ where α_{sm} corresponds to the blade section Mach number M (see Table IV)

3. Compute the equivalent incompressible angle of attack $\alpha_{M=0} = \sigma_m (\alpha_{sm})_{M=0}$

4. Enter the pitching moment tabulation (Table II) with $\alpha_{M=0}$, A, B, and extract an incompressible moment coefficient $(c_{m_{c/4}})_{\sigma_m,M=0}$ which appears in Eq. (20)

5. Apply Eq. (20) to scale $(c_{m_{c/4}})_{\sigma_m,M=0}$ to the blade section Mach number

6. Result: $(c_{m_{c/4}})_{\sigma_m,M}$

This sequence is repeated for adjacent blade sections and for each blade azimuth angle.

Following the initiation of this investigation, additional data on the effect of compressibility on aerodynamic damping in pitch (equivalently, $c_{m_{c/4}}$) were published in Reference 19. These data are presented as the dashed curves in Figure 25, where the boundaries encompassing the negative damping region are shown as functions of section angle of attack and Mach number. The solid curves in the left-hand panel of Figure 25 represent the equivalent boundary defined by the scaling procedure using $c_{m_{c/4}}$ data from Table II and the original values of α_{sm} from Table IV. In an attempt to improve the agreement between scaled results and Reference 19 results, a revised α_{sm} tabulation was generated (see Table IV) and used to produce the comparison shown in the right-hand panel of Figure 25. These revised results became available in time for use by the Sikorsky Division in their correlation studies. However, all parametric and sensitivity study results presented in this report are based on the original α_{sm} tabulation given in Table IV.

EXPLORATORY STALL FLUTTER STUDIES

This section of the report describes the results of exploratory calculations made to assess the effect of several blade design and flight condition parameters on the susceptibility of rotor blades to stall flutter. Presented are (1) a description of the blade designs and flight conditions selected for investigation, (2) results of a study conducted for a reference blade design to establish the sensitivity of the predicted torsional response (and associated root pitching moment) to certain parameters in the general aerodynamic model used, and (3) results showing how the stall flutter characteristics of the reference design are affected by changes in certain design parameters.

BLADE DESIGNS AND FLIGHT CONDITIONS

The parameters expected to be pertinent to the stall flutter problem of rotor blades are listed below:

1. Rotor lift, C_L/σ
2. Rotor advance ratio, μ
3. Rotor propulsive force, C_{PF}/σ
4. Blade twist rate, θ_1
5. Blade airfoil section
6. Blade elastic axis location
7. Blade torsional stiffness (or, equivalently, torsional frequency ratio, $\bar{\omega}_{\theta_1}$)
8. Blade center-of-gravity axis location (cg).

Items 1 through 4 principally influence the extent to which the steady-state stall angles of attack will be exceeded over the rotor disc for a given flight condition. Items 5 and 6 affect the unsteady aerodynamic hysteresis characteristics of the blade as it oscillates above and below the steady-state stall angle, while Items 7 and 8 contribute to the torsional dynamic response characteristics of the blade.

The parameters considered in this investigation were Items 1, 4, 7, and 8 (lift, twist, torsional frequency, and section cg location). Items 5 and 6 were not considered because of a lack of appropriate unsteady airfoil data; all calculations herein are based on data for an NACA 0012 airfoil oscillating sinusoidally in pitch about its quarter-chord. In addition, rotor advance ratio and propulsive force were not considered as variables. Rather, as discussed below, typical values of these parameters at which the stall flutter phenomenon might be expected to occur were selected. Table V indicates the blade designs investigated. The Reference Blade was substantially an S-61F blade (Reference 20) except for its torsional natural frequency (frequency of blade when mounted on control system), which was increased from 6.5P to 8.2P (through control system stiffness increases) to provide a greater range of $\bar{\omega}_{\theta_1}$. The principal characteristics of this blade are given in Table VI. All other blades studied were identical to the Reference Blade except for the parameters noted in Table V. In the case of the Low-Frequency Blade, the reduction in frequency was achieved by reducing the control system spring rate from 1.2×10^6 ft-lb/rad to 0.07×10^6 ft-lb/rad. Figure 26 compares the mode shapes and frequencies of the first two torsional modes for these two blades.

All blades were considered to form parts of five-bladed rotors which were operated at an advance ratio μ of 0.4 in the pure helicopter mode (i.e., rotor providing a propulsive, as opposed to a drag, force). A propelling rotor condition was selected as being more critical from the stall flutter standpoint since the depth of rotor stall at a given C_L/σ increases with increasing propulsive force (see Reference 18). Rotor shaft angle was fixed at a typical value for the propulsive flight mode ($\alpha_S \sim$ -8 deg, $C_{PF}/\sigma \sim 0.009$ for Reference Blade), and the torsional response characteristics of each blade design were computed at rotor lift values corresponding to nominal incipient, moderate, and deep stall operating conditions. (Stall here is defined as steady-state stall.) Increases in lift and, hence, penetration into stall were accomplished by means of collective pitch (θ_{75}) variations. The required values of θ_{75} were estimated from the charts of Reference 18 for the Reference Blade as

Condition	θ_{75}, deg
Incipient Stall	12.2
Moderate Stall	14.2
Deep Stall	15.2

These values of collective pitch were also found to be appropriate for the other blade designs considered. Cyclic pitch control angles (A_{1_s} and B_{1_s}) were arbitrarily estimated from Reference 18 using the requirement of

approximately zero flapping with respect to the shaft for the Reference Blade for incipient stall operation. The cyclic pitch values were A_{1_s} = -2 deg and B_{1_s} = 9 deg.

SENSITIVITY STUDIES

As originally envisioned, the analysis developed in this investigation was to use experimental unsteady data for Mach numbers up to 0.6. However, as discussed previously, this proved to be impossible, and it was necessary to use scaling procedures in an attempt to account for the effects of compressibility. Because of possible uncertainties introduced by such an approach, a limited number of calculations were made for the Reference Blade to establish the general nature of its computed torsional response and the sensitivity of this reponse to arbitrary changes in certain parameters introduced into the aerodynamic model by the scaling procedures. Also included in this study was an evaluation of the sensitivity of the results to the number of iterations performed between the Blade Response Program and the Circulation Program (see Figure 1). In addition to indicating the relative significance of the various parameters, these calculations also aided in establishing the final aerodynamic model used to calculate the torsional response and pitching moment characteristics of the remaining blade designs.

General Response Characteristics

Figure 27 indicates (for the Reference Blade) the general effect of increasing blade collective pitch (equivalently, rotor loading) on the time history of blade root pitching moment. This moment, which is nondimensionalized as noted, is imposed on the rotor control system and thus is a direct measure of push rod or pitch link loads. To a good first approximation, the moment also is proportional to the elastic torsional response of the blade. For comparative purposes, results obtained using both conventional steady-state aerodynamic data (of Reference 18) and scaled unsteady data (from Tables I and II) are presented. Corresponding time histories of angle of attack at the three-quarter radius are also given in Figure 28.

The results of Figures 27 and 28 indicate that increasing θ_{75} causes the angle of attack on the retreating blade ($\psi \sim$ 270 deg) to increase and eventually to exceed the nominal steady-state stall angle ($\sim$ 12 deg). At the lowest θ_{75}, the oscillatory pitch moment is small, and the use of unsteady aerodynamic data has little effect because of the relatively low section angles of attack. Increasing collective pitch to 14.2 deg results

in an oscillation at the first torsional natural frequency of the blade when unsteady aerodynamic data are used. This is due to a self-excited torsional oscillation of the blade which appears to be initiated at about a ψ of 220 deg. The oscillation grows in amplitude until the blade reenters the region of higher dynamic pressures and lower angles of attack in the first quadrant, where both stall and unsteady effects are reduced and the motion is quenched.

The torsional oscillation noted is characteristic of stall flutter and is reflected in the angle of attack time history for θ_{75} = 14.2 deg in Figure 28. The oscillation also appears to be superimposed on a lower frequency moment variation which is partially characterized by a positive moment peak on the advancing blade. This peak results from a relatively rapid unstalling of the blade and a resulting dynamic overshoot as the blade seeks a new equilibrium position.

As the blade collective pitch angle is increased further to 15.2 deg, the characteristics of the blade moments described above are accentuated. Additional information about the self-excited oscillation noted at θ_{75} = 15.2 deg is given in Figure 29, where the relative magnitude and phasing of the angle of attack, angular velocity parameter, angular acceleration parameter, aerodynamic moment coefficient, and elastic twist at the 75 percent radius station of the blade are compared.

When steady-state aerodynamics are used, the angles of attack on the blade for a given collective pitch value are higher while the rotor lift is lower (see Figure 28). This is due directly to the occurrence of classical steady-state stall; however, despite the apparent deep penetration into the stall regime, no stall flutter type of oscillation occurs. The higher lift observed with unsteady aerodynamics is of some significance, in that this observation is qualitatively consistent with delays in rotor lift stall noted in several experimental investigations (e.g., References 5 and 21).

The general effect of including the velocities induced by the rotor wake (variable inflow) in the unsteady aerodynamic model is shown in Figure 30. In this figure, blade pitching moments predicted using variable inflow are compared with corresponding constant inflow results from Figure 27. This comparison indicates that the blade moments predicted with variable inflow, while exhibiting some differences in shape, have characteristics essentially similar to those predicted with constant inflow. Stall-flutter-type oscillations again occur at θ_{75} = 14.2 and 15.2 deg and have the same frequency and approximately the same amplitude. Rotor lift is substantially unchanged by the inclusion of variable inflow.

Effect of Variations in Aerodynamic Model

The results using unsteady aerodynamic data, presented in Figures 27 through 30 and discussed in the preceding section, were based on the following assumptions in the aerodynamic model:

1. The limit Mach numbers (M_1, M_2) to which the incompressible unsteady data could be scaled at angles of attack above and below the steady-state stall angle were 0.5 and 0.85, respectively. (Figure 31 indicates the parameters used to define the operating regions where scaled unsteady aerodynamic data were used; values of α_{sn} and α_{sm} were taken from Table IV.)

2. The Prandtl-Glauert compressibility factor $\sqrt{1-M^2}$ could be applied at all blade section operating conditions regardless of whether they involved potential or nonpotential flow.

3. All results using variable inflow could be generated using one iteration between the Blade Response and Circulation Programs (see Figure 1). This was equivalent to two passes through the Blade Response Program and one pass through the Circulation Program.

A limited number of calculations were made to examine the general sensitivity of the blade root pitching moment to each of these assumptions. Results for the important 14.2 collective pitch condition are presented in Figure 32 and are discussed below.

The effect of decreasing M_1 from 0.5 to 0.4 and M_2 from 0.85 to 0.6 is shown in the top panel of Figure 32. The results indicate that both the initiation and the growth of the self-excited oscillation in the third and fourth quadrants are substantially unaffected by the values selected for these parameters. This results from the fact that the local angle of attack-Mach number combinations over the important outer region of the blade are such that unsteady aerodynamic characteristics are used for both sets of M_1 and M_2. It is seen, however, that in the first quadrant the selection of the upper values of M_1 and M_2 leads to a somewhat larger high-frequency torsional oscillation. This is due to the more extensive use in this region of unsteady data with their inherent destabilizing effects at high angles of attack. The higher values for the scaling limits, $M_1 = 0.5$ and $M_2 = 0.85$, were arbitrarily selected for use in all remaining calculations.

The effect of increasing the number of iterations between the Blade Response Program and the Circulation Program (cf. Figure 1) from 1 to 2 is shown in the center panel of Figure 32. As indicated, little additional information is obtained on either the character or the amplitude of the blade moment by the second iteration. A single iteration was therefore selected as being cost effective.

The bottom panel in Figure 32 shows the effect of arbitrarily removing the Prandtl-Glauert scaling factor for those conditions where the angular velocity parameter A of the blade section was negative. This eliminates the major nonpotential flow operating regimes where this scaling factor is invalid. As shown in Figure 32, the moment results are insensitive to the treatment of the Prandtl-Glauert factor. For the remaining calculations, the Prandtl-Glauert factor was, for convenience, applied for all section operating conditions.

PARAMETRIC STUDIES

As indicated previously, the objective of the parametric studies was to investigate the effect of variations in blade twist, first-mode torsional frequency (i.e., torsional stiffness), and chordwise cg position on blade stall flutter characteristics. The basic results of the calculations based on a constant inflow assumption are presented in Figures 33 through 35. In these figures, the time histories of blade root pitching moment for the various blade designs are compared with those for the Reference Blade at the same values of blade pitch. Note that rotor lift for a given pitch setting did not always remain constant as the blade configuration was changed. Therefore, results of Figures 33 through 35 have been cross-plotted in Figure 36 as functions of rotor lift. In Figure 36, the $\frac{1}{2}$ peak-to-peak amplitude ($\frac{1}{2}$PTP) of both the total blade pitching moment and that portion of the moment corresponding to the self-excited torsional oscillation is presented. The latter amplitude was arbitrarily defined as the maximum amplitude of the self-excited response on the retreating blade ($180 \leq \psi \leq 360$ deg). Larger amplitudes of the self-excited oscillation are noted for the highest pitch setting in the first quadrant; however, these occur in a region where the results are sensitive to the choice of Mach number scaling limits (M_1 and M_2) and are, therefore, subject to some question. Results similar to those of Figures 33 through 36, but including variable inflow effects, are presented in Figures 37 through 40. Discussion of all results follows.

Constant Inflow Results

The effect of blade twist on blade root pitching moment characteristics at constant pitch setting is shown in Figure 33, where the results for the Reference Blade (θ_1 = -4 deg) are compared with those for the High Twist Blade (θ_1 = -8 deg). (The blades were identical in all other respects.) Increases in blade twist were expected to be beneficial from a stall flutter standpoint, inasmuch as the angles of attack of the high-velocity outboard sections of the blade are reduced at a given rotor lift. Close examination of the results of Figure 33 indicates that increasing blade twist does, in fact, result in smaller moment oscillations at the same rotor lift. Further, the reduction is primarily due to a delay in the onset of the self-excited oscillation. These trends are more clearly shown in Figure 36, where the amplitudes of the total moment and self-excited moment component are presented as functions of rotor lift.

The effect of varying the frequency of the blade first torsional mode ($\bar{\omega}_{\theta_1}$) is shown in Figure 34. Results are presented for the Reference Blade, which had an $\bar{\omega}_{\theta_1}$ of 8.2P, and for the Low-Frequency Blade, which had an $\bar{\omega}_{\theta_1}$ of only 4P. As noted in an earlier section of the report, the reduction in $\bar{\omega}_{\theta_1}$ was accomplished by arbitrarily reducing the stiffness of the control system. This, of course, altered the first torsional mode's shape as well as its frequency (see Figure 26).

Examination of the results for the Low-Frequency Blade leads to the following important observations. First, a marked reduction in the rotor lift for a constant pitch setting occurs when $\bar{\omega}_{\theta_1}$ is lowered. This is due to the larger nosedown elastic twist angles which are produced by steady centrifugal and aerodynamic stall moments. The magnitude of these moments is essentially unaffected by $\bar{\omega}_{\theta_1}$ and, to provide equilibrium, the less-stiff blade must deflect a greater amount. A second noteworthy point is the apparent absence of large-amplitude, self-excited moment oscillations that could be clearly attributed to stall flutter. Although there are some moment oscillations at a frequency approaching that of the first torsional mode, there is no clear indication of a growth and decay of a self-excited oscillation. This characteristic appears to be reasonable if one assumes, on the basis of the results for the Reference Blade, that one or two cycles of the self-excited oscillation must occur before significant amplitudes are developed. Under such conditions, a self-excited oscillation at a frequency of 4P may never have an opportunity to grow significantly within the limited azimuthal range where negative damping exists. Conversely, whatever oscillation does develop may never be completely quenched on the advancing side where positive damping exists. The plots of moment amplitudes as a function of lift shown in Figure 36 indicate clearly that the Low-Frequency blade exhibits significantly lower oscillatory moments

at a given lift coefficient than does the Reference Blade. It should be remembered, of course, that the comparison would be less favorable if made on the basis of the elastic torsional deflections of the blades.

The final design parameter investigated was the blade cg chordwise position. The results for an Aft cg Blade (cg at 30 percent c) are presented in Figure 35, where they are compared with the results for the Reference Blade (cg at 25 percent c). All moment time histories for the Aft cg Blade are characterized by a particularly severe oscillation on the advancing blade, coupled with a tendency for oscillations near the first torsional frequency (~ 8P) to persist over much of the azimuth range. The former characteristic is a steady-state aerodynamic phenomenon, being observed even when steady-state aerodynamics were used throughout the calculations. It appears to be the result of destabilizing dynamic forces associated with higher harmonic blade flapping and bending motions. The time histories of blade pitching moment and the flapping mode acceleration are shown in Figure 41 for both the Reference Blade and the Aft cg Blade. The basic characteristics of the flapping acceleration are the same for both blades. However, for the Reference Blade, the coupling with the torsional mode is very small because of the coincident cg and elastic axes. For the Aft cg Blade, dynamic coupling exists and is destabilizing since the torsional response produced is such as to amplify the original dynamic excitation. The high-frequency oscillations occurring in the azimuth range of 140 to 120 deg are not due to stall but, rather, are believed to be transient motions induced by the nearly impulsive dynamic excitation that occurs on the advancing blade. It is apparent from the results of Figure 35 and from the cross plots of Figure 36 that a cg axis aft of the blade elastic axis is very detrimental, although not necessarily from a stall flutter point of view.

Variable Inflow Results

Blade pitch moment results obtained when variable inflow effects are included are presented in Figures 37 through 40. In general, the previously discussed observations and conclusions regarding the occurrence of stall flutter for the Reference Blade and the relative advantages and disadvantages of the Low-Frequency and Aft cg Blades are unaltered by the inclusion of variable inflow. However, a comparison of the results for the Reference Blade and the High Twist Blade is somewhat inconclusive. The delay in the onset of self-excited moment oscillations with increased twist predicted using constant inflow theory no longer appears to exist when variable inflow is included, at least for C_t/σ's up to 0.082. This is probably caused by the unloading of the blade tip region due to the tip vortex, factor that makes additional unloading associated with increased

twist not as important. At C_L/σ's greater than 0.082 (e.g., for θ_{75} = 15.2 deg), the computed results with variable inflow indicated a marked reduction in the amplitude of the self-excited oscillation for the High Twist Blade. Because of the number of variables involved, the exact cause of this reduction in response is difficult to pinpoint. It was noticed, however, that for this condition the phasing of the aerodynamic moments exciting the blade tended to vary more along the span of the blade, thereby diminishing their effectiveness.

CORRELATION STUDIES

The objective of the correlation studies was to determine whether the technology available in unsteady aerodynamics and rotor dynamics could be used to accurately predict stall-flutter-induced control loads. To evaluate correlation, two significant examples of stall flutter were chosen: the S-61F (NH-3A) in high-speed unaccelerated flight and the CH-53A during maneuvers at high load factor. The stall flutter characteristics in the two flight regimes differ significantly. The S-61F exhibited strong oscillations at the blade torsional natural frequency, which initiated over the nose of the aircraft and persisted over the retreating side of the disc (Figures 42-47). Attempts to duplicate these oscillations analytically included examination of the effects of airload variations (Figures 48-55). In addition, the effects on control loads correlation of collective pitch setting, unsteady aerodynamics and blade stress predictions are considered in Figures 56-60.

The CH-53A maneuver conditions exhibited oscillations in the region of the torsional natural frequency, which persisted over a major portion of the disc during maneuvers while rotor lift and control load amplitudes varied (Figures 61-65). In some cases these oscillations persisted fully around the rotor disc for several revolutions (Figure 66). The greater azimuthal persistence in these instances is attributed to the high rotor loading, which results in penetration of the stall region by a significant portion of the disc.

S-61F FLIGHT TEST CORRELATION

The S-61F flight test program provided an excellent case for correlation because of the clear examples of several cycles of high-frequency oscillations beginning over the nose of the aircraft. In addition, a great deal of in-flight data, including airloads data, is available from the USAAVLABS/NASC-sponsored rotor loads measurement program (Reference 22). In the referenced program, the airframe and rotor system were heavily instrumented to obtain in-flight airloads, hub forces, control loads, blade responses, and airframe responses.

In performing the correlation, a variation of flight speed and rotor thrust was considered since the amplitude and azimuthal persistence of the instability are dependent upon these parameters. The conditions analyzed are referred to by the case numbers as described in Reference 22. Six cases were analyzed: four 185-kt cases at C_T/σ's varying from .018 to .058, and two 165-kt cases at C_T/σ's of .021 and .054. A summary of the principal parameters describing these cases is provided in Table VII.

Mathematical Model

The rotor blade was modeled with two rigid-body degrees of freedom (flap and lag), five flatwise elastic modes, two edgewise elastic modes, and two torsional elastic modes. The modal response showed that the energy

of the two highest flatwise modes was negligible, and results were not sensitive to the deletion of the fourth and fifth flatwise modes.

When constant inflow was used, analytical rotor forces and head moments did not agree with flight test values at the measured settings of cyclic pitch, collective pitch, and shaft angle. The analysis contains provisions that permit the computer to vary pitch in a prescribed iterative manner to converge on lift, propulsive force and/or head moments. Of the parameters that could be varied, cyclic pitch values were the most accurately known from tests; therefore, the shaft angle, which is extremely sensitive to rotor-body or rotor-wing interference, was varied to obtain the analytical value of the collective pitch required. It was determined that other inflow models did not significantly disturb the trim, and the settings determined using constant inflow were retained throughout the analysis.

Experimental and Analytical Push Rod Moments

As can be seen in Figures 42 through 47, the flight test push-rod moment increases in amplitude with increasing rotor lift and speed and exhibits oscillations at a frequency in the vicinity of the blade's torsional natural frequency (approximately 6.5 cycles/revolution). The oscillations initiate over the nose and continue over the retreating side of the rotor disc. Also shown are analytical moment time histories based on a constant inflow assumption, which do not show stall flutter oscillation. An attempt was made to induce the oscillations by increasing rotor lift beyond the test values, thus increasing the penetration of the stall region. The results, Figure 56, show that the oscillation can be induced in this manner, although the instability is limited to the region beyond 270 deg. This characteristic is similar to that obtained in the sensitivity study and again substantiates the requirement for unsteady aerodynamics.

Upon noting a lack of correlation with constant inflow, all cases were rerun with variable inflow. (The variable inflow program has previously been referred to as the Circulation Program.) Results were examined and no significant change in the character of the response was exhibited. A typical comparison of constant and variable inflow results is shown in Figure 43.

The presence of wings and auxiliary propulsion implies rotor-wing interference and small values of shaft angle. Rotor-wing interference corrections were not attempted in the initial correlation studies discussed above. At the small shaft angles characteristic of compound operation, the rotor wake passes close to the disc. In such cases, the variable inflow program's accuracy, and thus the resulting airload distribution, is somewhat degraded.

In an attempt to improve the correlation between predicted and measured airloads for the S-61F, a combined analytical and empirical method

was used to modify the rotor inflow. The original S-61F correlation cases were run with constant inflow. Four of these cases were rerun with variable inflow, using the same inflow analysis as in the sensitivity studies. The airload distributions resulting from these cases were analyzed, and a further modification to inflow was made in an effort to match the test airloads. The modification was based on the effect of wing lift on rotor inflow. The inflow due to the wing causes a downflow over the rear half of the rotor disc and a smaller upflow over the front half. This inflow variation was approximated at each blade radial station by an azimuthal inflow distribution consisting of a constant and one- and two-per-rev cosine terms. Relative amplitudes were 1:8:4 for the steady, one-per-rev, and two-per-rev coefficients. All three terms have maximum values over the tail of the aircraft. The sum, which is the total increment on rotor inflow at azimuth zero, was chosen to provide a sufficiently large change in blade angle of attack to make the analytical airloads agree with the measured airloads at the tail. This modification in inflow was added to the previously calculated variable inflow distribution. For Case 43, this approach had to be modified. For this flight condition, the rotor wake, as given by the variable inflow analysis, remained very close to the rotor plane. This calculated inflow gave large distortions in rotor loads. More accurate airloads were found by using the modification method with the constant inflow case as the base. The only harmonics of inflow used for this case were the one- and two-per-rev components required to improve airloads at the tail.

As shown in Figures 48 through 51, this procedure did improve the airload correlation. The change in blade flapping resulting from the inflow modification washed out part of the change in angle of attack so rotor loads at the tail did not correlate exactly. The airloads in the region of azimuth 90 deg (over the right wing) did not show much improvement in correlation. The reason is probably the local complexity in inflow due to the proximity of the wakes of the preceding blades for a compound aircraft. The variable inflow analysis used does not consider wake distortions which result from wake interaction. Thus, the true location of the blade wake near azimuth 90 deg is not given in the analysis. This is why Case 43 could not be used with variable inflow. Research is under way at United Aircraft for the development of a program which does yield wake distortions. This will permit a more accurate description of airloads.

The cases run with modified airloads showed a slight increase in the oscillatory push rod loads but did not improve correlation significantly. Results are shown in Figures 52 through 55.

Additional Investigation of the Stall Flutter Mechanism

In reviewing the results of the Sensitivity, Parametric, and Correlation Studies, a number of facts indicate the need for a further investigation of the stall flutter mechanism. The stall-flutter-type oscillation was achieved in the Sensitivity Study, substantiating the theory that unsteady aerodynamics are necessary for stall flutter prediction.

However, the azimuthal persistence of the oscillation is significantly less than that exhibited by test. It was determined that the use of unsteady aerodynamic data tends to reduce angles of attack for the same lift, thus reducing the penetration of the stall region and, consequently, control loads. This phenomenon is exhibited in the Correlation Study, where an increase in rotor lift to levels above test was needed in order to initiate the oscillation. An attempt to modify the analytically developed airload distribution, using measured airloads, resulted in no significant improvement in the correlation. Because of the self-excited oscillations observed in the parametric studies, it was concluded that the general analytical approach can lead to a valid prediction method. However, the lack of substantial aerodynamic excitation, with unsteady aerodynamics only, implies the possibility of additional effects that cause the lack of correlation. The following discussion reviews the results of additional studies into the stall flutter mechanism.

A major consideration is the inability of the analysis to initiate the oscillation prior to azimuth 270 deg. The character of the push-rod load oscillation is somewhat different from that measured in flight. The flight test oscillations begin earlier in the rotor disc, before azimuth 180 deg rather than in the vicinity of azimuth 270 deg.

Since the blade is not in stall on the advancing half of the rotor disc, some other mechanism appears to contribute to the push-rod load oscillation. Torsional moments at the blade root can be generated by the coupling of flatwise and edgewise response. For example, among the components of torsional moments reacted at the push rods are those produced by the product of blade lift and edgewise blade displacement due to bending and by the product of drag load and flatwise displacement. These products are referred to as load-deflection terms. A direct determination of the importance of such terms could not be made from flight test data, since blade deflections were not measured directly. However, blade bending moments are a measure of both loading on the blade and the deflection of the blade. A product of the flatwise and edgewise bending moments at a point on the blade serves as an indicator of the significance of the load-deflection terms. If the azimuthal variation of this moment product correlates with the push-rod load azimuthal variation, the load-deflection effects may be significant. Figure 57 shows a typical correlation of these terms. Relative magnitudes have no importance in this figure since the units of the two curves differ and are therefore not indicated. However, it is significant that the maxima and minima of the moment product consistently lead (by a small phase angle) the maxima and minima of the push-rod load curve. In the region from 270 deg to 360 deg the moment product has a small value, but the push-rod load oscillation increases in amplitude. It is precisely in this region that stall flutter oscillations were predicted by the analyses. This pattern was found consistently for the flight conditions examined.

This correlation of moment product and push-rod loads suggests that the oscillations of the S-61F push-rod loads are initiated before the blade

reaches the stall region by a combination of flatwise and edgewise response of the blade, and that the stall flutter mechanism further amplifies the push-rod loads on the retreating half of the rotor disc.

As part of the evaluation of the correlation, Case 43 was rerun using steady-state aerodynamics. Blade pitch and aircraft attitude were held the same as in the unsteady aerodynamic analysis. A comparison of the two cases provides some insight into the reasons for lack of correlation of push-rod loads (Figures 58 through 60). As compared with steady aerodynamic results, the inclusion of the unsteady aerodynamic terms results in greater rotor lift, but generally lower flatwise and edgewise vibratory blade stresses. The smaller load-deflection terms, which result from the lower stresses, do not contribute as much to the blade torsional response as the larger load-deflection terms found in the steady-state case.

This difference is evident in Figure 58, which shows the push-rod moment for both the steady and unsteady aerodynamic analyses. The use of steady aerodynamics does produce a small oscillating push-rod moment on the retreating half of the disc, while no such oscillation is evident with the unsteady aerodynamic analysis. It was shown in the Sensitivity Studies that unsteady aerodynamics in stall will induce flutter. That no such stall flutter occurred with unsteady aerodynamics in Case 43 as attributable to the low angle of attack on the retreating blade, so that the unstable region was not sufficiently penetrated to cause flutter. The previously mentioned load-deflection terms were unable to act as the oscillating mechanism here because of their small size, although they had done so in the steady-state aerodynamics case, where they were larger. One may then wonder why the presence of unsteady aerodynamics only was sufficient for flutter in Figure 28, regardless of the effects of the load-deflection terms. The answer would appear to lie in the higher torsional frequency used there, which seems to desensitize the rotor torsional response to load-deflection terms. Figures 65 and 66 show the flatwise and edgewise stress correlations at 65 percent and 46 percent of the rotor radius, respectively. Prediction of these stresses was better with the steady-state aerodynamics.

Good correlation of flatwise and edgewise blade stresses apparently is essential for good correlation of push-rod loads. However, even when blade bending stresses are fairly well predicted, as in the steady aerodynamic case, something more is needed for push-rod load correlations. From the Parametric Studies and from the S-61F cases in which collective pitch was incremented, it is evident that the use of unsteady aerodynamics can produce large stall-flutter-induced push-rod moments. This effect needs to be combined with an accurate prediction of flatwise and edgewise moments to provide the mechanism for initiating the oscillation before the blade reaches the stall region.

It is not evident at present that changes need to be made. It is possible that the present unsteady aerodynamic analysis can lead to correct results if rotor trim and rotor inflow variations are considered further. For example, the poor correlation of blade stress in certain azimuthal

regions suggests that local effects such as wake distortions, radial flow, or airframe-rotor interference can be most important. Possibly, a change is needed in the way in which the unsteady aerodynamic terms are used. This may include the incorporation of unsteady drag effects or a modification in the present method for determining blade lift and pitching moments.

The results of the S-61F correlation show that the analytical approach being used is generally valid. Continued investigation of the area of rotor trim and the characteristics of the unsteady aerodynamics of oscillating airfoils should lead to an accurate analysis for the prediction of push-rod loads. The continuing effort should include tests of a two-dimensional airfoil executing forced pure sinusoidal motion, forced multiharmonic motion, and self-excited stall flutter. These tests would be designed so as to examine the validity of a basic assumption made in this investigation; namely, that unsteady aerodynamic data for pure sinusoidal pitch motions can, in fact, be used to predict the unsteady characteristics of an airfoil executing multiharmonic pitch motions into stall. In addition, the tests would provide detailed stall flutter information on a simple model, thereby permitting a more direct evaluation of the stall flutter prediction analysis.

Additional sensitivity studies should be undertaken with the analytical method developed in the present program. The objective of these studies should be to determine if the unsteady moment data of Table II can be modified so as to reduce the discrepancies noted without destroying the basic ability of the tabulation to reproduce the general features of the original sinusoidal data from which it was derived. The possibility of developing semiempirical modifications to the compressibility scaling techniques used herein should also be examined. Satisfactory accomplishment of this objective would provide a stall flutter analysis that can be used as an interim design tool while more fundamental, long-range investigations of unsteady aerodynamic methods are pursued.

MANEUVERING FLIGHT TEST CORRELATION - CH-53A

The CH-53A flight test program for structural substantiation produced maneuvering flight data under conditions that had produced not only stall flutter of the previously observed form, but also cases in which the stall flutter oscillations persisted over much larger portions of the azimuth.

Two cases of CH-53A maneuvers were selected for correlation. A short transient of about 6 sec duration, involving a right turn at a nominal 120-kt speed and an angle of bank of approximately 60 deg, was the first case examined because it could be considered to be a quasi-steady maneuver for most of its length; that is, although it was accelerated flight, the accelerations and angular accelerations were close to constant, and there was little variation in the cyclic and collective pitch values. This made it an ideal choice for initial correlation of the accelerated flight provisions of the analysis, as well as being a test point in which stall flutter was observed. The last 2 sec of this flight test point involved a small (approximately 3 to 5 deg) increase in roll angle,

which was accompanied by severe vibrations on all channels of data and extremely high control load amplitudes. However, the data contained too much noise or vibrations to be easily used. It was therefore decided to attempt correlation up to the initiation of the noise.

The second maneuver examined was a longer transient of approximately 23 sec involving a nominal 150-kt right turn. The angle of bank for this point varied from under 30 deg at the start to approximately 60 deg, followed by a rollout back to level flight. The more complex form of this maneuver served to provide an opportunity for observing the effects of a changing load factor on the observed stall flutter and on the accelerated flight provisions of the analysis.

Mathematical Model

As in the Sensitivity and Parametric Studies, the modes used were two rigid-body degrees of freedom (flap and lag) and three flatwise, two edgewise, and two torsional vibratory modes.

The CH-53A flight test aircraft carried a large number of accelerometers, velocity pickups, and inclinometers at various locations. After suppression of the local vibration components of the signals and other corrections, these data were processed to provide 16 time histories of motion components in an axis system affixed to the rotor hub. These time histories represented 6 degrees of freedom of aircraft motion, their necessary time derivatives, and histories of control angles.

The maneuver option of the program was used for the time histories just mentioned; that is, fuselage motions were prescribed along with time histories of pilot hand motions on the cyclic and collective controls. The rotor transient response was examined, rather than allowing it to die away to steady state as in other sections of this report.

As in the S-61F cases, flight-test-reported cyclic pitch was accepted, and no attempt to trim head moments was made. While the head moments of the S-61F were measured, those on the CH-53A were unknown.

The CH-53A had carried no instrumentation to measure rotor lift. Load factor was available either from measured aircraft weight and motions or from a highly damped vertical accelerometer that acted as a load factor readout. Although the motion and load factor data were in general agreement, small differences, especially at the higher load factors, caused some uncertainty in rotor lift. With an assumed correction for fuselage vertical drag, the rotor lift was calculated in a band that varied from ± 3000 to ± 6000 lb about the mean value used for correlation. This represented a band of about ±8 percent in rotor lift.

Flight-test-reported collective pitch and shaft angle did not produce an analytic lift near the calculated experimental rotor lift. Therefore, collective pitch was adjusted until rotor lift near the initiation of

the maneuvers equaled the test lift as determined from gross weight, load factor, and estimated fuselage vertical drag. Once this was accomplished, the collective pitch was varied with time in a manner paralleling that of flight test; that is, the value of collective pitch reported by flight test at the instant of time in which lift was matched was not used, but the departures from this reference point were followed exactly.

Only constant inflow was used in the maneuvering cases, as the present variable inflow program is not applicable when the vorticity pattern is time varying. Although the inflow was held constant over the disc, it was time varying. On the basis of the time history of required rotor lift, itself generated from the load factor and an assumption concerning body vertical drag, a momentum value of inflow was computed.

Discussion of CH-53A Correlation

As in the S-61F study, the degree of correlation was less than satisfactory. However, good correlation was achieved in portions of the maneuvers, providing added confidence in the analysis. Figures 61, 63, and 64 show the variation in ½ peak-to-peak push-rod moment and rotor lift with time in the two transients. In the short (120-kt) transient, Figure 61, the analytical rotor lift was adjusted in an attempt to match test values, which are shown as a broad band because of the uncertainty of the fuselage vertical drag load. Collective pitch and rotor shaft angle were varied in an attempt to achieve the lift calculated to have been present in flight. The lifts shown are predominantly below the flight test band.

Because the analysis was unable to generate lifts higher than those shown, it is probable that the blade is heavily stalled over much of the azimuth and has penetrated deeply into, or possibly through, the region of negative damping. However, the fact that the analytical lift is lower than the flight lift would imply that the analytical load-deflection terms would be reduced. Since the 1/2 peak-to-peak push-rod moment is higher for analysis than for test in this case (Figure 61), it can be inferred that the unsteady aerodynamic effects predominate. The amplitude of this moment is largely the result of stall-flutter-type oscillations whose character is fairly similar to that of flight test, as can be seen in the plot of a representative revolution, Figure 62.

The attempt to match calculated flight lift for the longer (150-kt) transient (Figure 63) was less successful. Although the correct lift was generated in revolutions 10 through 20 (the area selected for trim), the remaining portions of the trace show sizable disagreements. However, the ½ peak-to-peak moment trace (Figure 64) is more encouraging, showing trends similar to flight test, with varying degrees of amplitude correlation. At the peak values (revolutions 40 to 50), the analytical amplitude is below that of flight test, whereas the opposite is true earlier in the maneuver.

In revolution 20 (Figure 65), stall flutter oscillations that correlate well with flight test can be observed. The discrepancies, which

account for the higher peak-to-peak amplitude, are on the advancing side of the disc. They seem to reflect slower damping out of the oscillation than occurs in flight test. On the other hand, revolution 41 (Figure 66) shows the correct amplitude but without the oscillation. This revolution occurs immediately after the drop in lift observed in Figure 63. Such a drop would indicate both a lowered angle of attack and smaller load-deflection terms. Thus, absence of oscillation on this trace is not surprising. The cause of this reduction in lift has not been established.

In general, the maneuvering flight correlations emphasize the same factors as the S-61F correlation. To correlate, one needs both unsteady aerodynamics in the stalled region and proper load-deflection terms to initiate oscillations prior to stall. In addition, the trend of the ½ peak-to-peak moments in Figure 64 is encouraging and tends to provide confidence in the maneuver modifications. The reasons for the lift discrepancies (Figures 61 and 63) are not clear, but the discrepancies seem to be connected with the constant inflow time histories used.

CONCLUSIONS AND RECOMMENDATIONS

CONCLUSIONS

The conclusions listed below were reached in the course of this study. Note that conclusions 6 through 10 should be applied only in the determination of possible trends. Further validation of these trends must await analytical improvements leading to a higher degree of correlation of the analysis with flight test data.

1. Incompressible unsteady aerodynamic normal force and moment characteristics generated by an NACA 0012 airfoil executing pure sinusoidal pitch motions into stall can be expressed with reasonable accuracy as functions of instantaneous angle of attack, angular velocity, and angular acceleration (see, for example, Figures 9 through 16).

2. Application of unsteady data in the form described in (1) above to compute rotor blade response at an advance ratio of 0.4 leads to the prediction of significant self-excited torsional oscillations of the stall flutter type. These oscillations, which occurred above a rotor lift coefficient/solidity ratio of about 0.065, directly impose large oscillatory moments on the control system.

3. The analysis presented in this report predicted stall-flutter-induced oscillations of the NH-3A (S-61F) push-rod loads initiating only at lifts greater than those at which oscillations were observed in flight.

4. Accurate correlation of flatwise and edgewise blade response is essential, since this response appears to contribute significantly to the NH-3A oscillatory push-rod loads, with unsteady aerodynamics serving to amplify such oscillations in the stalled flow region. However, replacement of steady-state aerodynamics with unsteady aerodynamics adversely affected correlation of flatwise and edgewise blade stress correlation for the NH-3A.

5. Analysis of the CH-53A maneuver cases supports the NH-3A conclusions that both unsteady aerodynamics and good flatwise and edgewise response predictions are needed to predict control loads adequately. In addition, correlation of control loads during the maneuvers was more encouraging than in steady flight.

6. For the flight conditions investigated in the Parametric Studies, reducing the natural frequency of the first torsional mode from 8.2P to 4P reduced the amplitude of the self-excited torsional oscillations at a given rotor lift because of the slower response of the 4P blade.

7. Movement of the blade center-of-gravity axis aft (from 25 percent to 30 percent chord) had a severe detrimental effect on blade torsional response and associated oscillatory moments. This is primarily due to the destabilizing dynamic coupling between the blade flapping and flatwise bending modes and the torsional mode. The effect of aft center of gravity on the self-excited moment components was small but generally detrimental.

8. Increasing blade twist reduced the self-excited moment oscillations at a given lift when rotor inflow was assumed to be constant.

9. Except for reducing significantly the beneficial effects of increased twist noted in (8) above, the inclusion of variable inflow effects had little effect on the general nature of the results obtained.

10. At conditions where retreating blade angles of attack exceeded steady-state stall values, significantly higher rotor lifts were predicted using unsteady aerodynamic data than were predicted using steady-state aerodynamic data.

RECOMMENDATIONS

At the present time, it is difficult to establish the reason(s) for the discrepancies noted between analytical and experimental results, principally because of the complexity of the experimental model used in the comparison - a full-scale helicopter. Achievement of good correlation in such circumstances requires that (1) detailed, accurate flight test data be available, (2) all facets of the aeroelastic analysis be accurate (inflow, applicability of sinusoidal unsteady data, use of compressibility scaling, etc.), and (3) factors neglected in the analysis such as radial flow, wake geometry distortions, etc., be, in fact, negligible. Many approaches could be followed in attempting to resolve the problem. One could, for example, eliminate the need for compressibility scaling assumptions by acquiring additional sinusoidal unsteady data at higher Mach numbers. It is believed, however, that this approach may be premature and that the two investigations recommended below represent the most logical next steps in the study of stall-flutter-induced control loads.

1. An experimental study should be undertaken, using a two-dimensional airfoil as a model, to examine the validity of an assumption that forms the basis for nearly all rotor dynamic stall analyses; namely, that unsteady aerodynamic data obtained for an airfoil executing sinusoidal motion can be used to predict the characteristics of an airfoil executing nonsinusoidal motions into stall. Conclusions from such a study would have

far-reaching effects on the course of future unsteady aerodynamic testing as applied to helicopter rotors.

2. An analytical study should be conducted to determine if the quantitative accuracy of the method described in this report can be improved to permit its use as an interim design tool while more fundamental, longer range studies of the type noted above are pursued. In this study consideration should be given to possible semiempirical modifications to the basic unsteady data tabulation and associated compressibility scaling procedures. In addition, the effect of possible refinements in rotor trimming and inflow modeling techniques on blade bending stress correlation should be examined.

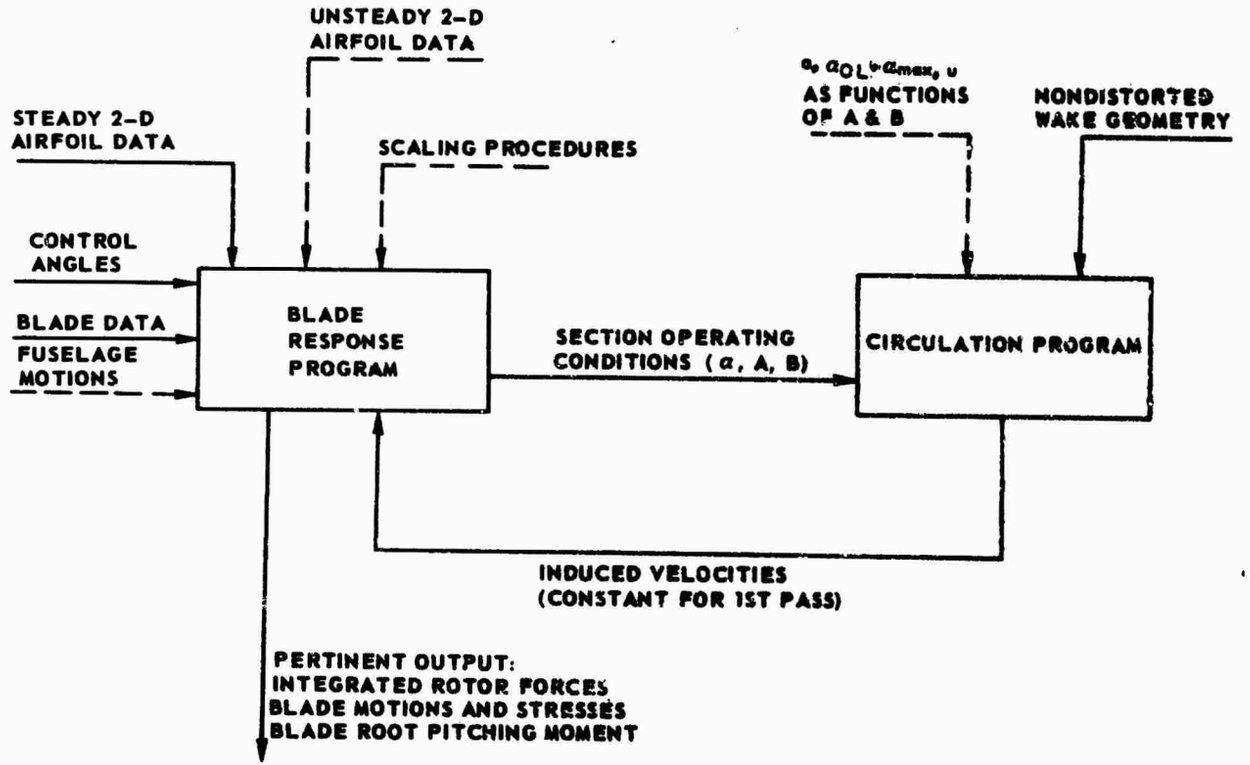

Figure 1. Modified UAC Rotor Analysis.

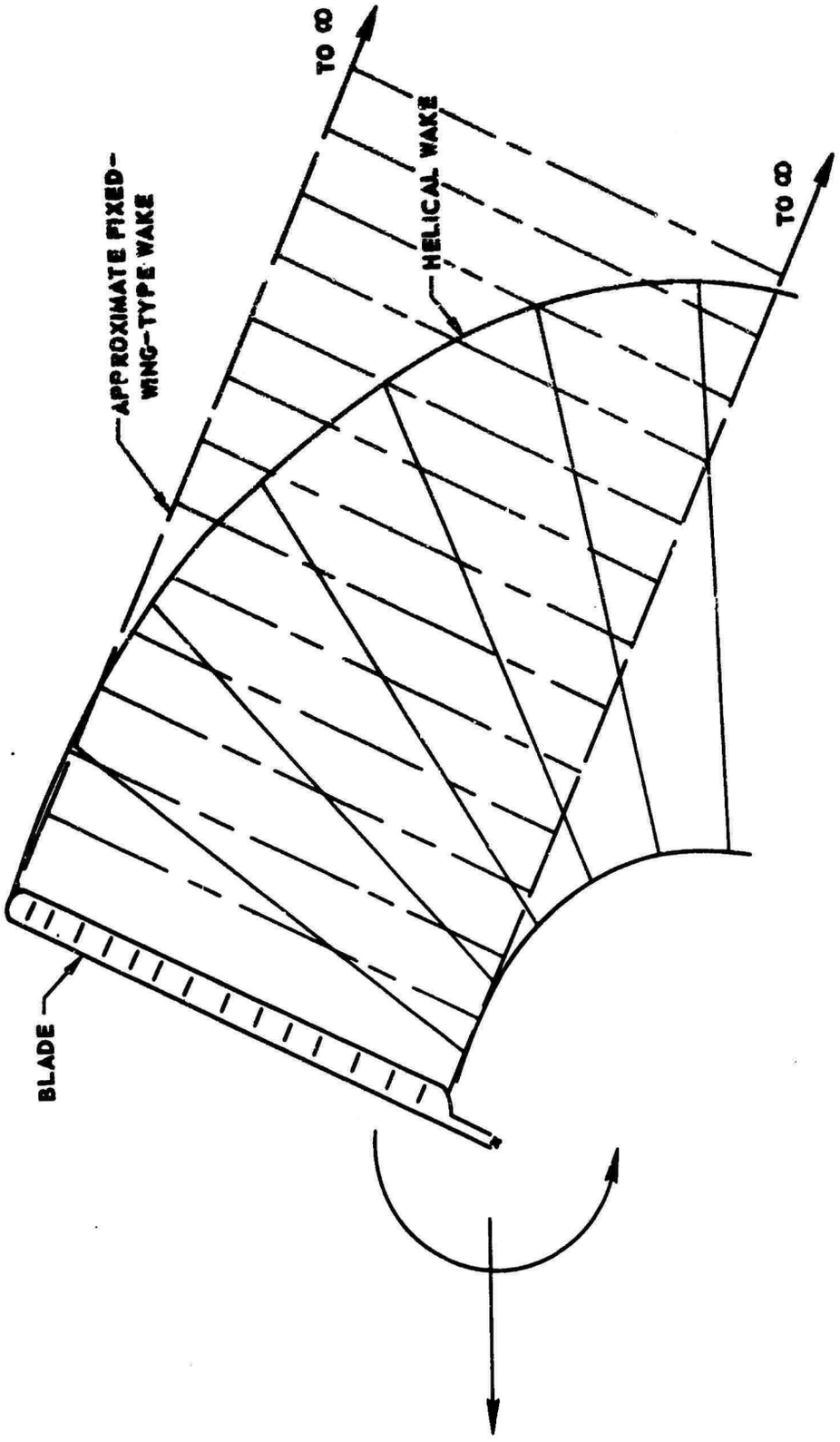

Figure 2. Blade Wake Approximation.

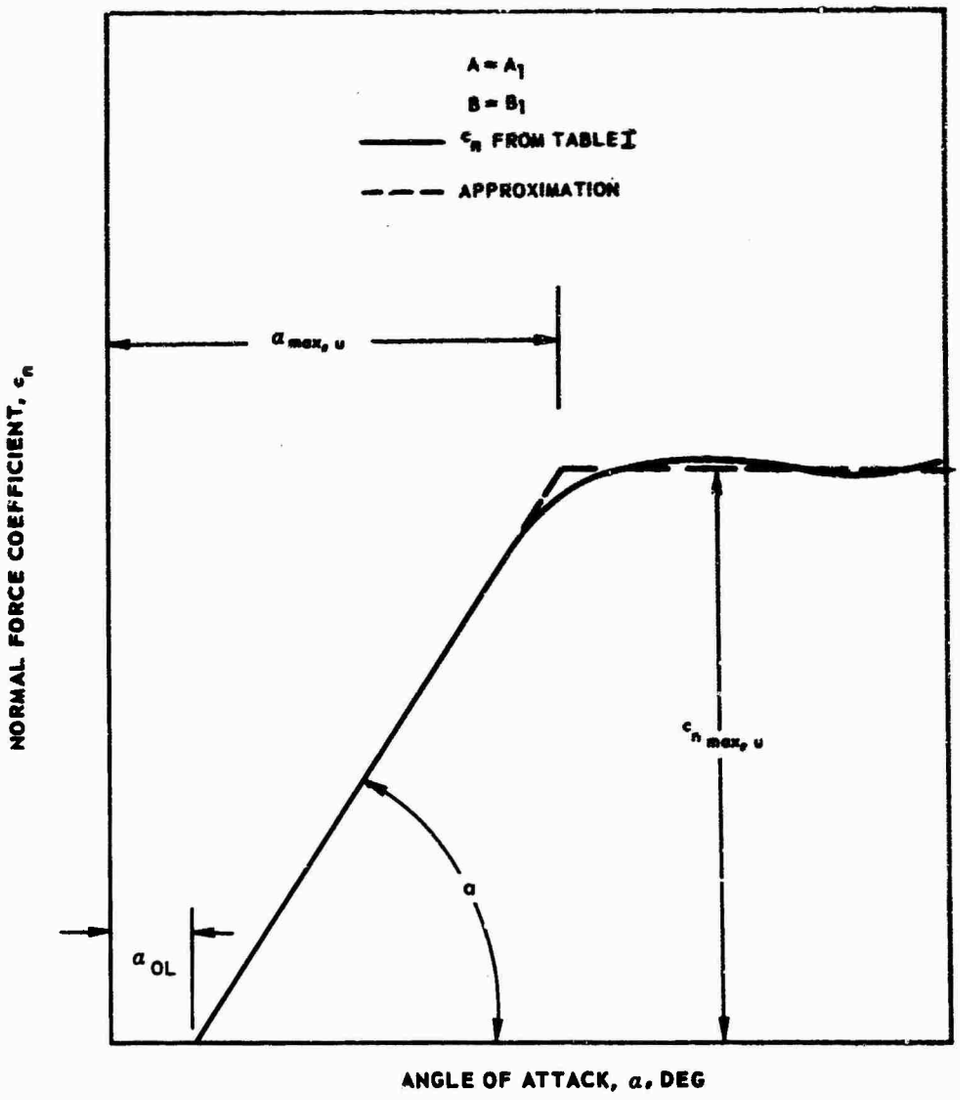

Figure 3. Approximation of Typical Unsteady Normal Force Curve.

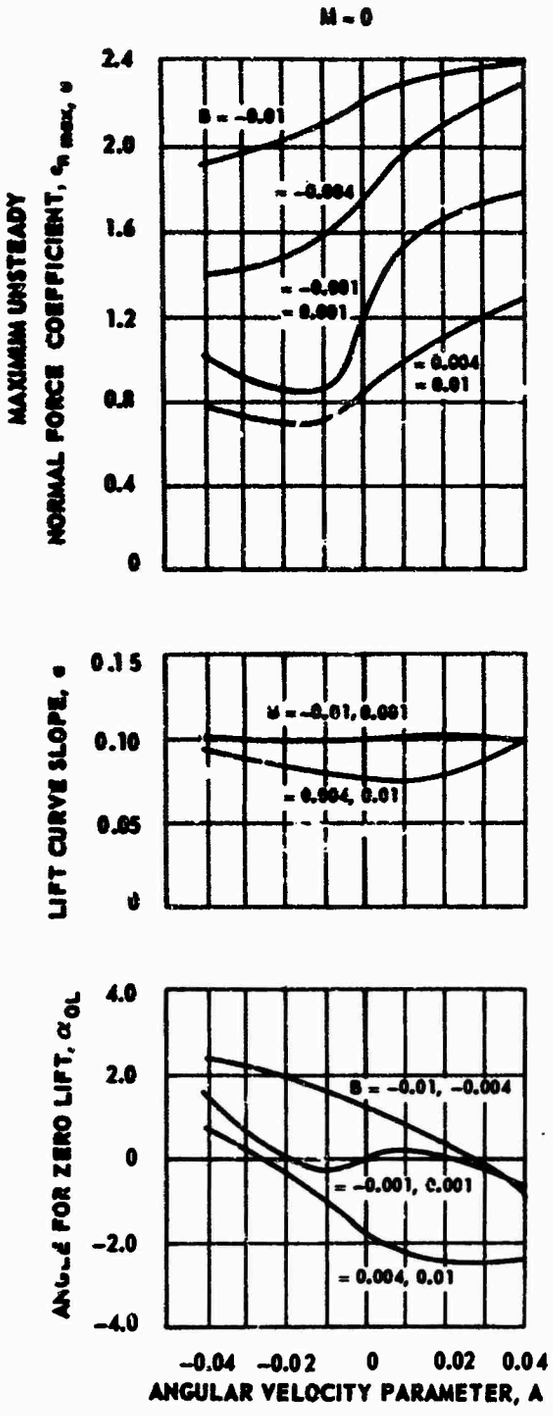

Figure 4. Variation of Maximum Normal Force Coefficient, Lift Curve Slope, and Angle for Zero Lift With Angular Velocity and Angular Acceleration Parameters.

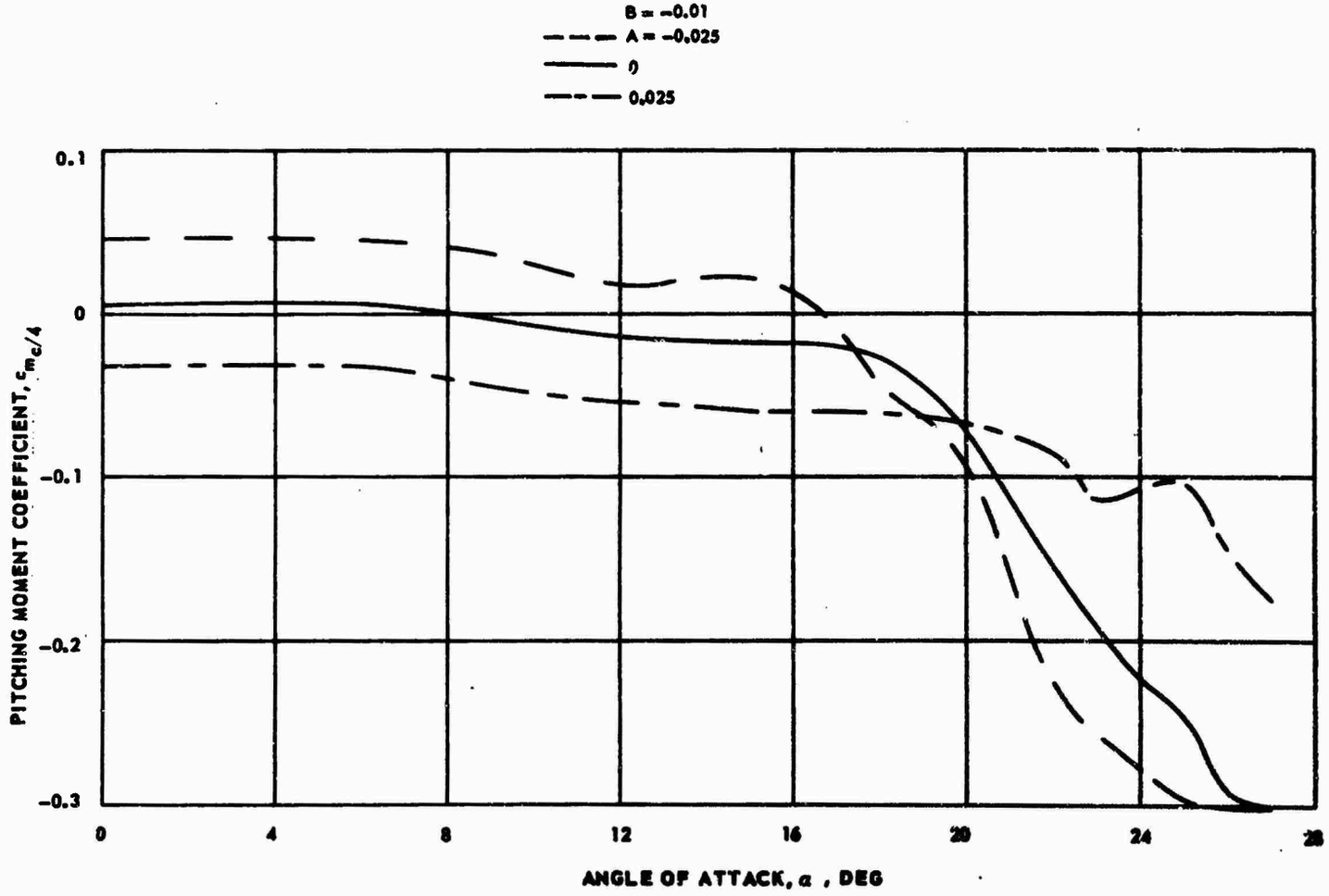

Figure 5. Dynamic Moment Characteristics - B = -0.01.

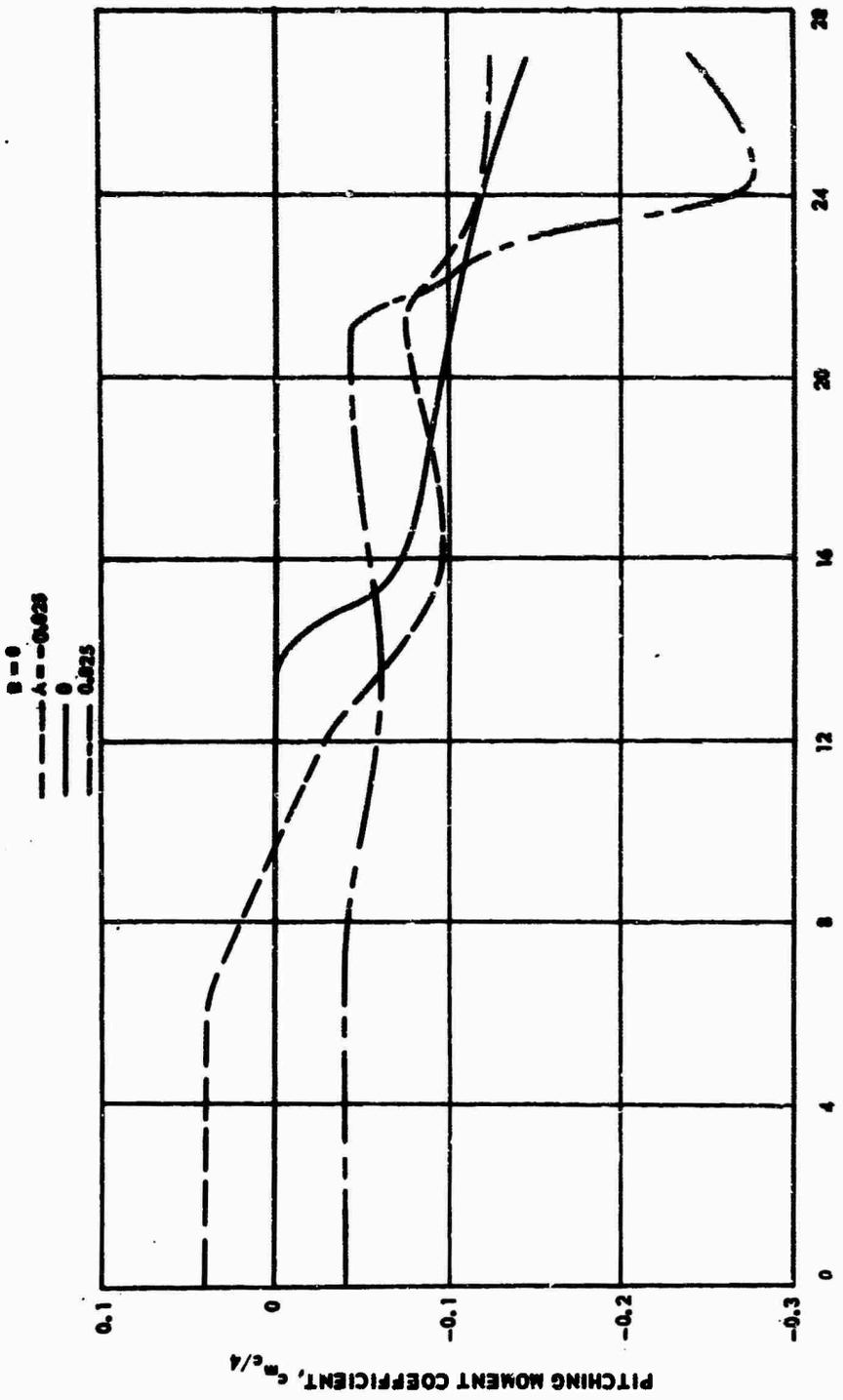

Figure 6. Dynamic Moment Characteristics - B = 0.

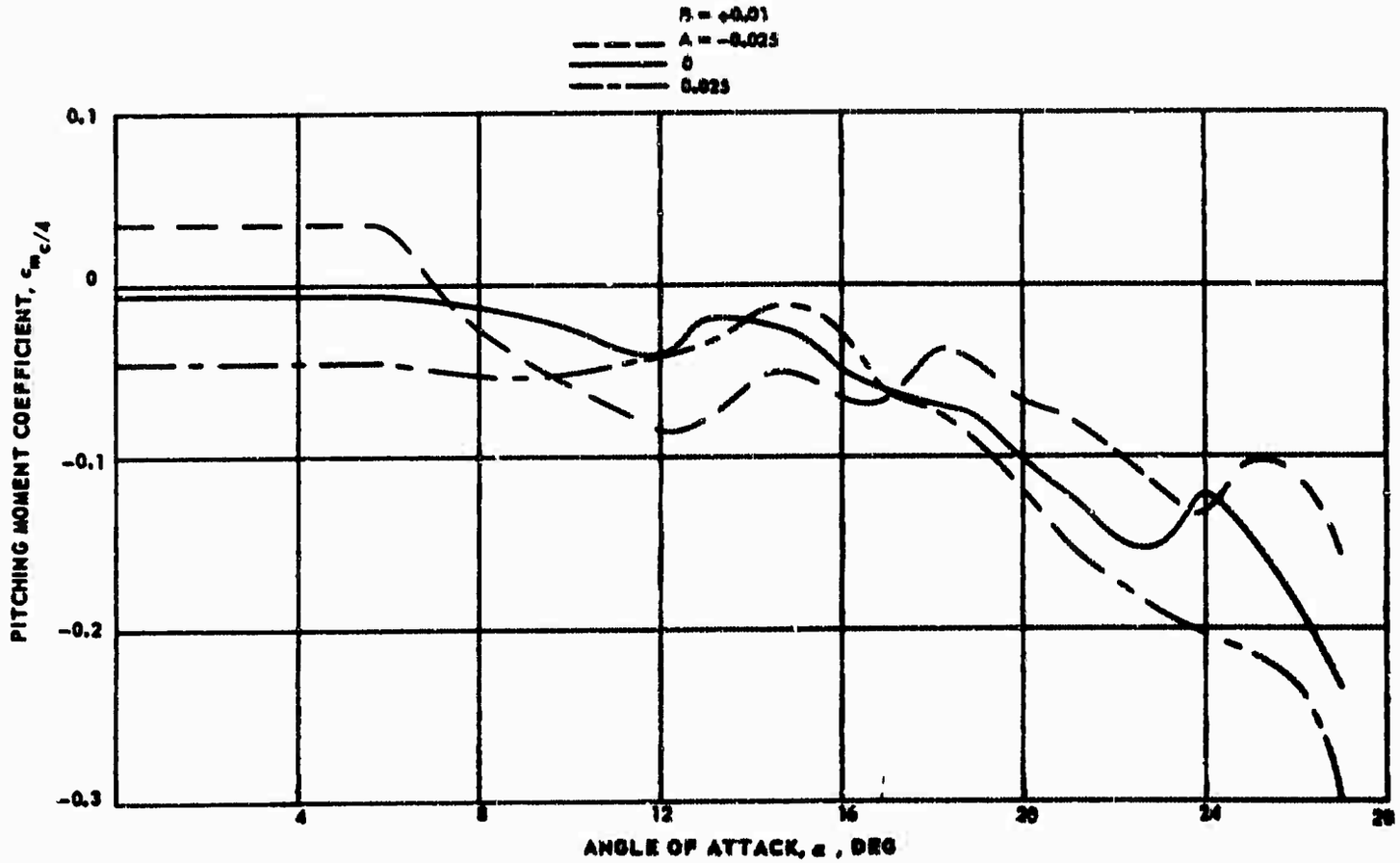

Figure 7. Dynamic Moment Characteristics - B = +0.01.

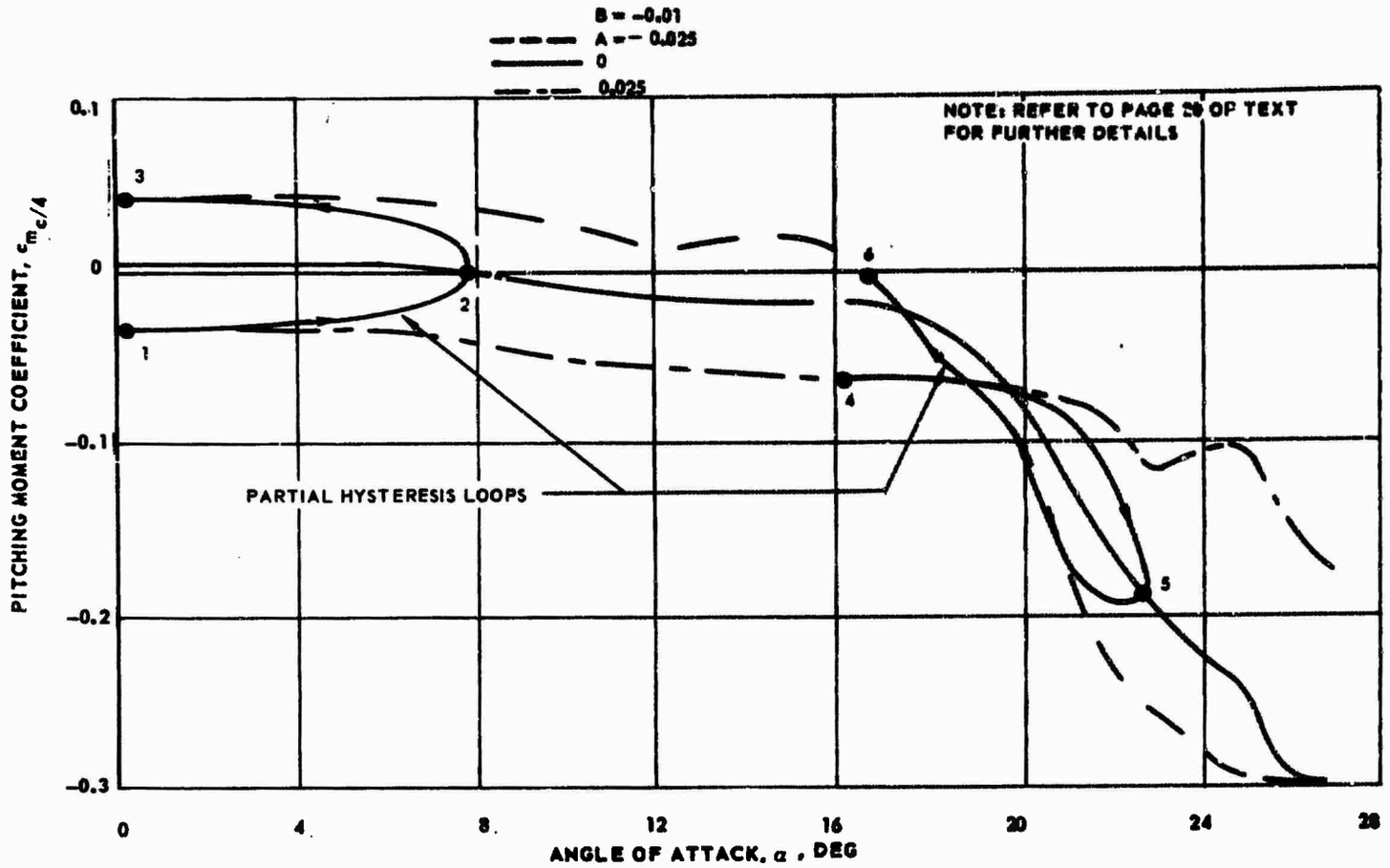

Figure 8. Schematic of Relation Between Dynamic Moment and Hysteresis Loops.

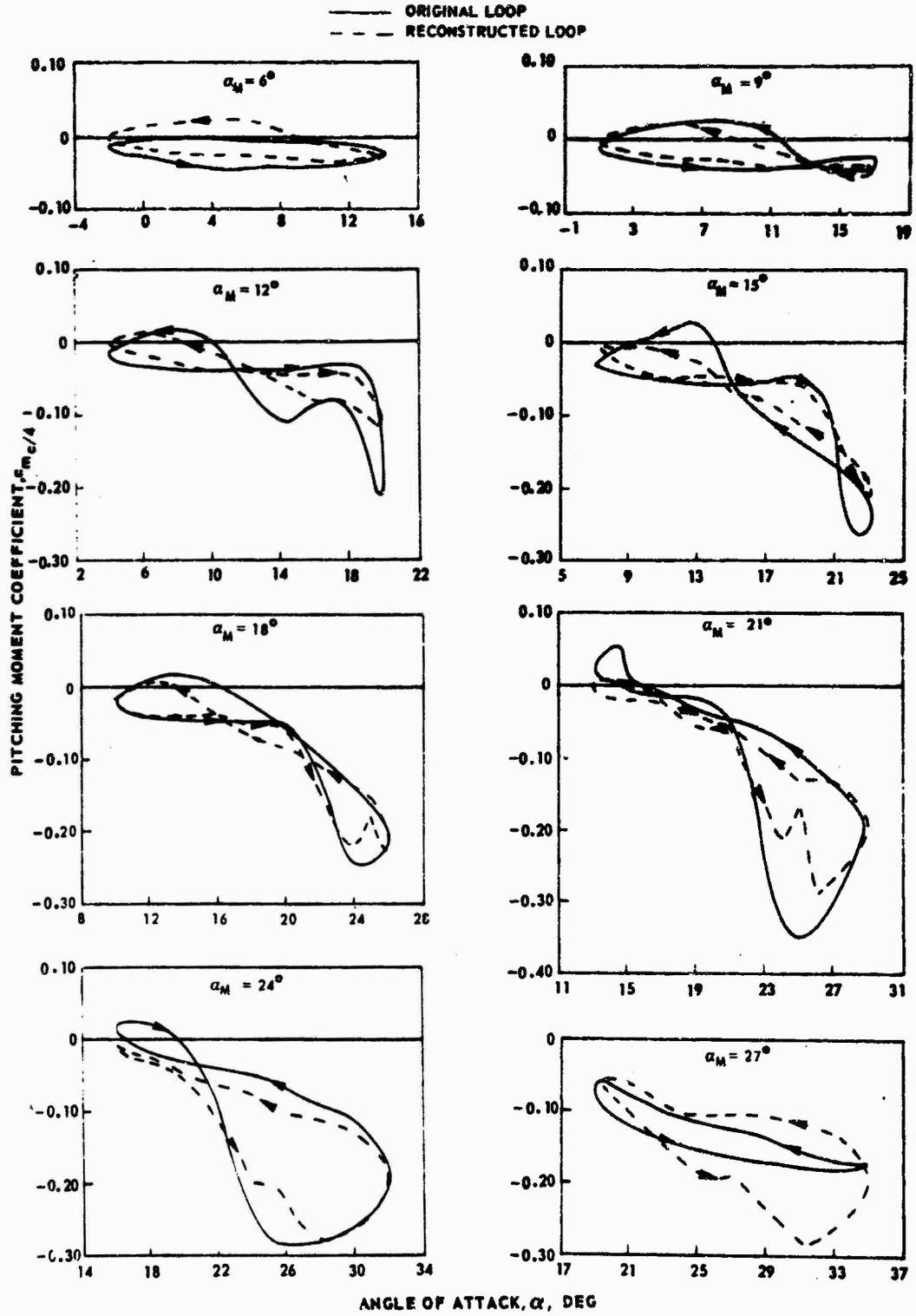

Figure 9. Comparison of Original and Reconstructed Moment Hysteresis Loops for Various Mean Angles of Attack - k = 0.112.

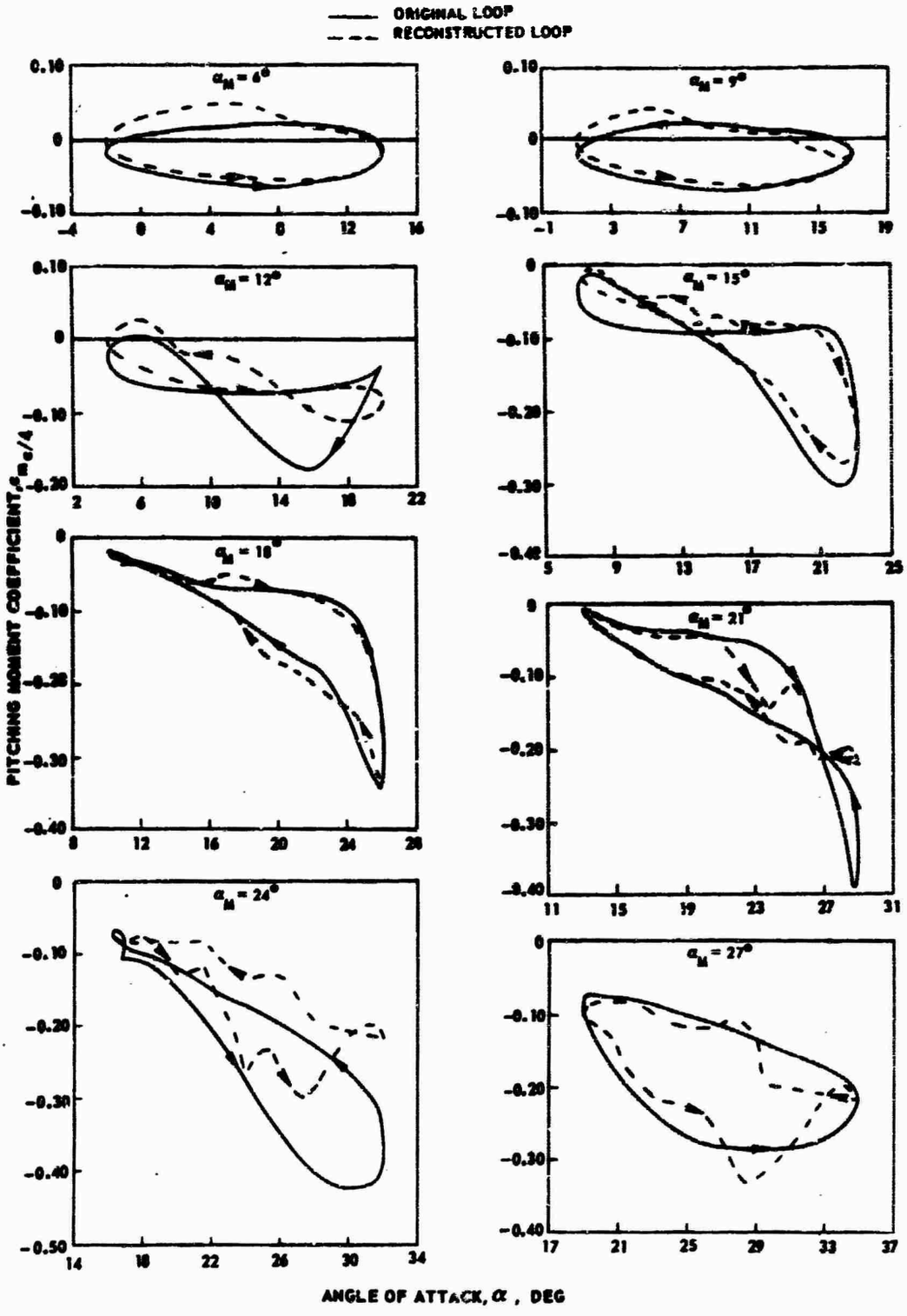

Figure 10. Comparison of Original and Reconstructed Moment Hysteresis Loops for Various Mean Angles of Attack - k = 0.225.

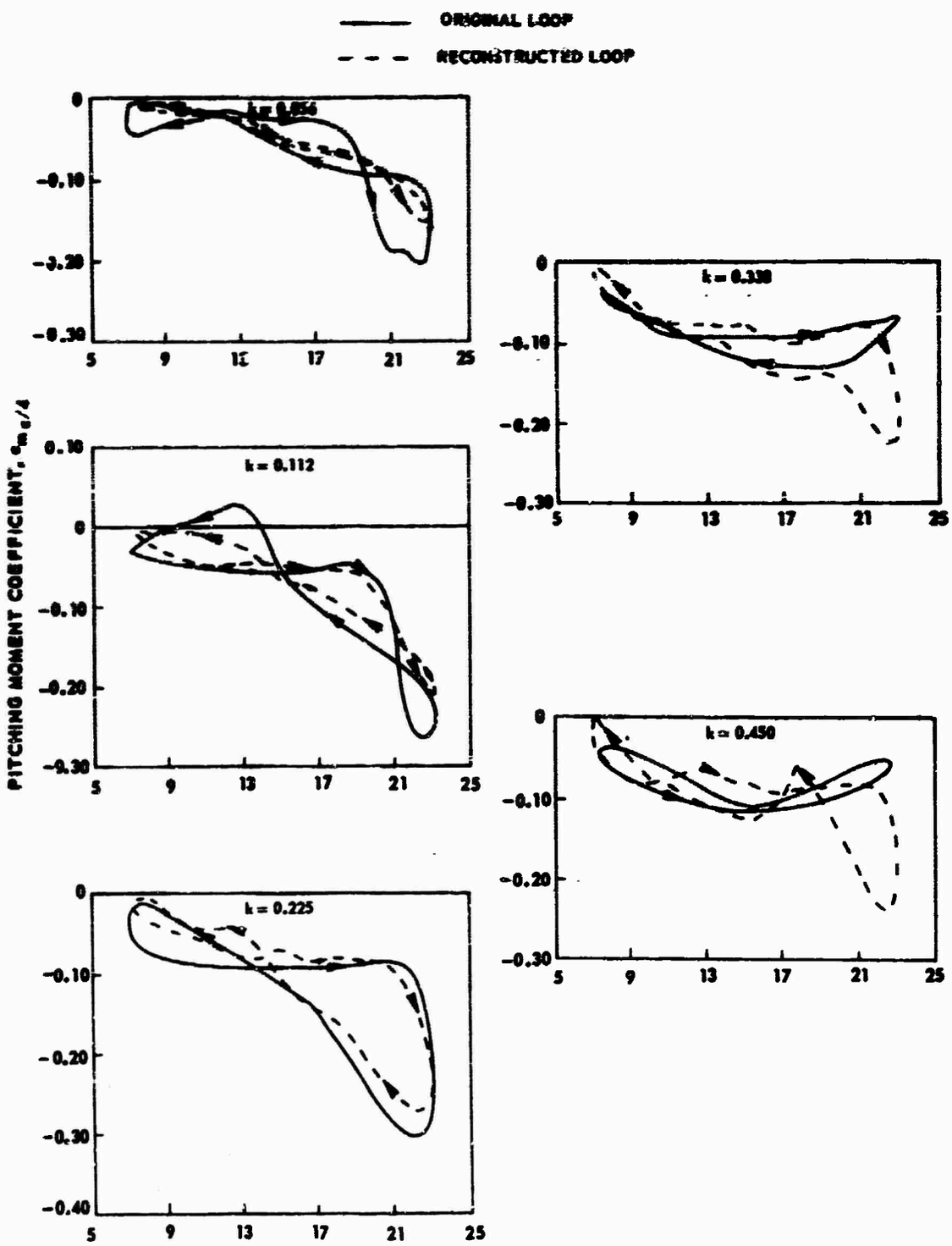

Figure 11. Comparison of Original and Reconstructed Moment Hysteresis Loops for Various Reduced Frequencies - α_M = 15 deg.

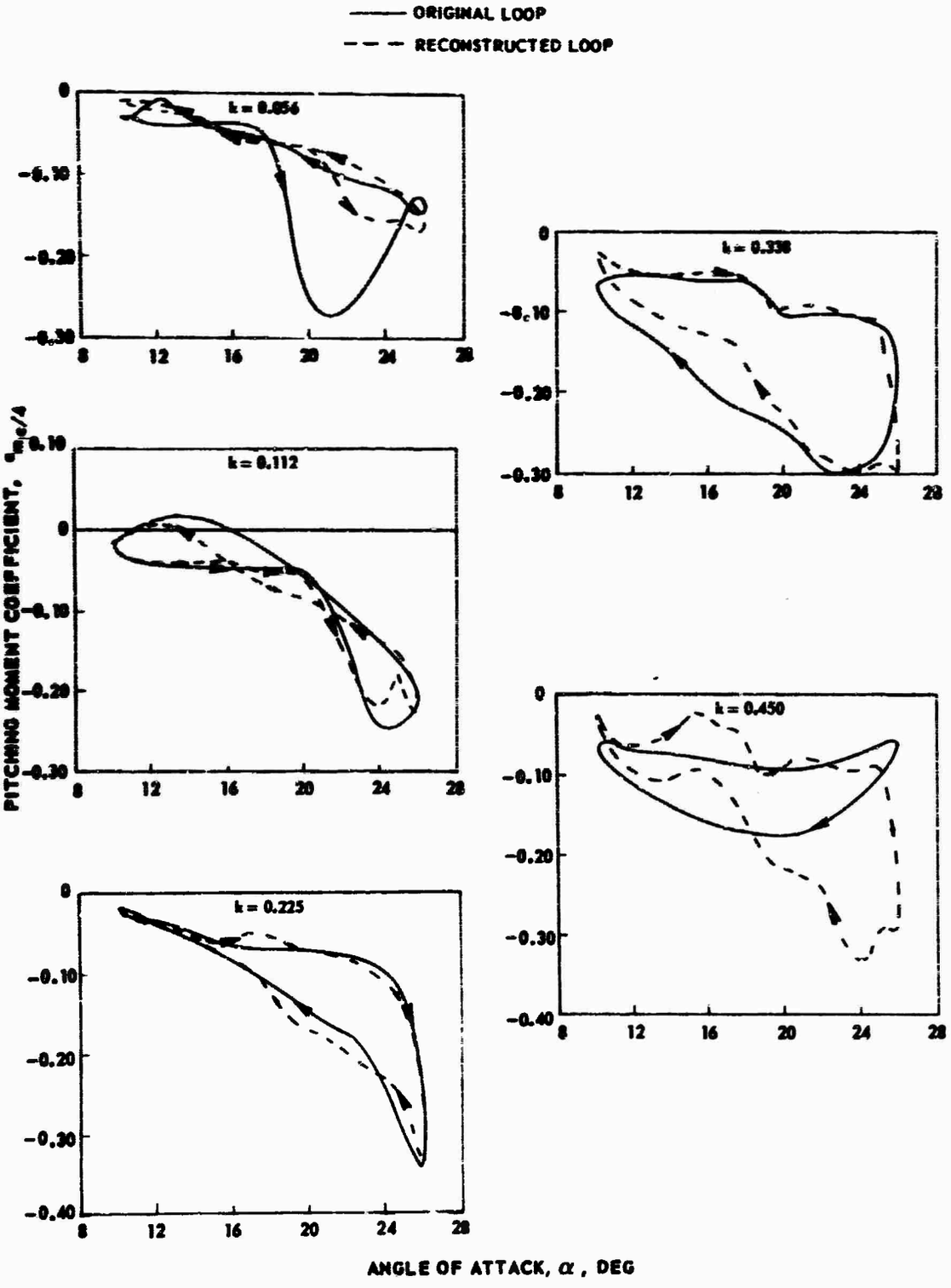

Figure 12. Comparison of Original and Reconstructed Moment Hysteresis Loops for Various Reduced Frequencies - α_M = 18 deg.

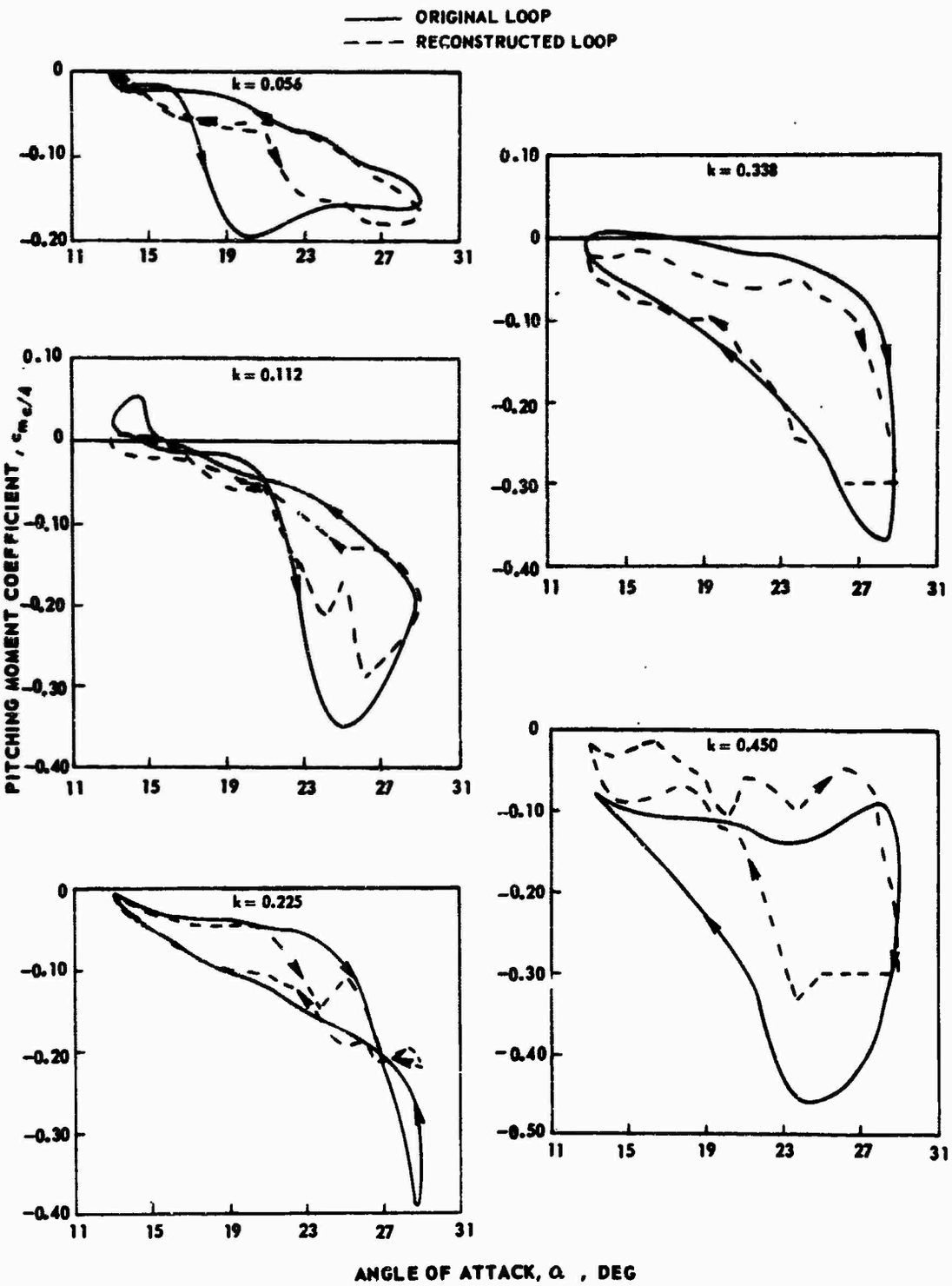

Figure 13. Comparison of Original and Reconstructed Moment Hysteresis Loops for Various Reduced Frequencies - α_M = 21 deg.

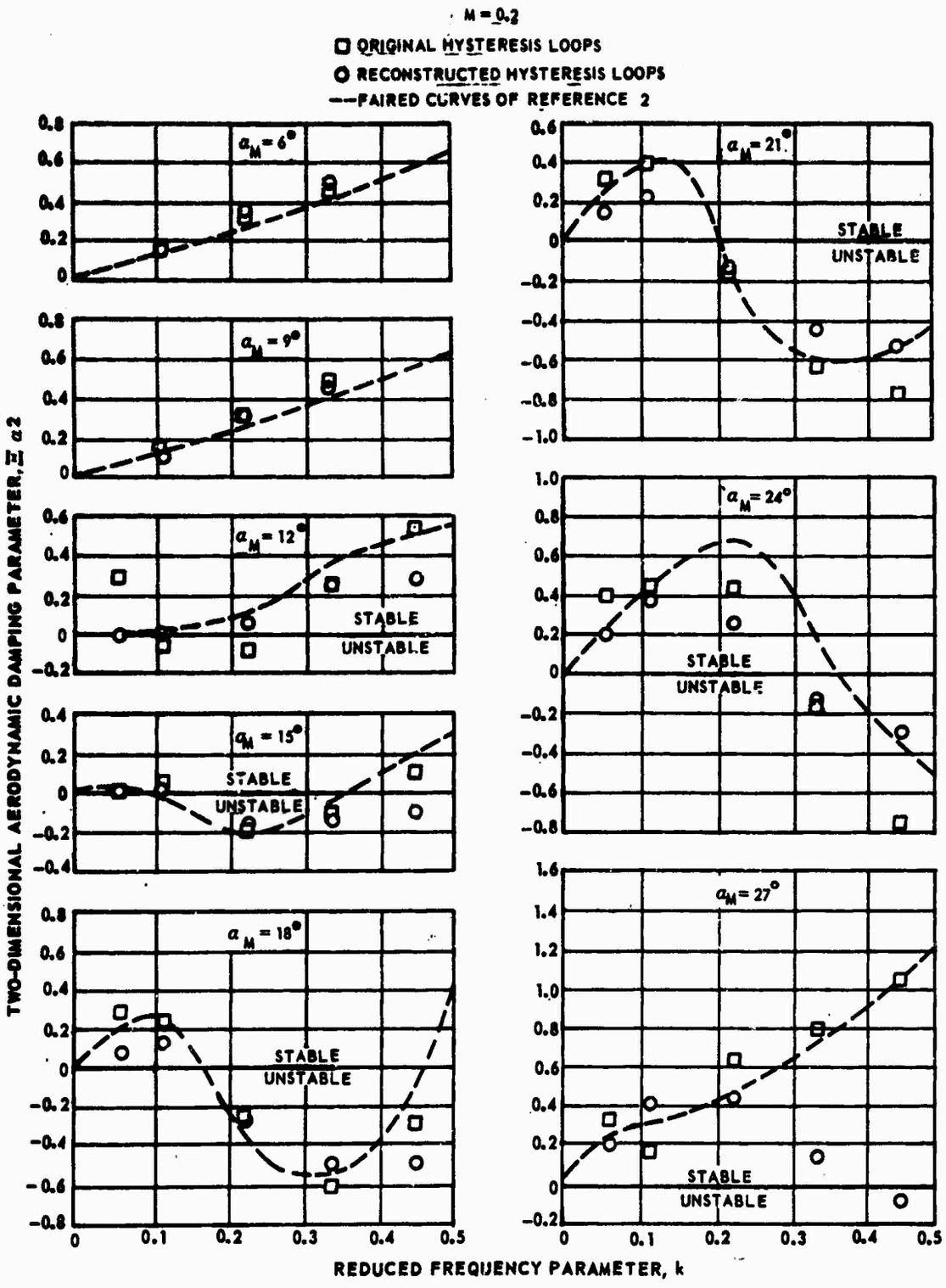

Figure 14. Comparison of Aerodynamic Damping Parameter Determined From Original and Reconstructed Moment Hysteresis Loops.

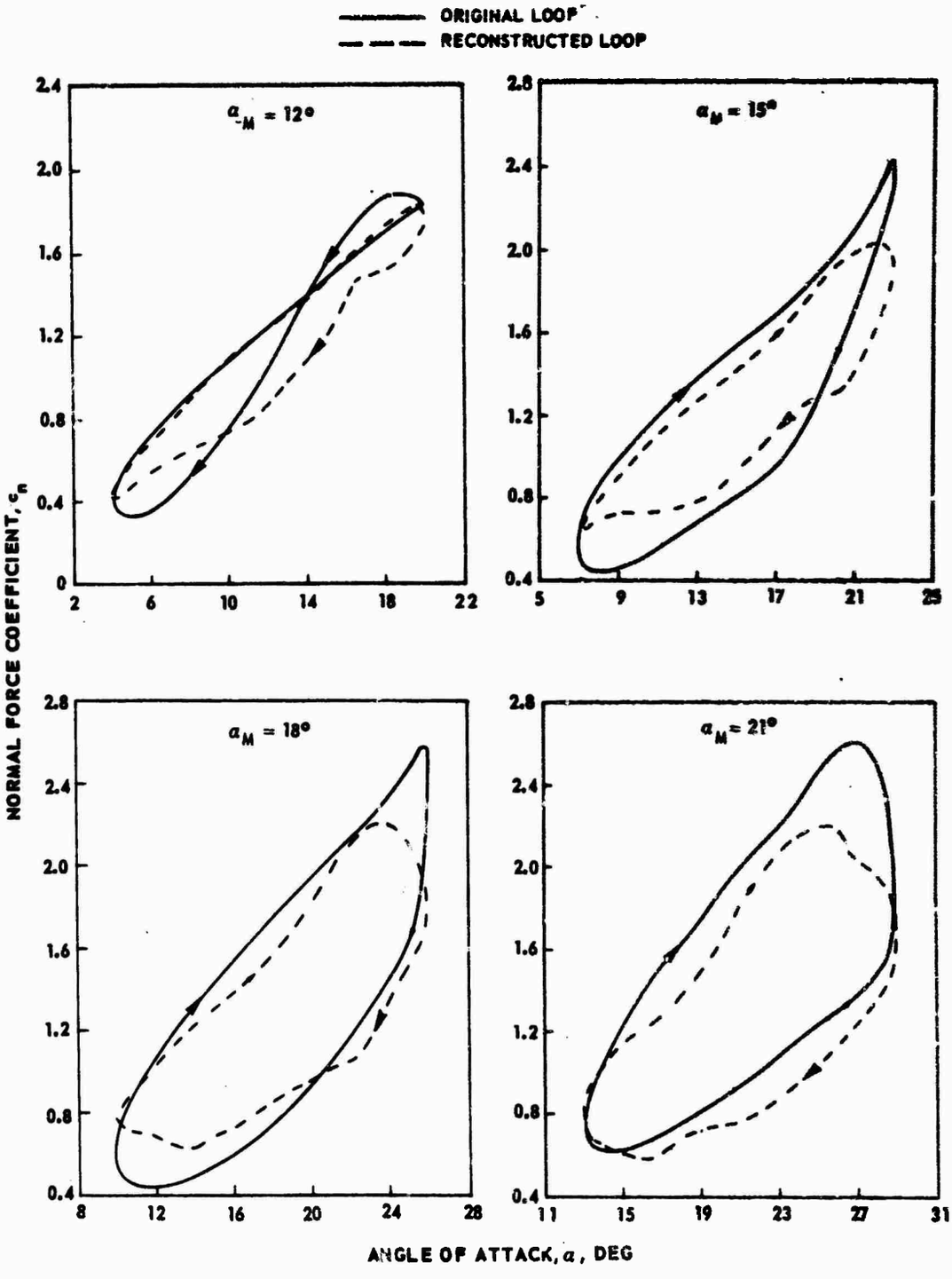

Figure 15. Comparison of Original and Reconstructed Normal Force Hysteresis Loops for Various Mean Angles of Attack - k = 0.225.

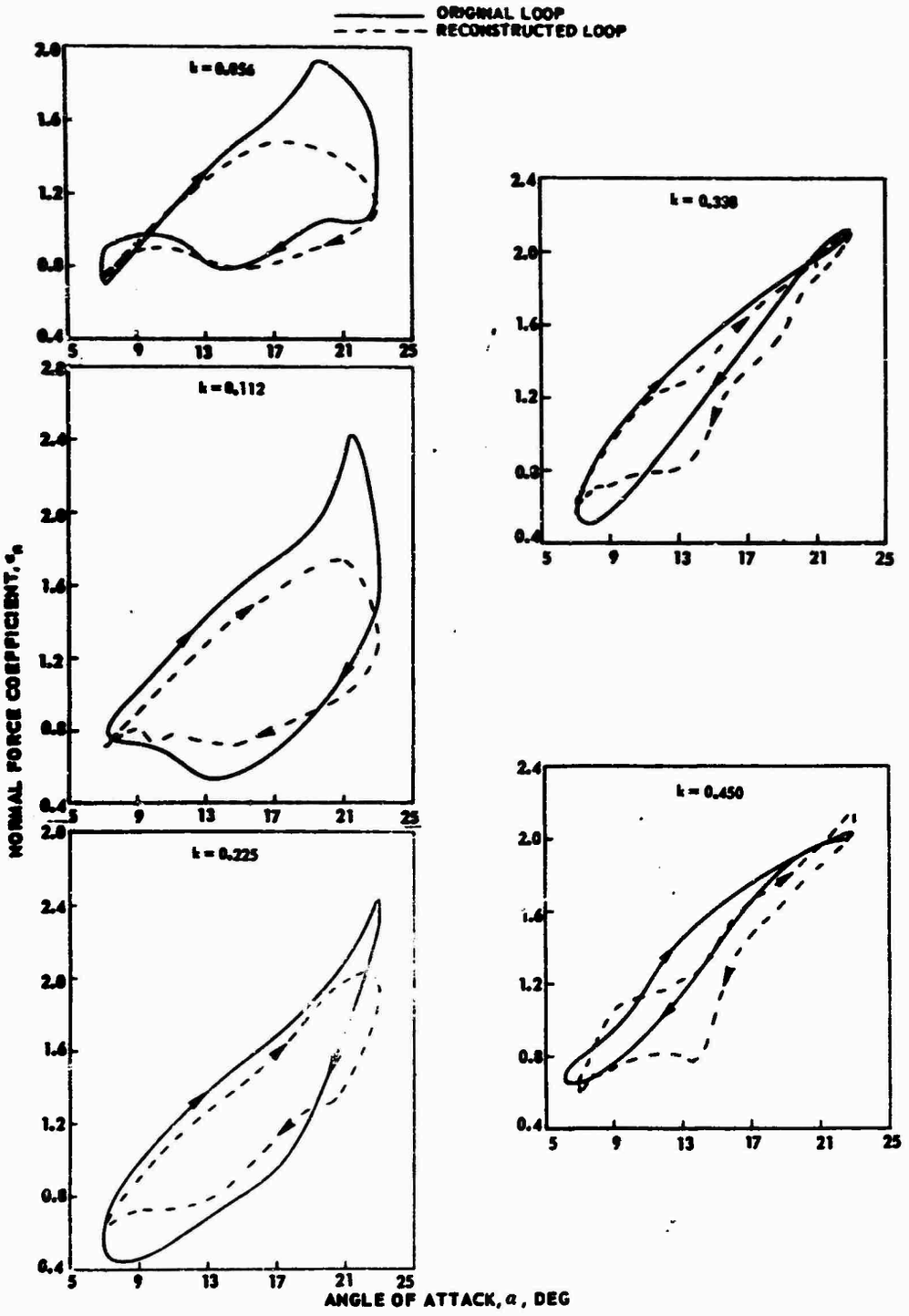

Figure 16. Comparison of Original and Reconstructed Normal Force Hysteresis Loops for Various Reduced Frequencies - α_M = 15 deg.

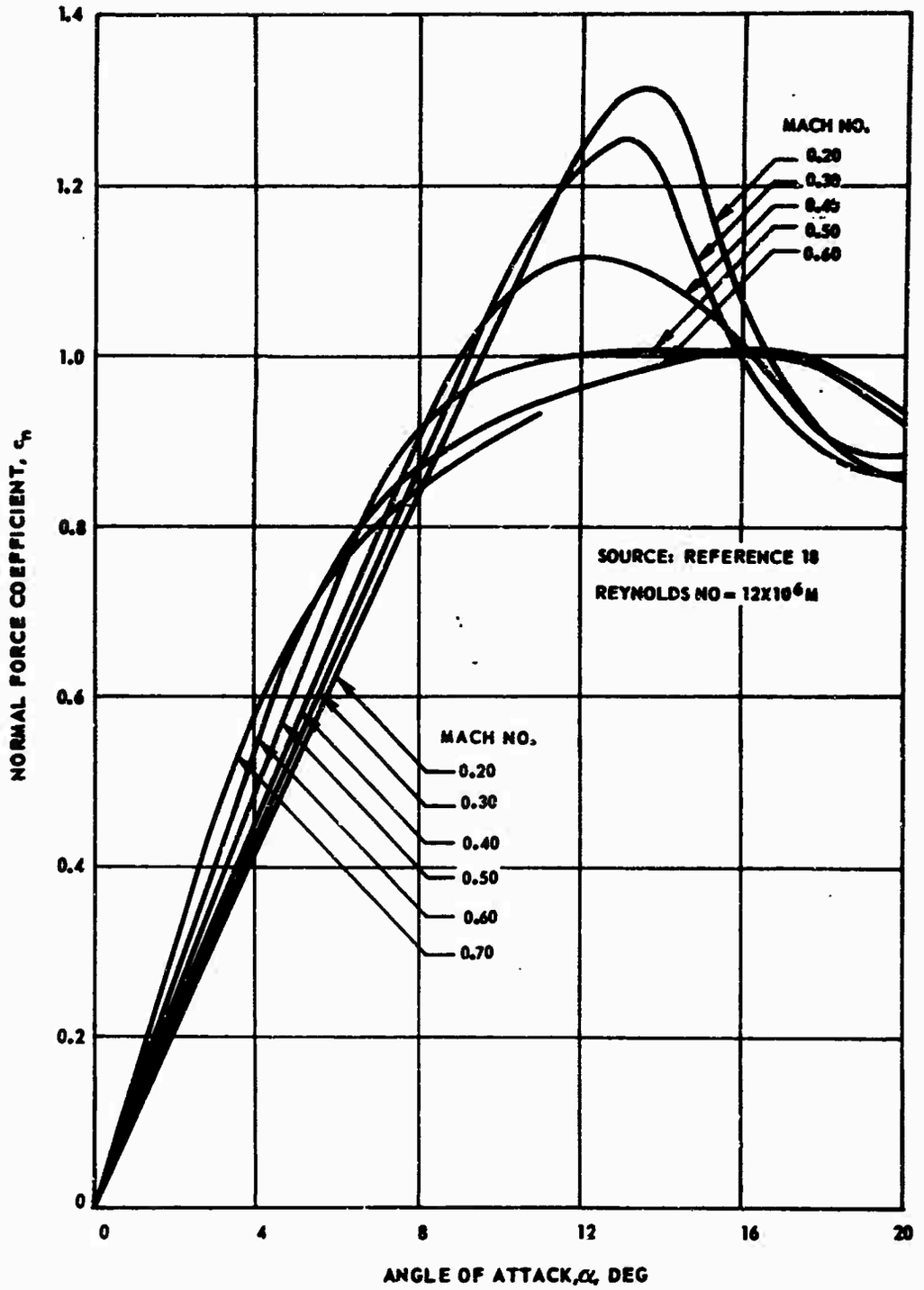

Figure 17. Steady-State Normal Force Characteristics for NACA 0012 Airfoil.

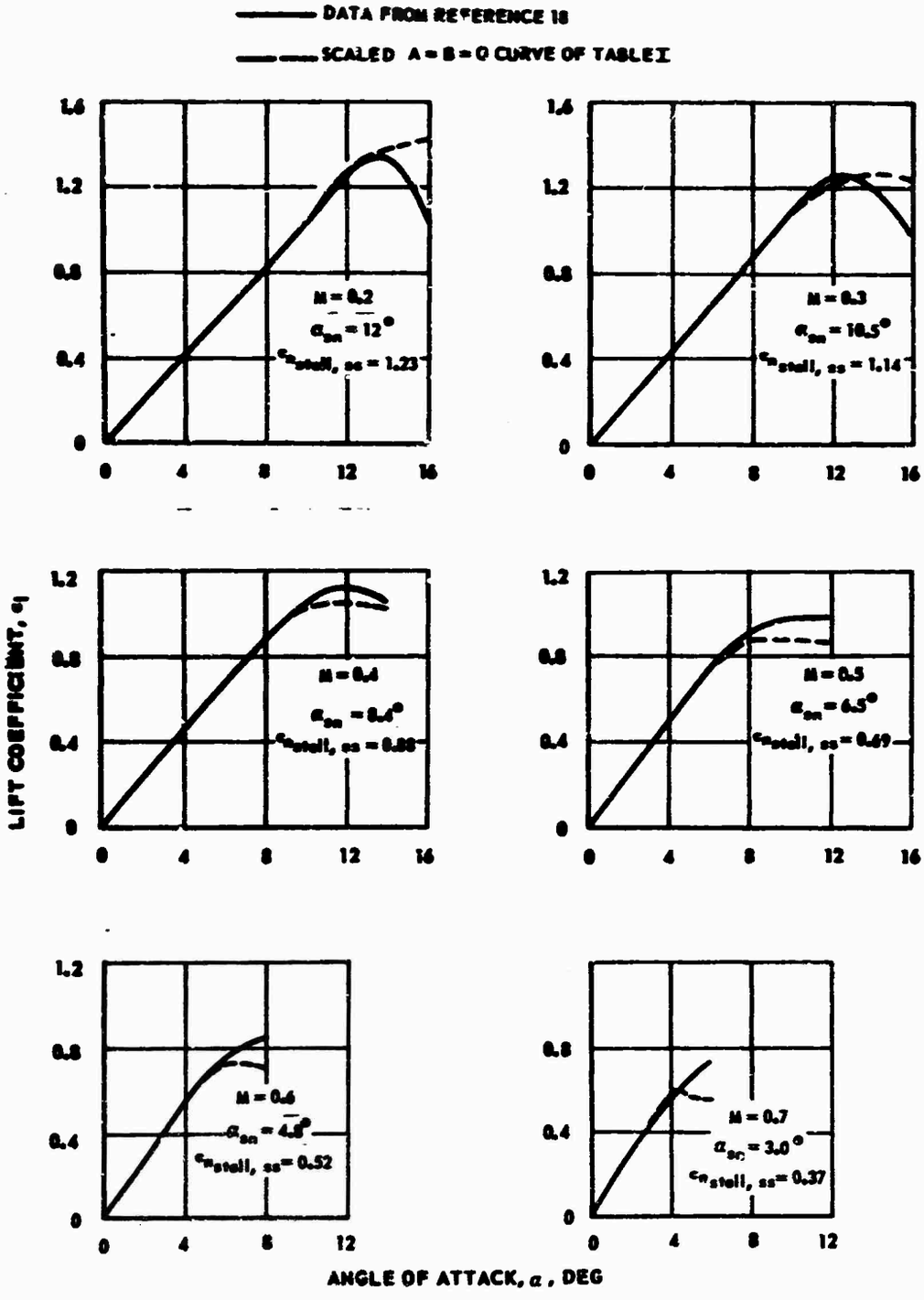

Figure 18. Comparison of Experimental Steady-State Lift Characteristics for NACA 0012 Airfoil With Characteristics Derived Using Scaling Procedures.

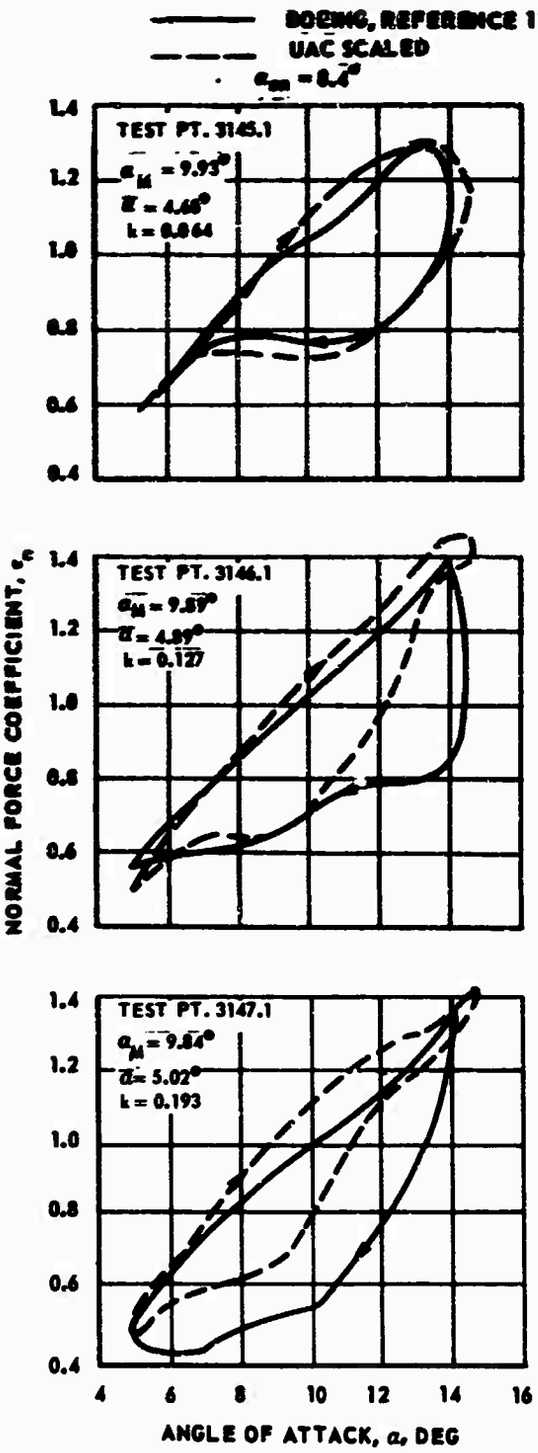

Figure 19. Comparison of Boeing Experimental Normal Force Hysteresis Loops With Loops Derived Using Scaling Procedures - M = 0.4.

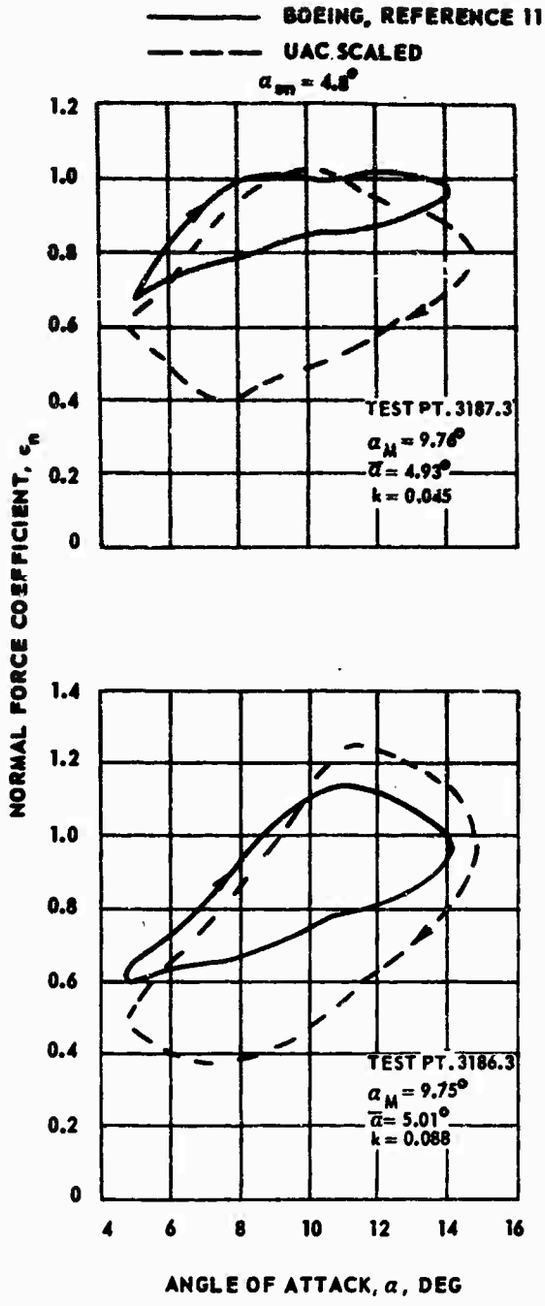

Figure 20. Comparison of Boeing Experimental Normal Force Hysteresis Loops With Loops Derived Using Scaling Procedures - M = 0.6.

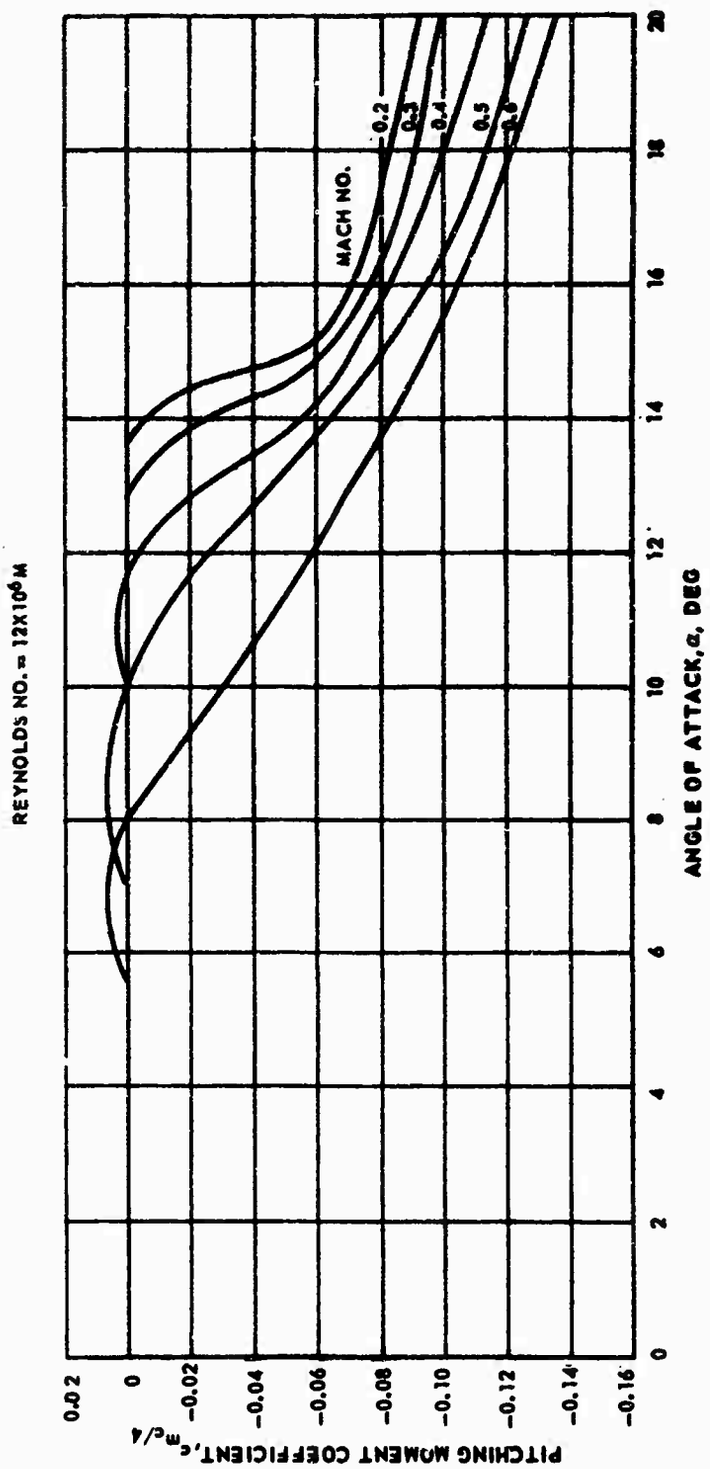

Figure 21. Steady-State Moment Characteristics for NACA 0012 Airfoil.

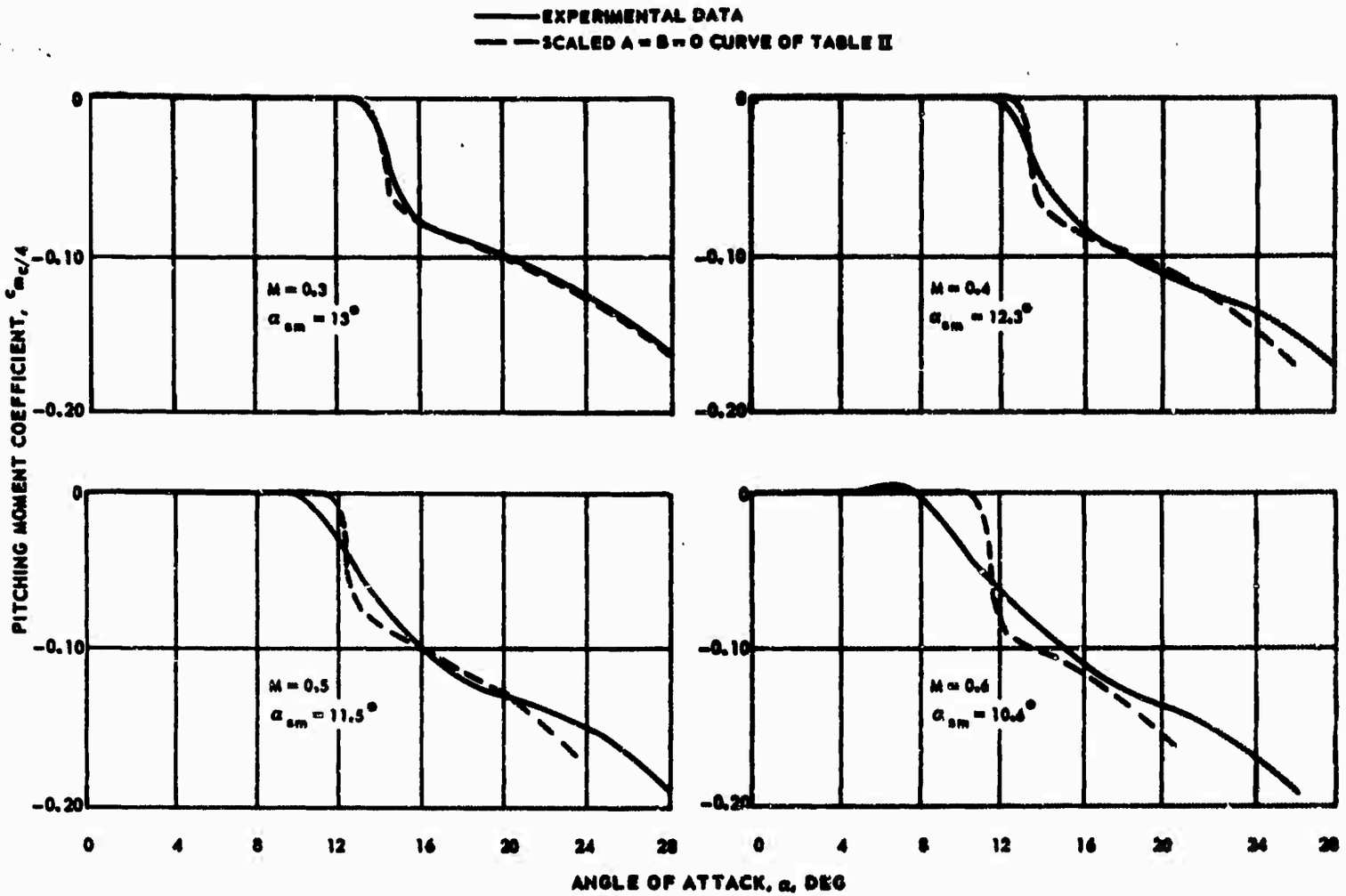

Figure 22. Comparison of Experimental Steady-State Moment Characteristics for NACA 0012 Airfoil With Characteristics Derived Using Scaling Procedures.

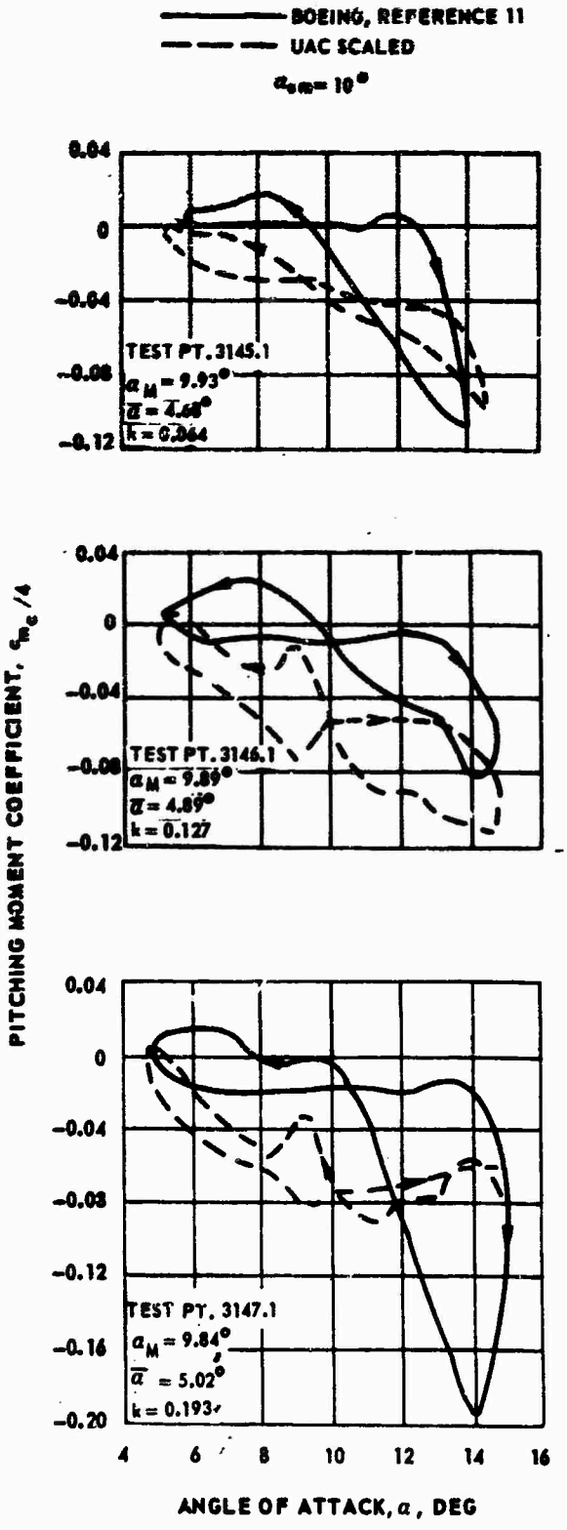

Figure 23. Comparison of Boeing Experimental Moment Hysteresis Loops With Loops Derived Using Scaling Procedures - M = 0.4.

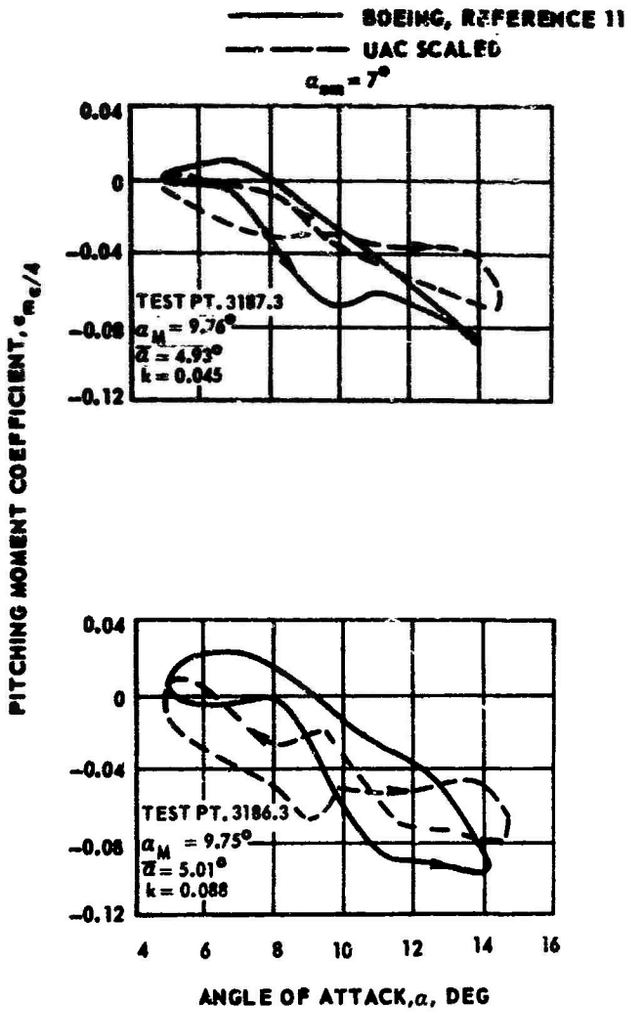

Figure 24. Comparison of Boeing Experimental Moment Hysteresis Loops With Loops Derived Using Scaling Procedures - M = 0.6.

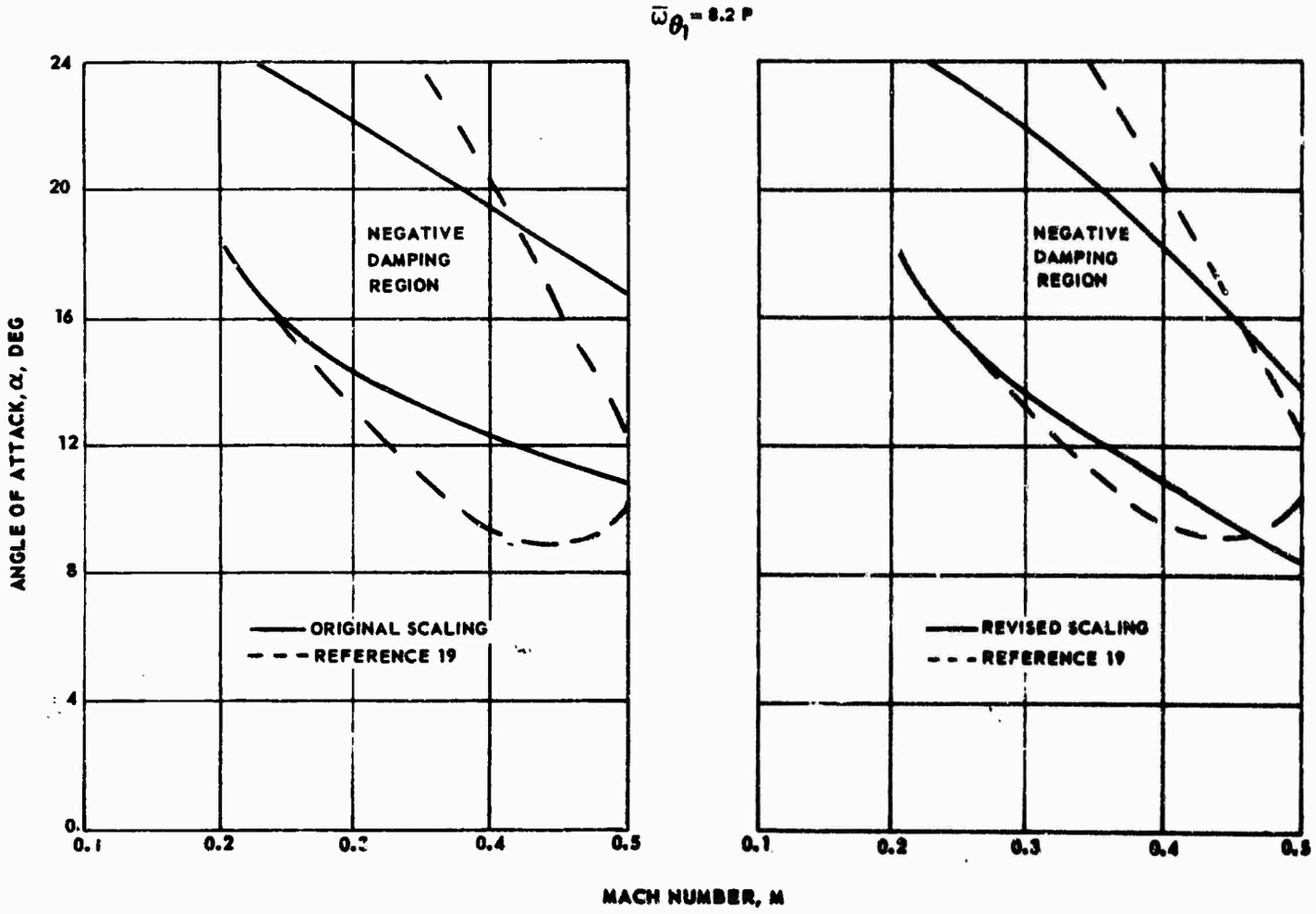

Figure 25. Comparison of Experimental Negative Aerodynamic Damping Region With Regions Derived Using Scaling Procedures.

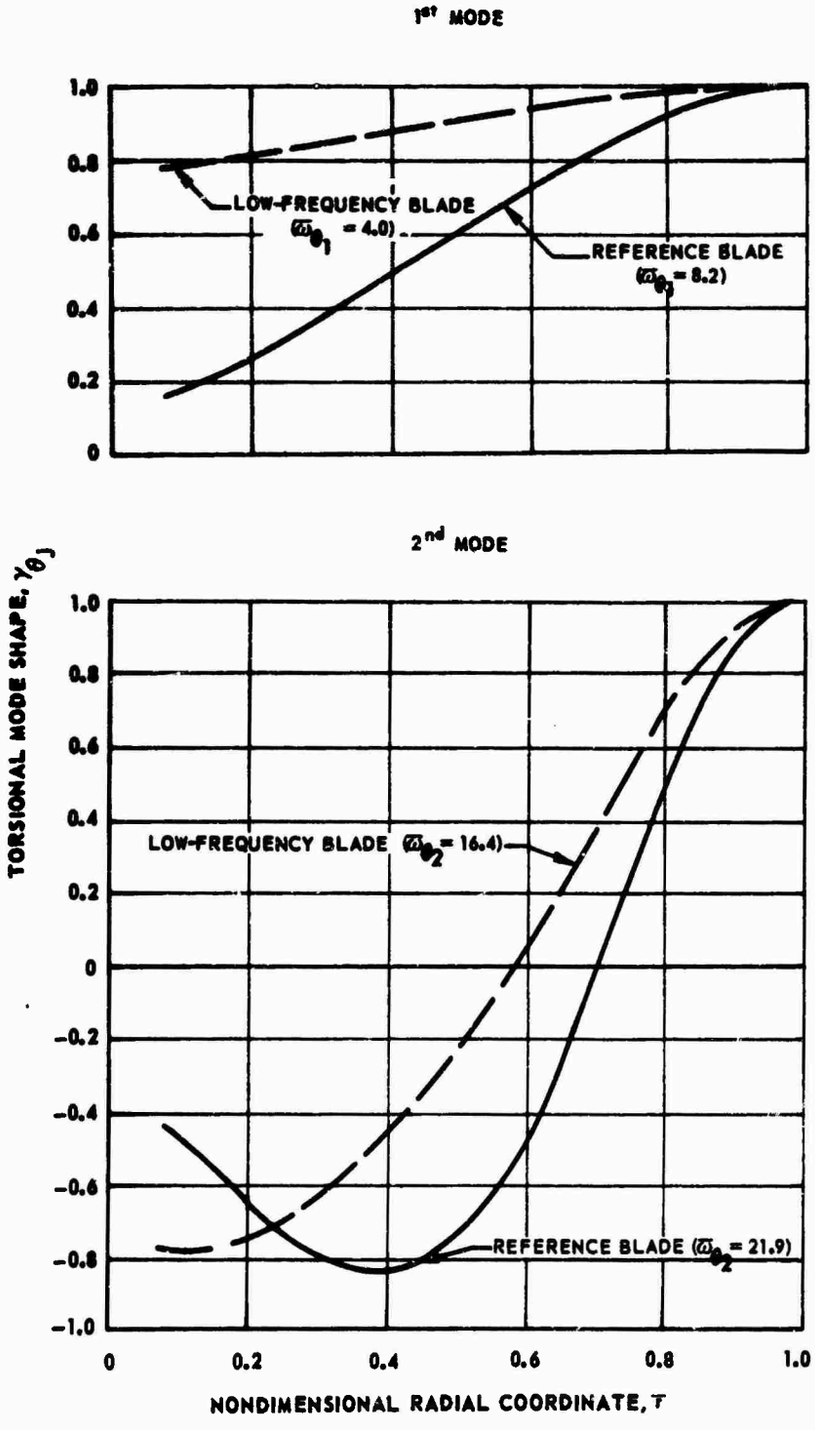

Figure 26. Comparison of Torsional Mode Shapes and Frequencies of Reference and Low-Frequency Blades.

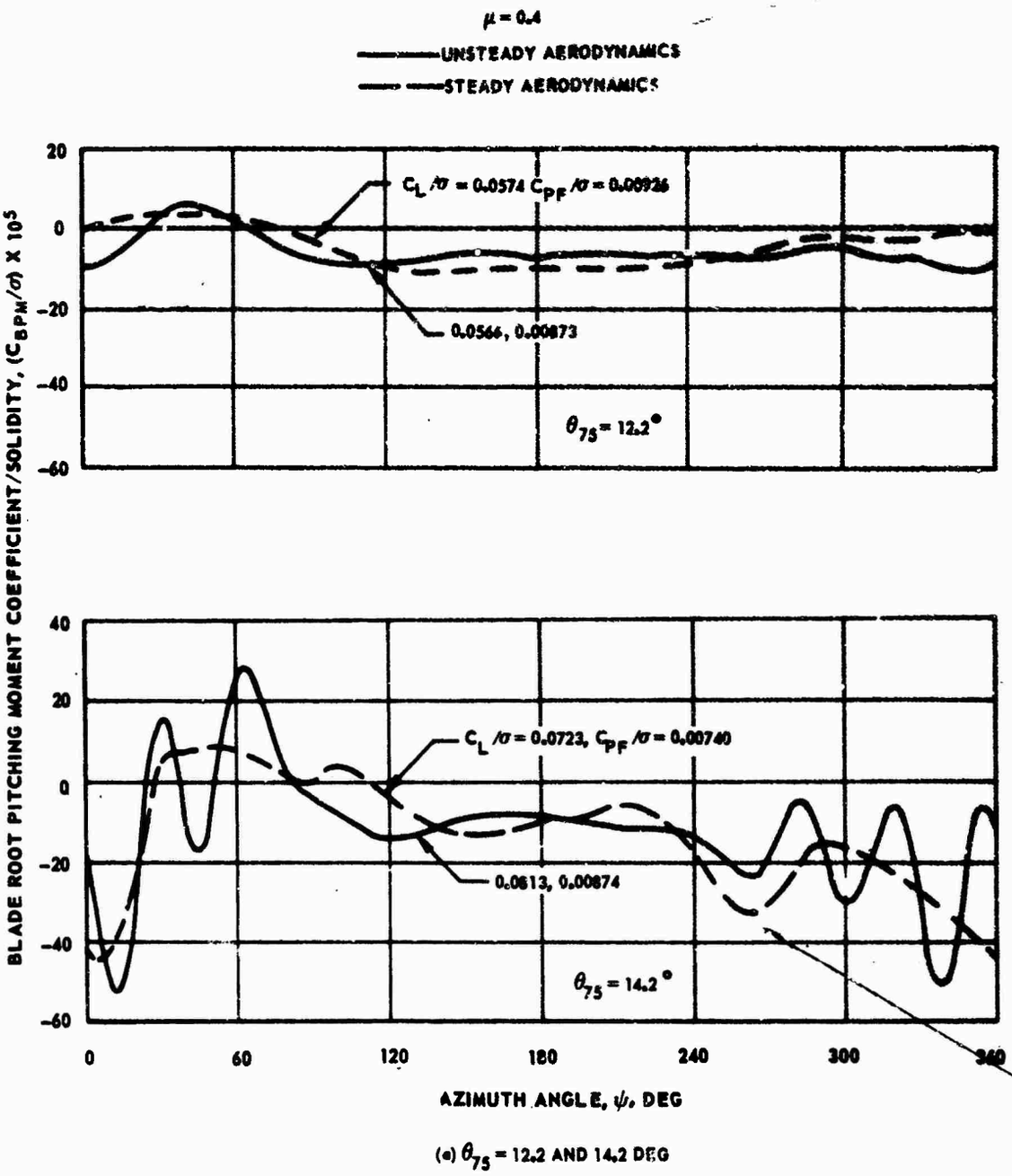

(a) θ_{75} = 12.2 AND 14.2 DEG

Figure 27. Effect of Unsteady Aerodynamics on Time Histories of Blade Root Pitching Moment - Reference Blade.

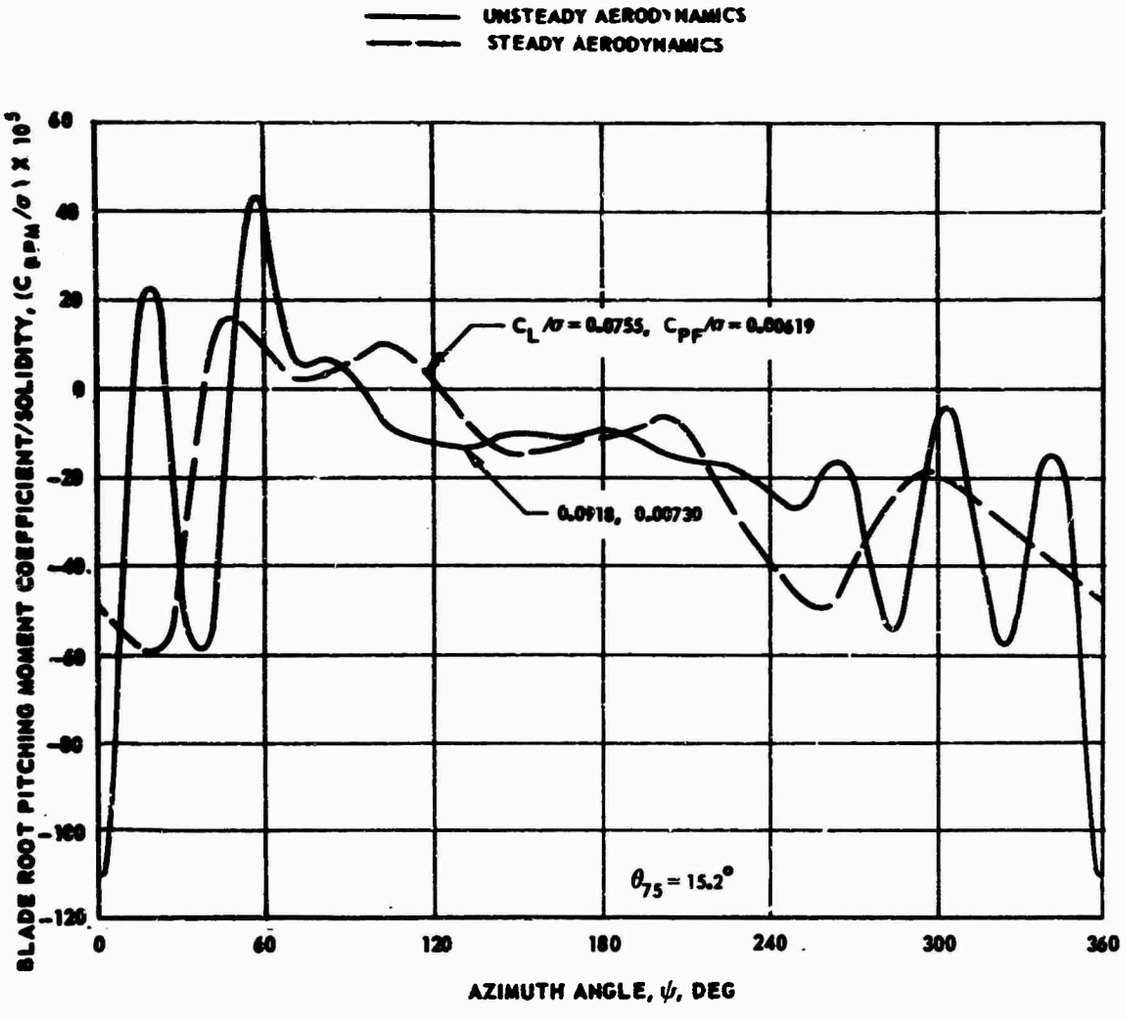

(b) θ_{75} = 15.2 DEG

Figure 27. Concluded.

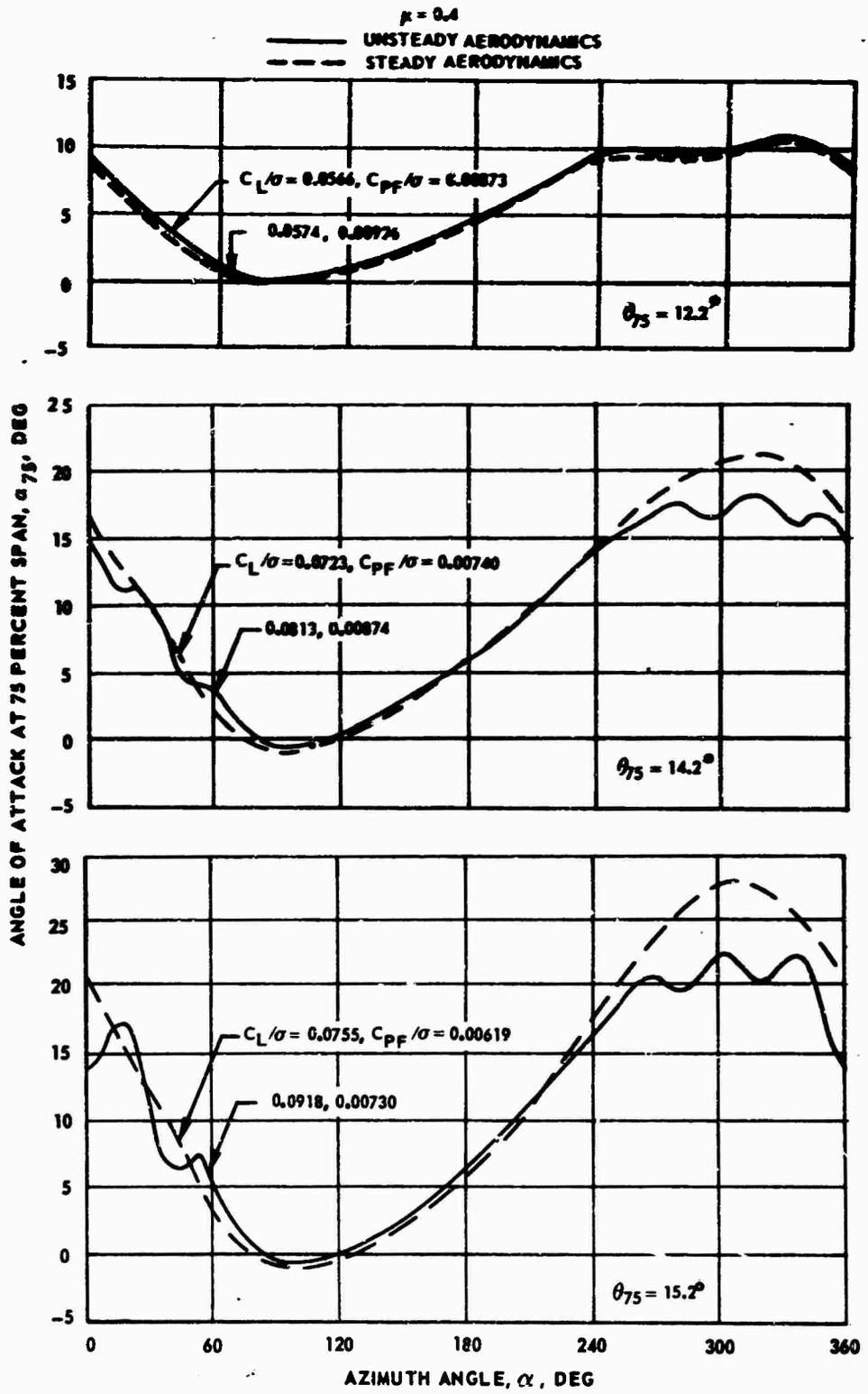

Figure 28. Effect of Unsteady Aerodynamics on Time Histories of Angle of Attack at 75 Percent Blade Span - Reference Blade.

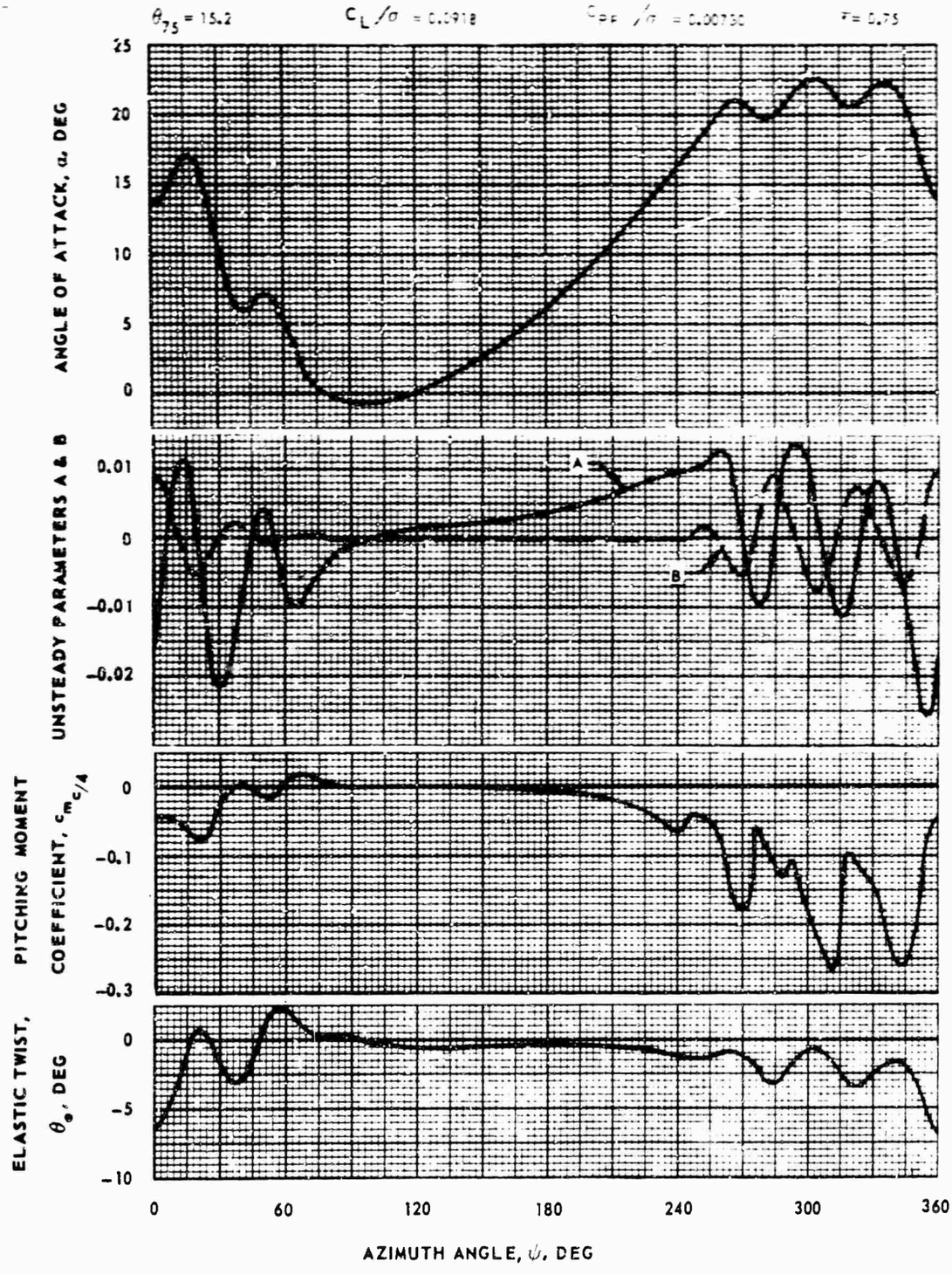

Figure 29. Details of Self-Excited Oscillation.

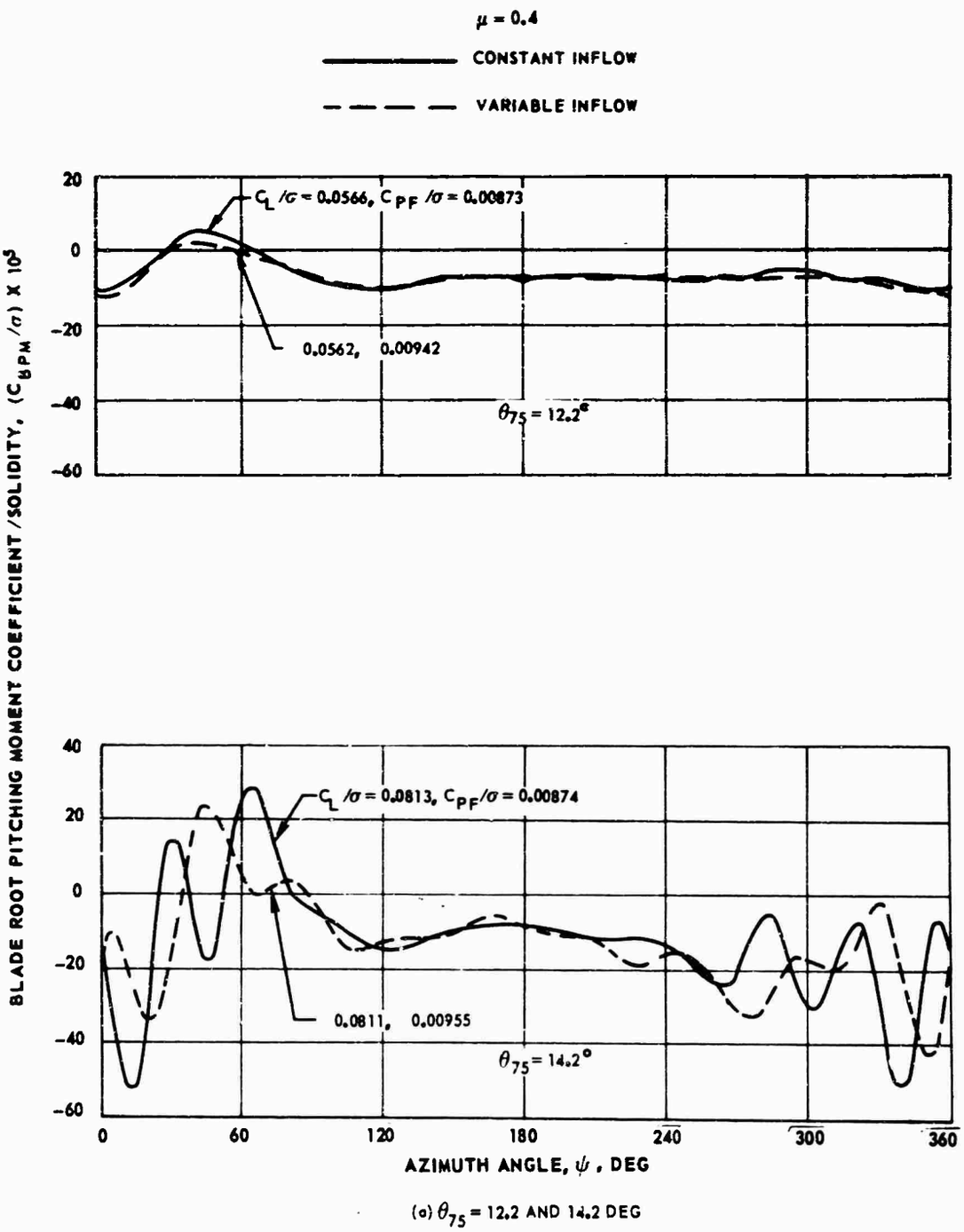

(a) θ_{75} = 12.2 AND 14.2 DEG

Figure 30. Effect of Variable Inflow on Time Histories of Blade Root Pitching Moment - Reference Blade.

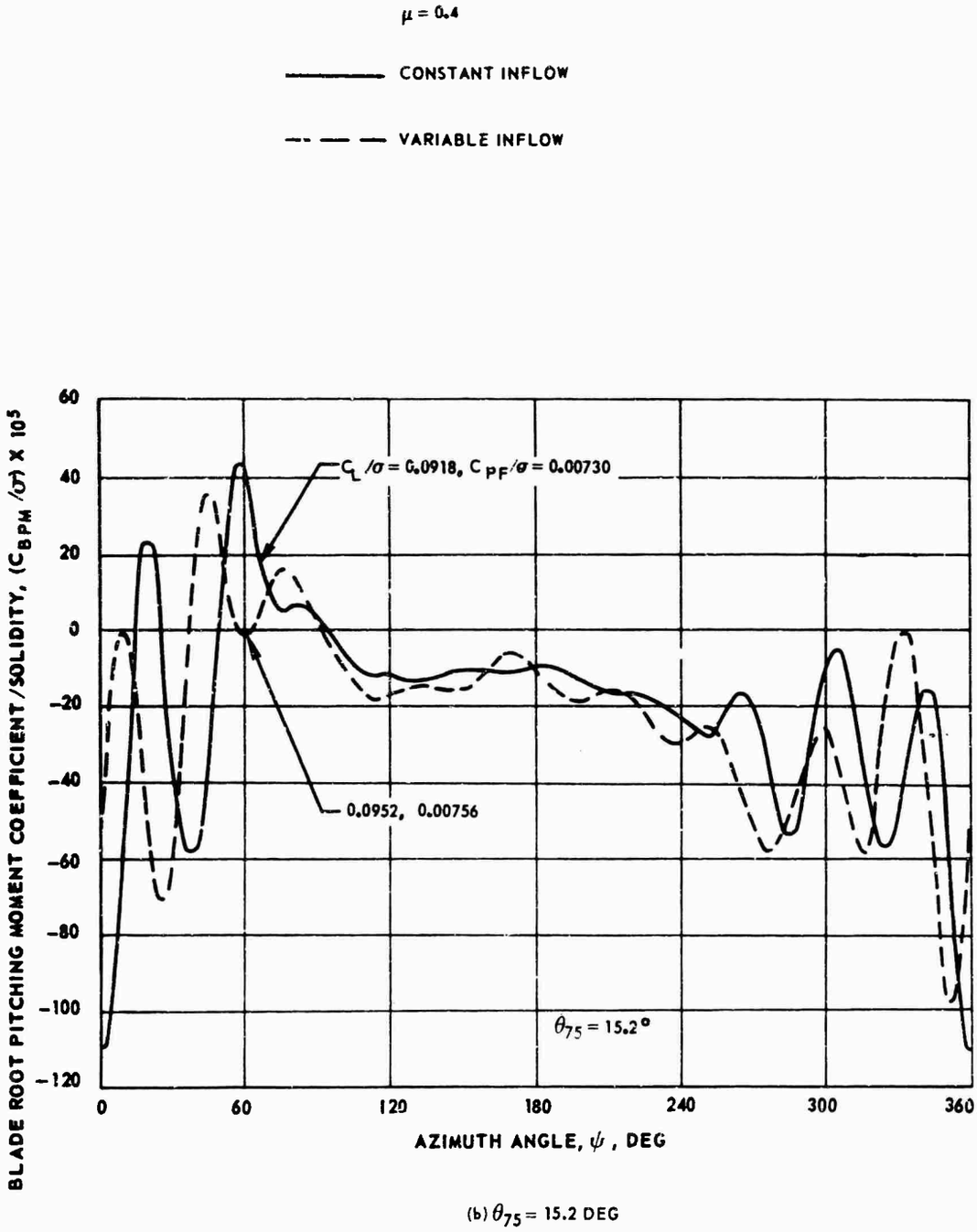

(b) θ_{75} = 15.2 DEG

Figure 30. Concluded.

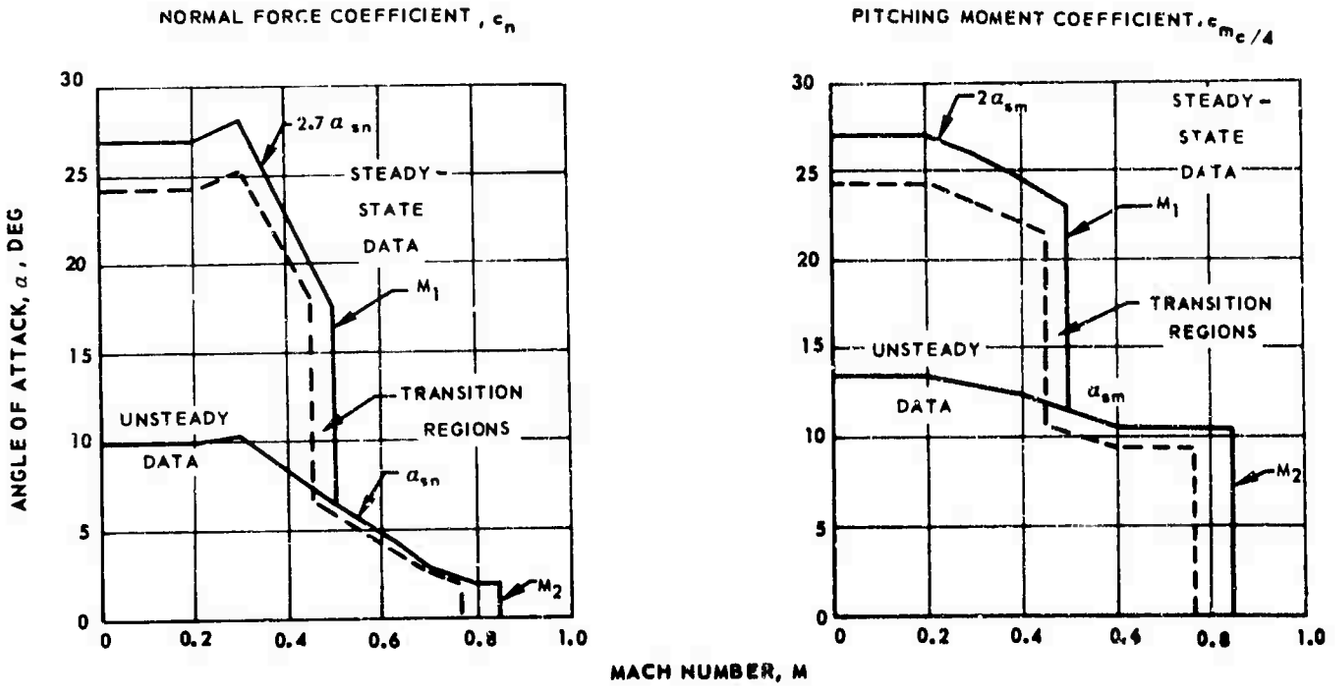

Figure 31. Parameters Defining Regions in Which Scaled Unsteady Aerodynamics Are Used.

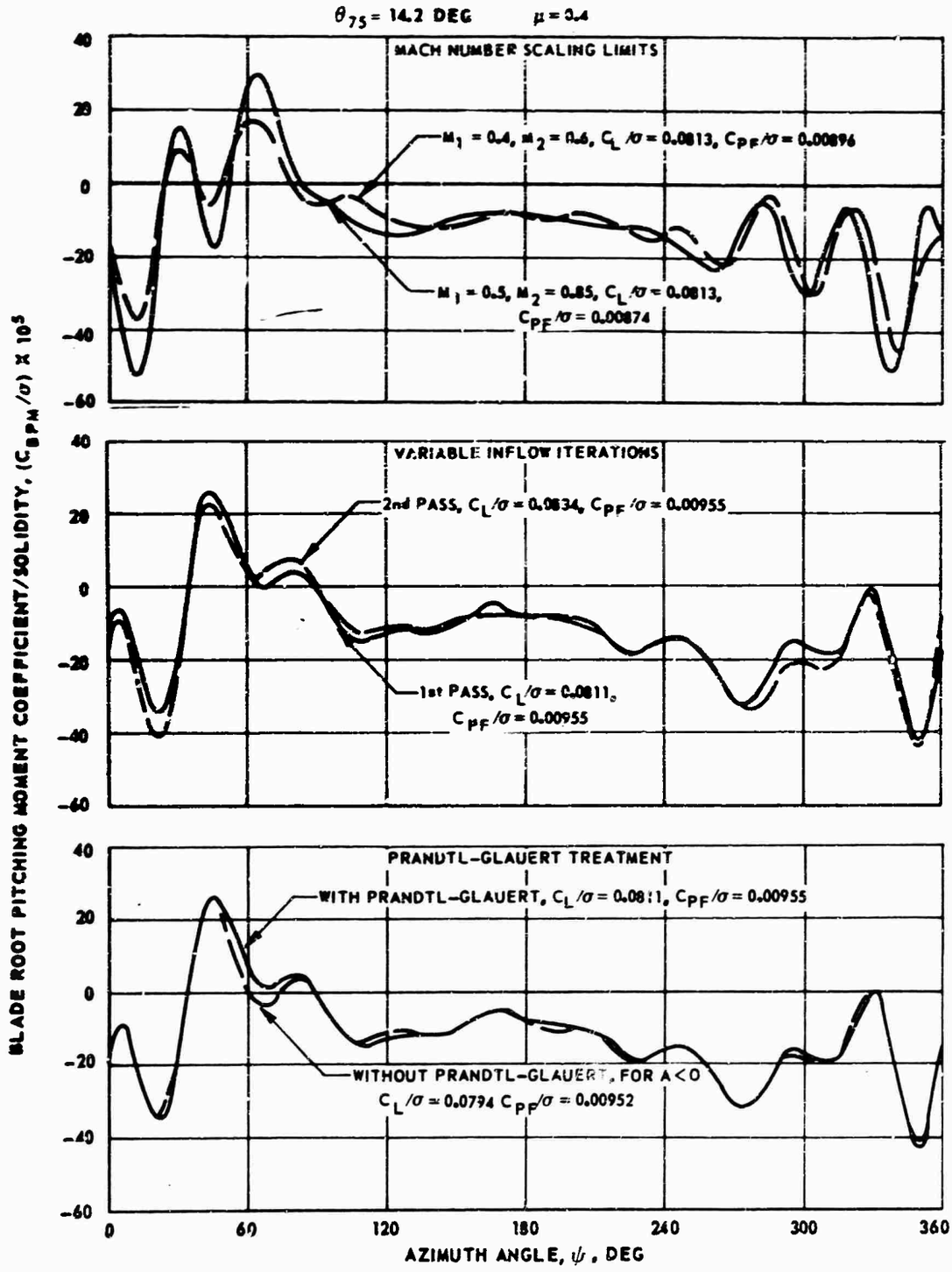

Figure 32. Sensitivity of Reference Blade Results to Mach Number Scaling Limits, Variable Inflow Iterations, and Treatment of Prandtl-Glauert Factor.

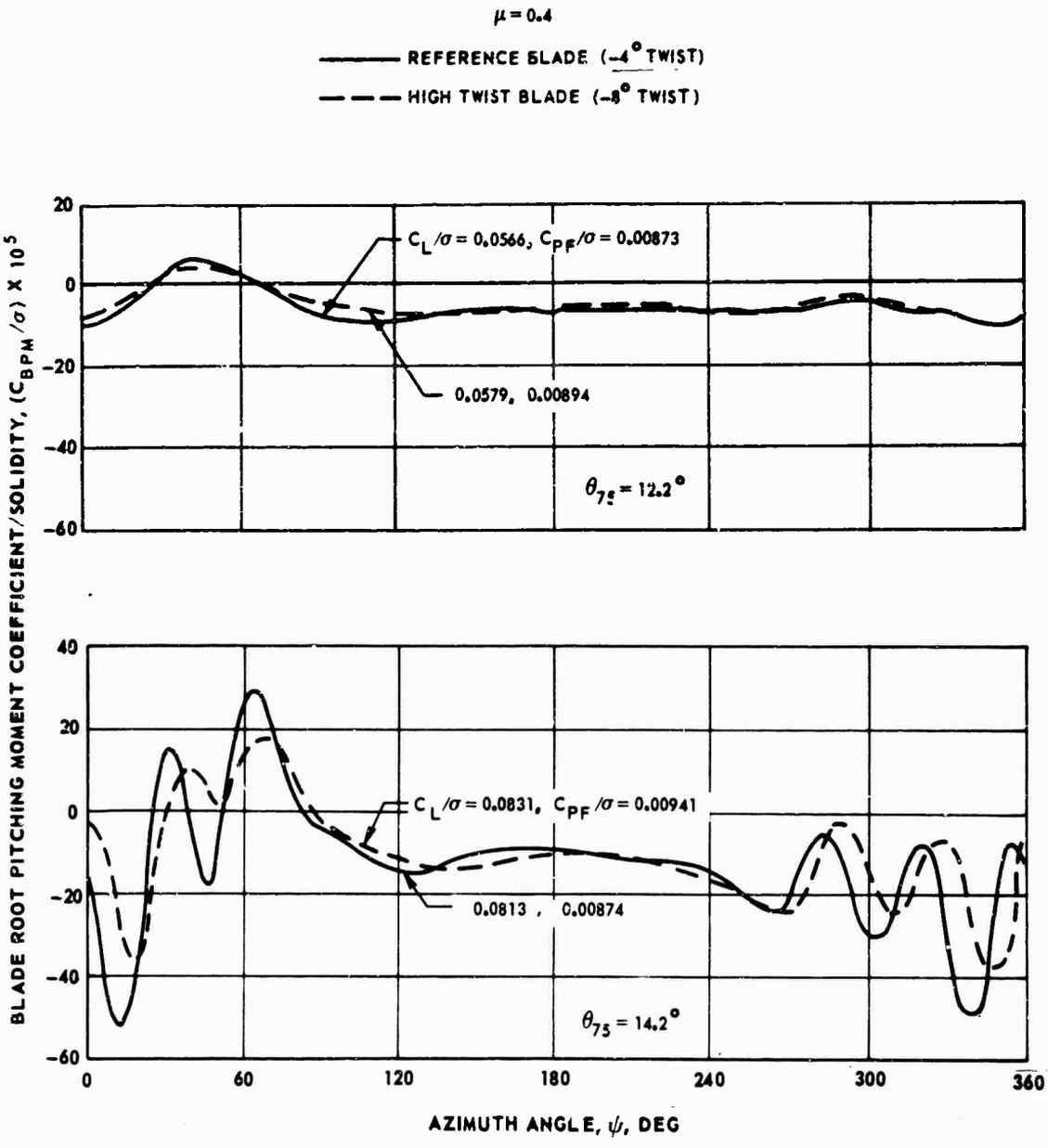

(a) θ_{75} = 12.2 AND 14.2 DEG

Figure 33. Effect of Blade Twist on Blade Root Pitching Moment-Constant Inflow.

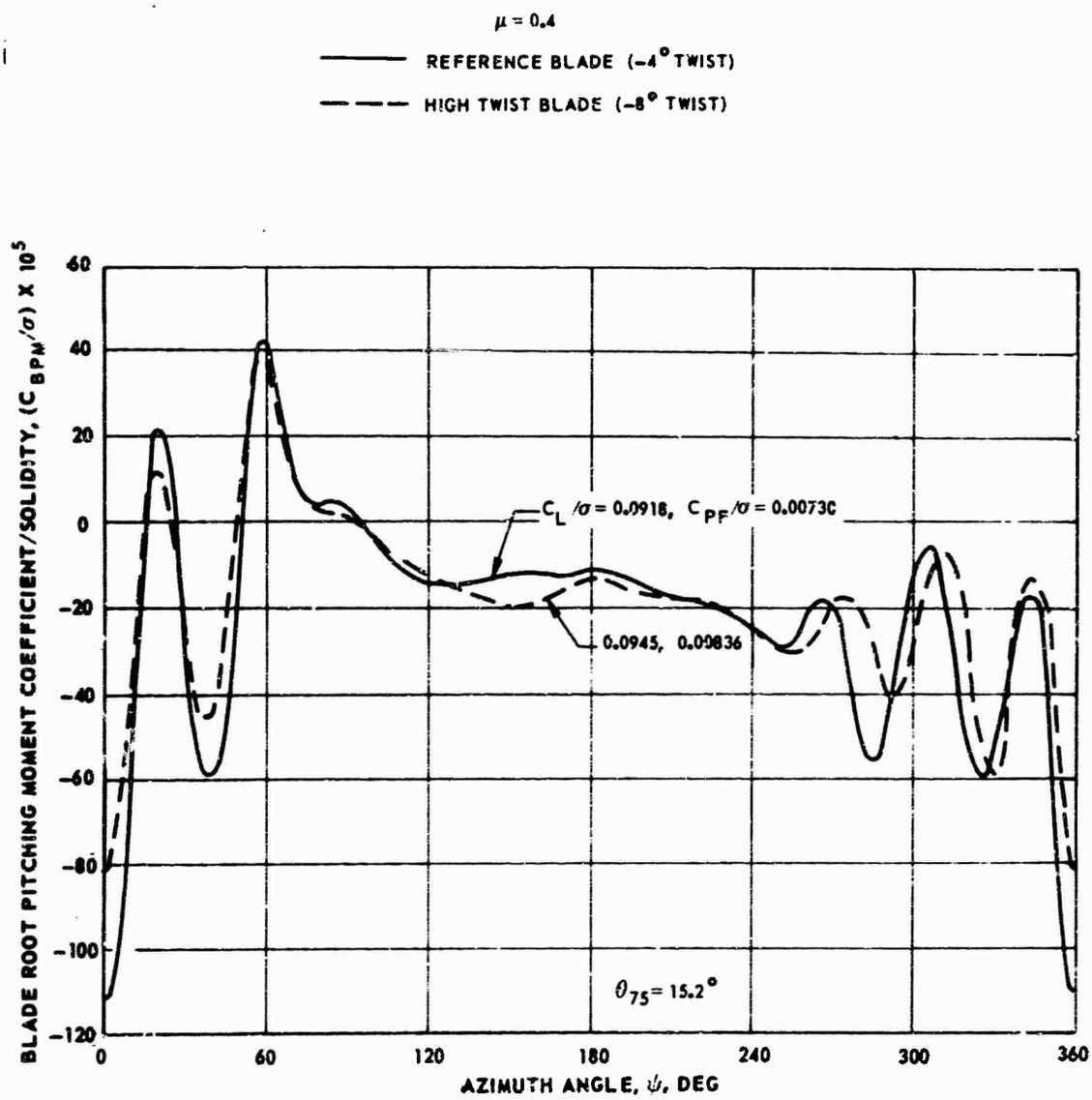

(b) θ_{75} = 15.2 DEG

Figure 33. Concluded.

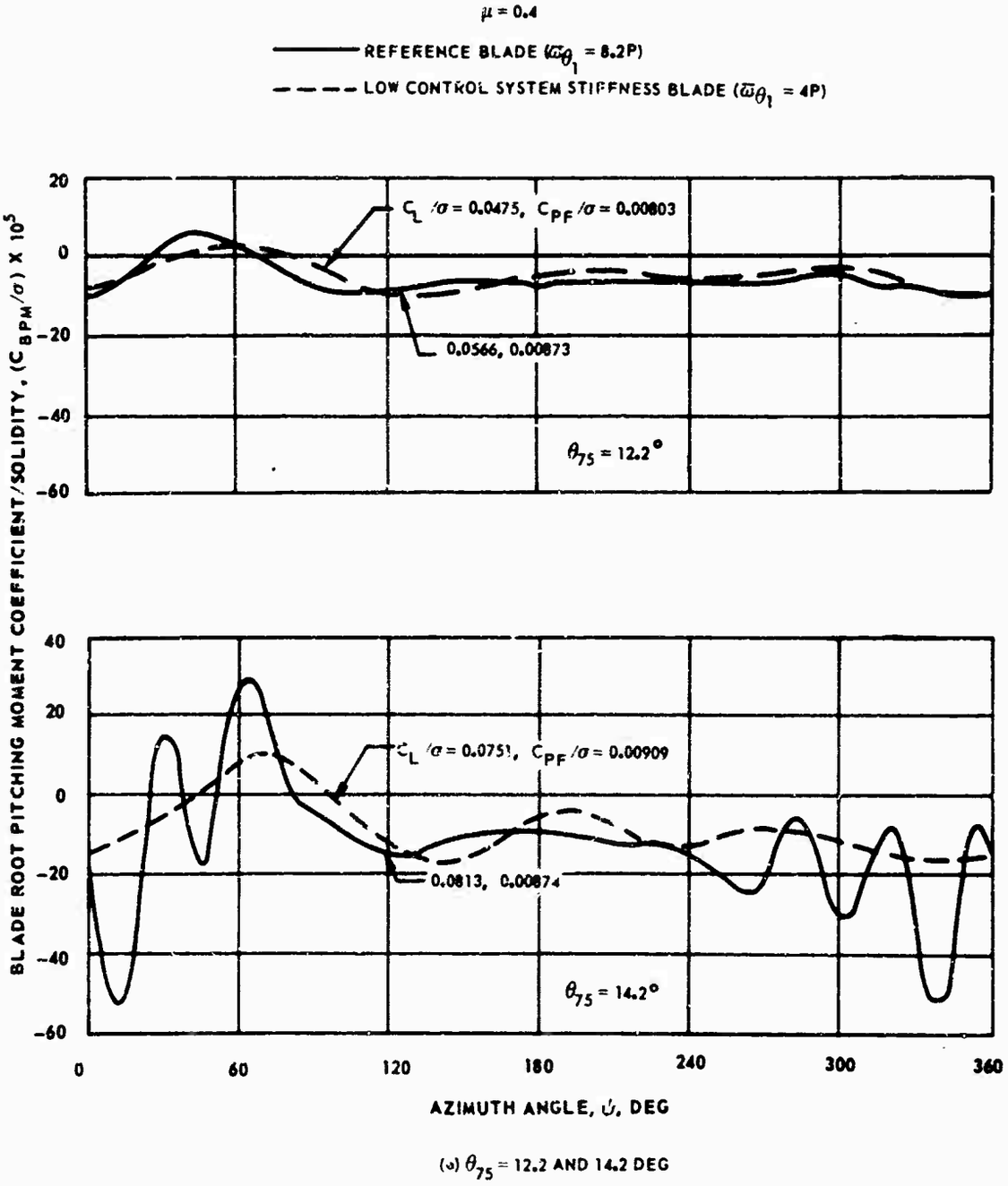

Figure 34. Effect of Torsional Frequency on Blade Root Pitching Moment - Constant Inflow.

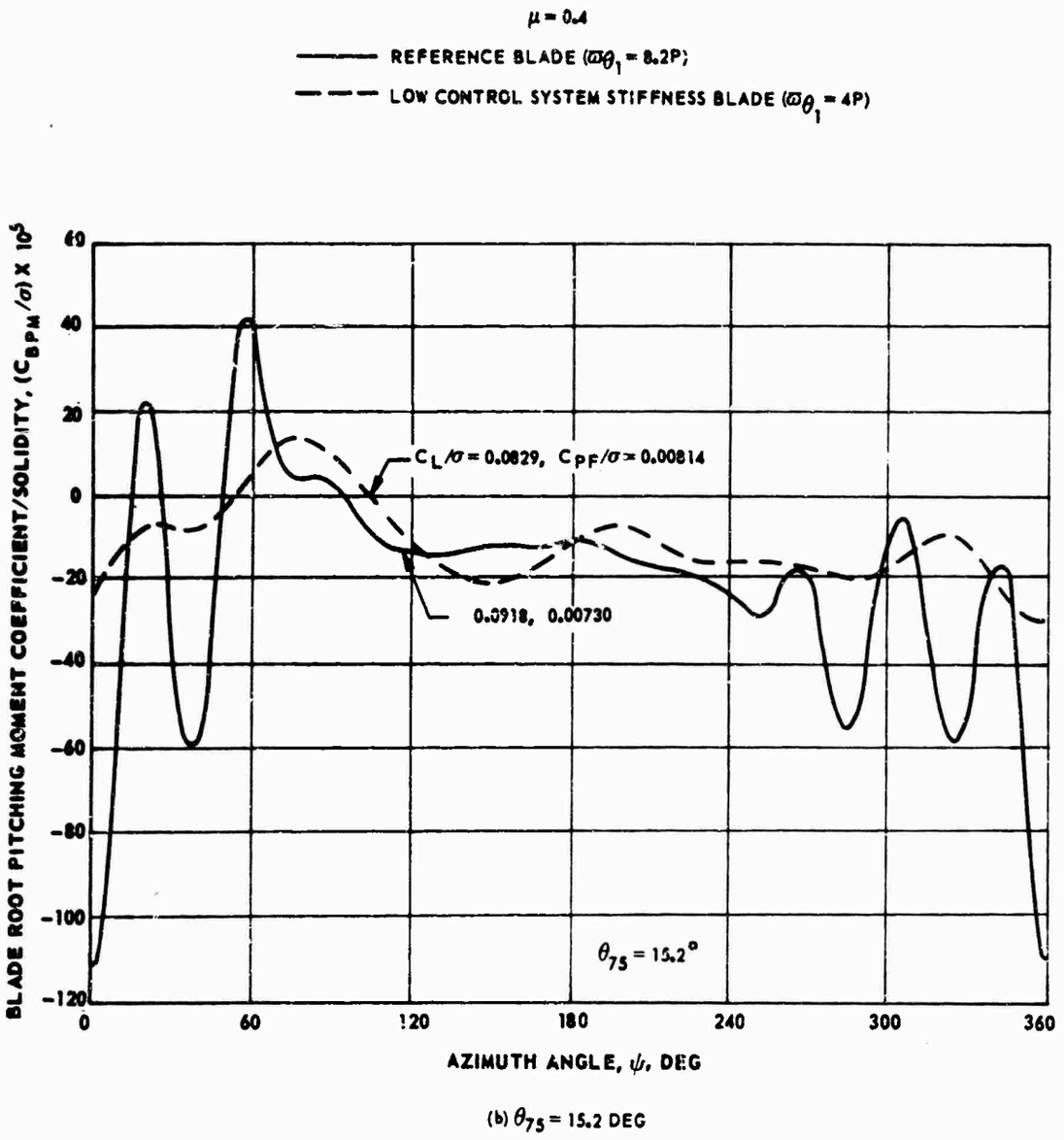

(b) θ_{75} = 15.2 DEG

Figure 34. Concluded.

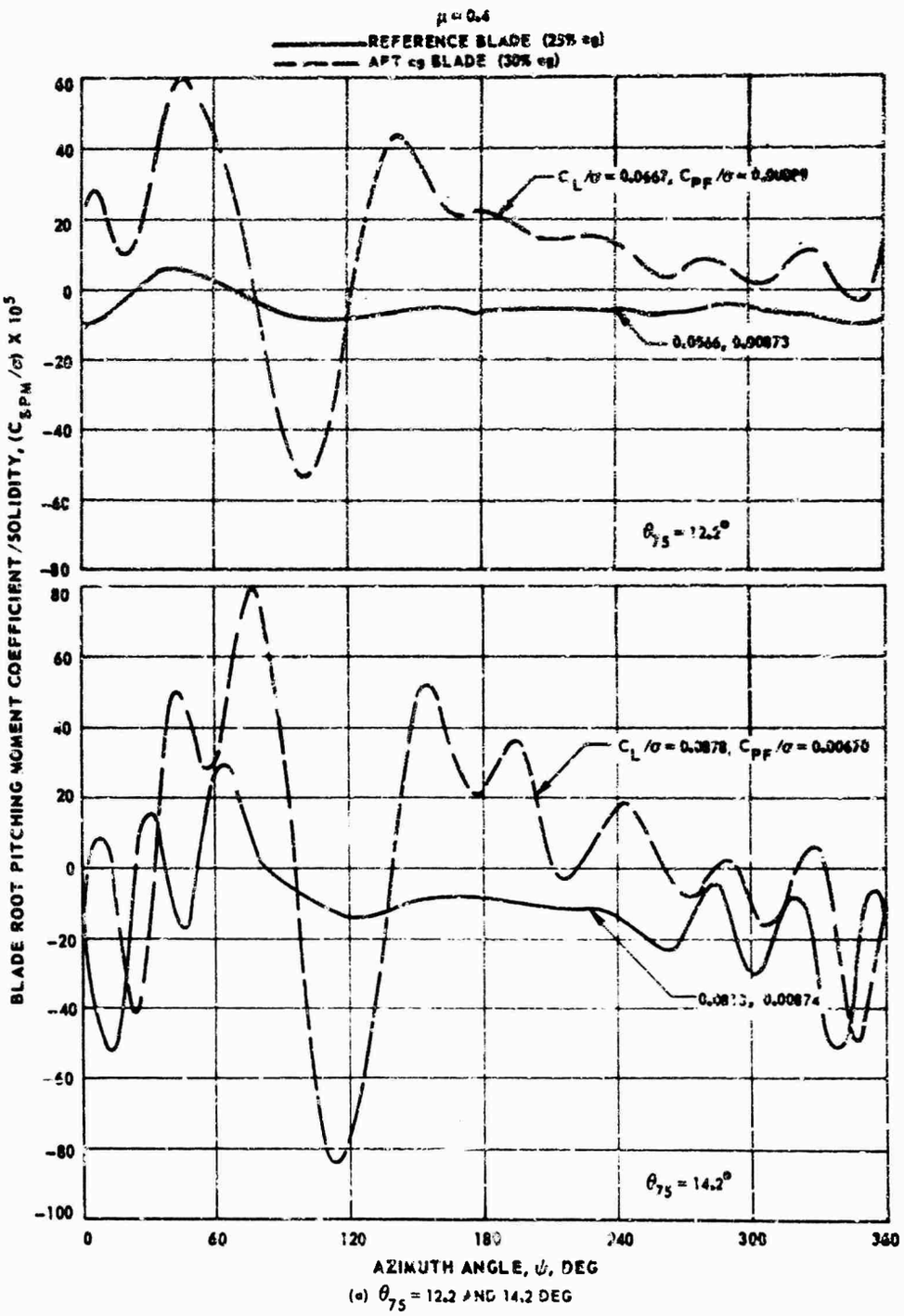

(a) θ_{75} = 12.2 AND 14.2 DEG

Figure 35. Effect of Blade Chordwise cg Position on Blade Root Pitching Moment - Constant Inflow.

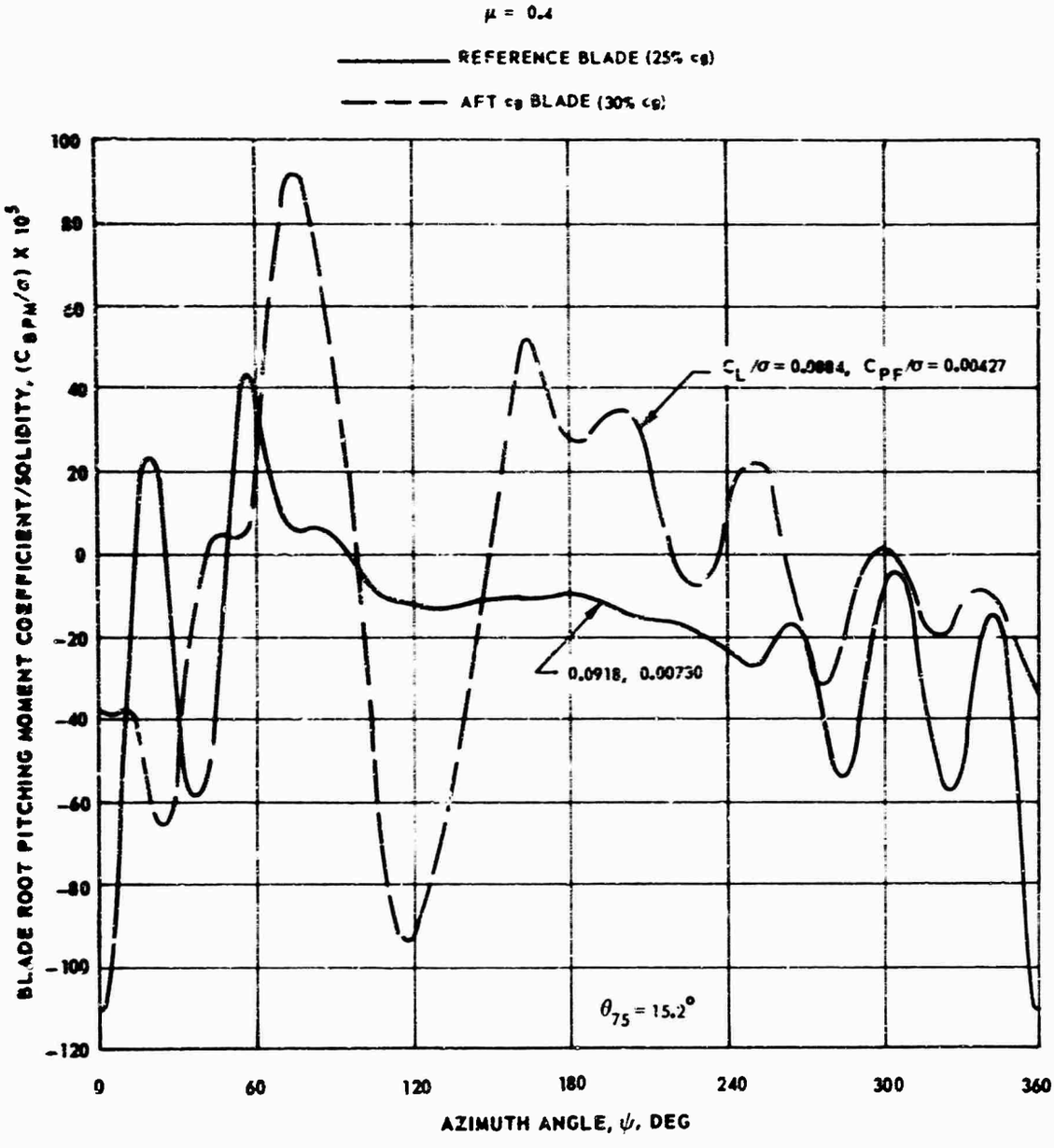

b) θ_{75} = 15.2 DEG

Figure 35. Concluded.

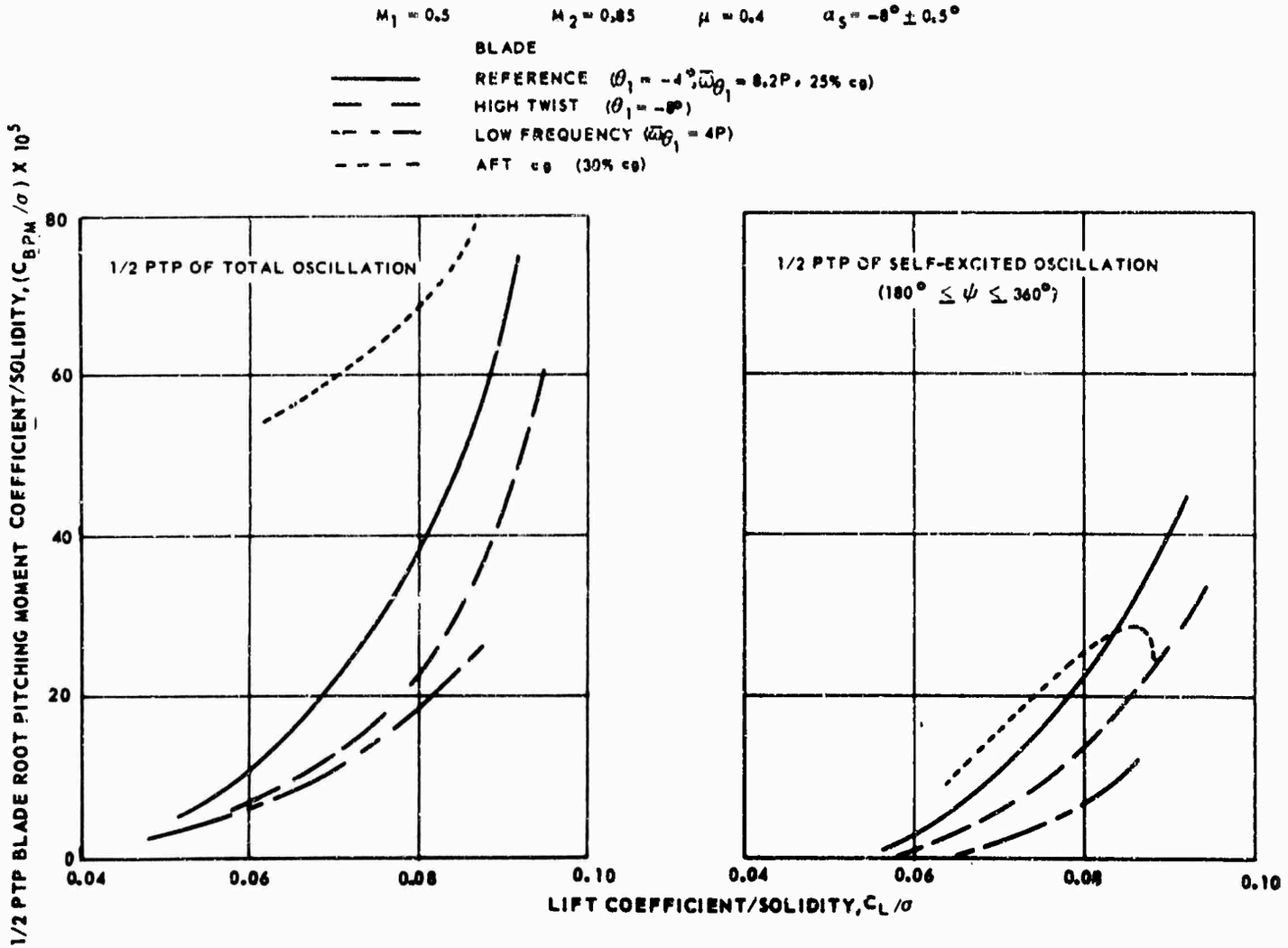

Figure 36. Comparison of Blade Root Pitching Moment Amplitudes for Various Blade Designs - Constant Inflow.

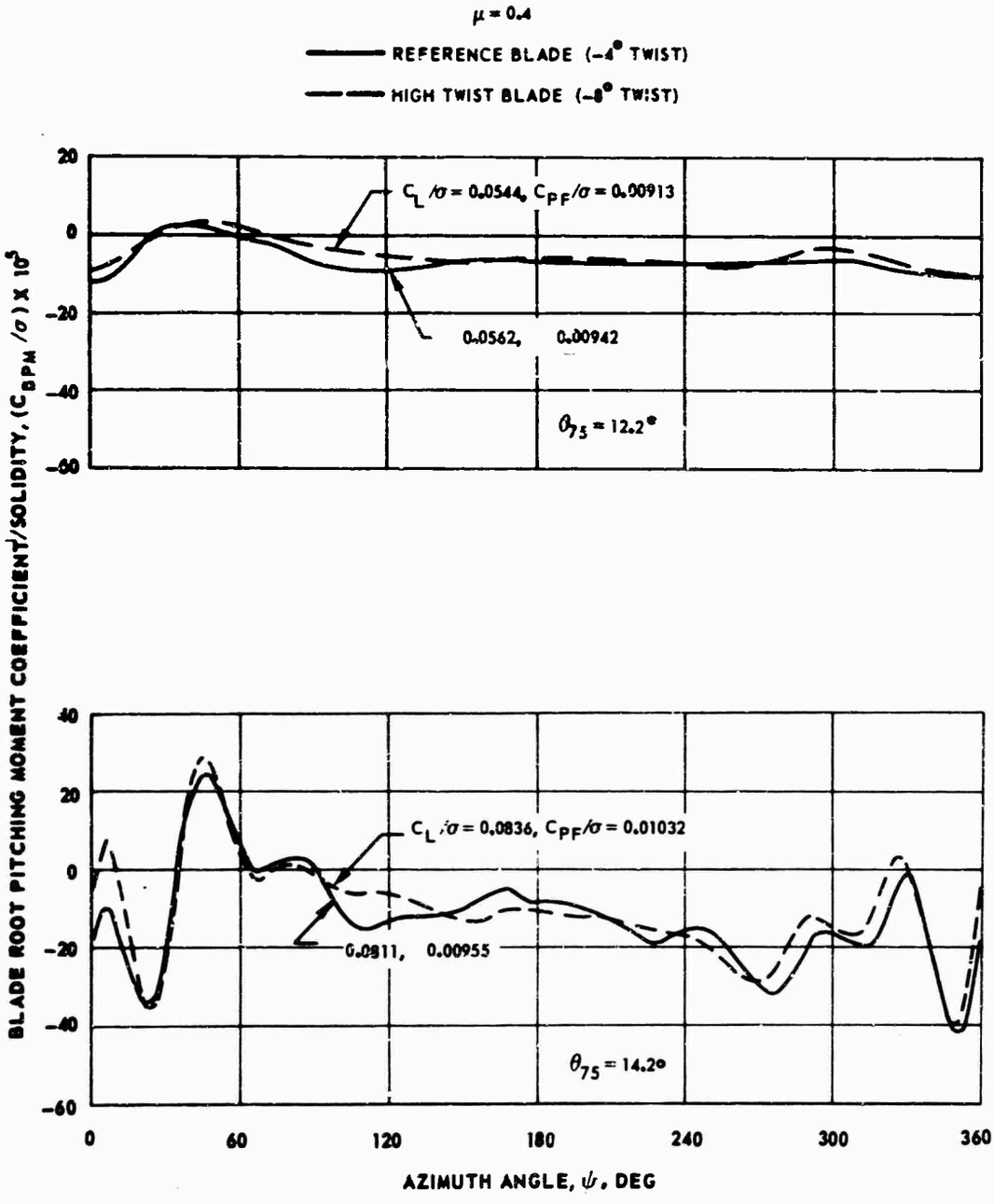

(a) θ_{75} = 12.2 AND 14.2 DEG

Figure 37. Effect of Blade Twist on Blade Root Pitching Moment - Variable Inflow.

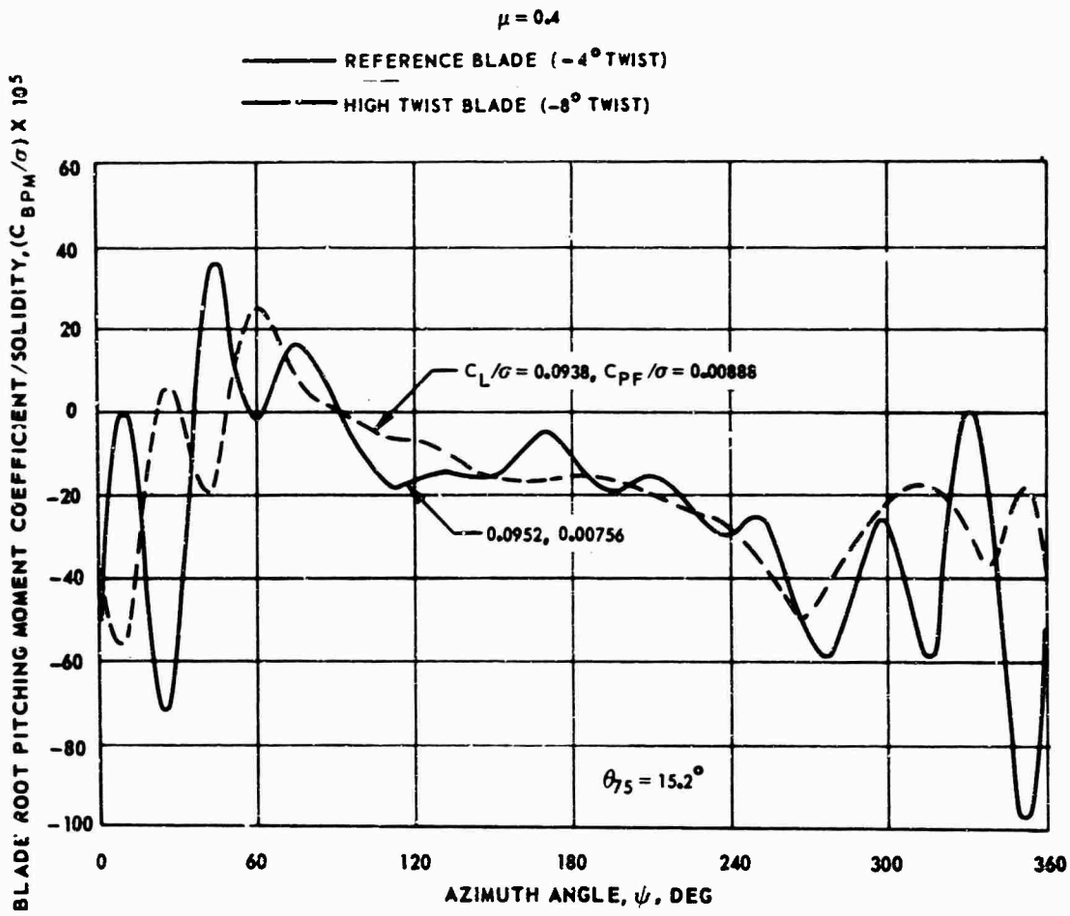

(b) θ_{75} = 15.2 DEG

Figure 37. Concluded.

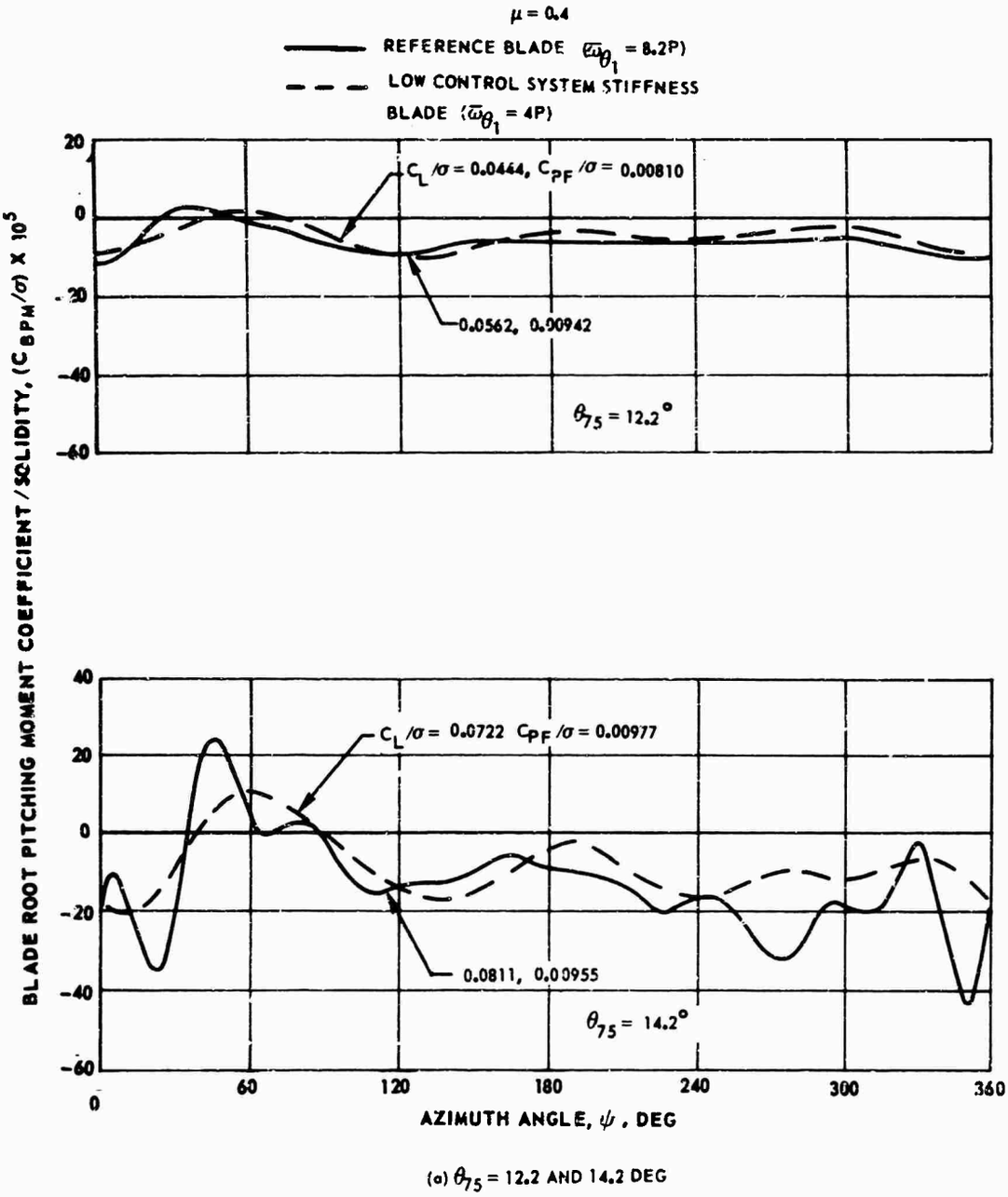

(a) θ_{75} = 12.2 AND 14.2 DEG

Figure 38. Effect of Torsional Frequency on Blade Root Pitching Moment - Variable Inflow.

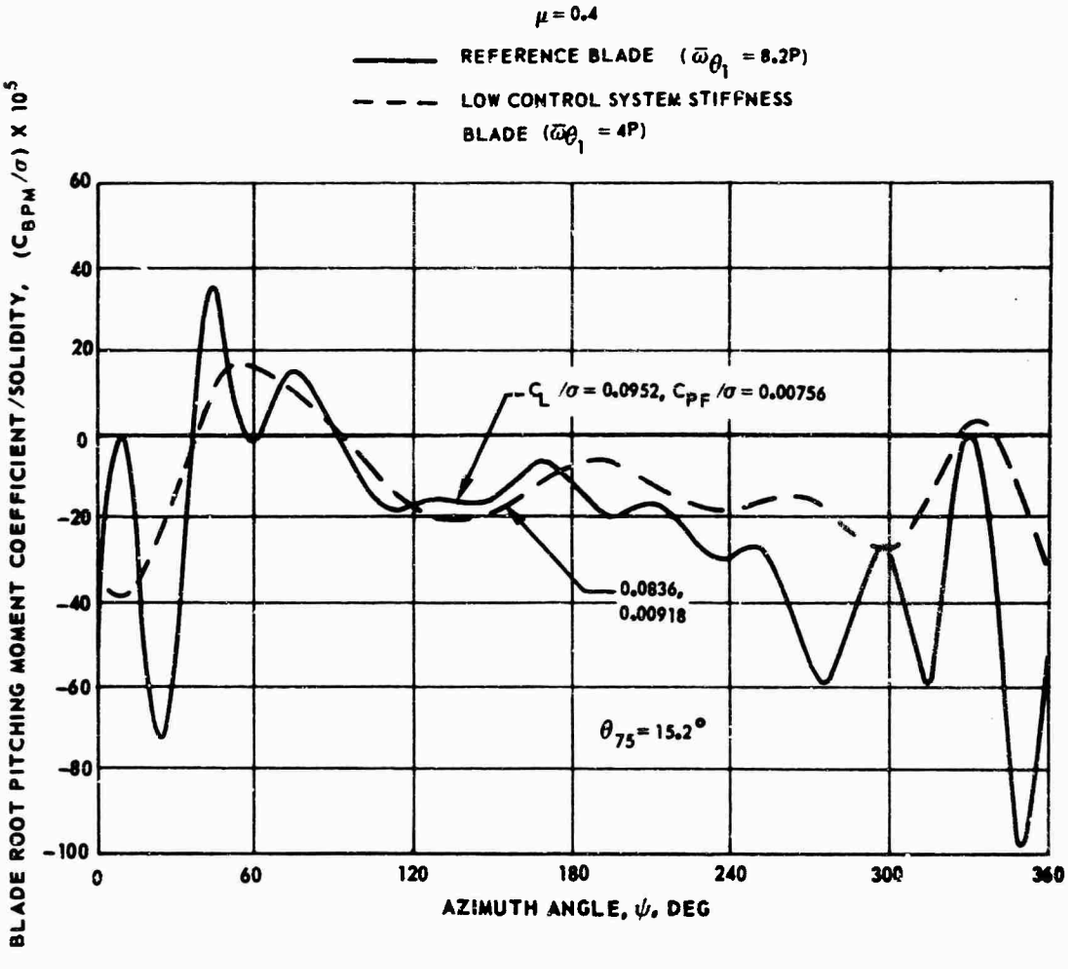

(b) θ_{75} = 15.2 DEG

Figure 38. Concluded.

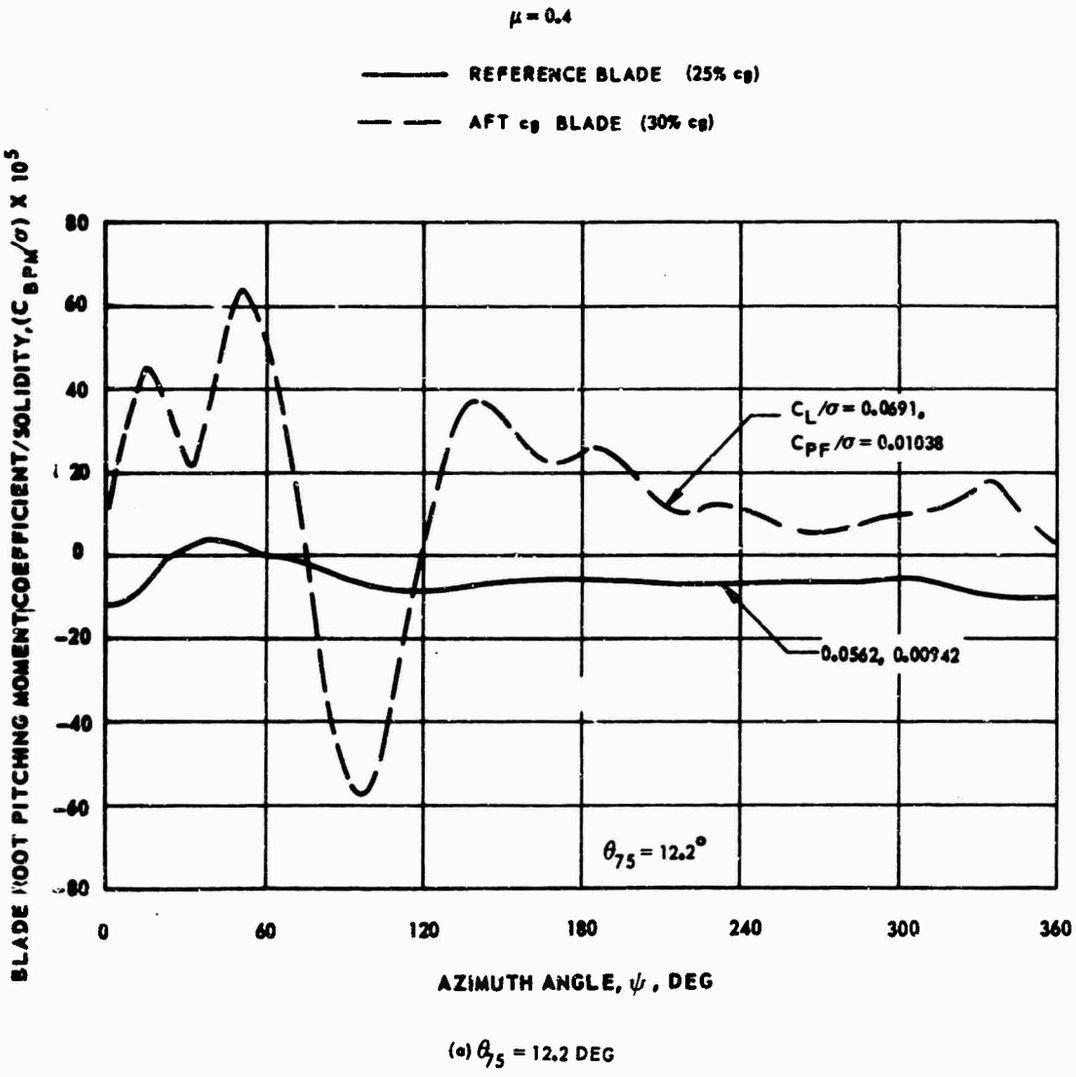

(a) θ_{75} = 12.2 DEG

Figure 39. Effect of Blade Chordwise cg Position on Blade Root Pitching Moment - Variable Inflow.

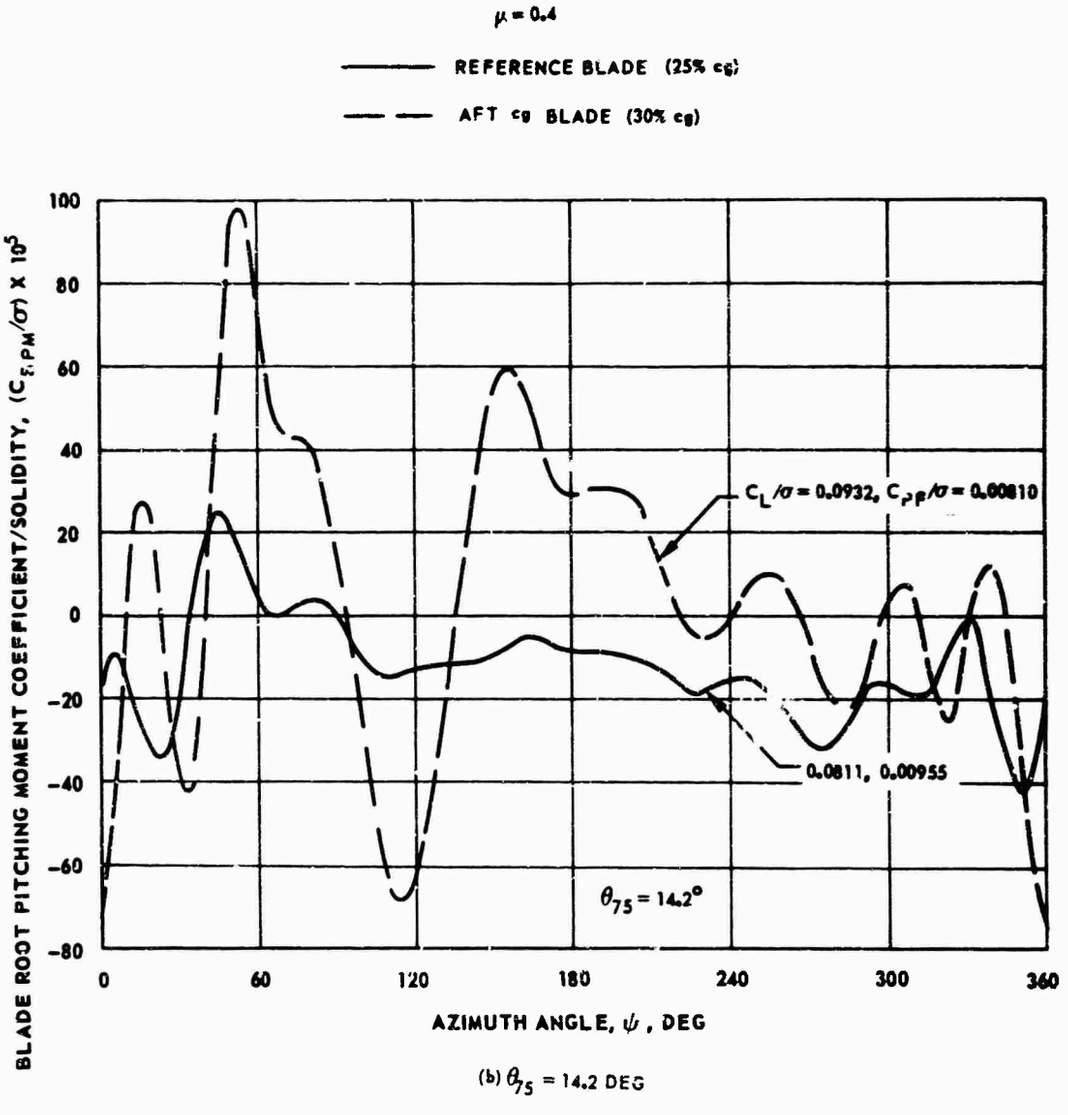

(b) θ_{75} = 14.2 DEG

Figure 39. Continued.

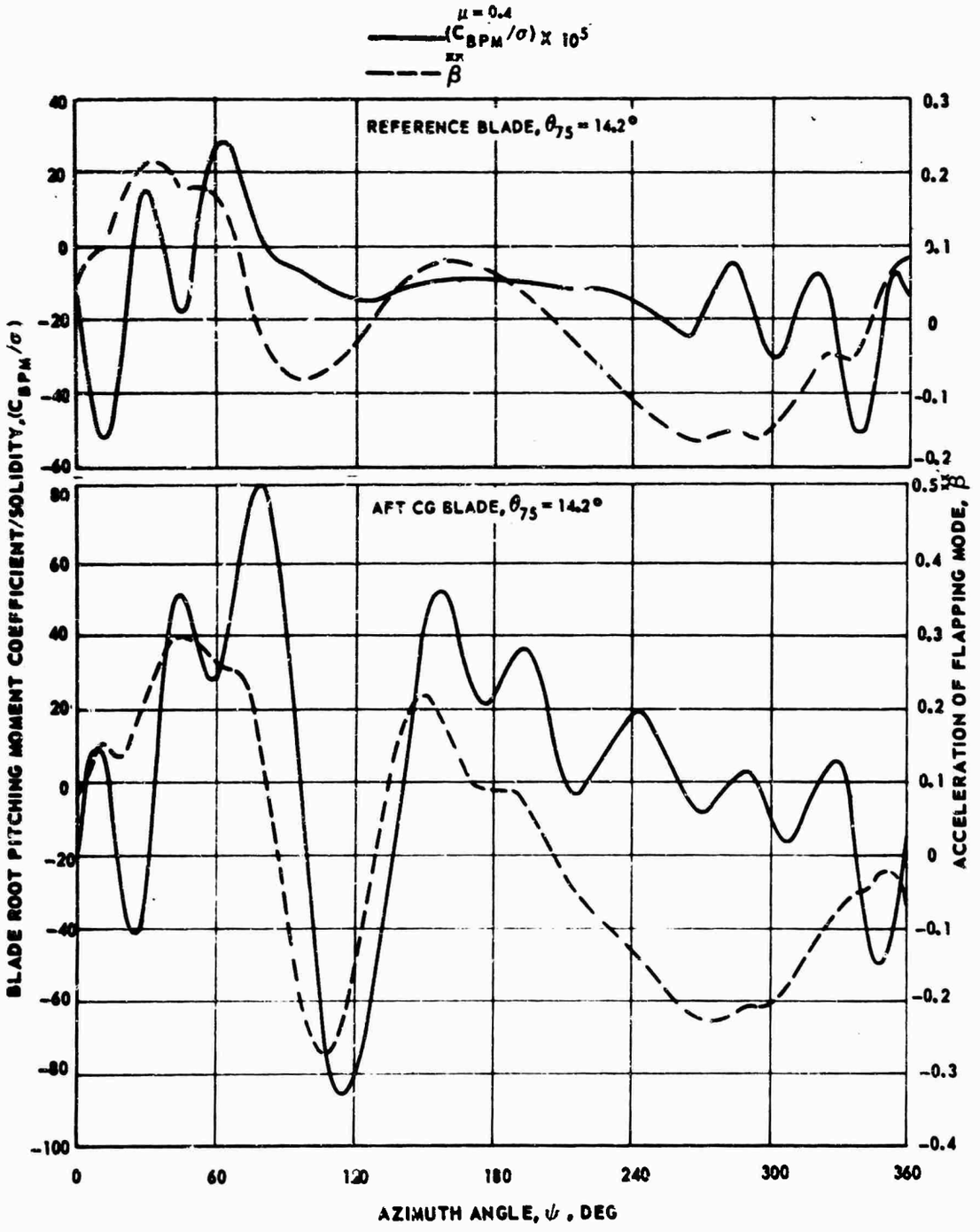

Figure 41. Comparison of Blade Root Pitching Moment and Flapping Mode Acceleration - Constant Inflow.

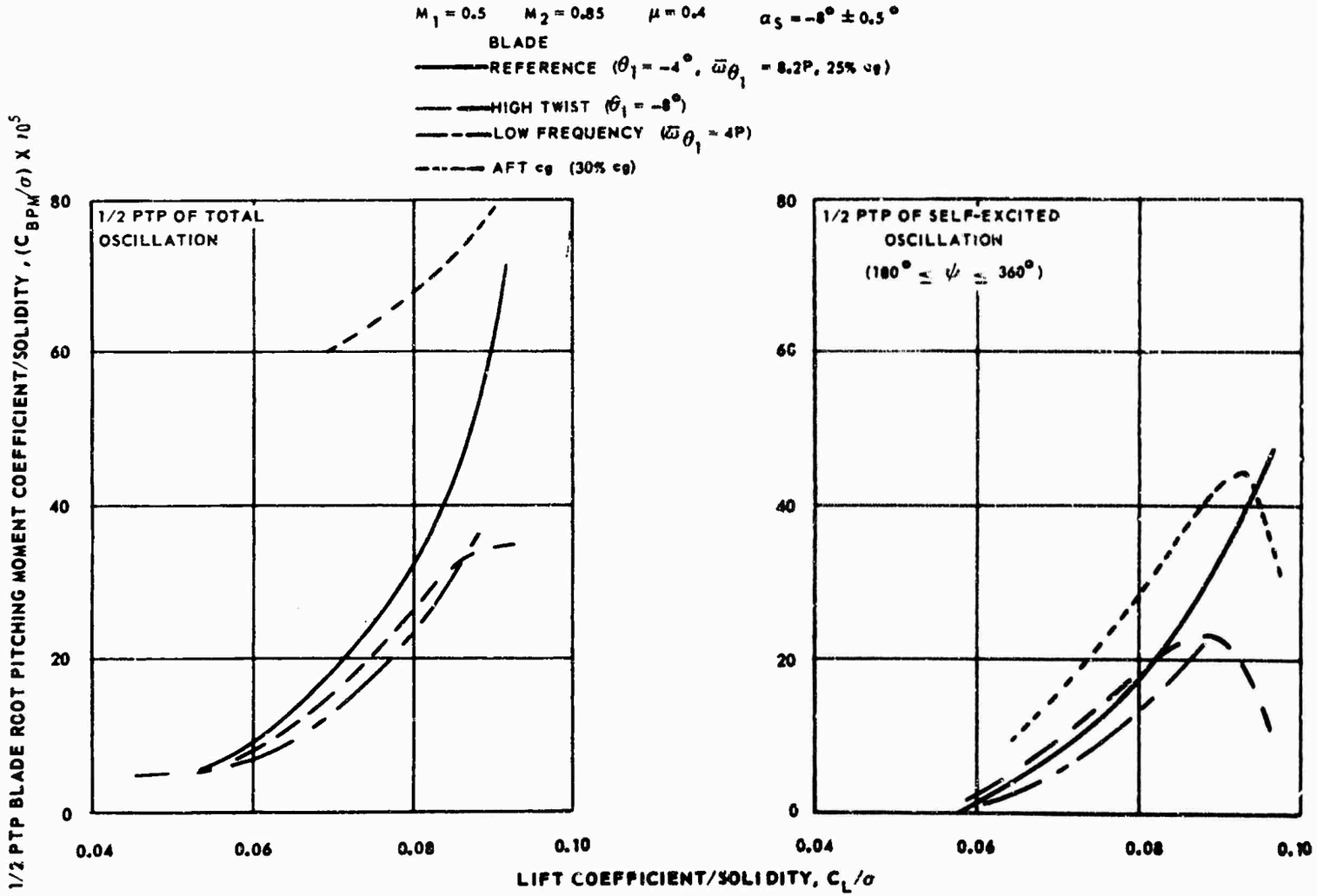

Figure 40. Comparison of Blade Root Pitching Moment Amplitudes for Various Blade Designs - Variable Inflow.

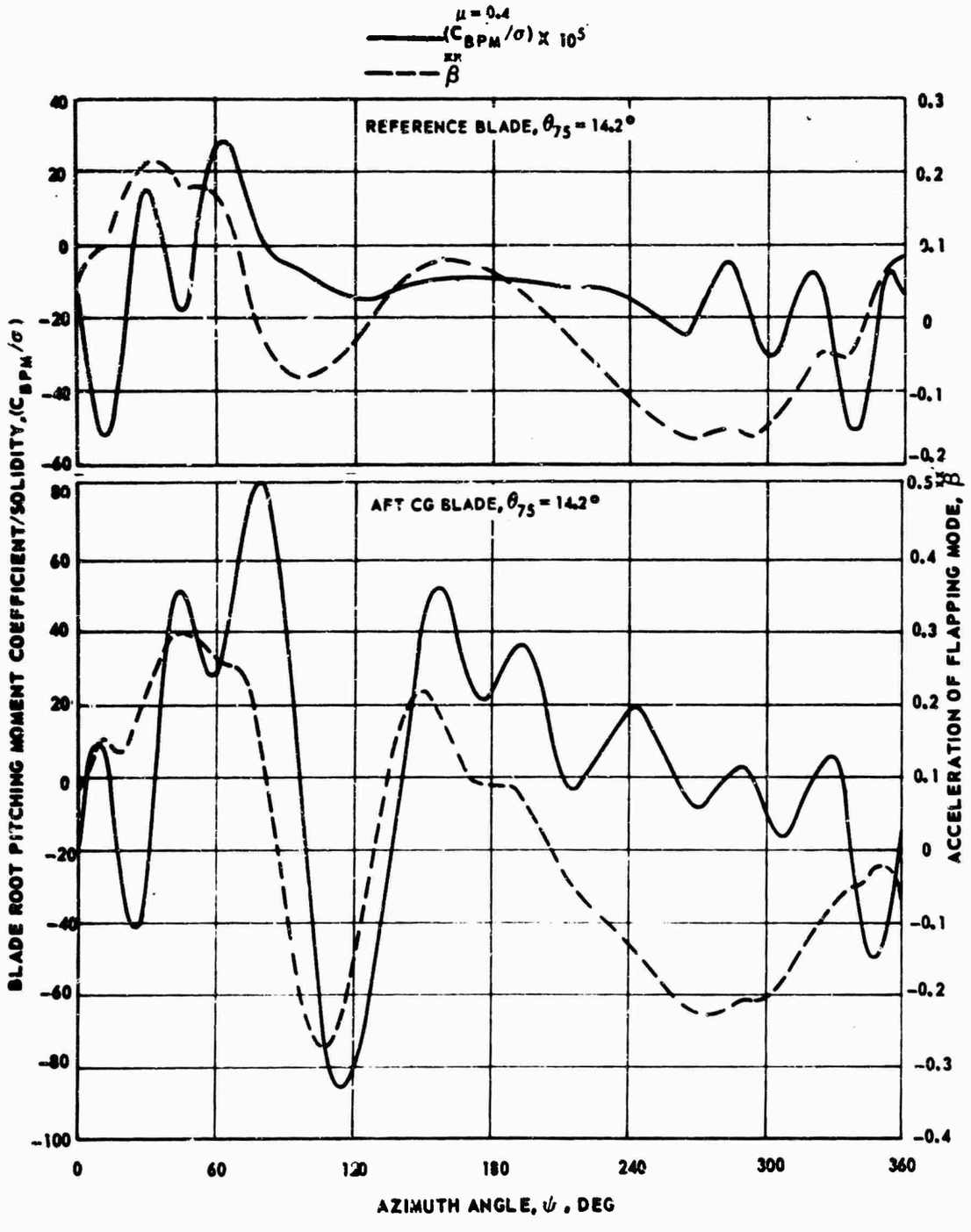

Figure 41. Comparison of Blade Root Pitching Moment and Flapping Mode Acceleration - Constant Inflow.

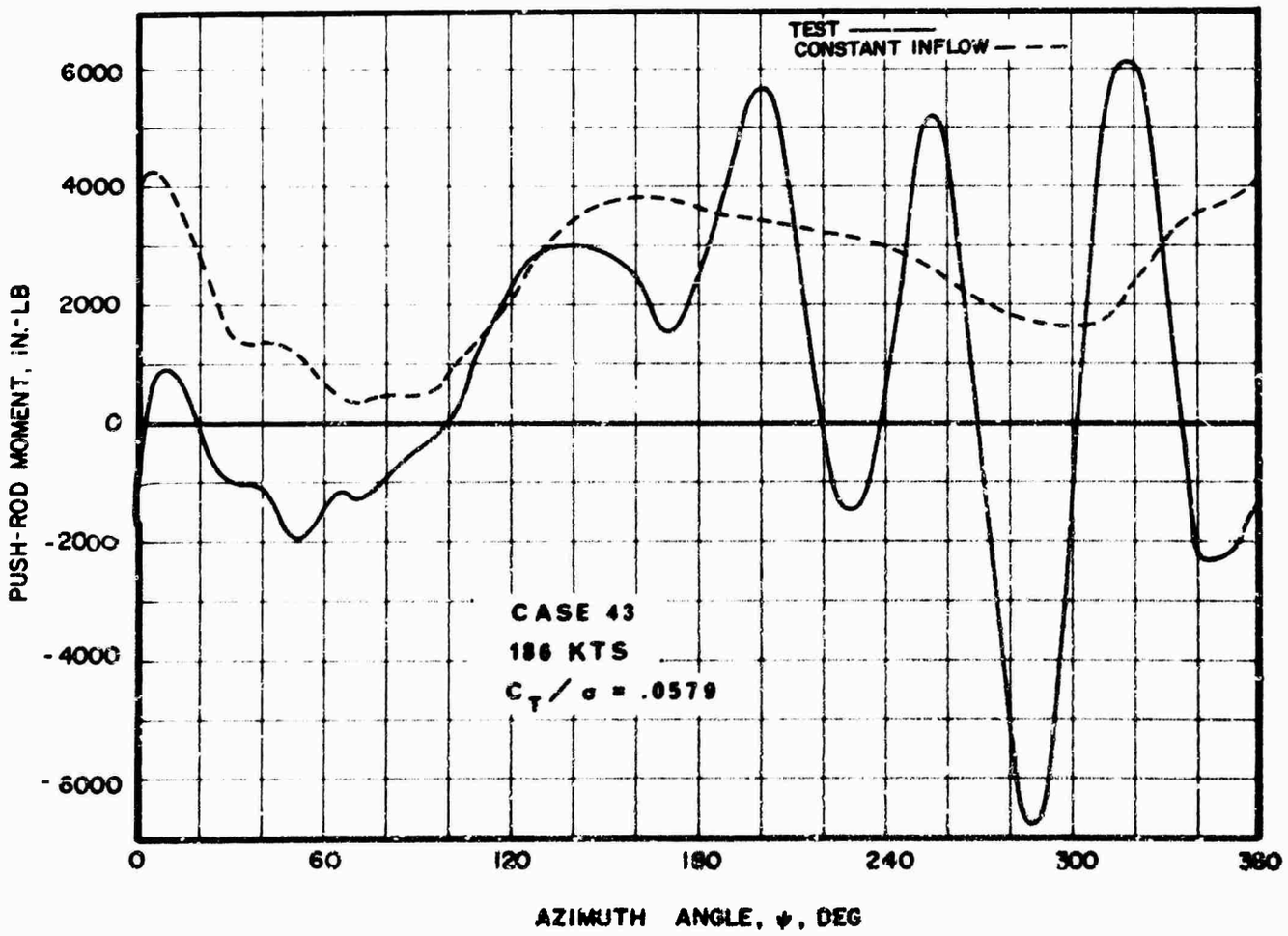

Figure 42. Comparison of Experimental and Constant Inflow Analytical Push-Rod Moments, S-61F, Case 43.

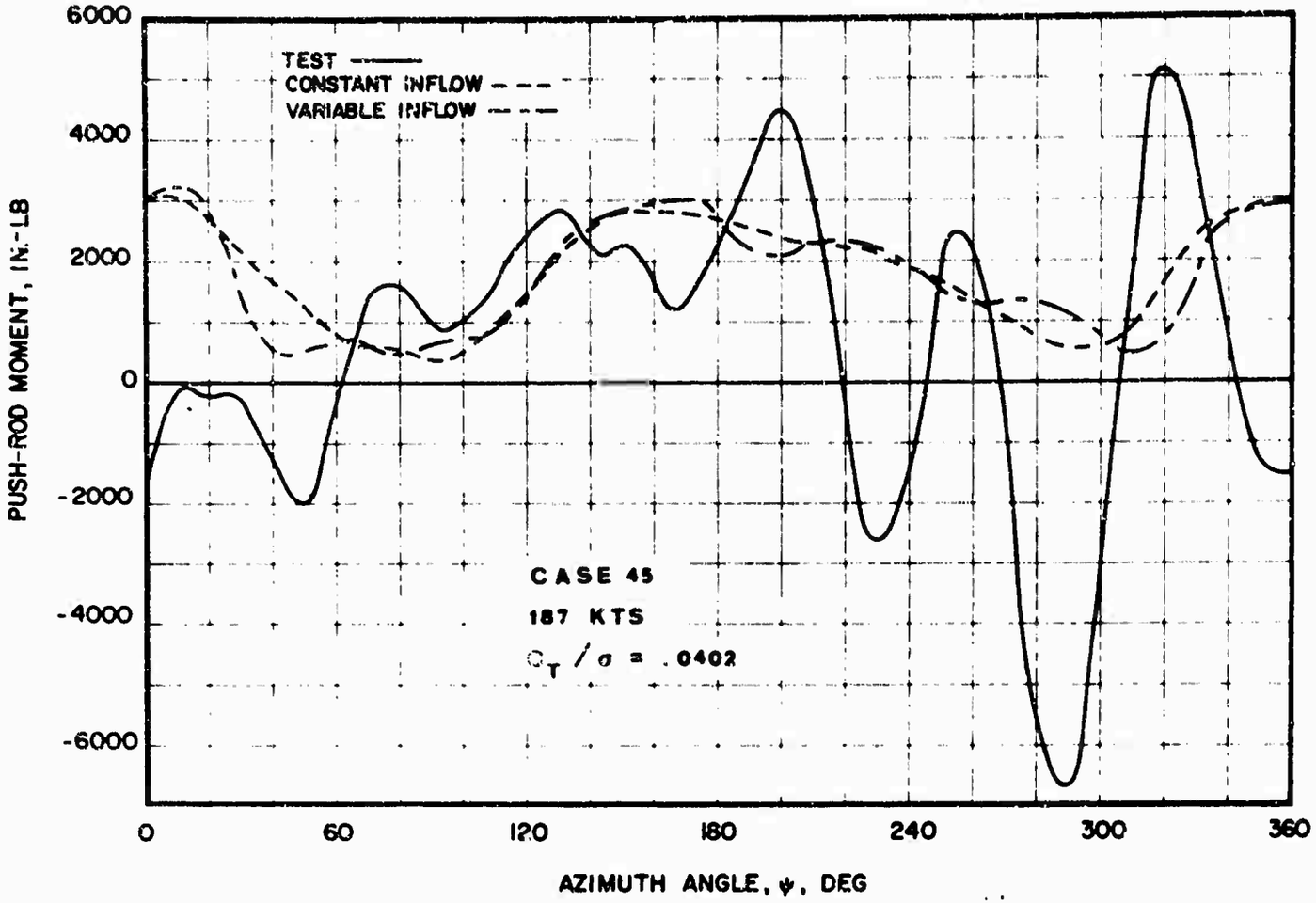

Figure 43. Comparison of Experimental, Variable, and Constant Inflow Analytical Push-Rod Moments, S-61F, Case 45.

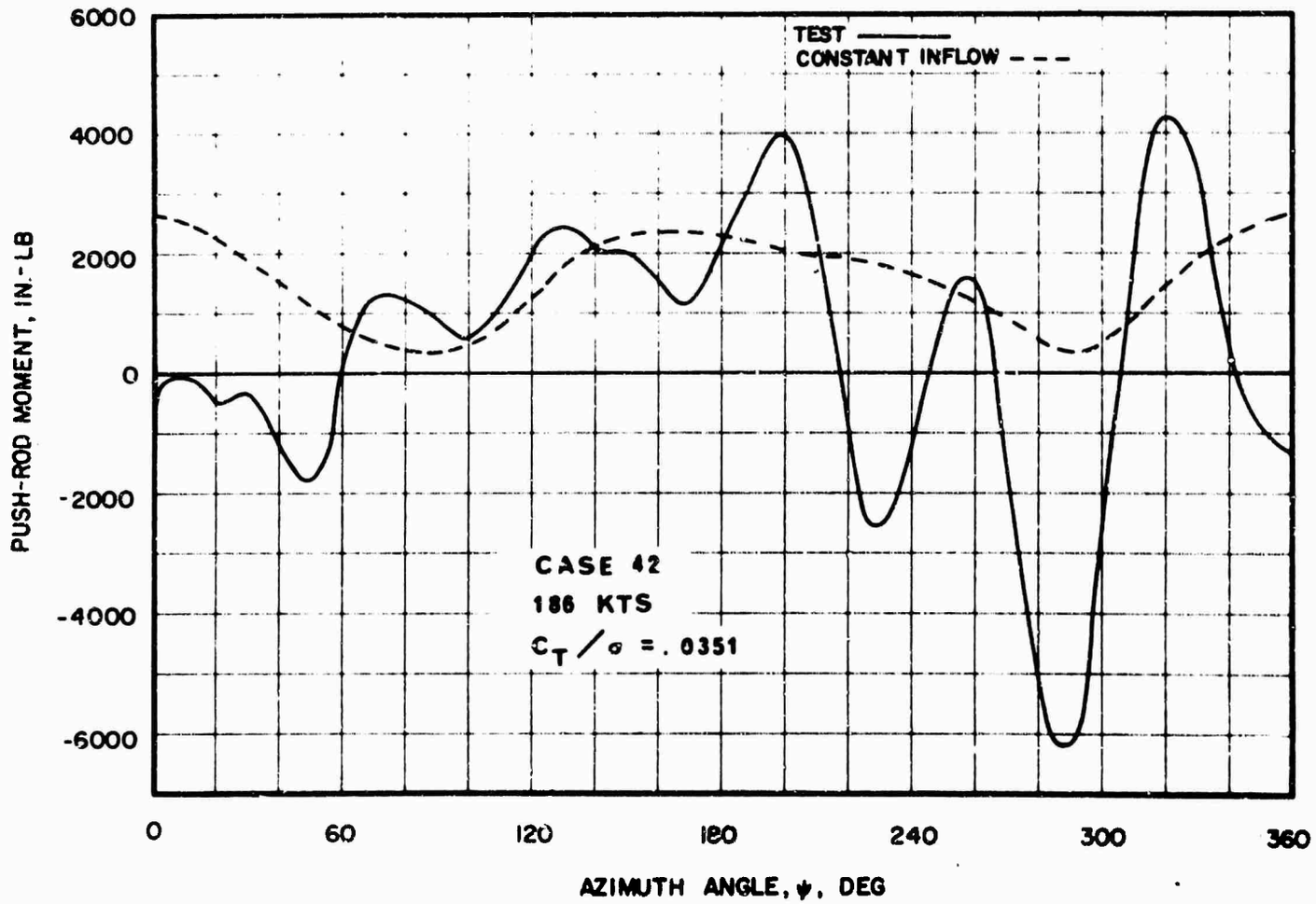

Figure 44. Comparison of Experimental and Constant Inflow Analytical Push-Rod Moments, S-61F, Case 42.

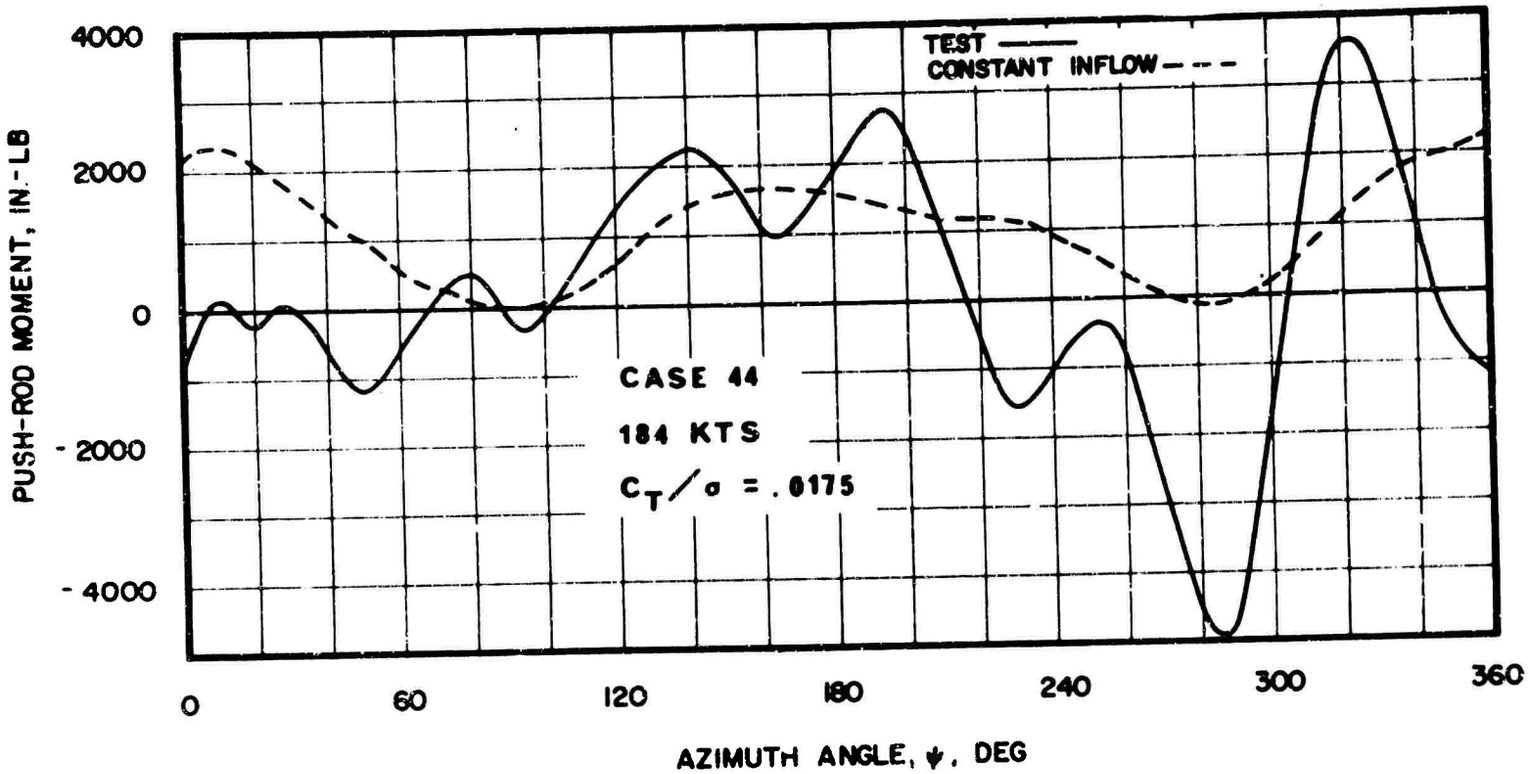

Figure 45. Comparison of Experimental and Constant Inflow Analytical Push-Rod Moments, S-61F, Case 44.

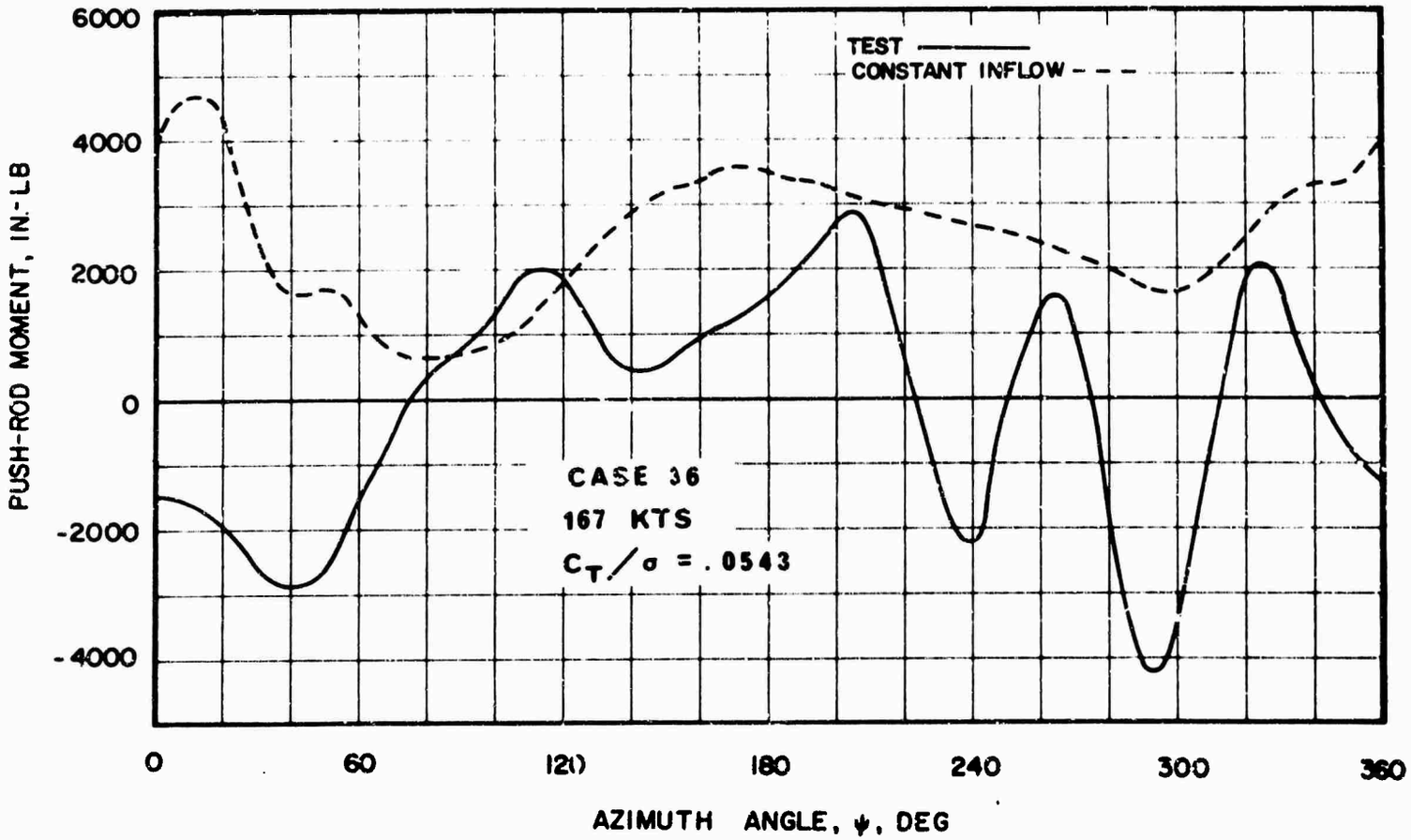

Figure 46. Comparison of Experimental and Constant Inflow Analytical Push-Rod Moments, S-61F, Case 36.

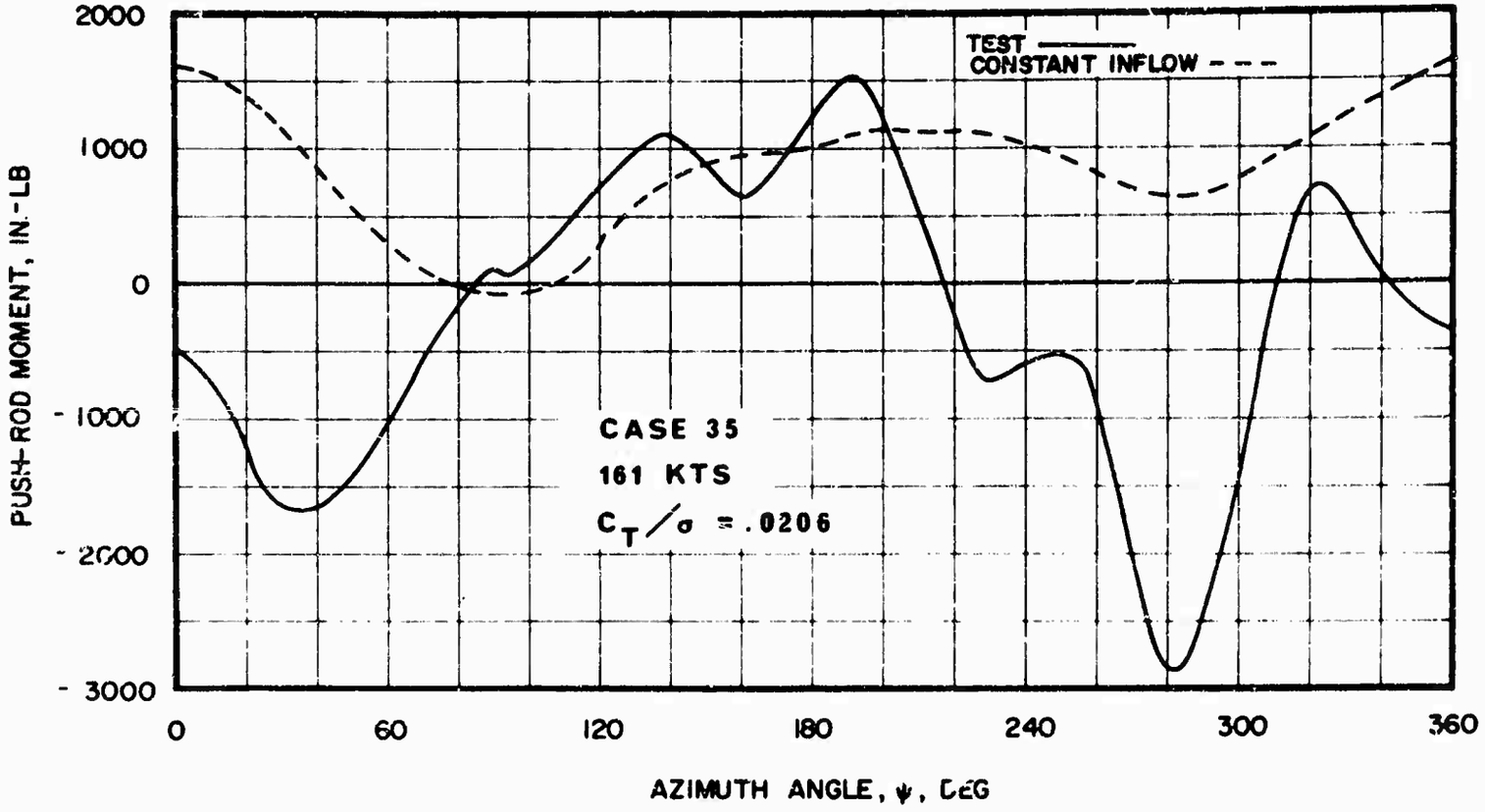

Figure 47. Comparison of Experimental and Constant Inflow Analytical Push-Rod Moments, S-61F, Case 35.

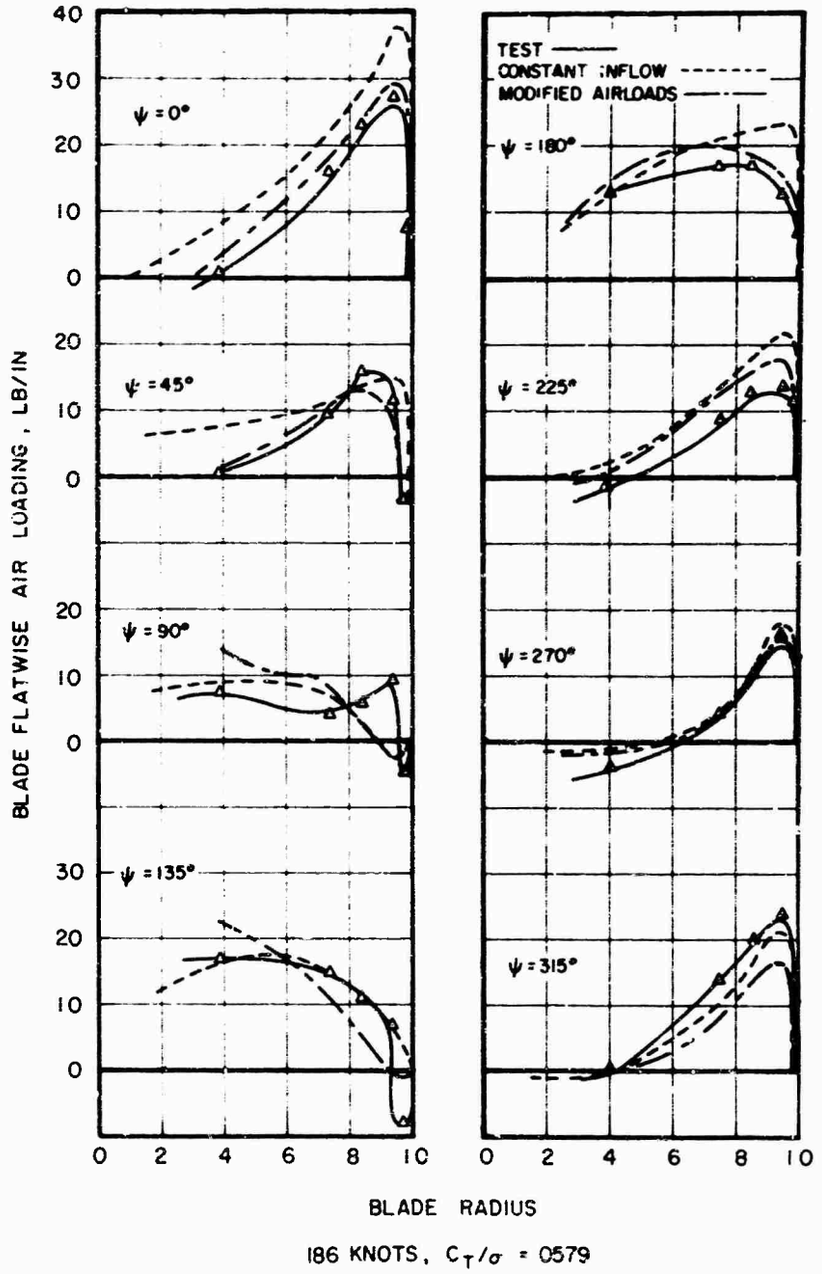

Figure 48. Comparison of Blade Flatwise Air Loading Distributions, S-61F, Case 43.

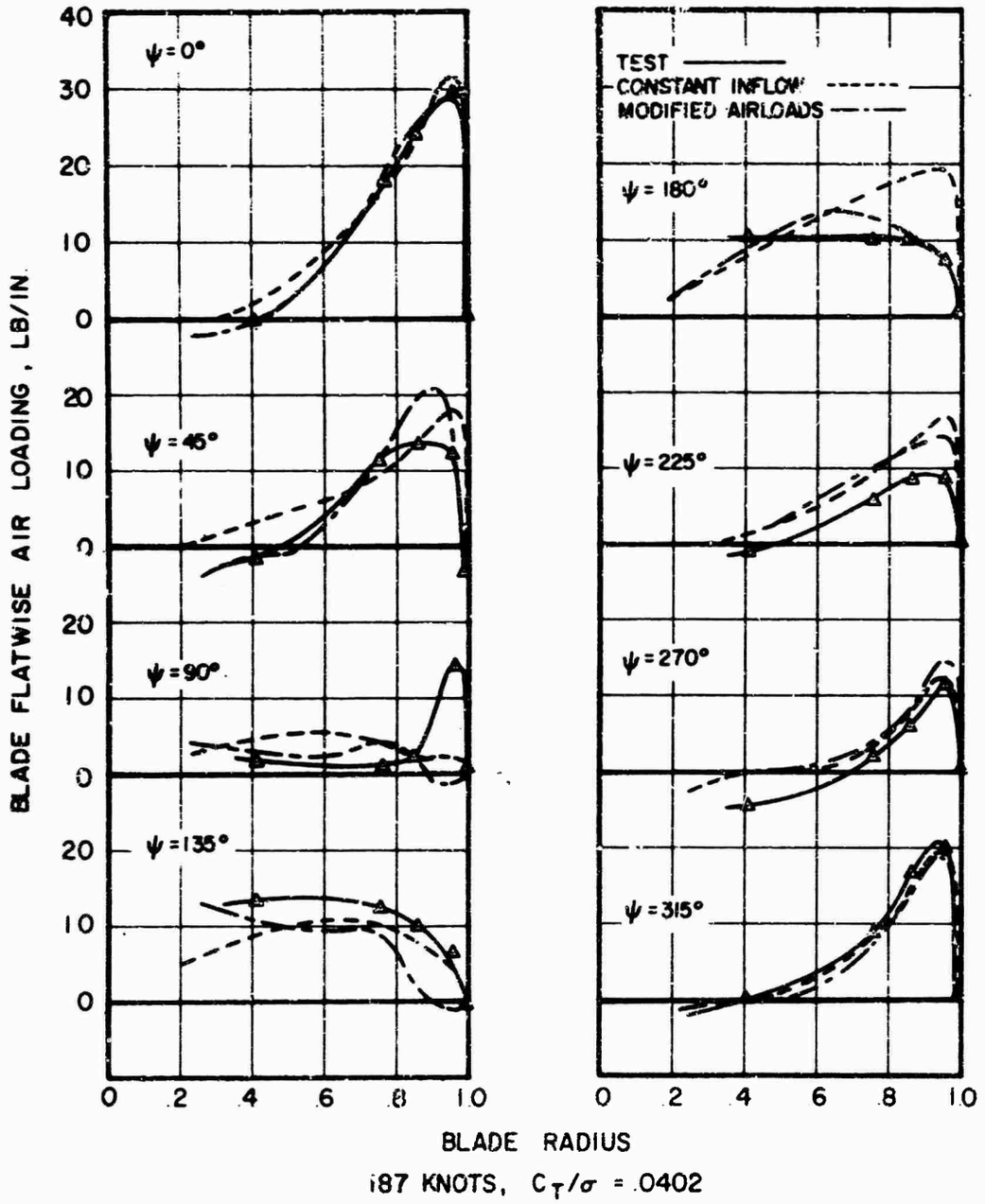

Figure 49. Comparison of Blade Flatwise Air Loading Distributions, S-61F, Case 45.

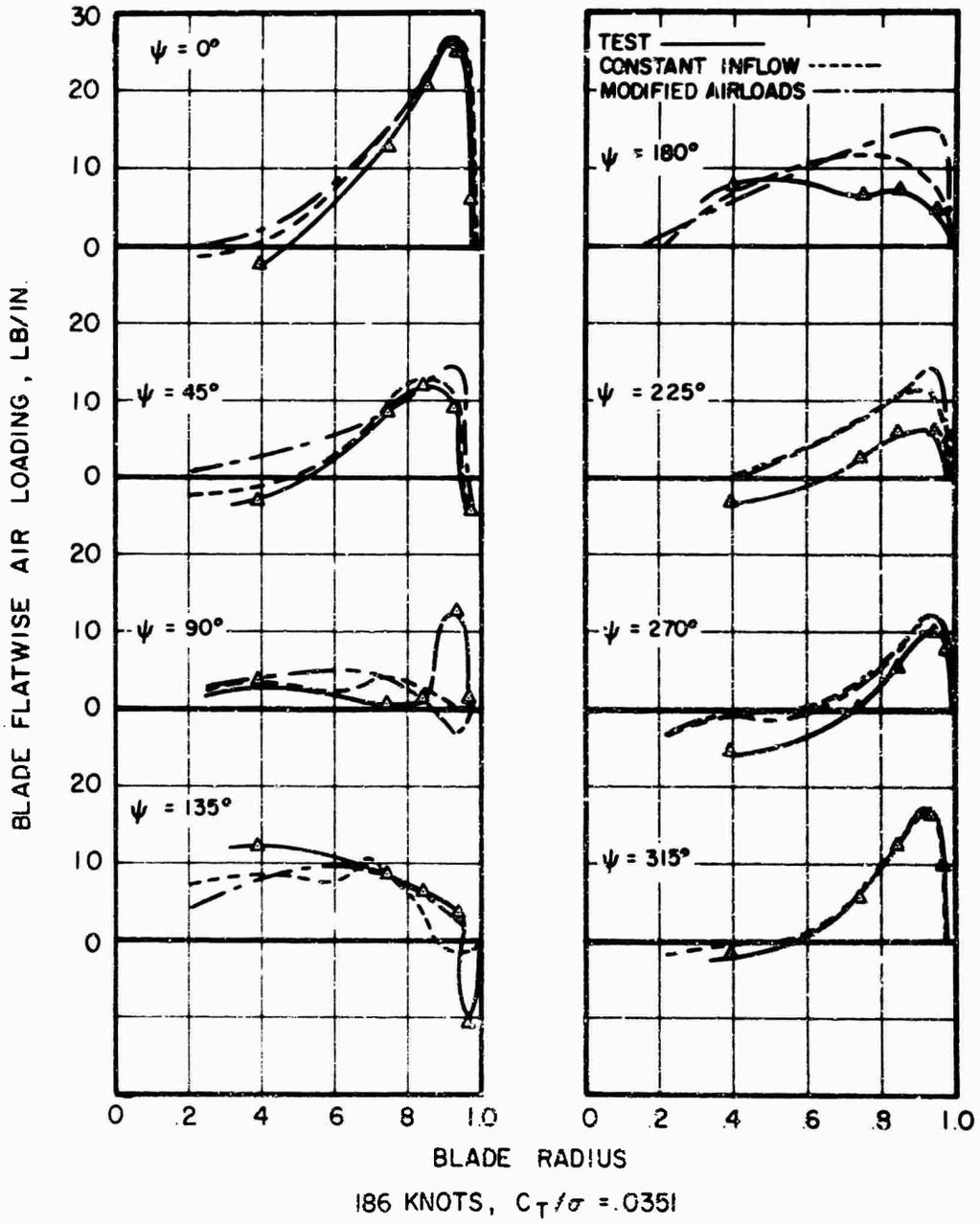

Figure 50. Comparison of Blade Flatwise Air Loading Distributions, S-61F, Case 42.

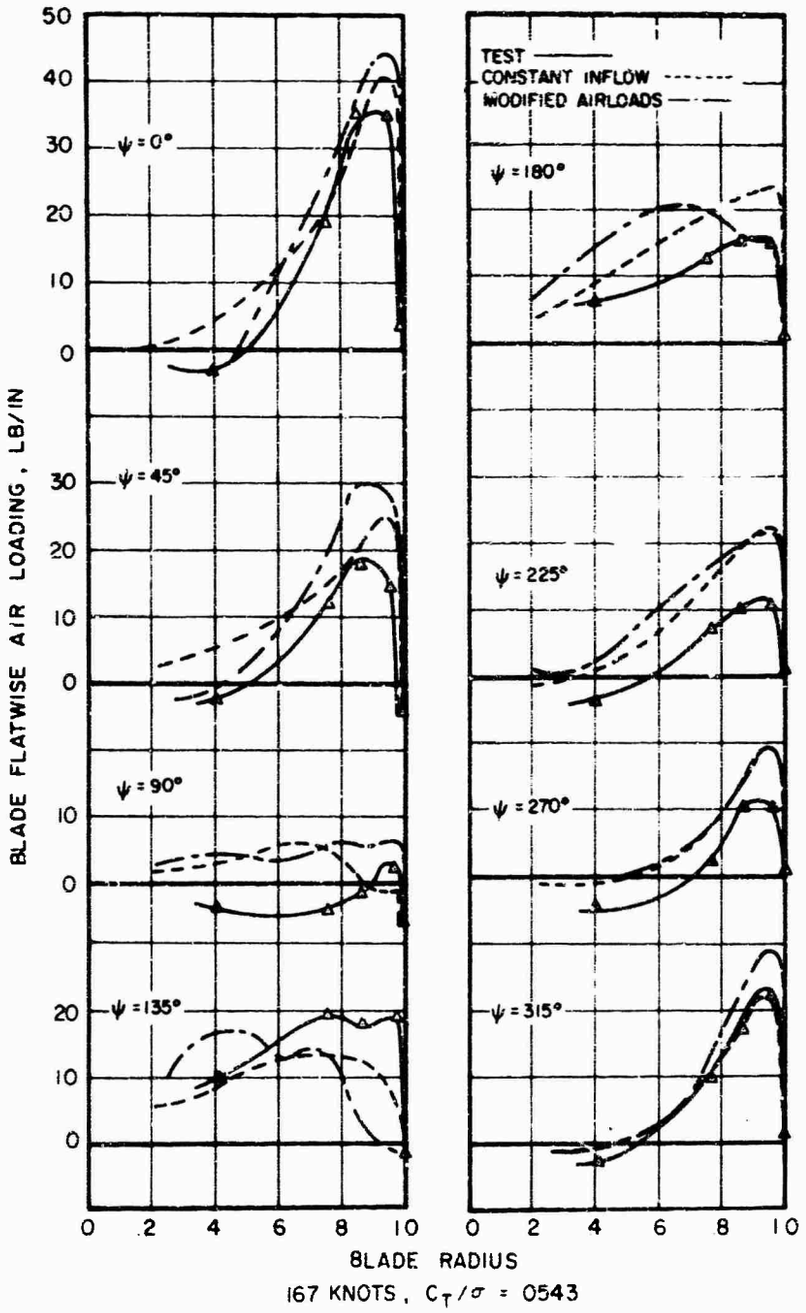

Figure 51. Comparison of Blade Flatwise Air Loading Distributions, S-61F, Case 36.

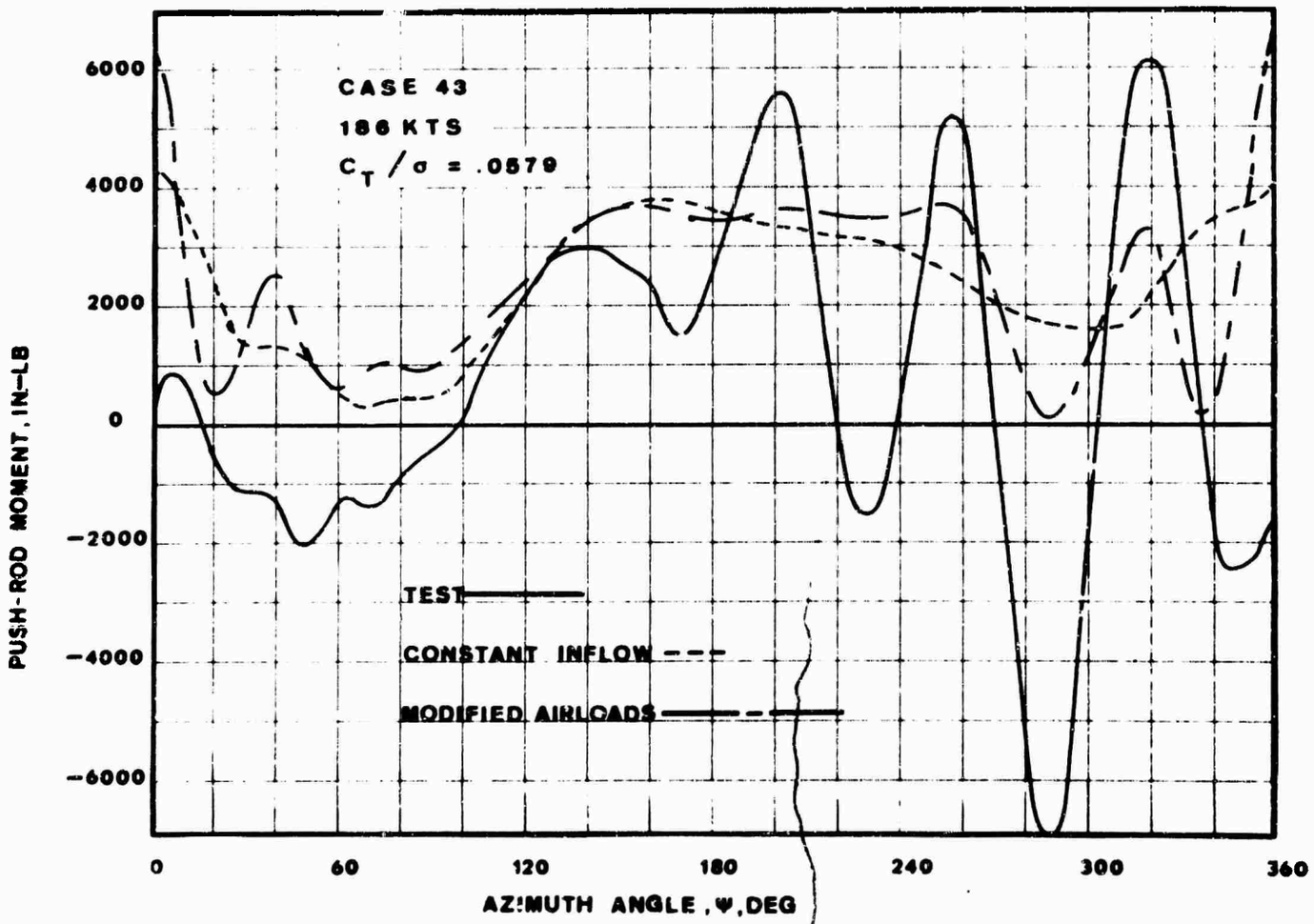

Figure 52. Comparison of Experimental, Constant Inflow, and Modified Airloads Analytical Push-Rod Moments, S-61F, Case 43.

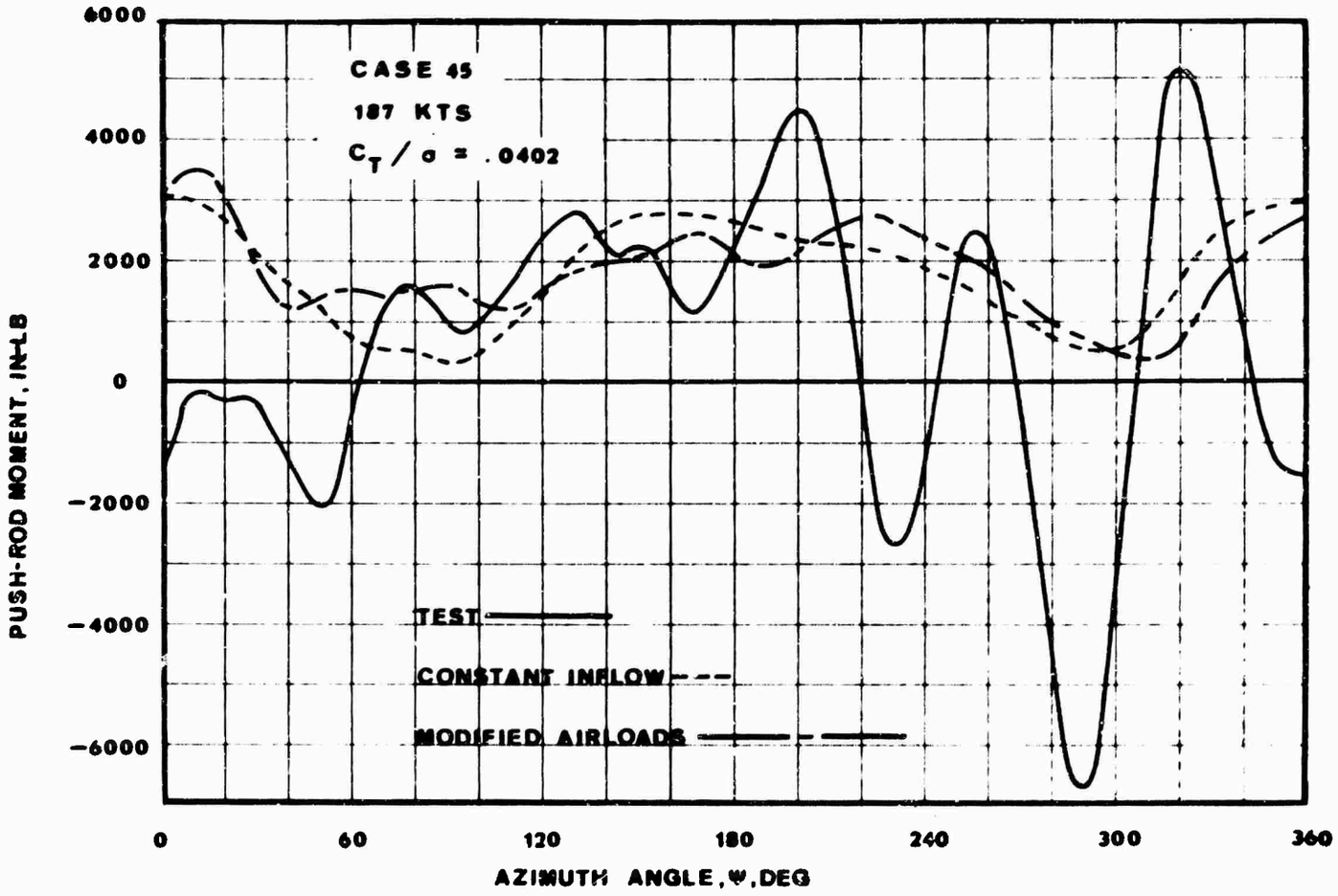

Figure 53. Comparison of Experimental, Constant Inflow, and Modified Airloads Analytical Push-Rod Moments, S-61F, Case 45.

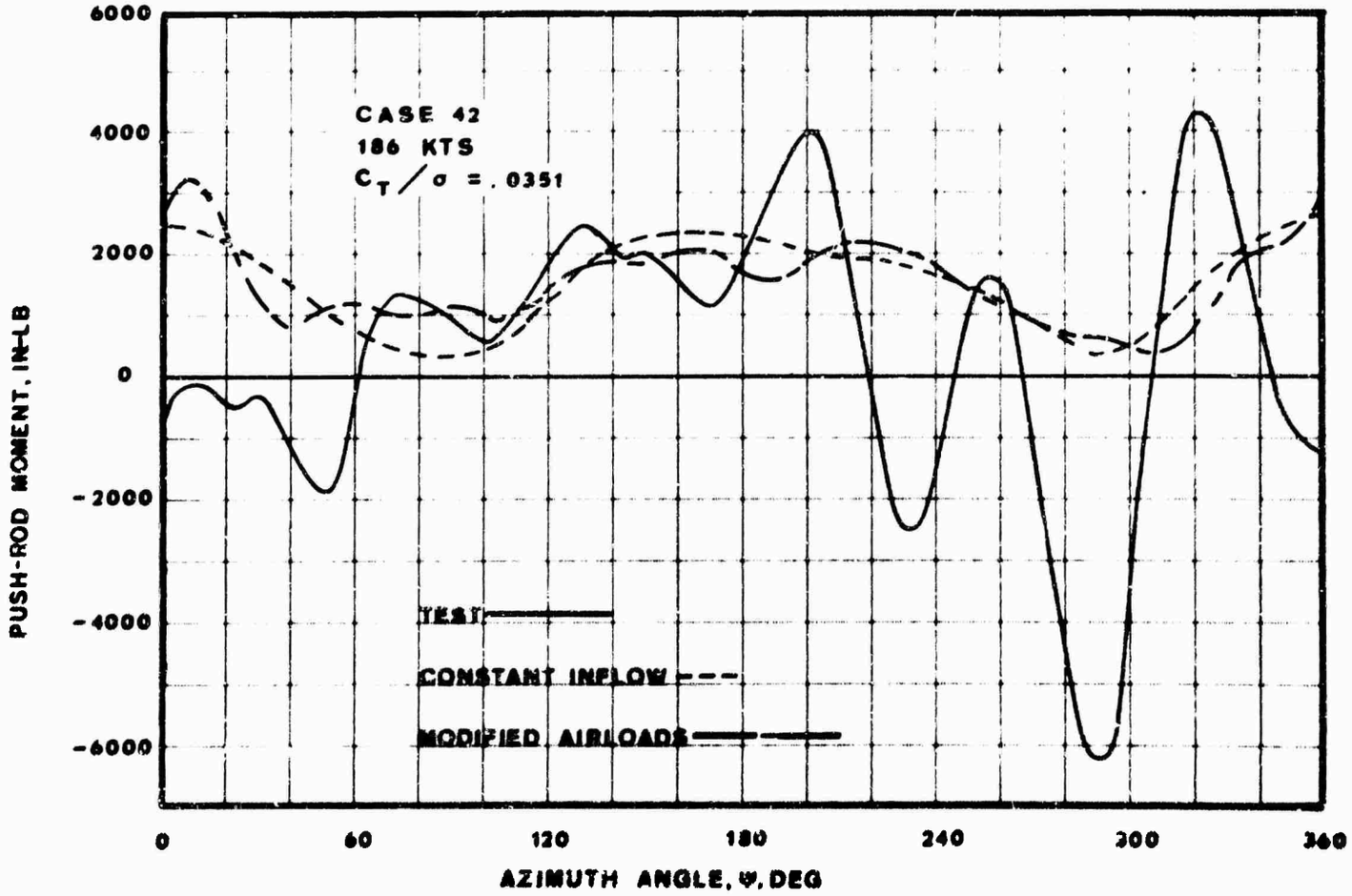

Figure 54. Comparison of Experimental, Constant Inflow, and Modified Airloads Analytical Push-Rod Moments, S-61F, Case 42.

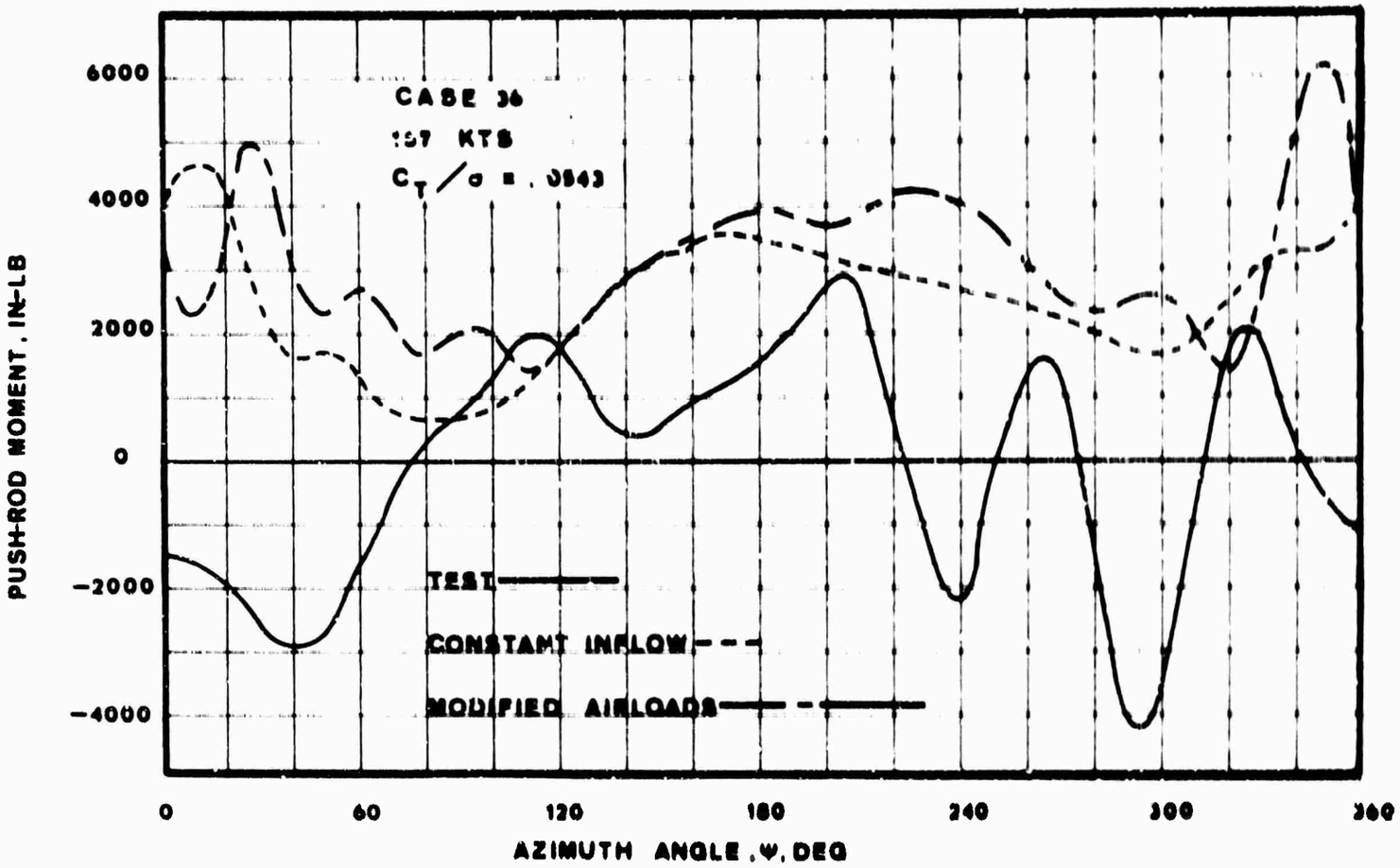

Figure 55. Comparison of Experimental, Constant Inflow, and Modified Airloads Analytical Push-Rod Moments, S-61F, Case 36.

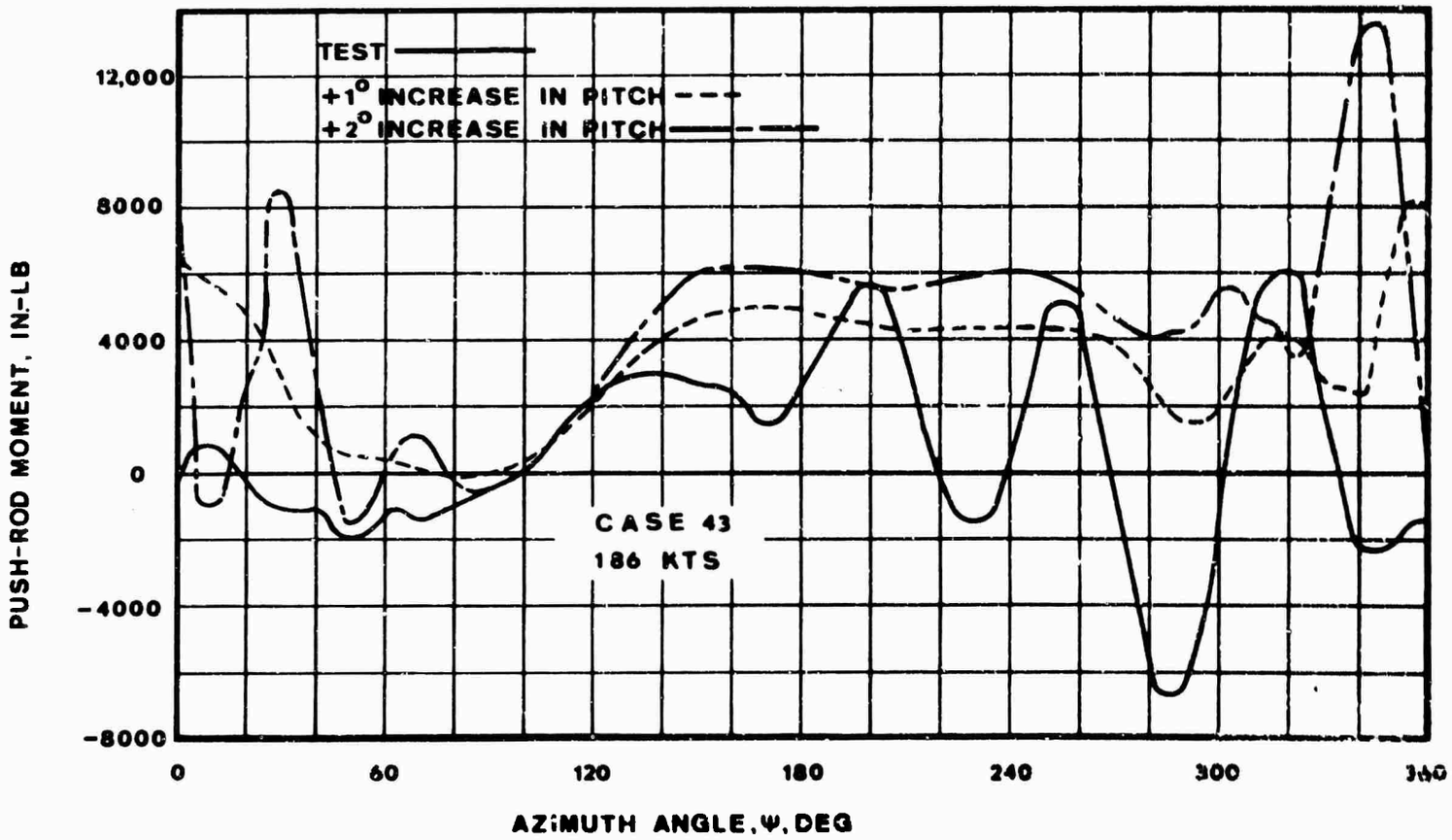

Figure 56. Comparison of Experimental Push-Rod Moment With Analytical Push-Rod Moment at Increased Collective Pitch, S-61F, Case 43.

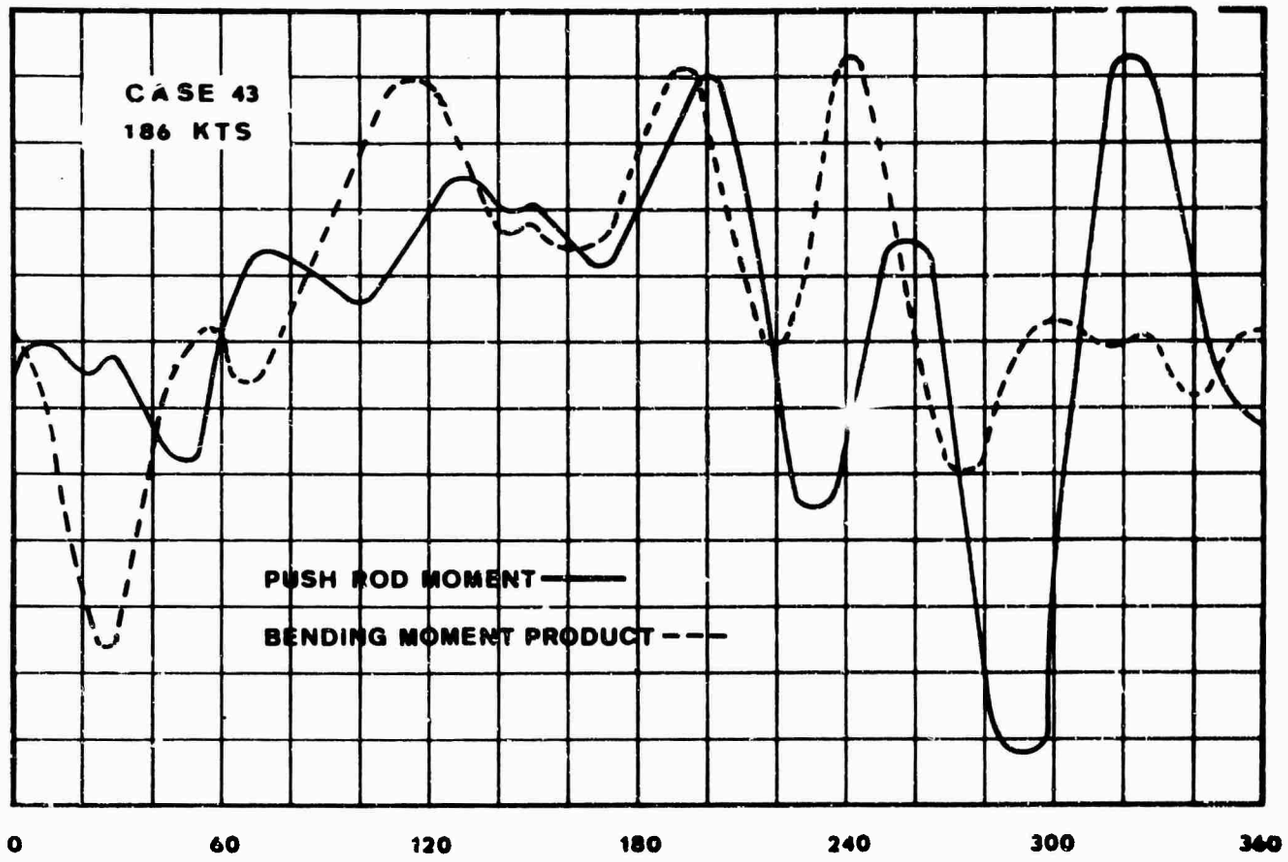

Figure 57. Comparison of Experimental Push-Rod Moment With Product of Experimental Flatwise and Edgewise Bending Moments, S-61F, Case 43.

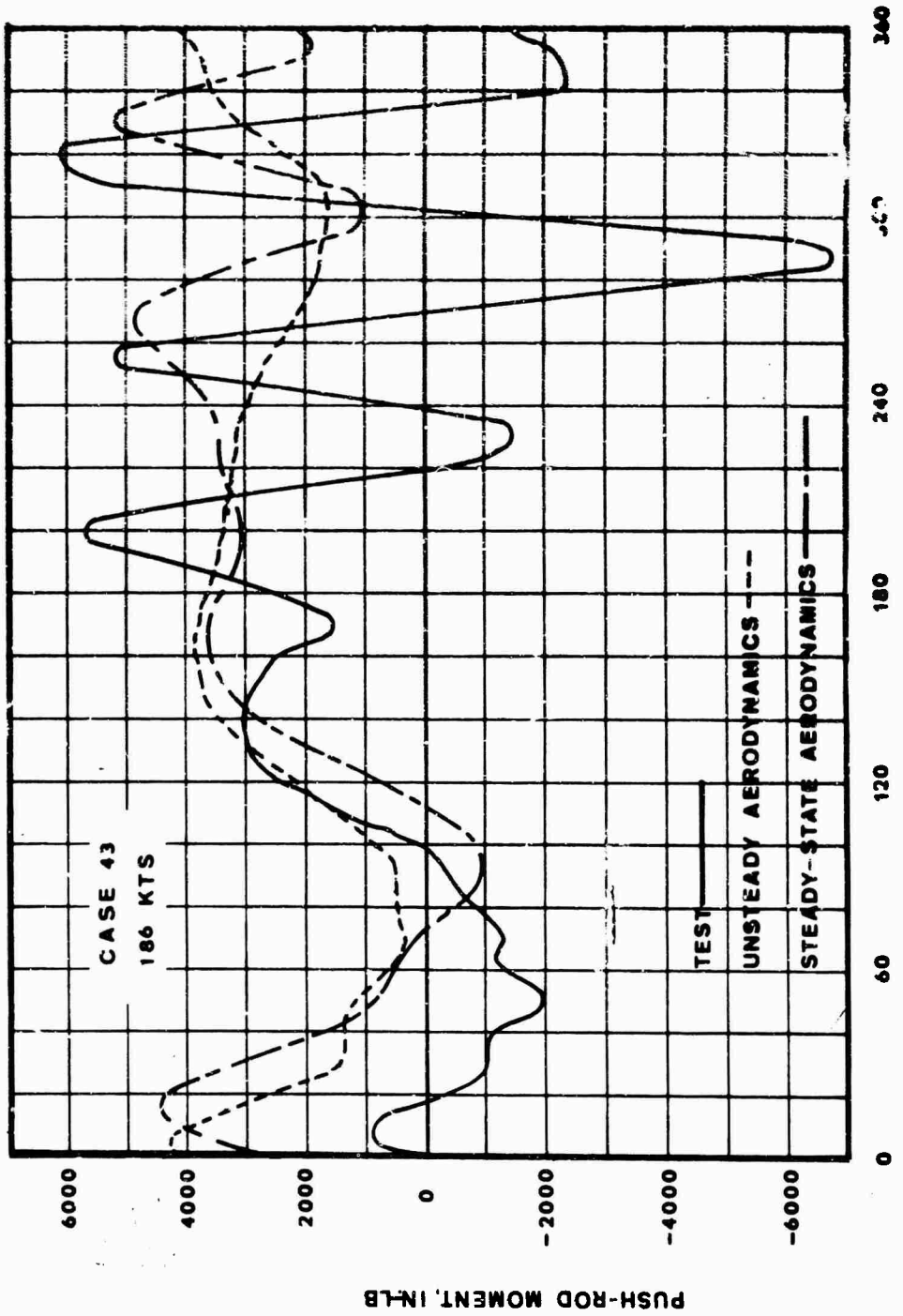

Figure 58. Comparison of Experimental Push-Rod Moment With Analytical Push-Rod Moments for Steady and Unsteady Aerodynamic Data, S-61F, Case 43.

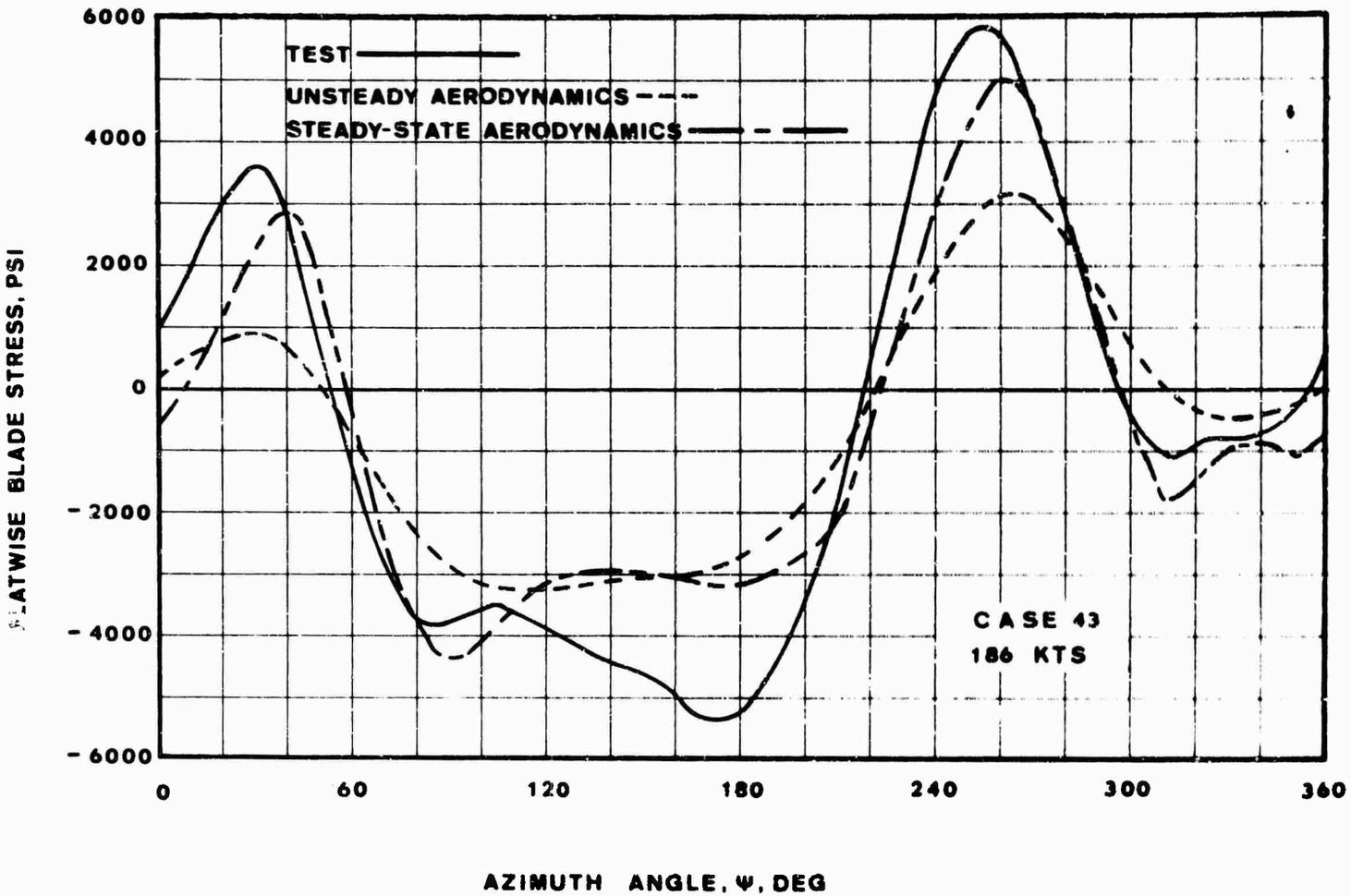

Figure 59. Comparison of Experimental and Analytical Flatwise Blade Stresses at 65 Percent Radial Station for Steady and Unsteady Aerodynamic Data, S-61F, Case 43.

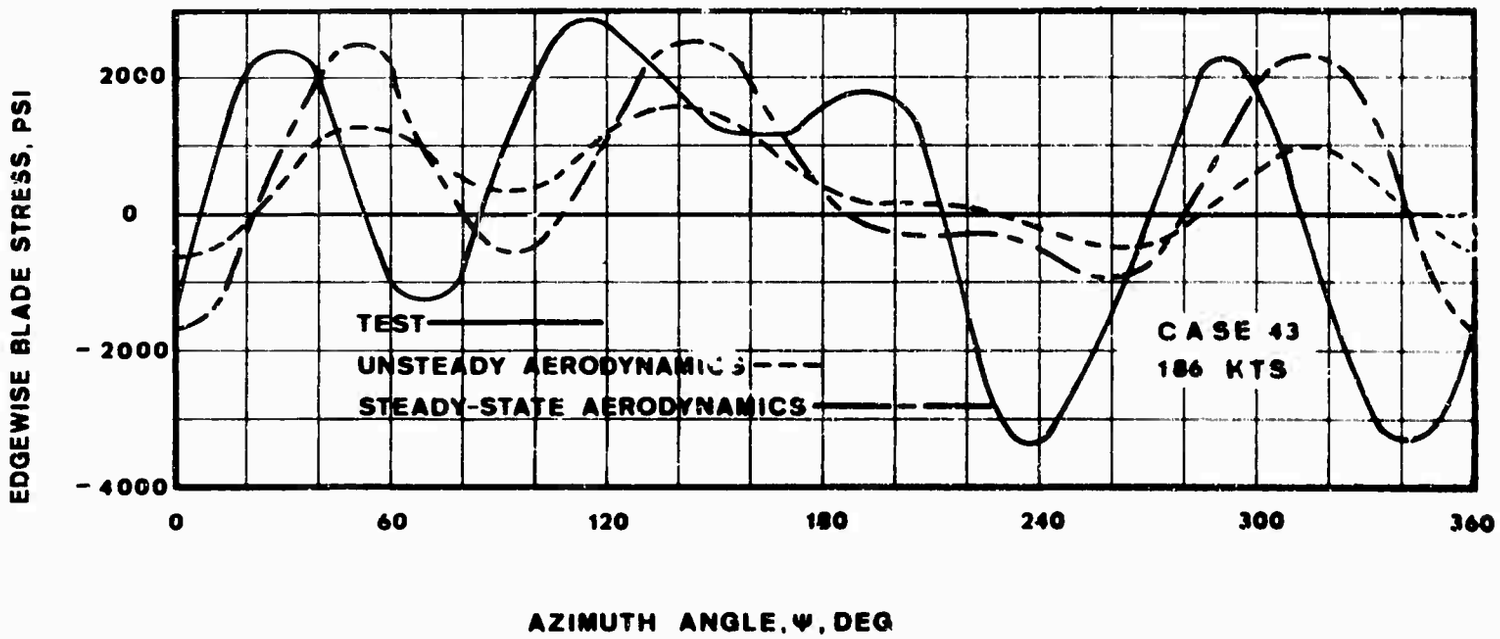

Figure 60. Comparison of Experimental and Analytical Edgewise Blade Stresses at 46 Percent Radial Station for Steady and Unsteady Aerodynamic Data, S-61F, Case 43.

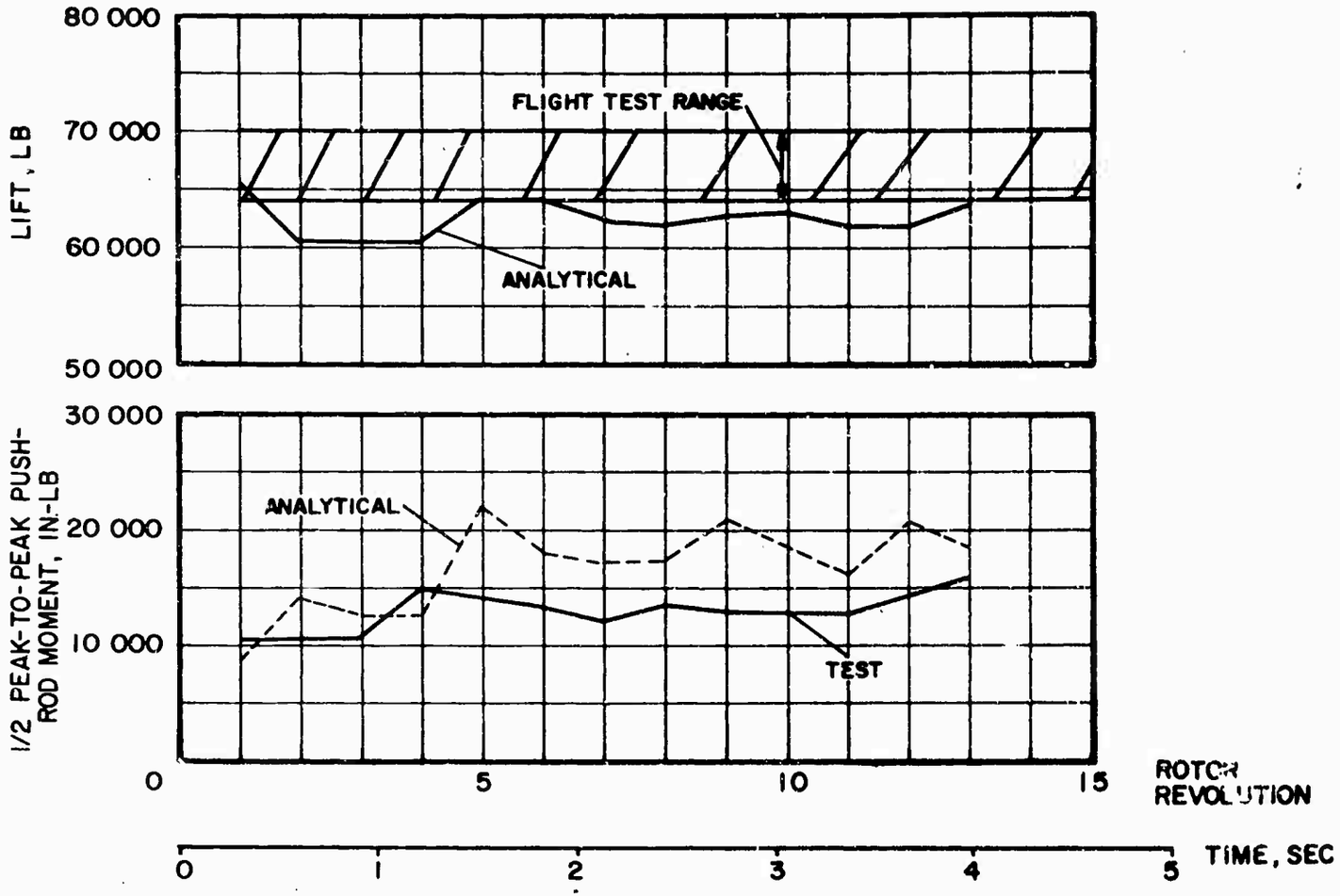

Figure 61. Time Histories of Lift and Push-Rod Moment Amplitude, CH-53A, 120-Knot, 60-Degree Right Turn.

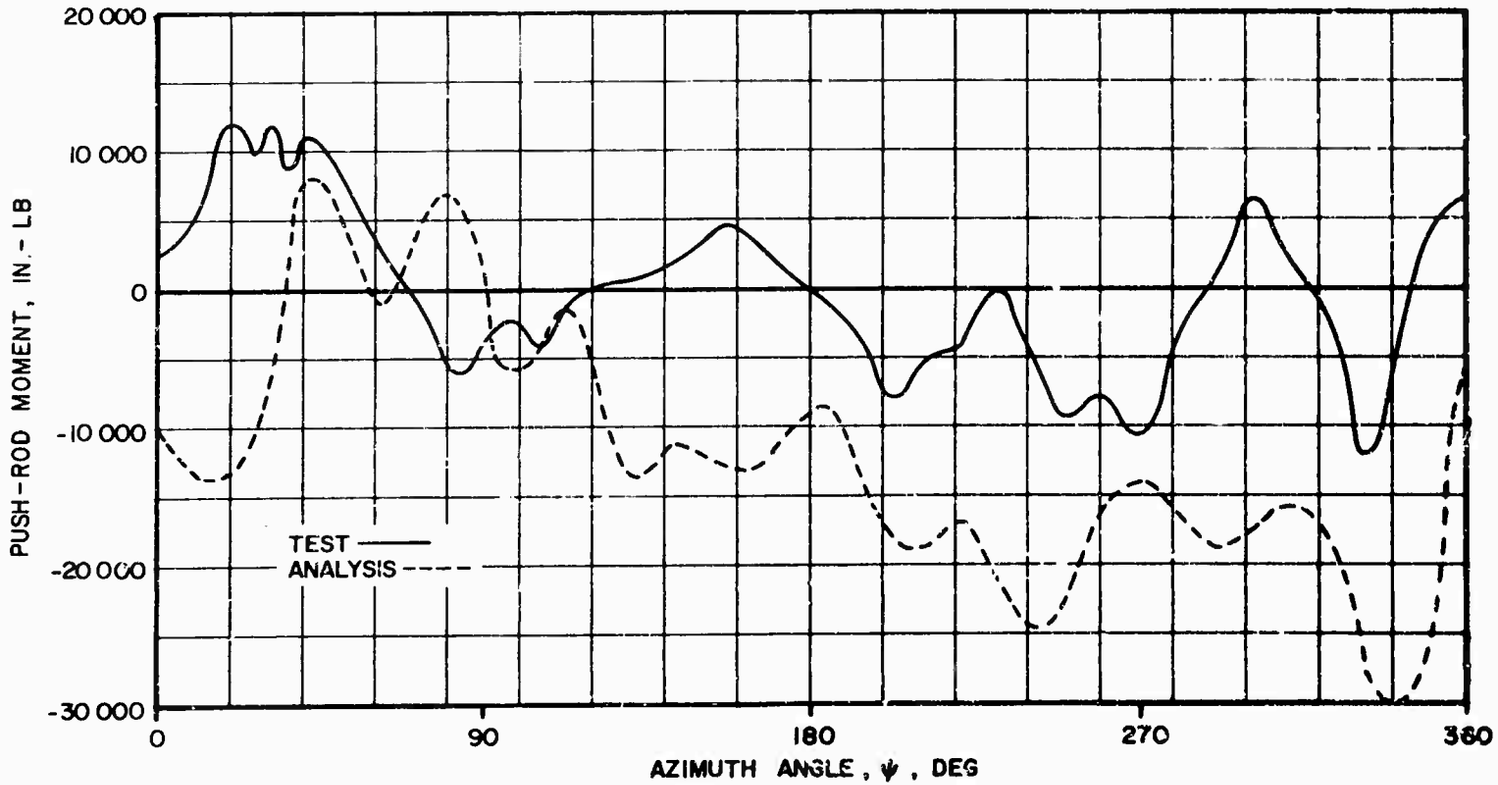

Figure 62. Comparison of Experimental and Analytical Push-Rod Moments for Tenth Revolution, CH-53A, 120-Knot, 60-Degree Right Turn.

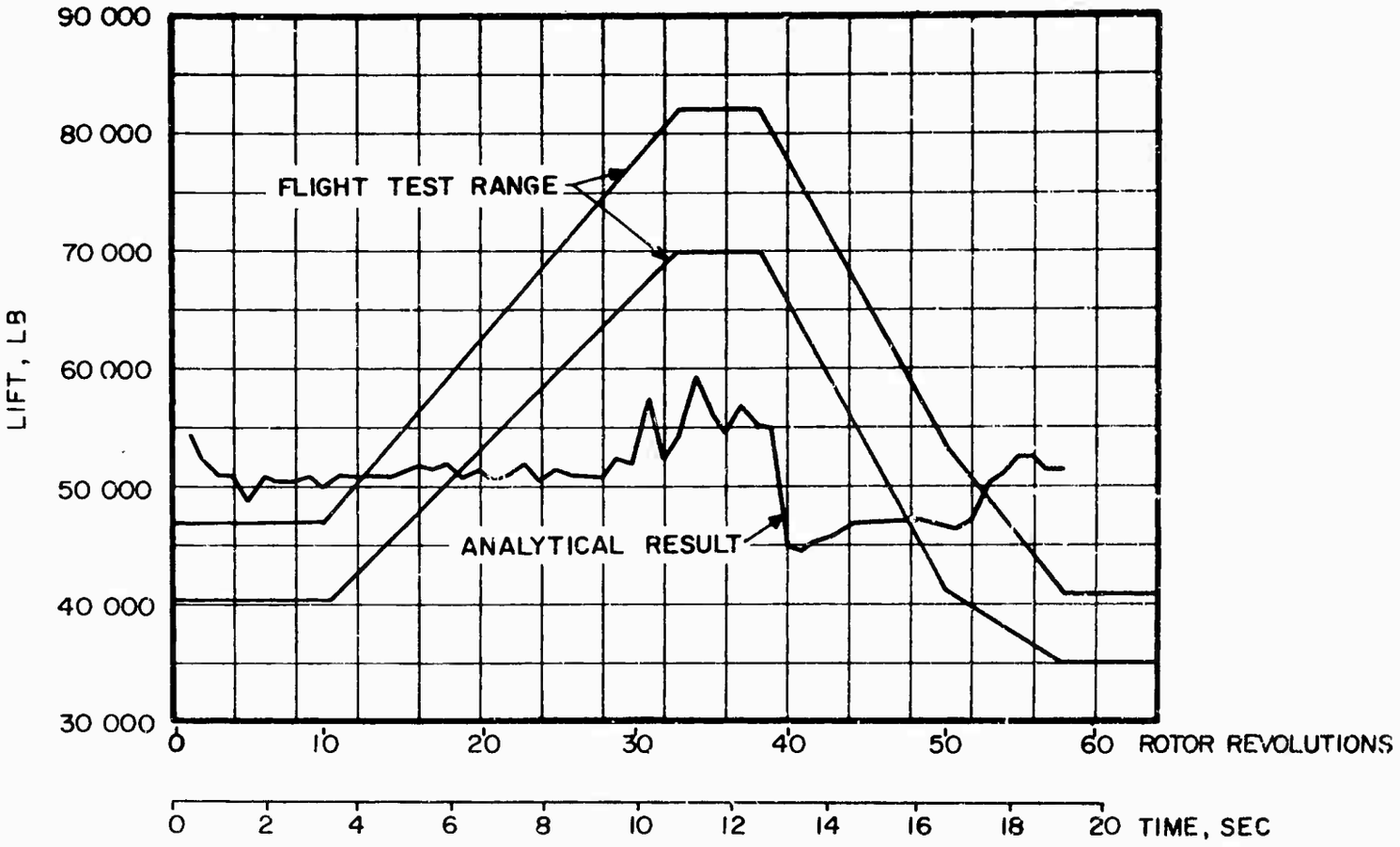

Figure 63. Time History of Lift, CH-53A, 150-Knot Right Turn at Varying Angle of Bank.

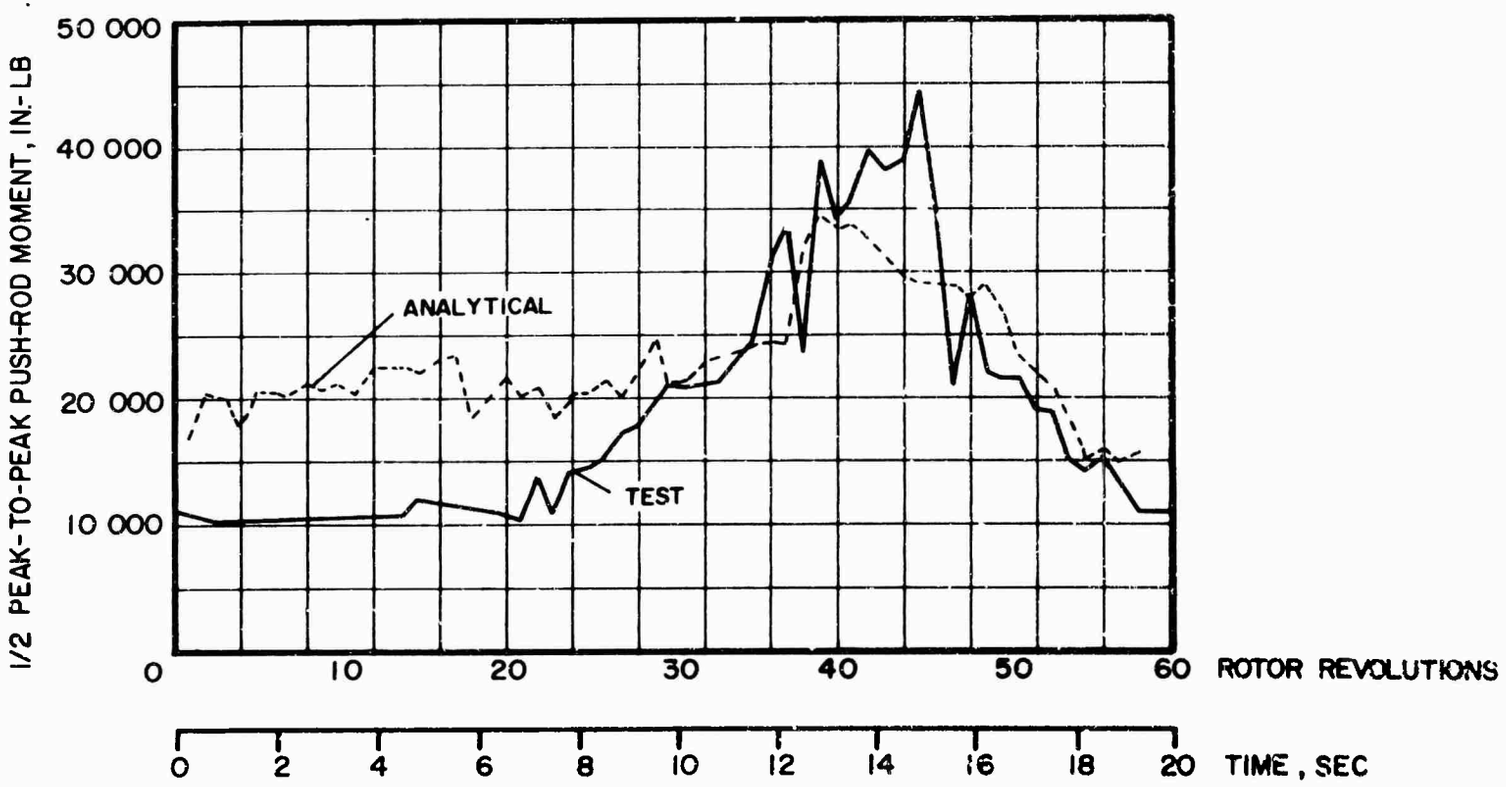

Figure 64. Time History of Push-Rod Moment Amplitude, CH-53A, 150-Knot Right Turn at Varying Angle of Bank.

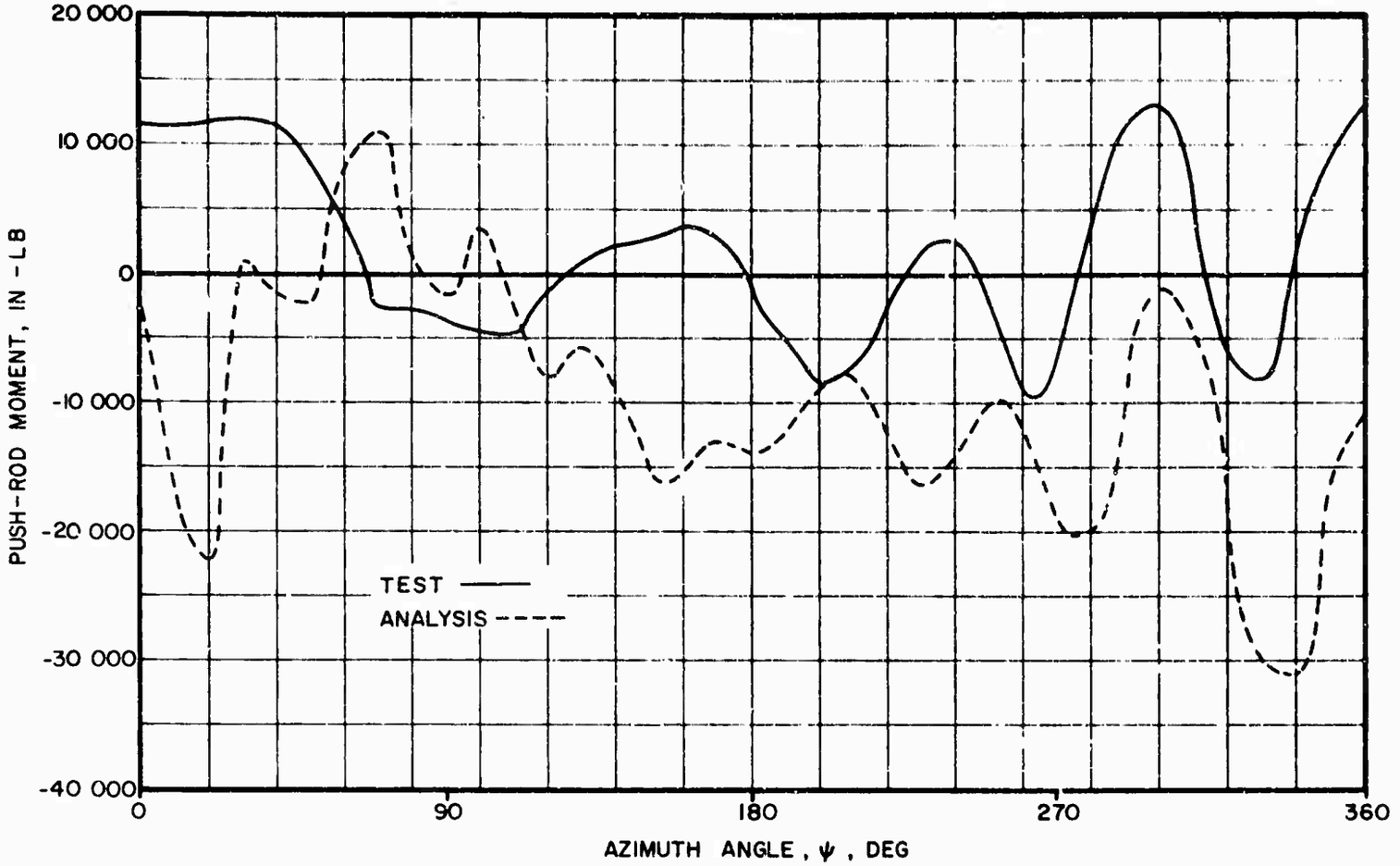

Figure 65. Comparison of Experimental and Analytical Push-Rod Moments for Twentieth Revolution, CH-53A, 150-Knot Right Turn at Varying Angle of Bank.

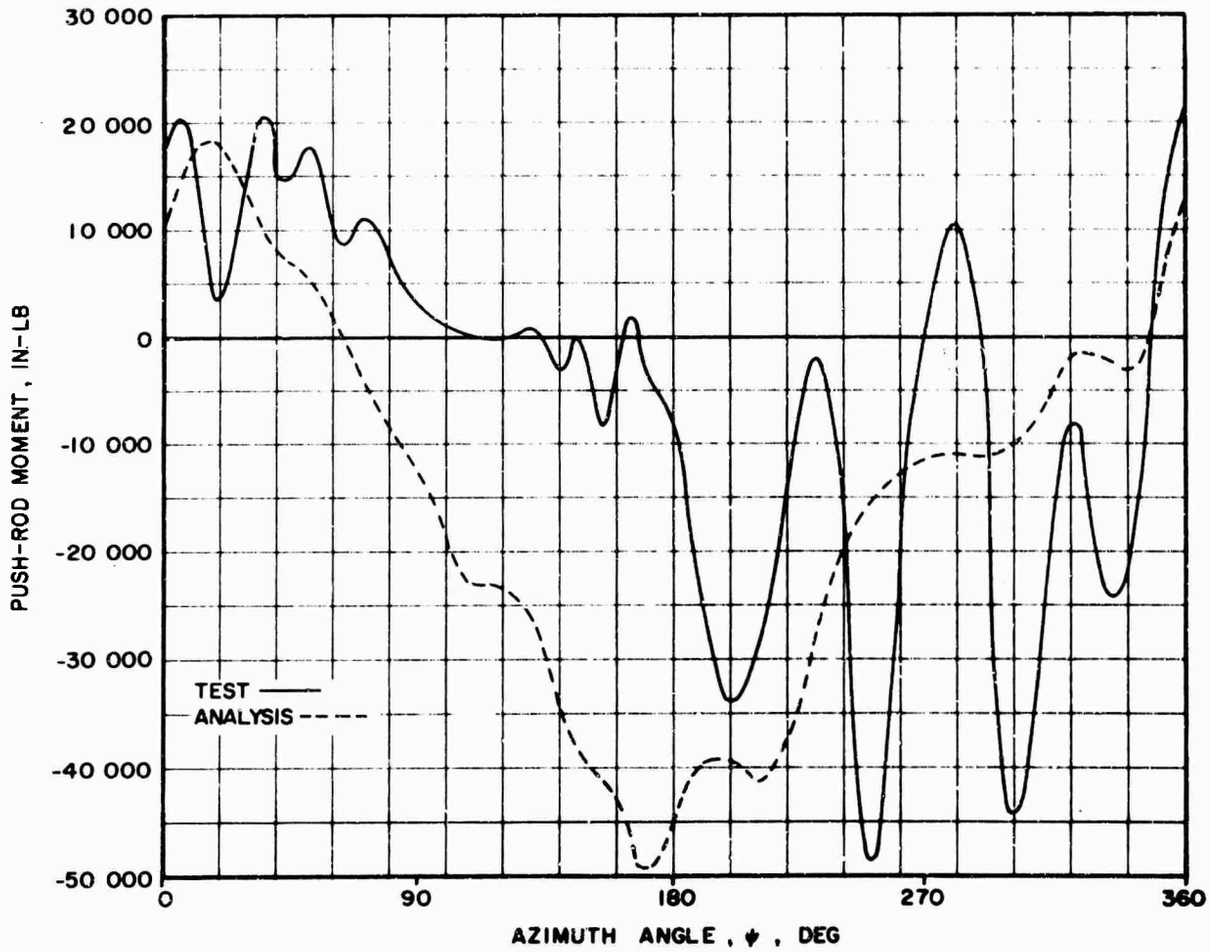

Figure 66. Comparison of Experimental and Analytical Push-Rod Moments for Forty-First Revolution, CH-53A, 150-Knot Right Turn at Varying Angle of Bank.

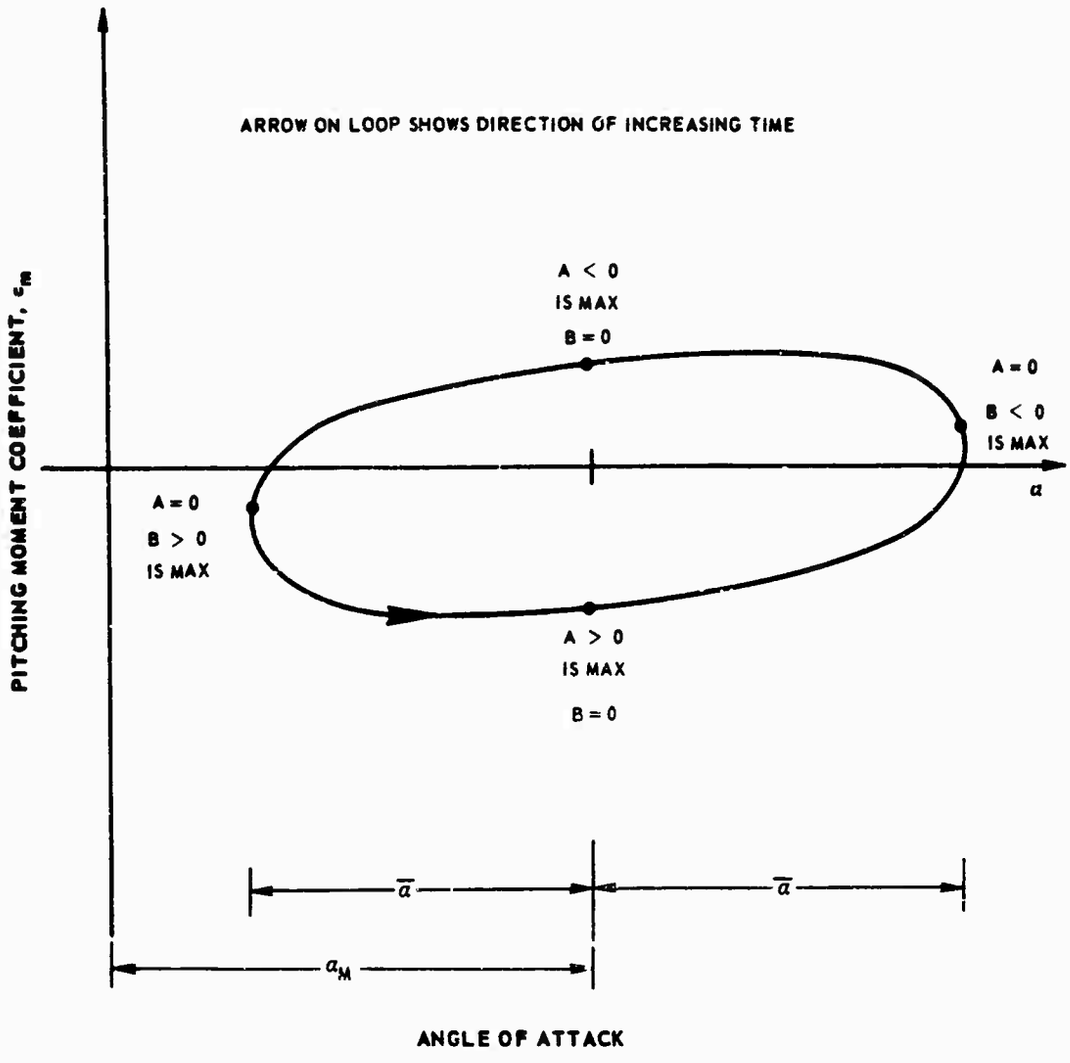

Figure 67. Moment Hysteresis Loop Schematic.

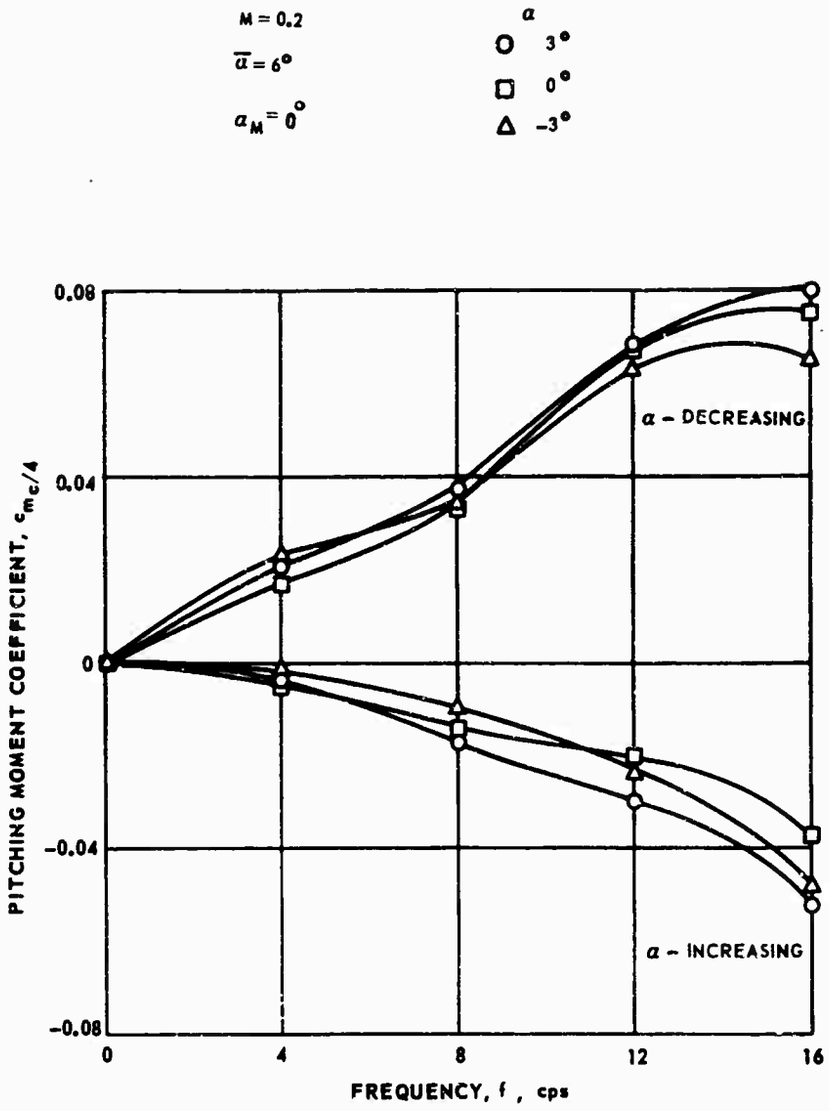

Figure 68. Typical Variation of Pitching Moment Coefficient With Frequency for Mean Angle Below Steady-State Stall Angle.

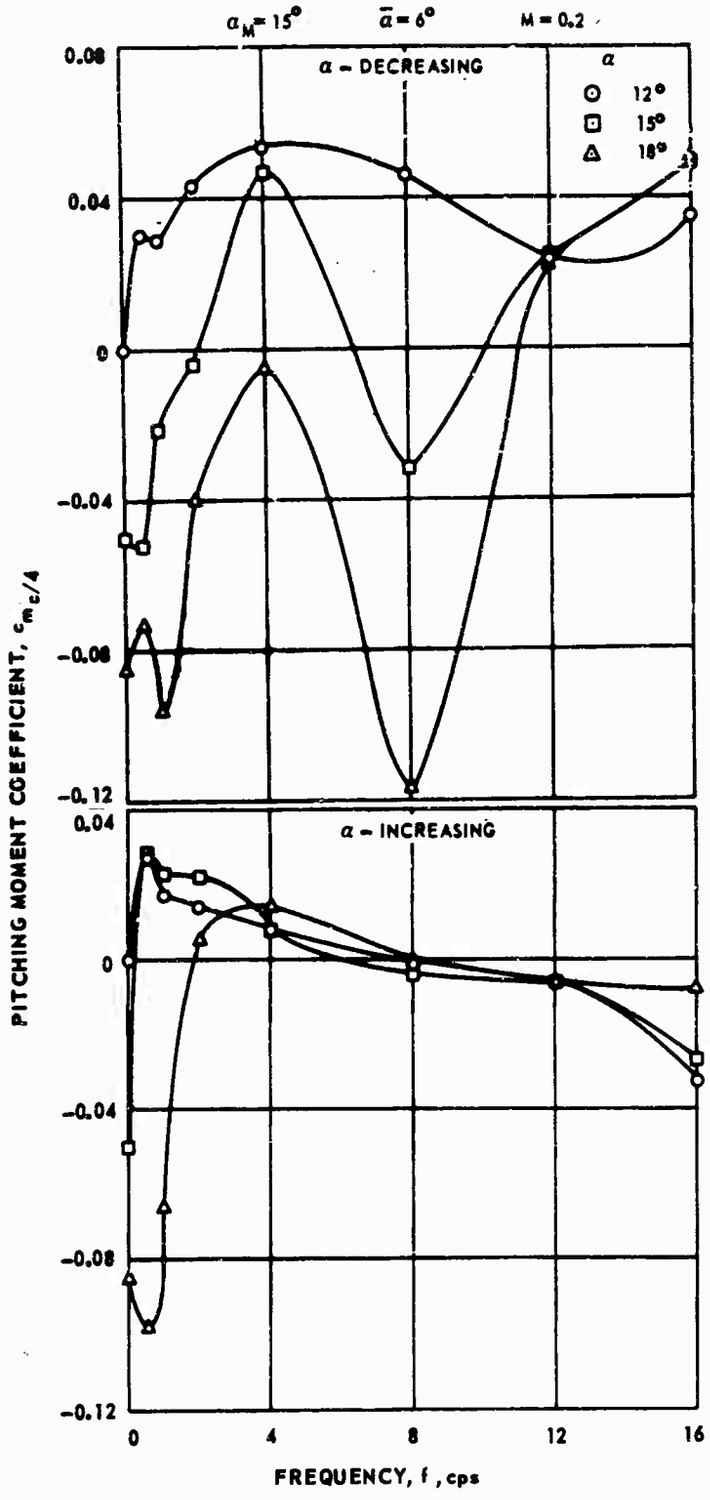

Figure 69. Typical Variation of Pitching Moment Coefficient With Frequency for Mean Angle Above Steady-State Stall Angle.

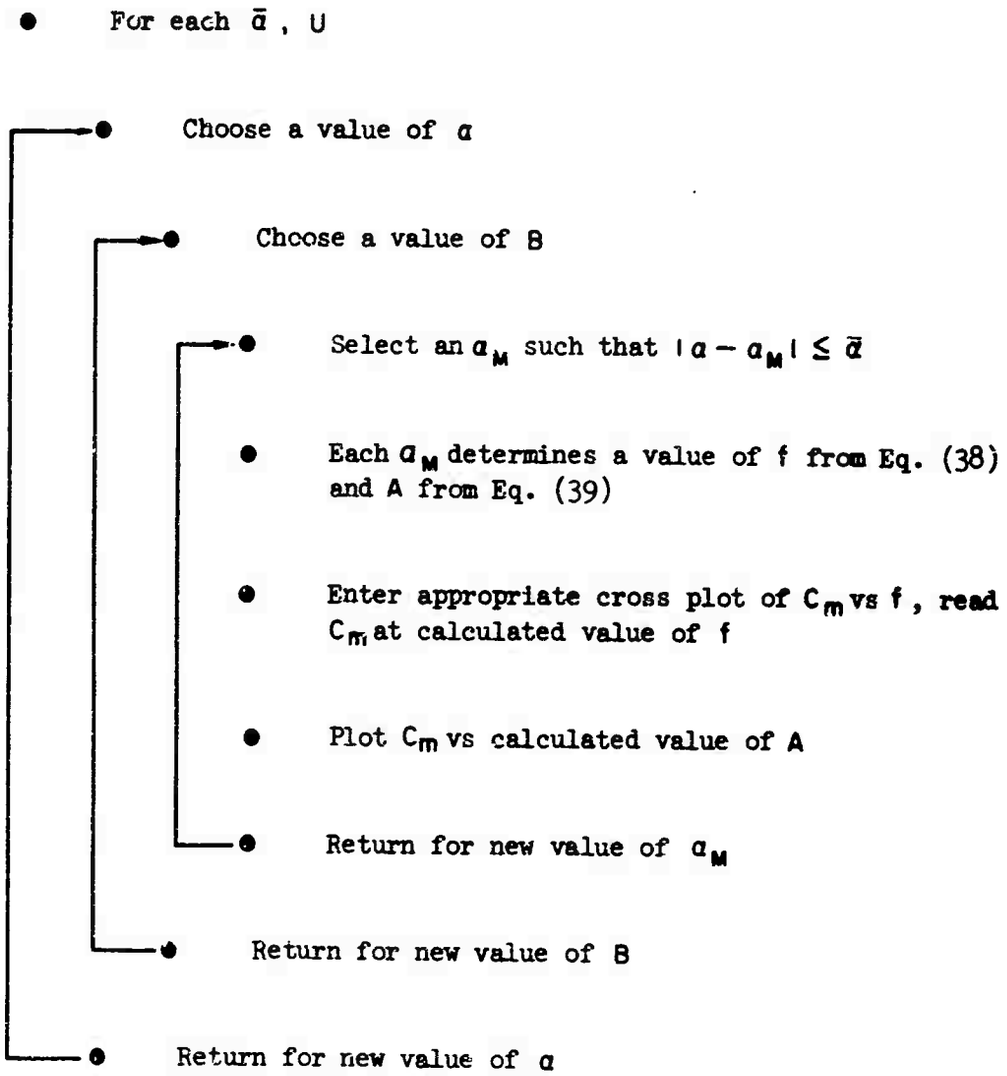

Figure 70. Flow Chart for Data Conversion to α, A, and B Form.

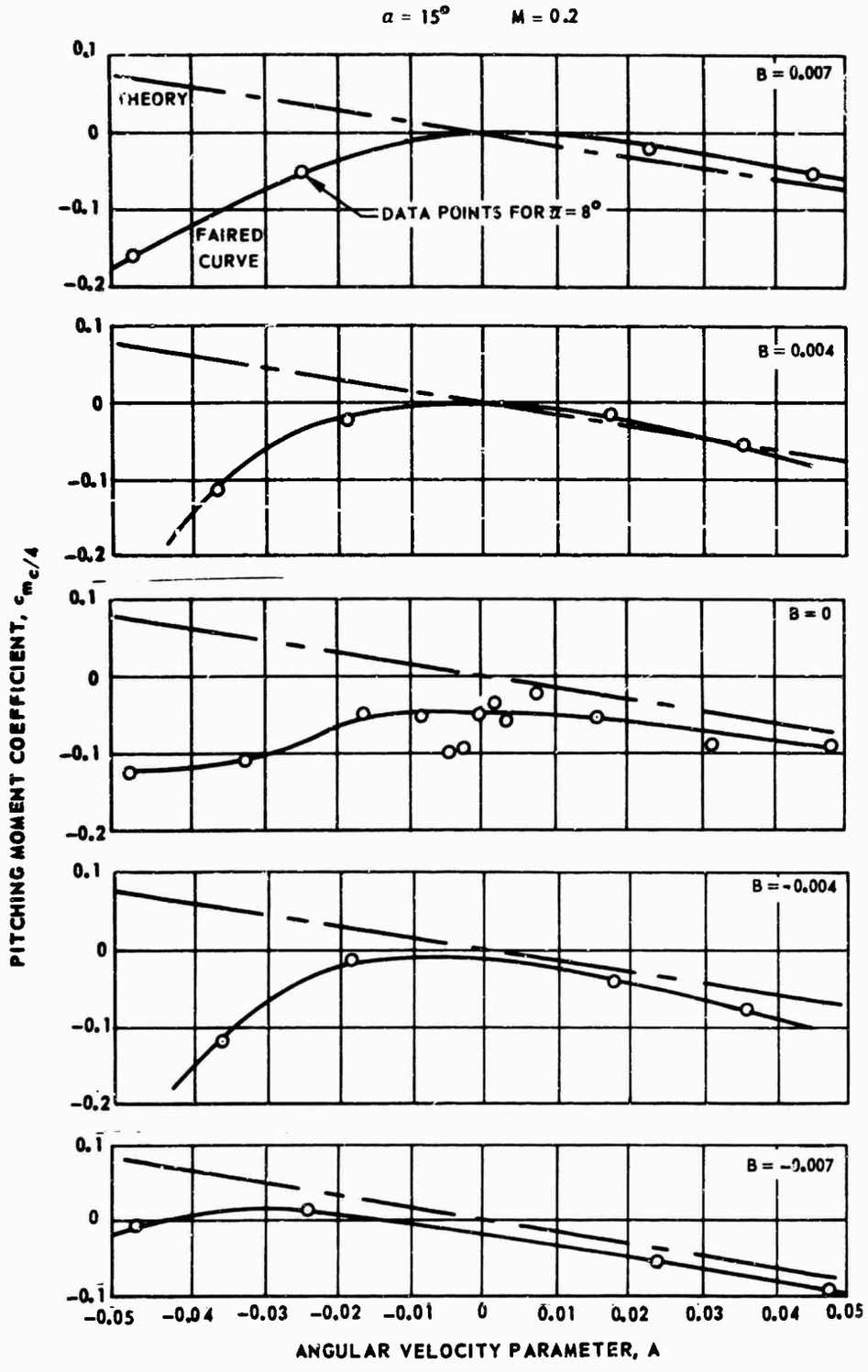

Figure 71. Typical Variation of Pitching Moment Coefficient With Angular Velocity Parameter and Comparison With Theory.

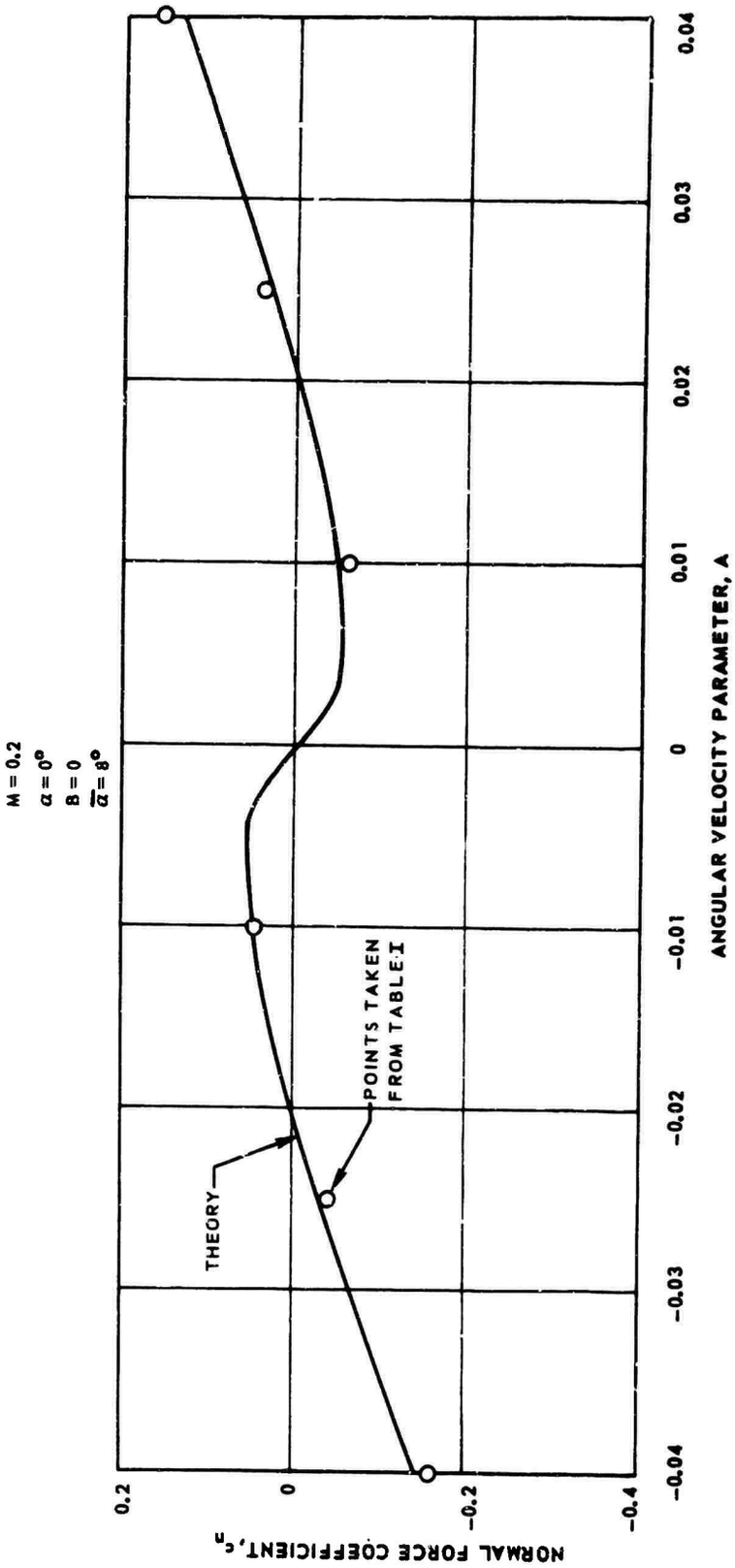

Figure 72. Typical Variation of Normal Force Coefficient With Angular Velocity Parameter and Comparison With Theory.

TABLE I. TABULATION OF UNSTEADY NORMAL FORCE COEFFICIENT C_n FOR M = 0

α = 0 DEGREES

B	A=-.04	-.025	-.01	0	.01	.025	.04
-.01	-.28	-.26	-.20	-.15	-.10	-.04	.05
-.004	-.20	-.17	-.13	-.09	-.07	-.03	.08
-.001	-.15	-.08	.01	-.04	-.02	0.0	.13
0	-.16	-.04	.05	0.0	-.06	.04	.16
.001	-.13	-.05	.02	.04	-.02	.08	.15
.004	-.08	.04	.07	.09	.13	.16	.20
.01	-.06	.04	.10	.16	.22	.27	.27

α = 6 DEGREES

B	A=-.04	-.025	-.01	0	.01	.025	.04
-.01	.34	.34	.38	.40	.45	.55	.67
-.004	.40	.44	.49	.50	.49	.57	.68
-.001	.43	.51	.60	.59	.56	.62	.74
0	.44	.54	.63	.63	.59	.66	.78
.001	.46	.53	.64	.64	.60	.67	.80
.004	.47	.52	.58	.56	.62	.70	.82
.01	.54	.62	.54	.56	.64	.73	.85

α = 8 DEGREES

B	A =-.04	-.025	-.01	0	.01	.025	.04
-.01	.54	.54	.58	.60	.64	.75	.86
-.004	.62	.65	.69	.70	.71	.79	.88
-.001	.62	.68	.78	.80	.79	.83	.93
0	.64	.66	.81	.84	.80	.86	.96
.001	.64	.65	.79	.84	.81	.87	.98
.004	.64	.66	.71	.69	.76	.87	1.01
.01	.68	.70	.65	.67	.73	.82	1.00

TABLE I - CONTINUED

α = 9 DEGREES

B	A=-.04	-.025	-.01	0	.01	.025	.04
-.01	.65	.65	.69	.71	.75	.85	.96
-.004	.72	.75	.79	.80	.82	.89	.98
-.001	.72	.75	.84	.88	.90	.93	1.03
0	.74	.70	.87	.93	.91	.95	1.05
.001	.73	.69	.84	.93	.91	.96	1.06
.004	.71	.71	.75	.74	.83	.96	1.10
.01	.74	.70	.68	.72	.78	.86	1.06

α = 10 DEGREES

B	A=-.04	-.025	-.01	0	.01	.025	.04
-.01	.75	.75	.80	.81	.85	.95	1.05
-.004	.83	.85	.88	.90	.93	1.00	1.07
-.001	.82	.80	.86	.97	1.01	1.03	1.11
0	.81	.76	.86	1.02	1.02	1.04	1.14
.001	.80	.71	.73	1.00	1.00	1.06	1.14
.004	.74	.73	.73	.77	.88	1.02	1.18
.01	.78	.68	.71	.75	.81	.88	1.11

α = 11 DEGREES

B	A=-.04	-.025	-.01	0	.01	.025	.04
-.01	.85	.86	.91	.93	.96	1.05	1.14
-.004	.93	.95	.98	1.00	1.06	1.10	1.17
-.001	.92	.86	.92	1.05	1.11	1.12	1.20
0	.89	.79	.84	1.08	1.12	1.12	1.21
.001	.86	.72	.80	1.02	1.10	1.14	1.21
.004	.76	.71	.70	.80	.93	1.08	1.23
.01	.80	.67	.72	.79	.84	.91	1.14

TABLE I— CONTINUED

α = 12 DEGREES

B	A=-.04	-.025	-.01	0	.01	.025	.04
-.01	.95	.96	1.01	1.03	1.06	1.14	1.23
-.004	1.03	1.06	1.08	1.10	1.17	1.20	1.27
-.001	1.00	.90	.94	1.12	1.22	1.21	1.27
0	.95	.80	.80	1.12	1.24	1.21	1.29
.001	.91	.72	.73	1.02	1.19	1.22	1.27
.004	.77	.68	.65	.81	.97	1.13	1.26
.01	.81	.67	.72	.80	.86	.93	1.17

α = 13 DEGREES

B	A=-.04	-.025	-.01	0	.01	.025	.04
-.01	1.05	1.06	1.11	1.13	1.16	1.24	1.31
-.004	1.14	1.15	1.18	1.20	1.28	1.30	1.35
-.001	1.08	.92	.95	1.17	1.32	1.29	1.34
0	1.00	.80	.76	1.12	1.33	1.28	1.34
.001	.94	.71	.66	1.01	1.26	1.28	1.32
.004	.77	.64	.61	.81	1.01	1.16	1.26
.01	.82	.68	.73	.82	.88	.96	1.19

α = 14 DEGREES

B	A=-.04	-.025	-.01	0	.01	.025	.04
-.01	1.15	1.17	1.21	1.24	1.26	1.32	1.40
-.004	1.24	1.26	1.28	1.30	1.38	1.39	1.44
-.001	1.14	.93	.96	1.22	1.41	1.36	1.40
0	1.04	.78	.74	1.12	1.41	1.35	1.39
.001	.96	.70	.61	1.00	1.32	1.34	1.37
.004	.76	.59	.59	.81	1.04	1.20	1.26
.01	.82	.68	.73	.84	.90	.98	1.21

TABLE I - CONTINUED

α = 15 DEGREES

B	A=-.04	-.025	-.01	0	.01	.025	.04
-.01	1.26	1.28	1.31	1.34	1.36	1.40	1.48
-.004	1.33	1.35	1.38	1.40	1.48	1.48	1.52
-.001	1.18	.92	.96	1.25	1.49	1.44	1.46
0	1.08	.76	.71	1.11	1.48	1.40	1.43
.001	.96	.68	.60	1.00	1.38	1.39	1.40
.004	.76	.57	.59	.82	1.07	1.22	1.25
.01	.81	.69	.74	.86	.92	1.01	1.23

α = 16 DEGREES

B	A=-.04	-.025	-.01	0	.01	.025	.04
-.01	1.36	1.38	1.41	1.44	1.46	1.49	1.56
-.004	1.40	1.43	1.46	1.50	1.58	1.57	1.60
-.001	1.19	.91	.96	1.28	1.57	1.50	1.51
0	1.08	.75	.69	1.10	1.53	1.46	1.46
.001	.95	.65	.60	1.00	1.43	1.43	1.43
.004	.75	.56	.62	.83	1.09	1.24	1.23
.01	.80	.70	.76	.88	.94	1.04	1.24

α = 17 DEGREES

B	A=-.04	-.025	-.01	0	.01	.025	.04
-.01	1.46	1.48	1.51	1.54	1.56	1.58	1.64
-.004	1.39	1.49	1.53	1.58	1.66	1.66	1.67
-.001	1.15	.90	.96	1.28	1.62	1.57	1.55
0	1.04	.74	.70	1.10	1.58	1.53	1.50
.001	.93	.64	.62	1.00	1.46	1.47	1.44
.004	.74	.57	.65	86	1.11	1.25	1.20
.01	.78	.71	.77	.91	.96	1.08	1.25

TABLE I – CONTINUED

α = 18 DEGREES

B	A=-.04	-.025	-.01	0	.01	.025	.04
-.01	1.56	1.59	1.61	1.64	1.66	1.66	1.71
-.004	1.35	1.47	1.58	1.64	1.74	1.74	1.74
-.001	1.08	.89	.95	1.27	1.66	1.64	1.60
0	1.00	.75	.70	1.10	1.60	1.60	1.54
.001	.90	.64	.65	1.00	1.47	1.54	1.47
.004	.73	.60	.68	.88	1.13	1.27	1.22
.01	.76	.72	.79	.93	.99	1.12	1.26

α = 20 DEGREES

B	A=-.04	-.025	-.01	0	.01	.025	.04
-.01	1.77	1.79	1.80	1.84	1.86	1.84	1.87
-.004	1.17	1.25	1.56	1.71	1.87	1.93	1.91
-.001	.90	.84	.93	1.21	1.70	1.82	1.75
0	.84	.73	.75	1.08	1.61	1.73	1.67
.001	.83	.66	.71	1.00	1.47	1.64	1.59
.004	.72	.68	.76	.92	1.16	1.33	1.41
.01	.72	.74	.84	.99	1.06	1.21	1.31

α = 22 DEGREES

B	A=-.04	-.025	-.01	0	.01	.025	.04
-.01	1.91	1.95	1.99	2.02	2.06	2.05	2.07
-.004	1.07	1.08	1.47	1.70	1.95	2.13	2.12
-.001	.82	.78	.92	1.16	1.71	1.98	1.98
0	.78	.72	.79	1.07	1.58	1.85	1.91
.001	.76	.70	.79	1.02	1.42	1.72	1.84
.004	.72	.75	.85	.99	1.18	1.38	1.61
.01	.72	.81	.92	1.04	1.14	1.31	1.41

TABLE I—CONCLUDED

α = 24 DEGREES

B	A=-.04	-.025	-.01	0	.01	.025	.04
-.01	1.85	1.99	2.16	2.20	2.23	2.28	2.25
-.004	1.05	1.05	1.35	1.60	1.96	2.27	2.27
-.001	.86	.80	.91	1.15	1.58	1.95	2.10
0	.83	.78	.84	1.08	1.44	1.84	2.04
.001	.78	.76	.85	1.05	1.35	1.69	1.95
.004	.74	.81	.94	1.04	1.20	1.40	1.68
.01	.76	.93	1.05	1.09	1.25	1.37	1.50

α = 26 DEGREES

B	A=-.04	-.025	-.01	0	.01	.025	.04
-.01	1.67	1.80	2.02	2.14	2.21	2.34	2.35
-.004	1.06	1.07	1.22	1.42	1.83	2.17	2.32
-.001	.90	.87	.94	1.19	1.48	1.79	2.01
0	.86	.85	.90	1.14	1.40	1.64	1.84
.001	.82	.82	.91	1.11	1.34	1.54	1.68
.004	.76	.85	.99	1.06	1.20	1.35	1.52
.01	.84	.96	1.02	1.07	1.22	1.33	1.56

α = 27 DEGREES

B	A=-.04	-.025	-.01	0	.01	.025	.04
-.01	1.55	1.58	1.69	1.88	2.07	2.30	2.38
-.004	1.06	1.09	1.18	1.36	1.70	2.03	2.31
-.001	.92	.91	.98	1.22	1.47	1.72	1.91
0	.86	.88	.94	1.18	1.42	1.57	1.75
.001	.85	.85	.94	1.14	1.36	1.49	1.63
.004	.79	.85	.96	1.03	1.19	1.29	1.46
.01	.89	.90	.95	1.04	1.14	1.27	1.59

TABLE II. TABULATION OF UNSTEADY PITCHING MOMENT COEFFICIENT $C_{m_{c/4}}$ FOR M = 0

α = 0 THROUGH 6 DEGREES

B	A=-.04	-.025	-.01	0	.01	.025	.04
-.01	.069	.045	.022	.006	-.010	-.033	-.057
-.007	.067	.043	.020	.004	-.012	-.035	-.059
-.004	.065	.042	.018	.002	-.013	-.037	-.061
-.001	.063	.040	.016	.001	-.015	-.039	-.062
0	.063	.039	.016	0.0	-.016	-.039	-.063
.001	.062	.039	.015	-.001	-.016	-.040	-.063
.004	.061	.037	.013	-.002	-.018	-.042	-.065
.007	.059	.035	.012	-.004	-.020	-.043	-.067
.01	.057	.033	.010	-.006	-.022	-.045	-.069

α = 7 DEGREES

B	A=-.04	-.025	-.01	0	.01	.025	.04
-.01	.066	.043	.020	.003	-.013	-.035	-.058
-.007	.064	.040	.016	.001	-.013	-.038	-.062
-.004	.057	.035	.015	0.0	-.015	-.039	-.065
-.001	.056	.033	.010	-.002	-.018	-.043	-.065
0	.050	.031	.011	0.0	-.015	-.041	-.067
.001	.050	.030	.010	-.003	-.018	-.046	-.066
.004	.035	.020	.010	-.004	-.020	-.044	-.067
.007	.016	.013	.007	-.008	-.023	-.051	-.074
.01	-.010	-.002	0.	-.008	-.026	-.050	-.076

α = 8 DEGREES

B	A=-.04	-.025	-.01	0	.01	.025	.04
-.01	.059	.040	.016	0.0	-.015	-.040	-.061
-.007	.056	.034	.010	-.002	-.016	-.043	-.065
-.004	.045	.025	.010	-.005	-.017	-.043	-.067
-.001	.045	.024	0.0	-.005	-.021	-.045	-.068
0	.031	.020	0.0	0.0	-.016	-.045	-.071
.001	.028	.010	0.0	-.007	-.024	-.050	-.070
.004	-.010	-.016	.007	-.006	-.020	-.056	-.070
.007	-.015	-.007	0.0	-.010	-.023	-.054	-.074
.01	-.030	-.025	-.010	-.012	-.028	-.052	-.080

TABLE II – CONTINUED

α = 9 DEGREES

B	A=-.04	-.025	-.01	0	.01	.025	.04
-.01	.048	.035	.010	-.003	-.018	-.045	-.067
-.007	.044	.026	.006	-.007	-.020	-.047	-.071
-.004	.038	.020	.005	-.011	-.021	-.048	-.073
-.001	.035	.015	-.005	-.012	-.024	-.050	-.074
0	.020	.007	-.005	0.0	-.016	-.049	-.076
.001	.018	-.025	-.005	-.012	-.034	-.055	-.074
.004	-.028	-.027	0.0	-.009	-.020	-.049	-.074
.007	-.034	-.030	-.007	-.011	-.024	-.054	-.074
.01	-.054	-.044	-.021	-.018	-.029	-.053	-.080

α = 10 DEGREES

B	A=-.04	-.025	-.01	0	.01	.025	.04
-.01	.039	.029	.004	-.007	-.024	-.049	-.073
-.007	.038	.023	.002	-.011	-.024	-.050	-.075
-.004	.035	.016	0.0	-.016	-.027	-.053	-.077
-.001	.025	.010	-.009	-.017	-.027	-.054	-.080
0	.005	-.004	-.015	0.0	-.017	-.049	-.081
.001	.016	-.040	0.0	-.020	-.041	-.057	-.081
.004	-.047	-.035	-.002	-.010	-.020	-.050	-.076
.007	-.054	-.045	-.015	-.010	-.025	-.053	-.075
.01	-.075	-.060	-.033	-.025	-.028	-.052	-.078

α = 11 DEGREES

B	A=-.04	-.025	-.01	0	.01	.025	.04
-.01	.033	.023	-.001	-.012	-.027	-.053	-.077
-.007	.036	.021	.001	-.014	-.027	-.053	-.077
-.004	.032	.015	-.003	-.018	-.032	-.055	-.080
-.001	.010	.002	-.012	-.020	-.030	-.056	-.084
0	-.020	-.014	-.025	0.0	-.020	-.054	-.087
.001	-.005	-.035	0.0	-.023	-.044	-.071	-.086
.004	-.070	-.040	-.005	-.010	-.020	-.050	-.078
.007	-.078	-.053	-.025	-.022	0.025	-.052	-.075
.01	-.082	-.072	-.050	-.035	-.027	-.048	-.078

TABLE II - CONTINUED

α = 12 DEGREES

B	A=-.04	-.025	-.01	0	.01	.025	.04
-.01	.031	.016	-.003	-.015	-.030	-.054	-.080
-.007	.035	.020	0.0	-.015	-.030	-.055	-.080
-.004	.030	.015	-.005	-.020	-.035	-.057	-.083
-.001	-.008	-.010	-.013	-.022	-.031	-.058	-.085
0	-.040	-.028	-.033	0.0	-.023	-.057	-.089
.001	-.011	-.014	.007	-.019	-.043	-.087	-.088
.004	-.090	-.040	-.005	-.007	-.020	-.048	-.079
.007	-.096	-.062	-.028	-.025	-.023	-.038	-.072
.01	-.100	-.080	-.050	-.040	-.025	-.040	-.065

α = 13 DEGREES

B	A=-.04	-.025	-.01	0	.01	.025	.04
-.01	.034	.019	0.0	-.015	-.030	-.055	-.080
-.007	.034	.020	0.0	-.016	-.030	-.055	-.082
-.004	.011	.014	-.007	-.020	-.038	-.060	-.085
-.001	-.036	-.046	-.018	-.023	-.030	-.060	-.085
0	-.050	-.050	-.041	0.0	-.028	-.060	-.087
.001	-.050	-.031	.010	0.0	-.035	-.084	-.084
.004	-.100	-.042	-.005	0.0	-.015	-.045	-.079
.007	-.108	-.070	-.027	-.010	-.015	-.033	-.060
.01	-.108	-.072	-.040	-.021	-.020	-.037	-.057

α = 14 DEGREES

B	A=-.04	-.025	-.01	0	.01	.025	.04
-.01	.032	.022	.003	-.016	-.031	-.055	-.083
-.007	.025	.020	0.0	-.016	-.032	-.057	-.083
-.004	.030	0.0	-.010	-.021	-.038	-.060	-.087
-.001	-.080	-.095	-.032	-.026	-.032	-.056	-.085
0	-.090	-.072	-.047	-.005	-.036	-.060	-.083
.001	-.104	-.046	.010	.006	-.028	-.082	-.080
.004	-.112	-.046	-.007	0.0	-.012	-.042	-.076
.007	-.119	-.070	-.026	-.014	-.017	-.032	-.057
.01	-.106	-.057	-.036	-.020	-.020	-.023	-.050

TABLE II – CONTINUED

α = 15 DEGREES

B	A=-.04	-.025	-.01	0	.01	.025	.04
-.01	.020	.022	0.0	-.017	-.037	-.060	-.084
-.007	.008	.015	-.005	-.016	-.035	-.062	-.085
-.004	-.113	-.055	-.013	-.020	-.034	-.060	-.092
-.001	-.117	-.115	-.050	-.031	-.032	-.063	-.088
0	-.125	-.089	-.050	-.050	-.045	-.056	-.077
.001	-.127	-.040	.006	.007	-.015	-.070	-.078
.004	-.135	-.057	-.020	-.012	-.014	-.035	-.078
.007	-.120	-.060	-.035	-.025	-.027	-.031	-.045
.01	-.095	-.055	-.040	-.028	-.018	-.014	-.028

α = 16 DEGREES

B	A=-.04	-.025	-.01	0	.01	.025	.04
-.01	.003	.015	-.002	-.017	-.036	-.060	-.087
-.007	-.065	-.020	-.017	-.016	-.035	-.063	-.088
-.004	-.127	-.090	-.018	-.020	-.032	-.063	-.088
-.001	-.145	-.125	-.067	-.038	-.034	-.066	-.109
0	-.145	-.095	-.054	-.072	-.052	-.054	-.070
.001	-.140	-.041	.001	0.0	-.014	-.067	-.062
.004	-.130	-.061	-.036	-.030	-.027	-.035	-.052
.007	-.102	-.074	-.070	-.076	-.050	-.033	-.031
.01	-.081	-.067	-.060	-.049	-.036	-.027	-.010

α = 17 DEGREES

B	A=-.04	-.025	-.01	0	.01	.025	.04
-.01	-.030	-.011	-.010	-.020	-.033	-.060	-.085
-.007	-.105	-.085	-.034	-.020	-.036	-.069	-.093
-.004	-.145	-.120	-.055	-.020	-.034	-.061	-.100
-.001	-.164	-.135	-.068	-.041	-.034	-.074	-.106
0	-.157	-.096	-.054	-.080	-.057	-.051	-.063
.001	-.145	-.056	-.007	-.025	-.016	-.043	-.054
.004	-.126	-.076	-.055	-.055	-.060	-.048	-.039
.007	-.090	-.091	-.097	-.106	-.100	-.074	-.031
.01	-.079	-.068	-.070	-.061	-.075	-.065	-.030

TABLE II – CONTINUED

α = 18 DEGREES

B	A=-.04	-.025	-.01	0	.01	.025	.04
-.01	-.065	-.045	-.027	-.030	-.045	-.063	-.084
-.007	-.127	-.110	-.070	-.062	-.050	-.070	-.095
-.004	-.180	-.145	-.083	-.057	-.052	-.064	-.110
-.001	-.177	-.159	-.086	-.045	-.041	-.074	-.093
0	-.165	-.093	-.055	-.085	-.058	-.048	-.057
.001	-.145	-.065	-.017	-.045	-.023	-.025	-.047
.004	-.106	-.086	-.073	-.066	-.074	-.060	-.026
.007	-.100	-.092	-.091	-.101	-.102	-.092	-.047
.01	-.067	-.062	-.074	-.068	-.081	-.071	-.050

α = 19 DEGREES

B	A=-.04	-.025	-.01	0	.01	.025	.04
-.01	-.101	-.063	-.046	-.045	-.055	-.066	-.084
-.007	-.160	-.123	-.080	-.066	-.050	-.074	-.095
-.004	-.225	-.185	-.105	-.085	-.067	-.080	-.107
-.001	-.183	-.152	-.105	-.072	-.055	-.060	-.081
0	-.161	-.087	-.054	-.090	-.057	-.045	-.055
.001	-.144	-.070	-.030	-.065	-.032	-.019	-.060
.004	-.104	-.086	-.084	-.075	-.089	-.100	-.050
.007	-.091	-.077	-.085	-.105	-.100	-.103	-.063
.01	-.060	-.061	-.079	-.075	-.091	-.090	-.063

α = 20 DEGREES

B	A=-.04	-.025	-.01	0	.01	.025	.04
-.01	-.143	-.094	-.082	-.074	-.060	-.070	-.082
-.007	-.215	-.195	-.110	-.078	-.080	-.075	-.092
-.004	-.249	-.241	-.160	-.113	-.090	-.086	-.098
-.001	-.182	-.115	-.117	-.110	-.075	-.052	-.073
0	-.153	-.080	-.052	-.095	-.058	-.041	-.055
.001	-.137	-.070	-.040	-.082	-.067	-.025	-.063
.004	-.100	-.081	-.091	-.090	-.113	-.141	-.150
.007	-.076	-.075	-.086	-.116	-.130	-.128	-.082
.01	-.069	-.070	-.088	-.100	-.110	-.120	-.076

TABLE II – CONTINUED

α = 21 DEGREES

B	A=-.04	-.025	-.01	0	.01	.025	.04
-.01	-.192	-.162	-.140	-.120	-.100	-.075	-.080
-.007	-.260	-.260	-.223	-.151	-.124	-.077	-.090
-.004	-.240	-.240	-.260	-.195	-.127	-.088	-.083
-.001	-.161	-.093	-.124	-.150	-.135	-.063	-.064
0	-.143	-.073	-.045	-.100	-.065	-.042	-.060
.001	-.120	-.072	-.056	-.093	-.103	-.050	-.070
.004	-.095	-.073	-.095	-.112	-.140	-.162	-.149
.007	-.073	-.077	-.103	-.124	-.148	-.173	-.107
.01	-.071	-.077	-.104	-.118	-.133	-.150	-.140

α = 22 DEGREES

B	A=-.04	-.025	-.01	0	.01	.025	.04
-.01	-.244	-.228	-.186	-.157	-.120	-.084	-.086
-.007	-.300	-.295	-.275	-.208	-.140	-.085	-.095
-.004	-.211	-.217	-.260	-.220	-.172	-.091	-.060
-.001	-.140	-.095	-.123	-.195	-.175	-.080	-.050
0	-.140	-.092	-.049	-.106	-.135	-.095	-.094
.001	-.120	-.076	-.074	-.111	-.128	-.130	-.124
.004	-.090	-.082	-.100	-.118	-.154	-.195	-.151
.007	-.081	-.088	-.122	-.140	-.160	-.190	-.180
.01	-.080	-.100	-.132	-.145	-.160	-.170	-.180

α = 23 DEGREES

B	A=-.04	-.025	-.01	0	.01	.025	.04
-.01	-.310	-.255	-.230	-.200	-.150	-.115	-.094
-.007	-.294	-.275	-.260	-.260	-.211	-.115	-.095
-.004	-.190	-.206	-.220	-.255	-.195	-.088	-.040
-.001	-.128	-.100	-.126	-.195	-.205	-.140	-.111
0	-.155	-.107	-.049	-.112	-.145	-.143	-.178
.001	-.158	-.104	-.095	-.125	-.130	-.191	-.237
.004	-.089	-.098	-.127	-.130	-.155	-.214	-.224
.007	-.088	-.112	-.140	-.150	-.169	-.196	-.215
.01	-.083	-.120	-.150	-.150	-.160	-.188	-.205

TABLE II – CONTINUED

α = 24 DEGREES

B	A=-.04	-.025	-.01	0	.01	.025	.04
-.01	-.340	-.275	-.240	-.225	-.160	-.108	-.100
-.007	-.280	-.270	-.250	-.225	-.150	-.100	-.060
-.004	-.205	-.215	-.200	-.185	-.160	-.085	-.025
-.001	-.123	-.120	-.130	-.185	-.232	-.250	-.258
0	-.157	-.120	-.050	-.118	-.150	-.275	-.255
.001	-.148	-.118	-.118	-.147	-.142	-.185	-.255
.004	-.092	-.125	-.135	-.130	-.160	-.214	-.250
.007	-.100	-.142	-.125	-.105	-.154	-.213	-.235
.01	-.113	-.120	-.134	-.120	-.150	-.200	-.245

α = 25 DEGREES

B	A=-.04	-.025	-.01	0	.01	.025	.04
-.01	-.300	-.295	-.252	-.250	-.180	-.105	-.068
-.007	-.225	-.266	-.285	-.234	-.172	-.092	-.075
-.004	-.207	-.200	-.235	-.225	-.187	-.098	-.080
-.001	-.120	-.138	-.133	-.180	-.177	-.150	-.273
0	-.155	-.123	-.058	-.127	-.157	-.273	-.281
.001	-.120	-.107	-.145	-.172	-.166	-.201	-.269
.004	-.105	-.144	-.135	-.130	-.150	-.207	-.255
.007	-.133	-.120	-.090	-.142	-.140	-.193	-.266
.01	-.125	-.106	-.130	-.150	-.175	-.210	-.242

α = 26 DEGREES

B	A=-.04	-.025	-.01	0	.01	.025	.04
-.01	-.300	-.300	-.300	-.295	-.247	-.147	-.050
-.007	-.270	-.255	-.325	-.345	-.273	-.120	-.113
-.004	-.210	-.167	-.245	-.290	-.225	-.145	-.133
-.001	-.117	-.117	-.125	-.193	-.290	-.327	-.304
0	-.140	-.125	-.072	-.133	-.158	-.259	-.210
.001	-.108	-.125	-.185	-.195	-.165	-.210	-.284
.004	-.150	-.135	-.120	-.125	-.135	-.200	-.260
.007	-.125	-.095	-.100	-.162	-.123	-.173	-.258
.01	-.110	-.112	-.145	-.182	-.197	-.228	-.253

TABLE II - CONCLUDED

α = 27 DEGREES

B	A=-.04	-.025	-.01	0	.01	.025	.04
-.01	-.300	-.300	-.300	-.300	-.270	-.175	-.040
-.007	-.270	-.235	-.215	-.210	-.200	-.175	-.147
-.004	-.275	-.195	-.170	-.185	-.210	-.265	-.340
-.001	-.118	-.080	-.127	-.200	-.268	-.350	-.315
0	-.105	-.125	-.090	-.145	-.155	-.240	-.306
.001	-.125	-.120	-.215	-.210	-.197	-.210	-.293
.004	-.162	-.092	-.090	-.105	-.125	-.173	-.270
.007	-.097	-.088	-.110	-.130	-.150	-.190	-.238
.01	-.113	-.158	-.207	-.237	-.240	-.300	-.322

TABLE III. SCALING PARAMETER VALUES FOR BOEING AIRFOIL

Mach Number	Normal Force Stall Angle	Normal Force Coef. at Stall	Pitching Moment Stall Angle
M	α_{sn}, deg	$C_{n_{STALL,SS}}$	α_{sm}, deg
0.4	8.4	0.85	10.0
0.6	4.8	0.53	7.0

TABLE IV. SCALING PARAMETER VALUES FOR UAC AIRFOIL

Mach Number M	Normal Force Stall Angle α_{sn}, deg	Normal Force Coef. at Stall $C_{n_{STALL,SS}}$	Original Pitching Moment Stall Angle α_{sm}, deg	Revised Pitching Moment Stall Angle α_{sm}, deg
0	10.0	1.05	13.5	13.5
0.2	10.0	1.05	13.5	13.5
0.3	10.4	1.09	13.0	12.5
0.4	8.4	0.85	12.3	11.0
0.5	6.5	0.69	11.5	9.0
0.6	4.8	0.53	10.6	7.0
0.7	2.9	0.37	10.6	7.0
0.8	2.0	0.23	10.6	7.0
0.85	2.0	0.23	10.6	7.0

TABLE V. BLADE DESIGNS

Design	Twist Rate, θ_1, deg	Torsional Frequency, $\bar{\omega}_{\theta_1}$	Chordwise cg Location, $y_{10_{cg}}/c$
1. Reference Blade	-4	8.2P	0.25
2. High-Twist Blade	-8	8.2P	0.25
3. Low-Frequency Blade	-4	4P	0.25
4. Aft cg Blade	-4	8.2P	0.30

TABLE VI. REFERENCE BLADE CHARACTERISTICS

1.	Chord (ft)	1.52
2.	Twist rate (deg)	-4
3.	Radius (ft)	31
4.	Flap - lag hinge offset	0.034
5.	Tip speed (ft/sec)	662
6.	Pitch-flap coupling ratio	0.17
7.	Flatwise bending frequency ratios	2.68P, 4.87P, 7.68P
8.	Edgewise bending frequency ratios	3.44P, 9.0P
9.	Torsional frequency ratios	8.22P, 21.96P
10.	Control system stiffness (ft-lb/rad)	1.2×10^6
11.	Nominal section weight (lb/in.)	0.5
12.	Nominal section flatwise stiffness ($lb/in.^2$)	2.2×10^7
13.	Nominal section edgewise stiffness ($lb/in.^2$)	24×10^7
14.	Nominal section torsional stiffness ($lb\text{-}in.^2$)	2.9×10^7
15.	Nominal section torsional inertia ($lb\text{-}sec^2$)	0.024
16.	Section cg (percent chord)	25

TABLE VII. SUMMARY OF S-61F FLIGHT TEST CASES USED FOR CORRELATION

Case Number	Velocity, Knots	Rotor Axial Force, Pounds	Nominal Advance Ratio	Nominal Thrust Coefficient-Solidity Ratio
35	160.80	5060	.410	.0200
36	166.50	13300	.425	.0543
42	186.45	8630	.476	.0351
43	185.97	14200	.474	.0579
44	184.07	4290	.469	.0175
45	186.92	9870	.477	.0402

LITERATURE CITED

1. Ham, N. D., AN EXPERIMENTAL INVESTIGATION OF STALL FLUTTER, Journal of the American Helicopter Society, Vol. 7, January 1962, pp. 3-16.

2. Carta, F. O., and Niebanck, C. F., PREDICTION OF ROTOR INSTABILITY AT HIGH FORWARD SPEEDS, VOLUME III, STALL FLUTTER, USAAVLABS Technical Report 68-18C, U. S. Army Aviation Materiel Laboratories, Fort Eustis, Virginia, February 1969, AD 687322.

3. Ham, N. D., and Young, M. I., TORSIONAL OSCILLATION OF HELICOPTER BLADES DUE TO STALL, Journal of Aircraft, Vol. 3, No. 3, May-June 1966, pp. 218-223.

4. Niebanck, C. F., A COMPARISON OF DYNAMICALLY SCALED MODEL ROTOR TEST DATA WITH DISCRETE AZIMUTH AEROELASTIC STABILITY THEORY, Proceedings of the 25th Annual National Forum of the American Helicopter Society, Paper No. 341, May 1969. (Also, see published comments on paper No. 341 by N. D. Ham.)

5. Arcidiacono, P. J., AERODYNAMIC CHARACTERISTICS OF A MODEL HELICOPTER ROTOR OPERATING UNDER NOMINALLY STALLED CONDITIONS IN FORWARD FLIGHT, Journal of the American Helicopter Society, Vol. 9, No. 3, July 1964.

6. Rabbott, J. P., COMPARISON OF THEORETICAL AND EXPERIMENTAL MODEL HELICOPTER ROTOR PERFORMANCE IN FORWARD FLIGHT, TCREC Technical Report 61-103, U. S. Army Transportation Research Command, Fort Eustis, Virginia, July 1961.

7. McCloud III, J. L., and McCullough, G. B., COMPARISON OF CALCULATED AND MEASURED STALL BOUNDARIES OF A HELICOPTER ROTOR AT ADVANCE RATIOS FROM 0.3 to 0.4, NASA TN D-73, September 1959.

8. Sweet, G. E., and Jenkins, J. L., RESULTS OF WIND TUNNEL MEASUREMENTS ON A HELICOPTER ROTOR OPERATING AT EXTREME THRUST COEFFICIENTS AND HIGH TIP SPEED RATIOS, Journal of the American Helicopter Society, Vol. 8, No. 3, July 1963.

9. Harris, F. D., and Pruyn, R. R., BLADE STALL - HALF FACT, HALF FICTION, Proceedings of the 23rd Annual National Forum of the American Helicopter Society, Paper No. 101, May 1967.

10. Carta, F. O., EXPERIMENTAL INVESTIGATION OF THE UNSTEADY AERODYNAMIC CHARACTERISTICS OF AN NACA 0012 AIRFOIL, United Aircraft Research Laboratories Report M-1283-1, August 1960.

11. Liiva, J., et al., TWO-DIMENSIONAL TESTS OF AIRFOILS OSCILLATING NEAR STALL, Vol. I Summary and Evaluation of Results, USAAVLABS TR 68-13A, U. S. Army Aviation Materiel Laboratories, Fort Eustis, Virginia, April 1968, AD 670957.

12. Bisplinghoff, R. L., Ashley, H., and Halfman, R. L., AEROELASTICITY, Addison-Wesley Publishing Company, Cambridge, Massachusetts, 1955,

13. Arcidiacono, P. J., PREDICTION OF ROTOR INSTABILITY AT HIGH FORWARD SPEEDS, VOLUME I, STEADY FLIGHT DIFFERENTIAL EQUATIONS OF MOTION FOR A FLEXIBLE HELICOPTER BLADE WITH CHORDWISE MASS UNBALANCE, USAAVLABS Technical Report 68-18A, U. S. Army Aviation Materiel Laboratories, Fort Eustis, Virginia, February 1969, AD 685860.

14. Cooper, D., Hansen, K., and Kaplita, T., SINGLE ROTOR HELICOPTER DYNAMICS FOLLOWING POWER FAILURE AT HIGH SPEEDS, USAAVLABS Technical Report 66-30, U. S. Army Aviation Materiel Laboratories, Fort Eustis, Virginia, June 1966.

15. Piziali, R. A., and DuWaldt, F. A., A METHOD FOR COMPUTING ROTARY WING AIRLOAD DISTRIBUTIONS IN FORWARD FLIGHT, TCREC Technical Report 62-44, U. S. Army Transportation Research Command, Fort Eustis, Virginia, November 1962.

16. Miller, R. H., UNSTEADY AIRLOADS ON HELICOPTER ROTOR BLADES, Fourth Cierva Memorial Lecture, October 1963.

17. Landgrebe, A. J., AN ANALYTICAL METHOD FOR PREDICTING ROTOR WAKE GEOMETRY, AIAA/AHS VTOL Research, Design, and Operations Meeting, February 1969.

18. Tanner, W. H., CHARTS FOR ESTIMATING ROTARY WING PERFORMANCE IN HOVER AND AT HIGH FORWARD SPEEDS, NASA CR-114, November 1964.

19. Gray, L., and Liiva, J., WIND TUNNEL TESTS OF THIN AIRFOILS OSCILLATING NEAR STALL, USAAVLABS Technical Report 68-89A, U. S. Army Aviation Materiel Laboratories, Fort Eustis, Virginia, January 1969, AD 684323.

20. Hansen, K. C., BLADE DATA FOR THE CORRELATION PHASE OF THE HIGH SPEED ENGINE FAILURE CONTRACT, Sikorsky Aircraft Memorandum TEM-A-200. October 1964.

21. McCloud III, J. L., Biggers, J. C., and Stroub, R. H., AN INVESTIGATION OF FULL-SCALE HELICOPTER ROTORS AT HIGH ADVANCE RATIOS AND ADVANCING TIP MACH NUMBERS, NASA TN D-4632, July 1968.

22. Fenaughty, R., and Deno, E., NH-3A VIBRATORY AIRLOADS AND VIBRATORY ROTOR LOADS, Sikorsky Aircraft, Division of United Aircraft Corporation: NASC Report (in preparation. Contract NOw 64-0528-f, C/N 5368-65), Naval Air Systems Command, Washington, D.C.

APPENDIX I
MODIFICATIONS TO EQUATIONS OF REFERENCE 13

This appendix is intended to be used in conjunction with References 13 and 14 and, when so used, to provide documentation of the specific modifications made under this contract to the blade equations of motions given in those references. Inasmuch as Reference 13 and 14 are generally available and would be required for a detailed understanding of the blade equations used in this study, no attempt has been made to reproduce herein any parts of References 13 and 14. As a result, many of the symbols in the following equations are not included in the List of Symbols of this report but, rather, appear in the List of Symbols of References 13 and 14.

The basic equations governing the motion of rotor blades having chordwise mass unbalance and operating in steady, level flight are given in Reference 13. To extend these to the case of maneuvering flight, the equations were modified by adding terms representing the effect of fuselage motion on blade dynamic and aerodynamic forces. These terms were obtained directly from Reference 14 and, for convenience, are given below for each of the equations of Reference 13 to which they apply.

Flatwise Equation of Motion

To the right-hand side of Eq. (80) of Reference 13 is added

$$C_{13_i}\left(\bar{A}\sin\theta_o + \frac{\dot{X}}{\omega_{z_1}}\cos\theta_o\right) + \left(C_{12_i} - 0.75C_{10_i}\right)\theta_1\left(\bar{C}\sin\theta_o + \bar{B}\cos\theta_o\right)$$
$$+ C_{12_i}\left(-\bar{G}\cos\theta_o + \bar{F}\sin\theta_o\right) + C_{10_i}\left(-\bar{E}\cos\theta_o + \bar{D}\sin\theta_o\right) \tag{21}$$

Edgewise Equation of Motion

To the right-hand side of Eq. (86) of Reference 13 is added

$$C_{33_p}\left(-\bar{A}\cos\theta_o + \frac{\dot{X}}{\omega_{z_1}}\sin\theta_o\right) + \left(C_{47_p} - 0.75C_{15_p}\right)\theta_1\left(\bar{B}\sin\theta_o - \bar{C}\cos\theta_o\right)$$
$$- C_{15_p}\left(\bar{D}\cos\theta_o + \bar{E}\sin\theta_o\right) - C_{47_p}\left(\bar{F}\cos\theta_o + \bar{G}\sin\theta_o\right) \tag{22}$$

Torsional Equation of Motion

To the right-hand side of Eq. (89) of Reference 13 is added

$$-C_{\theta\theta_j}\left[\bar{\omega}_{x_1}\cos\psi + \bar{\omega}_{y_1}\sin\psi + \left(\bar{\omega}_{y_1}\cos\psi - \bar{\omega}_{x_1}\sin\psi\right)\left(1+\cos 2\theta_0\right)\right] \qquad (23)$$

Flapping Equation of Motion

To the right-hand side of Eq. (91) of Reference 13 is added

$$-\bar{M}_\beta\,\bar{r}_{cg}\,\bar{E} - \bar{I}_\beta\,\bar{G} \qquad (24)$$

Lead Angle Equation of Motion

To the right-hand side of Eq. (96) of Reference 13 is added

$$-\bar{M}_\beta\,\bar{r}_{cg}\,\bar{D} - \bar{I}_\beta\,\bar{F} \qquad (25)$$

Nominal Tangential Velocity Equation

To the right-hand side of Eq. (139) of Reference 13 is added

$$\left(1-\frac{\delta^2}{2}\right)\bar{v}_{o_{y_1}}\cos\psi + \left(\bar{e}+\bar{r}\right)\bar{\omega}_{z_1} - \delta\,\bar{v}_{o_{y_1}}\sin\psi - \bar{r}\beta\left(\bar{\omega}_{x_1}\cos\psi + \bar{\omega}_{y_1}\sin\psi\right)$$
$$-\bar{v}_{o_{y_1}}\left(\sin\psi + \delta\cos\psi\right)\left(\bar{v}_e'\cos\theta - \bar{\omega}_e'\sin\theta\right) \qquad (26)$$
$$+\theta_1\,\bar{v}_{o_{y_1}}\sin\psi\left(\bar{v}_e\sin\theta + \bar{\omega}_e\cos\theta\right)$$

Nominal Axial Velocity Equation

To the right-hand side of Eq. (140) of Reference 13 is added

$$(\bar{e}+\bar{r})(\bar{\omega}_{y_1}\cos\psi - \bar{\omega}_{x_1}\sin\psi) + \beta\,\bar{v}_{o_{y_1}}(\sin\psi + \delta\cos\psi)$$
$$-\bar{r}\,\delta\,(\bar{\omega}_{x_1}\cos\psi + \bar{\omega}_{y_1}\sin\psi) + \bar{v}_{o_{y_1}}(\sin\psi + \delta\cos\psi)\left[\bar{\omega}_e{}'\cos\theta + \bar{v}_e{}'\sin\theta\right] \quad (27)$$
$$+\theta_1\,\bar{v}_{o_{y_1}}\sin\psi\,(\bar{v}_e\cos\theta - \bar{\omega}_e\sin\theta)$$

In Eqs. (21) through (25), the following definitions apply:

$$\bar{A} = \dot{\bar{\omega}}_{x_1}\sin\psi - \dot{\bar{\omega}}_{y_1}\cos\psi + 2(\bar{\omega}_{x_1}\cos\psi + \bar{\omega}_{y_1}\sin\psi) \quad (28)$$

$$\bar{B} = \dot{\bar{v}}_{o_{y_1}}\cos\psi - \dot{\bar{v}}_{o_{x_1}}\sin\psi - \bar{v}_{o_{z_1}}(\bar{\omega}_{x_1}\cos\psi + \bar{\omega}_{y_1}\sin\psi) + \bar{\omega}_{z_1}(\bar{v}_{o_{y_1}}\sin\psi + \bar{v}_{o_{x_1}}\cos\psi) \quad (29)$$

$$\bar{C} = \dot{\bar{v}}_{o_{z_1}} - \bar{v}_{o_{x_1}}\bar{\omega}_{y_1} + \bar{v}_{o_{y_1}}\bar{\omega}_{x_1} \quad (30)$$

$$\bar{D} = \dot{\bar{v}}_{o_{y_1}}\cos\psi - \dot{\bar{v}}_{o_{x_1}}\sin\psi - \bar{v}_{o_{z_1}}(\bar{\omega}_{z_1}\cos\psi + \bar{\omega}_{y_1}\sin\psi) + \bar{\omega}_{z_1}(\bar{v}_{o_{y_1}}\sin\psi + \bar{v}_{o_{x_1}}\cos\psi) + \bar{e}\,\dot{\bar{\omega}}_{z_1} - \delta\,(\dot{\bar{v}}_{o_{x_1}}\cos\psi + \dot{\bar{v}}_{o_{y_1}}\sin\psi) - \bar{v}_{o_{z_1}}\delta\,(\bar{\omega}_{y_1}\cos\psi - \bar{\omega}_{x_1}\sin\psi) + \bar{\omega}_{z_1}\delta\,(-\bar{v}_{o_{x_1}}\sin\psi + \bar{v}_{o_{y_1}}\cos\psi) \quad (31)$$

$$\bar{E} = \ddot{\bar{v}}_{O_{z_1}} - \bar{\omega}_{y_1}\bar{v}_{O_{x_1}} + \bar{\omega}_{x_1}\bar{v}_{O_{y_1}} - \bar{v}_{O_{z_1}}\beta\,(\bar{\omega}_{y_1}\cos\psi - \bar{\omega}_{x_1}\sin\psi)$$

$$+ 2\dot{\beta}\,(\bar{\omega}_{y_1}\sin\psi + \bar{\omega}_{x_1}\cos\psi) - \bar{e}\,(\ddot{\bar{\omega}}_{y_1}\cos\psi - \ddot{\bar{\omega}}_{x_1}\sin\psi) \qquad (32)$$

$$-\beta\,(\ddot{\bar{v}}_{O_{x_1}}\cos\psi + \ddot{\bar{v}}_{O_{y_1}}\sin\psi) + \beta\bar{\omega}_{z_1}(\bar{v}_{O_{y_1}}\cos\psi - \bar{v}_{O_{x_1}}\sin\psi)$$

$$\bar{F} = \ddot{\bar{\omega}}_{z_1} - 2\dot{\beta}\,(\bar{\omega}_{x_1}\cos\psi + \bar{\omega}_{y_1}\sin\psi) - \beta\,(\ddot{\bar{\omega}}_{x_1}\cos\psi + \ddot{\bar{\omega}}_{y_1}\sin\psi) \qquad (33)$$

$$\bar{G} = \ddot{\bar{\omega}}_{x}\sin\psi - \ddot{\bar{\omega}}_{y_1}\cos\psi + 2(\bar{\omega}_{x_1}\cos\psi + \bar{\omega}_{y_1}\sin\psi) + 2\beta\bar{\omega}_{z_1}$$

$$+ 2\dot{\delta}\,(\bar{\omega}_{x_1}\cos\psi + \bar{\omega}_{y_1}\sin\psi) + \delta\,(\ddot{\bar{\omega}}_{x_1}\cos\psi + \ddot{\bar{\omega}}_{y_1}\sin\psi) \qquad (34)$$

$$+ 2\delta\,(\bar{\omega}_{y_1}\cos\psi - \bar{\omega}_{x_1}\sin\psi)$$

In addition to these modifications to the equations of Reference 13, other changes to the basic aerodynamic equations were necessary when unsteady data were used. Specifically, when a blade section was operating at a combination of a Mach number and an angle of attack where the unsteady data were to be used, the section angle of attack was defined by the velocity components at the quarter-chord rather than those at the three-quarter chord point, and the damping moment in pitch predicted by quasi-steady theory was eliminated. Formally, these changes were accomplished by setting $y_{IO_{3/4c}}$ equal to zero in Eqs. (139) and (140) of Reference 13 and a_0 equal to 0.5 in Eq. (146).

APPENDIX II
DETAILS OF THE CONVERSION OF SINUSOIDAL DATA TO α, A, AND B FORM

In any tabulation of data for subsequent use in a digital computer, it is imperative that the dependent quantity be associated with convenient tabular values of the independent parameters. In the present case, the dependent quantity was either C_n or $C_{m_{c/4}}$ and the independent parameters were α, A, and B. In this appendix, the method used for establishing this dependency of $C_{m_{c/4}}$ on α, A, and B will be described in detail. (Substantially the same method was used in Reference 10 to relate C_n to α, A, and B, but this earlier report lacks the detail of the present work.)

First, it is convenient to rewrite the reduced frequency of Eq. (14) as

$$k = \frac{c\omega}{2U} = \frac{\pi cf}{U} \tag{35}$$

and to insert this form into Eqs. (12) and (13) for A and B. The result is

$$A = \pm \frac{\pi cf}{U}\sqrt{\bar{\alpha}^2-(\alpha-\alpha_M)^2} \tag{36}$$

$$B = -\left(\frac{\pi cf}{U}\right)^2(\alpha-\alpha_M) \tag{37}$$

Now consider a typical hysteresis loop of $C_{m_{c/4}}$ versus α, as shown in the sketch in Figure 67. The angular velocity parameter A is positive over the lower half of the loop, which is the region in which α is increasing with time. A is negative over the upper half of the loop. A reaches its positive and negative maximums at $\alpha = \alpha_M$ and vanishes at both angular extremes of the loop. The angular acceleration parameter B is in exact antiphase with the angular displacement from the mean ($\alpha - \alpha_M$), reaching its negative maximum at maximum α and reaching its positive maximum at minimum α. B vanishes whenever $\alpha = \alpha_M$. It can be shown, both from Eqs. (36) and (37) and from a consideration of the typical loop in Figure 67,

that convenient tabular values of α, A, and B cannot be obtained directly from the loops. Hence, it is necessary to manipulate both the equations and the curves to produce cross plots suitable for interpolation. In subsequent paragraphs, each parameter in Eqs. (36) and (37) will be examined to determine its suitability as an interpolation variable.

The free parameters in A and B (Eqs. (36) and (37)) are the chord c, the amplitude of motion $\bar{\alpha}$, the velocity U, the angle of attack α, the mean angle of attack α_M, and the frequency f. (The local angle of attack α is not a free parameter since it has been selected as one of the three tabular quantities.) The chord c may be eliminated immediately because only a single value was available from the experiment, c = 2 ft. There were only three values of the amplitude $\bar{\alpha}$ and, as discussed in the main body of this report, most of the data were taken at $\bar{\alpha} = \pm 6$ deg and ± 8 deg. Similarly, there were only three values of the velocity U (or Mach number), and most of the data were taken at the lowest two values. The mean angle of attack α_M was taken every three degrees over a wide range of values. However, two factors must be considered here: (1) only integral values of α may be used as mesh points, and (2) the displacement relative to the mean position ($\alpha - \alpha_M$) may not exceed the motion amplitude $\bar{\alpha}$. Hence, this limits the number of values of α_M that could be used.

The only remaining parameter in Eqs. (36) and (37) is the frequency f. In most cases, the frequency values at which data were taken were f = 0 (steady state), 4, 8, 12, and 16 cps. This is a set of five equally spaced points that extend over a physically useful and realistic range. In many cases in the vicinity of the steady-state stall angle, the three additional values of f = 0.5, 1, and 2 cps were taken. Hence, it is logical to use f as an interpolation variable. This prospect is made even more attractive by the manner in which f appears explicitly in Eqs. (36) and (37).

To demonstrate the method used herein, first solve Eq. (37) for f to obtain

$$f = \frac{U}{\pi c} \sqrt{-\frac{B}{(\alpha - \alpha_M)}} \tag{38}$$

When Eq. (38) is substituted into Eq. (36), the equation for A becomes

$$A = \pm \sqrt{-\frac{B}{(\alpha - \alpha_M)}} \sqrt{\bar{\alpha}^2 - (\alpha - \alpha_M)^2} \qquad (39)$$

The first step in reducing the data was to cross-plot $C_{m_{c/4}}$ versus f. The procedure followed here was to pick a value of each of the parameters U (or M), $\bar{\alpha}$, and α_M, and then to work with the set of loops associated with the values of f within the set. Two cross plots were made through the set for each integral value of α: one cross plot was made for the increasing α branch of the loop, and the other was made for the decreasing α branch of the loop. A few selected cross plots are shown in Figure 68 for α_M = 0 deg (representing the potential flow regime) and in Figure 69 for α_M = 15 deg (representing the stalled flow regime). In both figures, M = 0.2 and $\bar{\alpha}$ = 6 deg. It is interesting to note that in potential flow (Figure 68) the $C_{m_{c/4}}$ variation with f is well behaved over the entire range, which justifies a minimal number of frequency points. However, in stalled flow (Figure 69), the $C_{m_{c/4}}$ variation with f is very erratic, particularly in the range $0 \leq f \leq 4$ cps. These facts should be noted in the design of any future experiments on the unsteady response of oscillating airfoils.

After the cross plots were completed for all of the loops, the result was a multitude of curves of $C_{m_{c/4}}$ versus f. In this set of curves, all values of the parameters α, α_M, $\bar{\alpha}$, and U were represented within the limitations of the experiment. Each individual curve was associated with a particular set of values of α, α_M, $\bar{\alpha}$, and U, and with either $\dot{\alpha} > 0$ or $\dot{\alpha} < 0$.

In the next part of the data reduction procedure, a number of interrelated steps were taken (see the flow chart in Figure 70). Initially, a value of $\bar{\alpha}$ and a value of U were chosen (e.g., $\bar{\alpha}$ = 6 deg, U = 230 ft/sec). Then an integral mesh point value of α was chosen. Next, a convenient mesh point value of B was chosen. (The set of B values used in the present study was B = 0, $\pm$0.001, $\pm$0.004, $\pm$0.007, $\pm$0.01.) At this point, the only undetermined free parameter in Eqs. (38) and (39), or in the family of curves of $C_{m_{c/4}}$ versus f, is the mean angle of attack α_M. A series of values of α_M was chosen next, subject to the restriction that $|\alpha - \alpha_M| \leq \bar{\alpha}$. For each value of α_M, a value of f was calculated from Eq. (38) and a value of A was calculated from Eq. (39). Next, the two curves of $C_{m_{c/4}}$ versus f for the specific values of $\bar{\alpha}$, U, α, and α_M were selected from the set, one for increasing α and one for decreasing α. These curves were entered at the calculated value of f, and the interpolated values of $C_{m_{c/4}}$ were plotted versus the calculated value of A. The value of $C_{m_{c/4}}$ associated

with increasing α was plotted at the positive value of A, and the value of $C_{m_{c/4}}$ associated with decreasing α was plotted at the negative value of A. For the special case of α stationary (i.e., at the end points of a loop), the interpolated $C_{m_{c/4}}$ was plotted at A = 0. After this had been done for all possible values of α_M, a faired curve was passed through the points, representing the variation of $C_{m_{c/4}}$ with A for a single value of α and B. A new value of B was then sought, and the entire process was repeated.

An example of these curves is shown in Figure 71 for M = 0.2 and for a mesh point value of α = 15 deg. In this figure a set of values of B ranging from -0.007 to +0.007 was selected. As discussed in the text, most of the data were originally obtained at $\bar{\alpha} = \pm 8$ deg; hence, the faired curves are biased to conform to these points. The theoretical variation of $C_{m_{c/4}}$ versus A, which is derived in Appendix III, is also plotted in this figure. It is interesting to note that even at this high incidence angle, some measure of agreement still exists between theory and experiment for large positive values of A (i.e., for $\dot{\alpha} > 0$). A study of any of the actual loops described elsewhere in this report will show that almost the entire branch of the loop for $\dot{\alpha} > 0$ tends to behave like a theoretical loop, even when the local angle exceeds the stalling angle, provided that the frequency of motion is high enough.

The faired curves of $C_{m_{c/4}}$ versus A were then cross-plotted with respect to B at constant α for a selected set of values of A, namely, A = 0, $\pm$0.01, $\pm$0.025, $\pm$0.04. Once again curves were faired through the points, and adjustments were made in the faired curves to provide as smooth a set as possible. A third and final cross plot was then made of $C_{m_{c/4}}$ versus α for constant values of A and B (see Figures 5 through 7). After the curves were smoothed through these points, a number of correlations were performed between the original loops and the faired curves. In many cases, a normal scatter was observed in correlating the smoothed data with the original loops, but in a few cases a consistent discrepancy was observed. In these cases, the faired data points and curves were adjusted to produce better agreement with the original loops. This level of agreement is discussed in the main body of this report (Figures 9 through 14). Finally, after a satisfactory agreement had been attained, the data points were tabulated and are presented in Table II.

APPENDIX III
THEORETICAL NORMAL FORCE AND MOMENT COEFFICIENTS FOR SINUSOIDAL MOTION IN TERMS OF α, A, AND θ

The expressions for the complex, unsteady normal force and moment coefficients for sinusoidal pitching motion will be taken from Eqs. (4) and (5). The Theodorsen function, C(k), will be substituted from Eq. (6), and the complex angular displacement will be taken from Eq. (7). In accordance with the statements in the text following Eq. (7), the first terms of Eqs. (4) and (5) will be rewritten as

$$2\pi C(k)\alpha^{*} \longrightarrow 2\pi\alpha_{M} + 2\pi C(k)\bar{\alpha}e^{i\omega t} \tag{40}$$

$$\pi\left(a_0+\tfrac{1}{2}\right)C(k)\alpha^{*} \longrightarrow \pi\left(a_0+\tfrac{1}{2}\right)\alpha_{M} + \pi\left(a_0+\tfrac{1}{2}\right)C(k)\bar{\alpha}e^{i\omega t} \tag{41}$$

Hence, Eqs. (4) and (5) become

$$c_n^{*} = 2\pi\alpha_{M} + \pi\bar{\alpha}e^{i\omega t}\left\{2(F+iG) + \frac{ic\omega}{2U}\left[1+2(F+iG)\left(\tfrac{1}{2}-a_0\right)\right] + a_0\left(\frac{c\omega}{2U}\right)^{2}\right\} \tag{42}$$

$$\begin{aligned} c_m^{*} = {} & \pi\left(a_0+\tfrac{1}{2}\right)\alpha_{M} + \pi\bar{\alpha}e^{i\omega t}\left\{\left(a_0+\tfrac{1}{2}\right)(F+iG)\right. \\ & \left. + \frac{ic\omega}{2U}\left(\tfrac{1}{2}-a_0\right)\left[\left(a_0+\tfrac{1}{2}\right)(F+iG)-\tfrac{1}{2}\right] + \tfrac{1}{2}\left(\frac{c\omega}{2U}\right)^{2}\left(\tfrac{1}{8}+a_0^{2}\right)\right\} \end{aligned} \tag{43}$$

In the present study the pivot axis was located at the quarter-chord, or $a_0 = -1/2$. When this value is substituted into these equations, the complex exponential is expanded, and the real part of each equation is taken; the result is

$$c_n = 2\pi\alpha_M - \pi\left[k(1+2F) + 2G\right]\bar{\alpha}\sin\omega t - \pi\left[\frac{k^2}{2} + 2kG - 2F\right]\bar{\alpha}\cos\omega t \tag{44}$$

$$c_m = \frac{\pi}{2}\left[k\bar{\alpha}\sin\omega t + \frac{3}{8}k^2\bar{\alpha}\cos\omega t\right] \tag{45}$$

where

$$k = \frac{c\omega}{2U}$$

is the reduced frequency for sinusoidal motion. From Eqs. (8) through (13) it is easily shown that, for sinusoidal motion,

$$\bar{\alpha}\sin\omega t = -\frac{A}{k} \tag{46}$$

$$\bar{\alpha}\cos\omega t = -\frac{B}{k^2} \tag{47}$$

Hence, Eqs. (44) and (45) may be reduced to the form

$$c_n = 2\pi\alpha_M + \pi A\left[1 + 2F + \frac{2G}{k}\right] + \pi B\left[\frac{1}{2} + \frac{2G}{k} - \frac{2F}{k^2}\right] \tag{48}$$

$$c_m = -\frac{\pi}{2}\left[A + \frac{3}{8}B\right] \tag{49}$$

Although the torsional stall flutter phenomenon is primarily associated with the behavior of the unsteady pitching moment, it is instructive to look at the variations in normal force coefficient with changes in the relevant parameters. One such variation is shown in Figure 72, in which c_n is plotted versus A for the special case of $B = 0$. In calculating this theoretical curve, the angles $\alpha = \alpha_M = 0$ deg and $\alpha = 8$ deg were chosen, as was a series of values of k. Equation (12) was then used to calculate a comparable series of values of A, and then Eq. (48) was used to calculate c_n. The circled points in Figure 72 were taken from the original tabulation of Reference 10, which has already been discussed in Appendix II. In this case, the agreement between the tabulated results and the theory is quite good.

Unclassified

Security Classification

DOCUMENT CONTROL DATA - R & D

(Security classification of title, body of abstract and indexing annotation must be entered when the overall report is classified)

1. ORIGINATING ACTIVITY (Corporate author)	2a. REPORT SECURITY CLASSIFICATION
Sikorsky Aircraft Division of United Aircraft Corporation Stratford, Connecticut	Unclassified 2b. GROUP

3. REPORT TITLE

INVESTIGATION OF HELICOPTER CONTROL LOADS INDUCED BY STALL FLUTTER

4. DESCRIPTIVE NOTES (Type of report and inclusive dates)

Final Report

5. AUTHOR(S) (First name, middle initial, last name)

Peter J. Arcidiacono — Lawrence M. Casellini
Franklin O. Carta — Howard L. Elman

6. REPORT DATE	7a. TOTAL NO. OF PAGES	7b. NO. OF REFS
March 1970	177	22

8a. CONTRACT OR GRANT NO.	9a. ORIGINATOR'S REPORT NUMBER(S)
DAAJ02-68-C-0048 b. PROJECT NO. Task 1F162204A14604 c. d.	USAAVLABS Technical Report 70-2 9b. OTHER REPORT NO(S) (Any other numbers that may be assigned this report)

10. DISTRIBUTION STATEMENT

This document is subject to special export controls, and each transmittal to foreign governments or foreign nationals may be made only with prior approval of U. S. Army Aviation Materiel Laboratories, Fort Eustis, Virginia 23604.

11. SUPPLEMENTARY NOTES	12. SPONSORING MILITARY ACTIVITY
	U. S. Army Aviation Materiel Laboratories Fort Eustis, Virginia

13. ABSTRACT

An analytical study was conducted to determine if available unsteady aerodynamic test data could be used with existing helicopter rotor aeroelastic and variable inflow analyses to predict the stall flutter response of a helicopter rotor blade. Incompressible unsteady aerodynamic data for an NACA 0012 airfoil executing pure sinusoidal pitching motions were employed. To apply such data under rotor blade operating conditions where multiharmonic motions and velocity variations exist, the data were expressed as functions of instantaneous section angle of attack and its derivatives. In addition, scaling procedures were developed in an attempt to account for the effects of compressibility.

Limited application of the resulting analysis to define the aeroelastic characteristics of several blade designs showed that significant self-excited torsional oscillations of the stall flutter type could be predicted for certain combinations of flight conditions and blade designs. Control load correlation studies were performed with CH-53A maneuvering flight test data and with level flight test data from the NH-3A (S-61F). Although the analyses produced self-excited stall flutter oscillations, the degree of correlation indicates the need for further development. Recommendations for such development are described in the report.

DD FORM 1 NOV 68 1473 REPLACES DD FORM 1473, 1 JAN 64, WHICH IS OBSOLETE FOR ARMY USE.

Unclassified

Security Classification

14. KEY WORDS	LINK A		LINK B		LINK C	
	ROLE	WT	ROLE	WT	ROLE	WT
Helicopter Rotor Blades						
Rotor Aeroelasticity						
Rotor Blade Control Loads						
Unsteady Aerodynamics						
Stall Flutter						
Dynamic Stall						